The Role of Wall Shear Stress in the Failure of Arteriovenous Fistula for Hemodialysis Vascular Access

Thesis

The Role of Wall Shear Stress in the Failure of Arteriovenous Fistula for Hemodialysis Vascular Access

Thesis submitted by

Marco Franzoni

for the degree of

Doctor of Philosophy

Discipline of Life Science

Open University research school, UK

"Mario Negri" Institute for pharmacological research, ITA

Director of Studies

Andrea Remuzzi, EngD

Second Supervisor

Andrew Narracott, MPhys, PhD

28 September 2015 DATE OF SUBMISSION

7 JANUARY 2016 DATE OF AWARD

The Role of Wall Shear Stress in the Failure of Arteriovenous Fistula for Hemodialysis Vascular Access

Marco Franzoni

Open University research school, UK
"Mario Negri" Institute for pharmacological research, ITA
Doctor of Philosophy
September 2015

Abstract

Native arteriovenous fistulas created in the forearm between the radial artery and the cephalic vein are currently considered the best vascular access for hemodialysis in terms of outcome and safety. However, this type of access is associated with a significant failure rate that is generally caused by intimal hyperplasia development and consequent stenosis. Computational studies have shown that intimal hyperplasia is preferentially localized in regions of the fistula that are exposed to disturbed wall shear stresses. This thesis reports the development and testing of a novel, real-time controlled cone-and-plate device to assess the role of changes in shear stress induced by fistula creation on the activation state of endothelial cells and paracrine signalling in vitro. The selected shear stress waveforms were representative of the pulsatile/unidirectional waveforms in zones that are generally not affected by hyperplasia or the disturbed/reciprocating waveforms present in the high-risk stenosis areas. Experimental results showed that after 48 hours of flow exposure, these stimuli elicited differential effects on human umbilical vein endothelial cells monolayers. Pulsatile waveforms induced major cellular shape remodeling and upregulation of the transcription factor KLF2 mRNA expression. On the contrary cells exposed to reciprocating flows showed a lack of cytoskeletal remodeling, upregulation of the enzyme PLD1, the integrin subunit ITGA4 and RASA1 (coding for the protein activator p120RasGAP) mRNA expression and an increased production of chemoattractant cytokines MCP-1 and IL-8. Furthermore, it was observed that human smooth muscle cells incubated for 24 hours with medium conditioned by endothelial cells exposed to reciprocating shear stress stimuli, had an increased rate of proliferation compared to smooth muscle cells cultured in medium conditioned by endothelial cells exposed to pulsatile waveforms. These results confirm potential links between disturbed wall shear stress and arteriovenous fistula failure.

Thesis index

Figures index

Tables index

List of abbreviations (alphabetical order)

ACW	Actin cortical web
AJ	Adherens junction
AKT	Protein kinase B
ALK	Activin receptor-like kinase
Ang-II	Angiotensin II
AP-1	Activator protein 1
AV	Arteriovenous fistula
AVG	Arteriovenous graft
BAEC	Bovine aortic endothelial cell
BMP	Bone morphogenic protein
BMPR	Bone morphogenic protein receptor
CCN	Matricellular proteins family
CCN1	Cysteine-rich angiogenic inducer 61
CCN2	Connective tissue growth factor
CCN3	Nephroblastoma overexpressed
CCR2	Chemokine receptor 2
CD49d	Integrin alpha4
CDC42	Cell division control protein 42
cDNA	complementary deoxyribonucleic acid
CFD	Computational fluid dynamic
CGX	Glycocalyx
CK1	Casein kinase 1
CK1α-LS	Casein-kinase-α-LS
CKD	Chronic kidny disease
COLLS	Collagenase solution
CPD	Cone-and-Plate device
CVC	Central venous catheter
DAPB	Dense peripheral actin band

DAPI	4',6-diamidin-2-fenilindolo
DMSO	Dimethyl sulfoxide
DNA	deoxyribonucleic acid
Dnase	Deoxyribonuclese
DPBS	Dulbecco's phosphate buffered solution
EC	Endothelial cell
ECGS	Endothelial cell growth supplement
ECM	Extracellular matrix
EM	Experimental medium
EndMT	Endothelial-to-mesnchymal transition
Eng	Endoglin
eNOS	Endothelial nitric oxide synthase
EphB4	Ephrin type-B receptor 4
ERK	Extracellular-signal-regulated kinase
ESL	Endothelial surface layer
ESRD	End-stage renal disease
ET1	Endothelin 1
FA	Focal adhesion
FACS	Fluorescence-activated cell sorting
FAK	Focal adhesion kinase
FB	Fibroblast
FF	Feed-forward block
FGF	Fibroblast growth factor
FITC	Fluorescin isothiocyanate
GAG	Glycosaminoglycan
GDP	Guanosine diphosphate
GFR	Glomerular filtration rate
GJ	Gap junctions
GM	Growth medium
GTP	Guanosine triphosphate

GTPase	Guanosine triphosphate hydrolase enzyme
H2O2	Hydrogen peroxide
HAOSMC	Human aortic smooth muscle cell
HD	Hemodialysis
HDMS	Hexamethyldisilazane
hnRNP-C	Heterogeneous nuclear ribonucleoprotein-C
HO	Heme-oxygenase
HS	Hepran sulfate
HUVEC	Human umbilical vein endothelial cell
ICAM	Intacellular adhesion molecule
IF	Interferon
IH	Intimal hyperplasia
IL-6/8/10/1β	Interleukin 6, 8, 10 or 1β
ITGA	Integrin alpha
ITGB	Integrin beta
JNK	JUN n-terminal kinase
KLF2/4	Krüppel-like factor 2 or 4
MAPK	Mitogen-activated protein kinase
MCP-1	Monocyte chemoattractant 1
MEJ	Myoendothelial junctions
MET	Hepatocyte growth factor receptor
MF	Myofibroblast
miRNA	Micro ribonucleic acid
MMP	Metalloproteinase
mRNA	Messanger ribonucleic acid
MTOC	Microtubule-organizing center
MTS	3-(4,5-dimethylthiazol-2-yl)-5-(3-carboxymethoxyphenyl)-2-(4-sulfophenyl)-2H-tetrazolium
NADPH	Nicotinamide adenine dinucleotide phosphate-oxidase
NF-κB	Nuclear factor κB

NIB	Acquisition data board
NKF-KDOQI	National Kidney Foundation -Kidney Disease Outcomes Quality Initiative
NO	Nitirc oxide
Nrf-2	Nuclear factor-erythroid 2-like 2
OSI	Oscillatory shear index
PA	Phosphatidic acid
PAI-1	Plasminogen activator inhibitor-1
PAK	Serine/Threonine-protein kinase
PC	Phosphatidylcholine
PD	Peritoneal dialysis
PDGF	Platelet derived growth factor
PECAM	Platelet-endothelial cell adhesion molecule
PI3K	phosphatidylinositol-3-kinases
PID	Proportional-integral controller
PKA	Protein kinase A
PLD	Phosolipase D
PUL_A	Pulsatile waveform A
PUL_V	Pulsatile waveform V
Rac	Ras-related C3 substrate
RasGAP	Ras GTPase activating protein
RBP-Jk	Recombinant binding protein-Jk
Re	Reynolds number
REC_A	Reciprocating waveform A
REC_B	Reciprocating waveform B
RGB	Red-green-blue color model
Rho	Ras homolog
RNA	Ribonucleic acid
Rnase	Ribonuclease
ROCK	Rho-associated protein kinase

ROS	Reactive oxygen species
RRT	Renal replacement therapy
RT-PCR	Reverse transcriptase-polymerase chain reaction
SEM	Scanning electron microscopy
SMAD	Small mother against decapentaplegic proteins
SMC	Smooth muscle cell
TAWSS	Time averaged wall shear stress
TGF-β	Tranforming growth factor β
TIMP	Tissue inhibitor metalloproteinase
TJ	Tight junction
TNF	Tumor necrosis factor
TβR	Transforming growth factor β receptor
VA	Vascular access
VCAM	Vascular adhesion molecule
VEGF	Vascular endothelial growth factor
VEGFR	Vascular endothelial growth factor receptor 2
VLA4	Very late antigen 4
vWF	Von Willebrand factor
Wo	Womersley number
WSS	Wall shear stress
ZO	Zonula occludens
α-SMA	α smooth muscle actin

Introduction

I.A) Chronic kidney disease and therapies

Chronic kidney disease (CKD) has been recently identified as the 18th major cause of global mortality with the third highest increase (82.3%) in the last two decades, resulting in the recognition of CKD as a public health priority (1). CKD severity is defined by five stages based on renal function and assessed by measuring the Glomerular Filtration Rate (GFR, table 1) (2, 3).

CKD stage	GFR [mL/min/1.73m^2]
1	90+
2	60-89
3a	45-59
3b	30-44
4	15-29
5 or ESRD	<15

Tab.1: CKD stages defined by GFR according to the Kidney Disease Outcome Quality Initiative (3).

The fifth and worst CKD stage, also referred as end-stage renal disease (ESRD), occurs in~ 10% of the population and requires renal replacement therapies (RRT) to address the diminished renal function that jeopardizes patient survival (3). RRT however, have very high social and economic costs. In developed countries, the 0.1-0.2% of the population that is affected by ESRD absorbs 2-3% of total health-care expenditure (4). In the future the problem will become worse due the increase of the older population. The therapies available to treat ESRD patients are transplant, peritoneal dialysis (PD) and haemodialysis (HD).

Transplant is considered the best solution in terms of outcomes and impact on patient lifestyle. However, the number of donors is not sufficient to provide organs for all waiting patients. According to the Italian Health Ministry data for 2014 transplantation activity, among the 8700 patients recorded in the kidney waiting list only 18.25% received a transplant and 1.8% did not survive. The average waiting time in the list is more than 3 years (5). In this context, dialysis techniques remain the only therapy available for those patients that do not match transplant requirements or are still waiting for a donor.

PD consists of a synthetic membrane surgically inserted into the patient abdominal cavity. The membrane is filled with dialysis solution that exchanges solutes with corporeal fluids and must be replaced periodically. Depending on the PD modality, dialysis solution is either replaced manually or by an automatic system that allows patients to perform PD during the night. Compared to HD, this dialysis technique presents some advantages including the possibility to perform it autonomously, at home, according to patient necessities. It also presents disadvantages including less efficient solute exchange, the necessity to train patients in PD management and high risks of infections such as peritonitis (6, 7).

HD is an RRT performed in specialized centres by dedicated personnel. It consists of connecting the patient to an extracorporeal device that provides filtration functions. It presents advantages with respect to PD in terms of better filtration efficiency. However, HD also has disadvantages as patients are required to go frequently and for several hours to a dialysis centre. Finally it requires also the surgical creation of a permanent vascular access (VA), able to provide adequate blood flow to the filtration system as well as resisting repeated puncture. The VA is both the "*lifeline*"

and the "*Achille's heel*" of HD treatment and its dysfunctions are the main causes of hospitalization among HD patients (8, 9).

Many studies have reported outcomes and patient satisfaction related to PD and HD, but results are controversial. According to very recent studies (10), no major differences between the two techniques emerged in long-term outcomes as well as no differences in hospitalization or infection rates. However, PD showed a slightly better outcome in the short-term (2-3 yrs). The authors proposed the maintenance of a higher residual renal function in PD patients compared to HD patients was the reason for improved initial PD outcomes (11). In the long-term PD loses this initial advantage, possibly due the degradation of the peritoneal membrane and the loss of ultra-filtration capacity. Regarding patient satisfaction (12, 13), despite higher symptoms of depression and poorer physical health, PD patients were more satisfied compared to HD patients due to the higher flexibility and autonomy guaranteed by the PD technique. In conclusion the choice between PD and HD should take into account patient lifestyle and preferences, together with clinical aspects. Several authors have underlined that the limited or partial information currently provided by clinicians to patients should be improved in order to define the best dialysis strategy (14, 15).

I.B) Vascular accesses for hemodialysis

Surgical creation of a Vascular Access (VA) is a key aspect of hemodialysis (HD) treatment. The VA is necessary to perform efficient HD and it consists of a usually permanent access to the bloodstream, that clinicians use to connect patients to dialyzer devices. To meet HD requirements, the VA has to ensure an adequate blood flow through the dialyzer, to withstand repeated cannulation and to avoid complications

like infection. Despite the efforts to ameliorate VA complications, no definitive solutions are currently available to completely avoid VA-related complications (16, 17).

Nowadays there are three main possibilities to create a VA (table 2). For long-term dialysis, the preferred techniques are the creation of a native arteriovenous fistula (AVF) or an arteriovenous synthetic graft (AVG). These VA require time to mature and meet requirements for dialysis thus are generally planned weeks before the commencement of dialysis. Alternatively, a central venous catheter (CVC) is a VA immediately available for HD and is generally used in patients that commence HD as emergency treatment (18).

Permanent vascular accesses	
Order of preference	**Type**
Arteriovenous fistula	Radial-cephalic fistula
	Brachial-cephalic fistula
	Brachial-basilic transposition fistula
Arteriovenous graft	Biological
	Synthetic
Central venous catheter	Internal jugular vein
	Femoral vein
	Subclavian vein

Tab.2: Permanent vascular accesses order of preference (19).

The AVF, introduced by Cimino-Brescia in 1966, consists of the surgical anastomosis between an artery and a vein in the arm. There are three basic types of AVF, the radial-cephalic, the brachial-cephalic and the brachial-cephalic transposition. There are different surgical techniques available to create the anastomosis. The possibilities are the end-to-end and the side-to-side anastomosis or the side-to-end of the

vein-to-artery or artery-to-vein. The radial-cephalic AVF created in the forearm with the side-to-end technique is considered the gold standard due its simplicity, low incidence of complication and long-term patency rate. Several studies addressed AVF outcomes and reported primary failure rates of 18%-28%, a one-year patency rate (including primary failure) of 56%-64% and a two-year patency of 44%-58%. Secondary patency rates of AVFs treated for primary failure were 64%-78% after one year and 56%-73% at two years (20-22). In recent years a major effort has been made to induce clinicians to adopt AVF creation in preference to other VA types. This has resulted in an increase in AVF placement in USA as reported in figures 1 and 2 (15, 23, 24).

The AVG consists of a high capacity synthetic or biological prosthesis, interposed between an artery and a vein, cannulated for HD. It allows clinicians to connect vessels that are distant or deep in subcutaneous tissues (25). Several materials and surgical techniques are available to create an AVG. Biological allo/heterografts as well as polymeric prosthesis (Dacron® or ePTFE) are currently used to obtain straight, curved or loop configurations that can be placed in the forearm, arm or thigh (26-28). Several studies attempting to determine the best choice between biological or synthetic grafts, failed to define a consistent result in terms of outcome or infection rate. AVG however, should be considered the second choice for VA creation due its lower patency rate, higher risk of infection and ischemia compared to AVF (29). Only in selected cases should the AVG be the preferred course of treatment. These cases include patients with lack or fragility of autologous vessels, with lack of access to superficial veins due to obesity or for short-term pediatric HD (30).

CVCs consist of thin synthetic tubes that are surgically inserted into large veins. They can be made from different materials and can have different geometries (31). CVCs are recommended for predicted short-term HD treatment or for emergency

initiation of HD (32). A non-tunneled CVC is usually used as a temporary (acute) access while for long-term HD purposes tunneled CVCs are preferable (33). Moreover tunneled CVCs usually also have a cuff that is placed in the subcutaneous tissue to provide a fibrotic seal for transcutaneous catheter passage, reducing infection risks. CVCs are considered the third choice for VA due to lower patency rates and higher risk of infection and complication related to the access procedure compared to AVF and AVG (34-36).

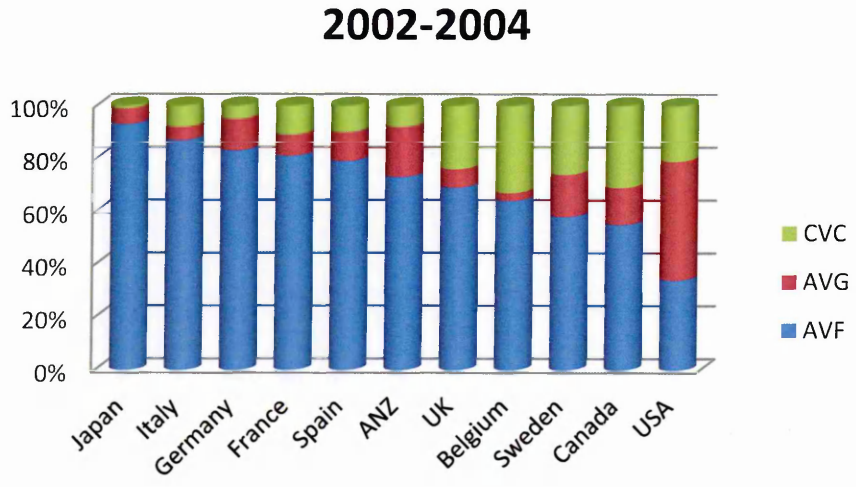

Fig.1: Percentage of VA types in 2002-2004 period of surveillance (23).

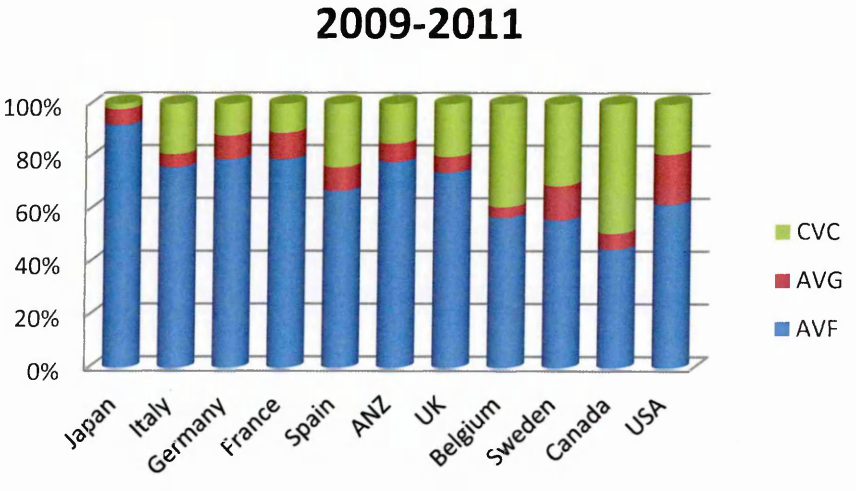

Fig.2: Percentage of VA types in 2009-2011 period of surveillance (15).

I.C) Native arteriovenous fistula for hemodialysis

National VA creation guidelines provide slightly different indications about preference for VA choice and HD requirements (37). However, in the last two decades common features have emerged to define the best practice to perform HD. As mentioned before, the radial-cephalic, side-to-end AVF is considered the gold standard (16, 17) as it comes closest to the ideal VA compared to other available techniques.

The success of a VA depends on the possibility for clinicians to repeatedly use it in order to perform efficient dialysis treatment. This means that a number of requirements must be met by the AVF (38). These requirements are reported in table 3.

Arterial requirements	Venous requirements
Pressure differences between arms < 20 mmHg	Patency of vessel and absence of obstructions
Patent palmar arch	Straight segment for cannulation
Lumen diameter at point of anastomosis ≥ 2 mm	Lumen diameter at point of anastomosis ≥ 2.5 mm
	Continuity with proximal central veins

Tab.3: Requirements for vessels eligible for AVF creation that should be evaluated prior to surgery (38).

Firstly an AVF must provide an adequate blood flow (350-500 mL/min) to the dialyzer. To remain patent during the procedure the AVF blood flow should be slightly greater than the demand of dialyzer. On the contrary, insufficient blood flow causes recirculation that forces clinicians to decrease the dialyzer demand with an increase of the time of treatment. Moreover, low AVF blood flow can negatively affect initial AVF

development causing early fistula failure due to the impossibility for clinicians to use it for adequate treatment.

The second requirement for a functional AVF is appropriate maturation of the fistula itself. This process needs time, flow and pressure in order to induce a series of events that lead to an increase in vein diameter and venous wall thickness (39, 40). A correctly matured AVF allows clinicians to undertake repetitive cannulations (3 sessions of 4 hrs per week) and to perform efficient HD treatment.

Another important AVF requirement relates to the AVF position in the surrounding tissues. The AVF must be within 1 cm from the skin surface to allow cannulation. A possible solution using deep vessels is called transposition and consists of the dissection of the deep vein and in the positioning to a more superficial position. To ensure an easy and safe cannulation, the AVF must also have a relatively straight segment of several centimeters (17).

A key point of a well functioning AVF is the time of maturation before use (41, 42). The general opinion is that the optimal time that should elapse between creation and first cannulation, is 3-4 months and strictly not less than 1 month (43, 44). A clinical study that assessed this problem found that no significant decrease in risk of failure was associated with AVFs cannulated 14 days after creation compared to those cannulated after 3 months (43, 45).

The timing of AVF placement should be optimised not only to ensure AVF maturation, but also to allow time to eventually create a second access in cases of early failure of the first VA and to avoid the use of a catheter as an initial dialysis access (16, 17). Since no disadvantages are related to early AVF creation, the National Kidney Foundation - Kidney Disease Outcomes Quality Initiative (NKF - KDOQI) guidelines suggest that patient clinical parameters, such as creatine clearance or stage of CKD,

indicate the anticipated need for AVF placement. A general rule for non-emergency dialysis patients is to create an AVF one year before dialysis is required to initiate the treatment.

To maximize AVF outcomes it is important to perform initial patient evaluation. Previous insertion of a CVC or major thoracic surgery and trauma will affect success of the AVF (46). Moreover, a detailed direct evaluation of both artery and vein functionality should be assessed to plan the access creation (47, 48). Doppler ultrasound is considered the best approach to perform pre-evaluation for AVF placement (49, 50). To visualize vessel anatomy angiography is also available. However, this requires the use of a radio-contrast liquid that should be avoided in CKD patients. Recent advances in medical imaging and in computer-assisted surgical planning have made AVF positioning a relatively simple and quick procedure that causes minimal patient morbidity, compared to graft insertion (51).

Other aspects that can be evaluated before AVF surgery with non-invasive methods are arterial narrowing and the presence of calcifications, usually related to co-morbidity such as hypertension and diabetes in ESRD patients. Also, the patency of the palmar arch should be evaluated with the Allen test together with Doppler ultrasonography examination (52). This ensures that the collateral circulation provided by the ulnar artery delivers enough blood flow to the hand when the dominant artery is used to create an AVF.

Venous evaluation is even more important to create a VA since vascular problems affecting AVF patency are more likely to be venous than arterial. The cephalic vein is considered the best choice to create an AVF due to its superficial location and easy access to the vein when the patient is sitting for dialysis treatment. Non-invasive venous assessment enhances the chance to successfully create an AVF rather than a

graft. Venous mapping also dramatically reduces unsuccessful surgical exploration since clinicians can evaluate the existence of vessels available for an AVF prior to surgery. Vein mapping is thus very important to increase AVF placement (53) (54).

A newly created AVF experiences large changes in blood flow and mechanical loads that induce vessel wall remodeling (55) to restore a more physiological condition. Successful vascular remodeling or maturation should end within few months. At this time point an experienced clinician should evaluate the maturation level and decide if the AVF is suitable for HD access. The protocol for accomplishing this evaluation requires a simple, cost-effective, physical examination, as this has been shown to result in 80% accuracy in identifying a mature AVF and allows the clinician to diagnose the major causes of failure (39).

Several complications can result in early or late failure of the AVF (56). Early failure causes can be divided into inflow and outflow problems (57). Since AVF maturation requires high blood flow and pressure, insufficient arterial diameter results in early failure. Despite pre-operative evaluation, which allows some causes of vessel diameter reduction to be identified, an acquired juxta-anastomotic or proximal venous stenosis can occur immediately after AVF creation, resulting in failure. Whilst the etiology of the stenosis is not clear, damage to the *vasa vasorum*, vessel manipulation during surgery and altered hemodynamics typical of anastomosis curvature may be involved in this process. This lesion is usually treated by angioplasty or surgically (58-61). However, even successfully treated AVFs have a lower long-term outcome compared to those that matured autonomously (62).

Outflow problems are related to abnormal increase of resistance to blood flow downstream of the AVF (56). This can be caused by lack of venous diameter increase after AVF creation or phenomena such as fibrosis and stenosis caused by trauma.

Another important aspect that should be evaluated prior to surgery is the presence of accessory veins (63, 64). The ideal anatomy for a vein suitable for AVF is the presence of a long straight segment and the absence of side branches. The presence of accessory veins could result in a drop in blood flow and pressure at the level of the AVF and negatively affect the maturation process. Some clinical controversies exist in how to avoid complications related to accessory veins (65). A recent study (66) suggests that these veins should be ligated or embolized to assist non-maturing AVFs. However, the lack of randomized clinical trials does not allow clinicians to confirm these procedures as more effective compared to angioplasty.

Successful maturation of the AVF does not prevent long-term failure (67). Failures that occur 3 months following AVF creation are referred to as late failure. Possible causes of AVF late failure are similar to causes of early failure and consist of venous stenosis and arterial lesions that develop progressively over time. Venous stenosis is the first cause of AVF late failure and consists mainly in an increase of wall thickness due to neointima formation, not adequately compensated for by outward remodeling (68). Intimal hyperplasia (IH) consists of an uncontrolled proliferation of cellular components of the vessel wall, especially smooth muscle cells (SMCs) and fibroblasts (FBs) that acquire an activated phenotype and migrate underneath the endothelial layer (69, 70). As shown in figure 3, this pathology develops mainly in specific areas of the AVF such as the venous side of the anastomosis or at the more proximal area above the juxta-anastomotic curvature between the feeding artery and the draining vein. Another high-risk stenosis area is the anastomotic floor of the feeding artery (71).

A further AVF dysfunction that leads to late failure is thrombosis (58). It occurs mainly on the venous side of the AVF and is identified by clinically undetectable blood

flow through the AVF. In certain cases, despite the stenosed AVF, the blood flow is preserved by the collateral venous branches. The stenotic lesion is commonly treated with angioplasty and failure is caused by the impossibility to intervene to reestablish an adequate blood flow through the AVF.

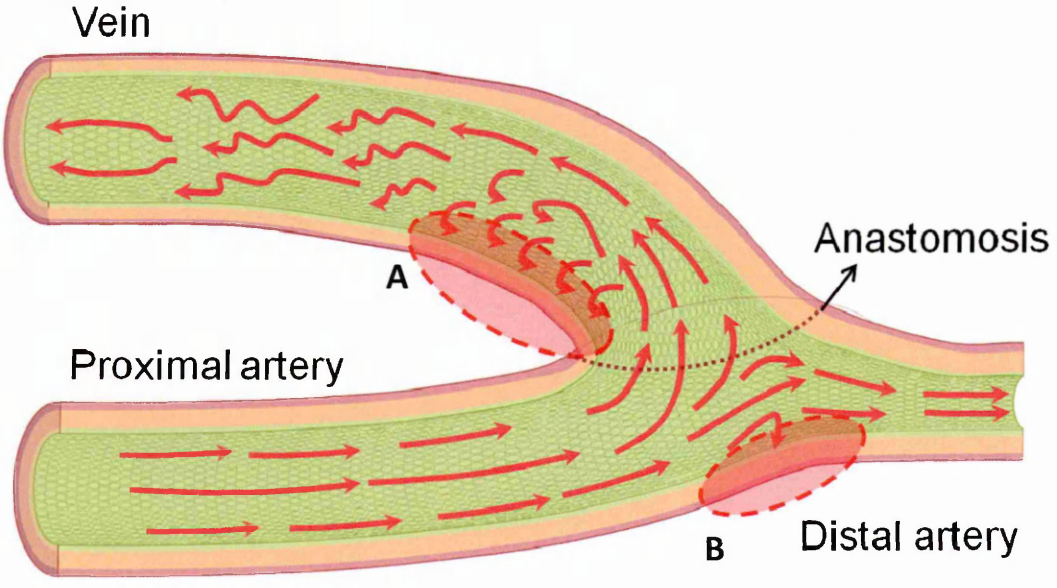

Fig.3: AVF anatomy. Blood coming from the proximal artery flows mainly toward the draining vein and only a small fraction continues to the distal artery. IH development results preferentially localized in specific AVF areas, A) the juxta-anastomotic curvature and B) the anastomosis floor of the feeding artery.

Despite the fact that the increase in blood flow is the main purpose of AVF creation, an excessive flow is also considered cause of AVF late failure (2). Excessive flow can result in ischemia of the hand due to the local high resistance of the hand compared to venous return through the AVF. Excessive flow (> 3-4 L/min) through the AVF can also lead to high output cardiac failure and requires ligation of the fistula itself. Finally, aneurysms can result from a continuous increase in vessel size (2). These

generally occur on the venous side due a downstream venous stenosis although the feeding artery can also experience local aneurysm due to repeated punctures.

Many different factors are involved in the development of IH. In common with other pathologies that affect vasculature like diabetes and hypertension, CKD seems to predispose patients to development of IH. However, the localization of lesions occurs in areas where blood flow experiences recirculation, high frequency fluctuations and disturbed flow. This association has led to the study of local hemodynamics as a potential trigger for IH development (72).

The features of local blood velocities, such as changes in direction and magnitude, have been shown to affect vascular function by modulating endothelial cell (EC) signalling. Wall shear stress (WSS), the frictional force per unit area exerted by the blood due its viscosity, has emerged as a stimulus able to regulate EC phenotype (73, 74). Observations focused on atherosclerosis development have reported that turbulent, oscillating or reciprocating blood flow induces activation of ECs leading to a proliferative, pro-inflammatory and pro-oxidant state (75-77) that can regulate the other cellular components of the vessel wall. The role of WSS in AVF maturation and failure is the main focus of the present study and will be addressed in the following chapters.

I.D) Aim of the study and structure of the thesis

As there continues to be a high rate of fistula failure despite major efforts of recent years (Introduction), this thesis investigates the hypothesis that reciprocating WSS waveforms are responsible for development of intimal hyperplasia, resulting in low AVF maturation rates and poor outcomes (78). The state-of-the-art in understanding of the biology of native AVF development is reviewed in Chapter 1 and Chapter 2 reviews the possible role of wall shear stress patterns in determining AVF

maturation. To examine this hypothesis wall shear stress (WSS) patterns representative of those experienced by high and low risk stenosis areas in an idealized model of a side-to-end AVF were defined, according to a previous study (79), these results are presented in Chapter 2.

To verify the hypothesis the following steps were undertaken, reported as indicated:

- Definition of endothelial cell biology relevant to fistula failure and potentially modulated by selected WSS waveforms (Chapter 2).

- Design and validation of an in-vitro cell shearing system capable of generating controlled, highly unsteady WSS stimulation on an endothelial cell monolayer (Chapter 3).

- In vitro flow exposure experiments to compare the effects of different WSS patterns on endothelial cells derived from human umbilical vein in regard to morphology (Chapter 4), gene expression (Chapter 5) and molecule release (Chapter 6) elicited by selected WSS waveforms

- Evaluation of proliferation of SMCs incubated with medium conditioned by ECs exposed to different flow stimulation (Chapter 7).

- Determination of a possible role of WSS in modulating the expression of genes known to be involved in neointimal hyperplasia development (Chapter 8).

Chapter 9 provides a summary and discussion of the outcomes of the study and a perspective on future areas for research.

CHAPTER 1: AVF development

Native Arteriovenous Fistula (AVF) creation is considered the best choice to create a vascular access for hemodialysis treatment. Despite many years of clinical practice and major efforts to ameliorate the outcome, AVF failure due to stenosis remains very frequent. This chapter reviews the current knowledge regarding AVF biology. Maturation of the AVF is addressed in the first part of the chapter together with the role of the endothelium in regulating vessel wall remodeling. AVF stenosis biology due to intimal hyperplasia (IH) is the topic of the second part of the chapter. This section also addresses the role of myofibroblasts in AVF remodeling, the consequences of chronic kidney disease on vascular function and the potential involvement of TGF-β pathways in IH development.

1.A) Native arteriovenous fistula maturation biology

1.A1) *Biology of AVF maturation.*

After surgical creation, AVFs are exposed to a high flow, high shear stress, low pressure arterial environment (80, 81). The surgical trauma and the increased blood flow initiate and regulate vessel wall remodeling in order to reestablish physiological mechanical stresses within the vessel wall (82-86). Inflammation and vascular tone are the two main regulators of this remodeling (68, 87).

Ideally, immediately after the vein is shunted to the artery, the acute blood flow increase causes the release of nitric oxide (NO) by the endothelium (88). NO induces elevated levels of cyclic guanosine monophosphate levels that cause vasorelaxation (89-91). Furthermore a sustained increase in blood flow induces superoxide production, which forms peroxynitrite combining with NO (92). Peroxynitrite induces

metalloproteinase 2 and 9 (MMP-2, -9) production, which leads to vascular dilatation by digestion and remodeling of the internal elastic lamina (93). The overall effect is an increase in vessel diameter (94-96).

Circumferential stress is defined as the tensile stress that develops within the vessel wall as a consequence of blood pressure increase. An increase in vessel tissue stretch results in SMC activation, increased cytokine expression and an increase in extracellular matrix turnover (97, 98). These pathways lead to vessel wall thickening in order to reestablish physiological transmural stress (99). This phenomenon is referred as medial hypertrophy (100).

In a successful maturation process (shown in figure 4), the altered blood flow in the AVF drives outward vessel remodeling balanced by induction of NO and limited IH formation caused by inflammation. This process is termed venous arterialization (101) and can be considered optimal to guarantee the success of an AVF. To preserve long-term patency after a correct maturation, AVF vessel tissues have to down-regulate the pro-inflammatory, proliferative activities that were activated by surgical trauma and onset of new hemodynamics. Central to this process is the restoration of the endothelial integrity, which is damaged by AVF creation.

All vessel layers participate in flow-induced adaptation. Endothelium however, due its position, the presence of numerous mechano-sensors (102, 103) and the extreme sensitivity (104) to changes in mechanical loading, may be considered the conductor of the orchestrated signalling that drives vessel remodeling (105).

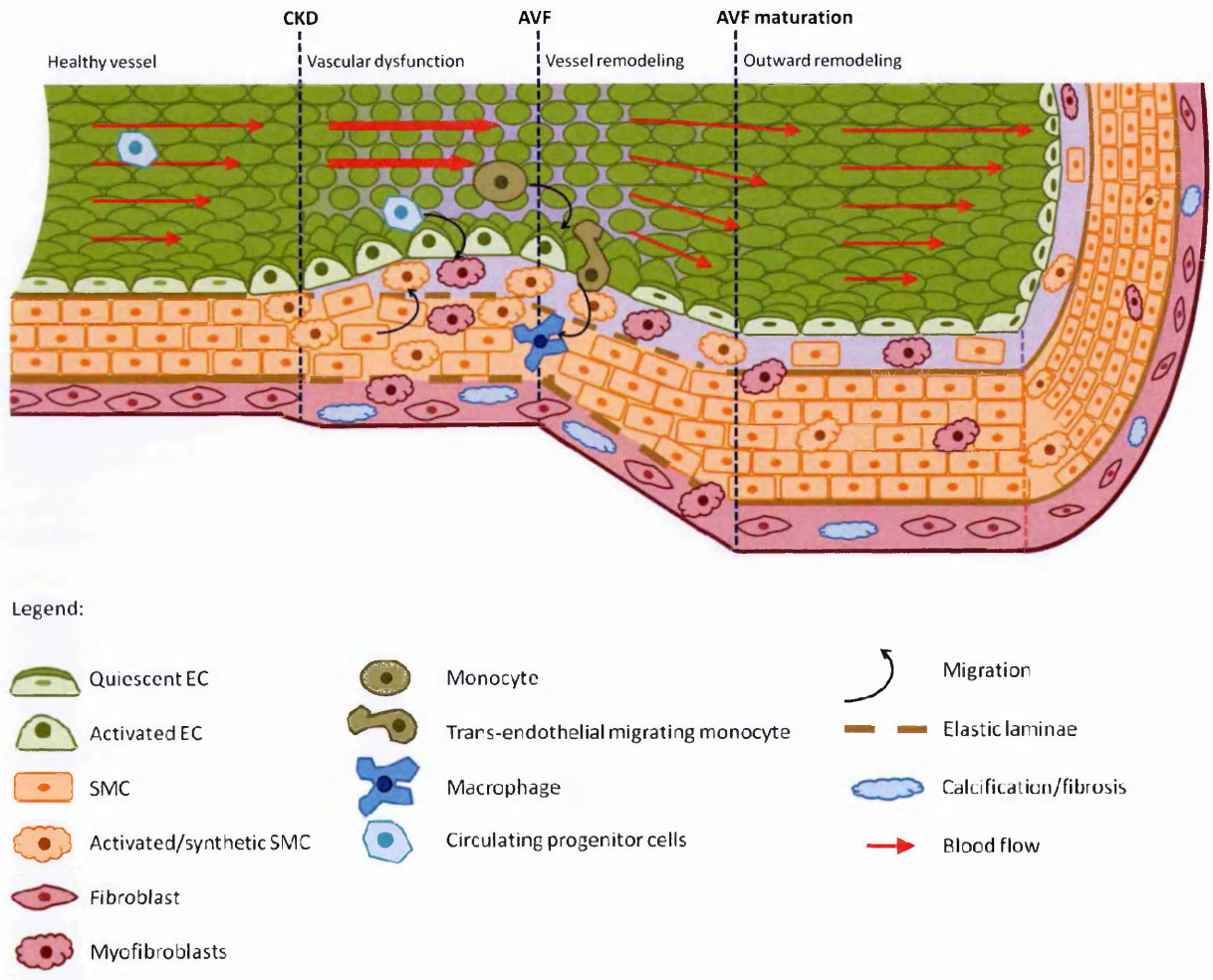

Fig.4: Potential mechanisms of AVF maturation. Pre-existing CKD may lead to vascular dysfunction by enhancing oxidative stress and fibrosis in the adventitia and by inducing IH prior to AVF creation. Surgical creation of the AVF causes endothelial denudation and increase in blood flow, these events induce release of vascular tone active molecules and inflammation. The equilibrium of these two aspects is reflected by the extent of vascular wall remodeling, tightly controlled by ECs. Unidirectional high WSS leads to endothelial NO release, causing vasodilation, promoting functional re-endothelization and suppressing inflammation. The overall effect is a structural vessel outward remodeling with limited IH development. This form of vessel remodeling is classed as successful fistula maturation and allows clinicians to use the AVF as access for HD treatment (68).

1.A2) *Role of the endothelium in AVF maturation*.

As shown in figure 5, endothelium is the master regulator in inflammation and vessel tone due to its ability to produce and control a plethora of autocrine and paracrine signals (106, 107). ECs release mitogens and chemotactic agents, regulators of extracellular matrix (ECM) remodeling, and vasoactive molecules that regulate dilation to allow vessel adaptation to flow, shear stress, pressure, and tension (68, 100).

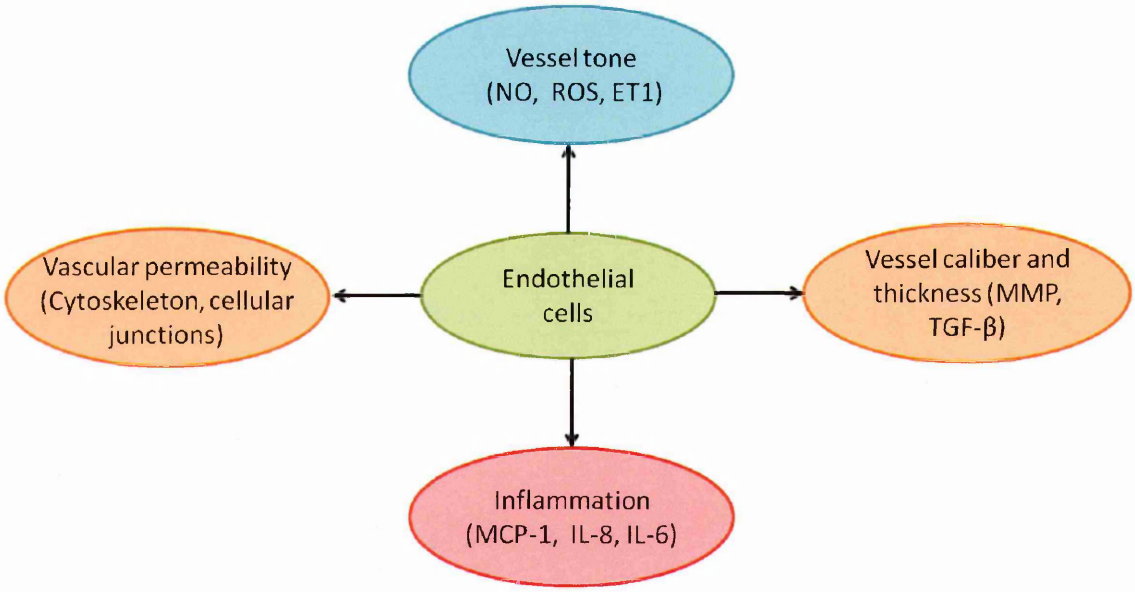

Fig.5: Endothelial cells control a number of pathways that are potentially involved in AVF vessel remodeling and inflammation.

Endothelial trauma caused by AVF creation affects endothelial integrity and alters EC signalling. Furthermore the increased blood flow can induce endothelial denudation within hours. Denudation leads to barrier dysfunction, exposure of subendothelial collagen, thrombus formation, and inflammatory cell extravasation into the vein wall (108, 109).

Endothelium controls the production of the main vasoactive signals (110). ECs produce endothelial nitric oxide synthase (eNOS) that synthesizes NO from L-Arginine

(111). However, ECs also produce reactive oxygen species (ROS) via the nicotinamide adenine dinucleotide phosphate-oxidase (NADPH oxidase) enzyme complex (112). The main EC ROS are free radicals such as superoxide anion and non-free radicals such as hydrogen peroxide (H_2O_2). H_2O_2 plays an important role in mediating vascular activation. Low levels of H_2O_2 induce vascular cell proliferation. Low levels of H_2O_2 exert a mitogenic function through the activation of casein-kinase-α-LS (CK1α-LS) (113), which then phosphorylates the heterogeneous nuclear ribonucleoprotein-C (hnRNP-C) (114). It is known that hnRNP-C modulates the expression of several genes regulating cell growth and survival, including PDGF-B (115).

In the vascular system, ROS play a physiological role in controlling endothelial function, vascular tone, integrity and remodeling (116). ROS production is closely linked to NO generation and elevated levels of ROS lead to low NO bioavailability. Humoral agents, such as Angiotensin II (Ang-II) and Endothelin 1 (ET1), platelet derived growth factor (PDGF) and thrombin can modulate basal superoxide production by NADPH oxidase (117). Ang-II and ET1 are inflammatory mediators of vasoconstriction and endothelial proliferation that can be produced by ECs as autocrine signals (118). PDGF is produced by EC and promotes vascular cell proliferation and migration (119). Thrombin modulates platelet activation and vessel permeability (120). Furthermore the activation of Phospholipase D (PLD) promotes hydrolyzation of the phosphatidylcholine (PC) to phosphatidic acid (PA) that mediates the ROS-induced endothelial permeability by modulation of Rho GTPases activity and actin cytoskeleton remodleing (121). PA also stimulates the NADPH oxidase system that increases levels of ROS and leads PLD and PA to form both positive feedback and feedforward loops that amplify and integrate the oxidative signalling pathways (122).

The equilibrium between NO and ROS production is fundamental in AVF maturation and is tightly controlled by ECs (117). A damaged endothelium leads to an increase in ROS necessary to promote inflammation and facilitate vessel remodeling. However, chronic increase in EC oxidative stress impairs vasodilation and leads to vessel inward remodeling (87, 123).

Endothelial integrity is fundamental to control NO/ROS production. The endothelium is regenerated 2 weeks after AVF surgery, although EC proliferation continues for months (109). Once vessels reestablish tissue continuity and physiological mechanical load, ECs should down-regulate their pro-inflammatory signals and acquire a quiescent phenotype.

Functional to this phenotype are several biological processes tightly related to WSS mechanotransduction (124). Quiescent ECs show sustained up-regulation of Krüppel-like factor 2 (KLF2) (125, 126) synthesis induced via the dual specificity mitogen-activated protein kinase 5/ Extracellular-Signal-Regulated Kinase 5 pathway (MAPK5/ERK5) (127).

KLF2 exerts a protective function by stabilizing EC activity mainly through the promotion of eNOS production and cytoskeletal remodeling. NO production controls SMC proliferation and migration (128). Communication between ECs and SMCs is provided in vivo by physical contact of the myoendothelial junctions (MEJs). MEJs regulate NO diffusion and provide a bidirectional cross talk between the two layers (129). NO also regulates endothelial barrier function through activation of focal adhesion kinase (FAK) and recruitment of additional focal adhesion complexes (FA) to the basal EC surface, in order to control barrier permeability during the inflammation process that occurs after AVF creation (130). NO/ROS balance is also involved in ECM turnover by its ability to activate MMPs that selectively degrade components of the

extracellular matrix and their inhibitors such as tissue inhibitor of metalloproteinases (TIMP) (131).

KLF2 is essential for cytoskeleton remodeling, especially F-actin stress fiber formation and cell alignment (132). This cytoskeletal reorganization is promoted by alteration in mechanical stresses and regulated by signalling from small Rho-GTPases (Ras homolog or Rho, Ras-related C3 substrate or Rac and cell division cycle protein or CDC42) (133, 134) to optimize mechanical loading distribution within the cell. The remodeling and stabilization of the cytoskeleton is promoted by physiological mechanical loading and is essential in EC to form stable junctions with other components of the tissue. ECs form different junctions with surrounding EC and with the elastic laminae and the medial SMCs below (135-138). The reorganization and stabilization of these junctions allows the endothelium to control permeability (139), proliferation, and ECM turnover and is ultimately involved in the protective effect exerted by re-endothelization after vascular trauma.

KLF-2 exerts a protective function by stabilizing EC autocrine and paracrine activity. KLF2 promotes thrombomodulin and inhibits vasoconstrictor agents such as ET1 and Ang-II (140). KLF-2 down-regulates the release of pro-inflammatory molecules such as the Monocyte Chemoattractant protein 1 (MCP-1) and Interleukin 8 (IL-8) (141, 142) and expression of adhesive molecules such as Vascular Adhesion molecule (VCAM) and Intercellular Adhesion molecule (ICAM) (143).

KLF2 expression inhibits tranforming growth factor β (TGF-β) (144) proliferative signalling and attenuates activation of several pathways including nuclear factor κB (NF-κB) (124), MAPKs dependant transcription of the Activator protein 1 (AP-1) (144) and the Serine/Threonine-protein kinase 1 (PAK1) (127, 145). Finally

KLF2 has been shown to be involved in antioxidant activity of Nuclear factor-erythroid 2-like 2 (Nrf-2) translocation to the nucleus (146).

Numerous studies have shown that mechanical loading, especially WSS, have a deep impact on EC biology by mediating KLF2 expression (147) and cytoskeletal remodeling. The beneficial effect of increase in WSS induced by AVF creation should guarantee endothelial quiescence and survival, orientation of EC in the direction of flow and the production of anti-inflammatory and anticoagulant mediators (110). On the contrary, low and reciprocating WSS prevent the expression of KLF2 and eNOS resulting in impaired cytoskeletal remodeling and cellular junction stabilization that leads to increased EC pro-inflammatory and procoagulant signalling, a pro-oxidant state, sustained cellular proliferation and impaired ECM turnover (148).

The majority of these studies have considered the effect of WSS on arterial endothelium while the response of the venous endothelium to WSS is not always the same (148). Furthermore, swine venous vessels have been shown to have a lower expression of antioxidant genes (eNOS, superoxide dismutases) compared to regionally linked arteries (149). This aspect could be detrimental when veins are directly connected to the arterial system. However, evidence focused on venous remodeling induced by an arterial flow environment in animal models, reported that veins share similar features to arteries and that ECs play a fundamental role in both vascular districts. Endothelium showed to be intimately connected with the environment and to be sensitive to mechanical stresses or oxygen tension that discriminate arterial and venous districts (86). ECs exposed to high magnitude arterial WSS presented a loss of Ephrin type-B receptor 4 (EphB4), a marker of venous identity but the arterial identity marker EphrinB2 was not gained (150-152). EphB4 expression has been shown to

prevent venous remodeling (153) but the precise role of the Ephrin-Eph pathway in controlling WSS-induced endothelial signalling is not known.

Despite the differences between arterial and venous endothelial sensitivity to WSS magnitude (154), reciprocating/disturbed WSS has been shown to deeply influence ECs independently of the vascular bed of origin, possibly leading to sustained inflammation and impaired wall remodeling. Within AVFs the lack of vessel stabilization could manifest in vessel diameter reduction and IH development (155). All this evidence demonstrates the importance of hemodynamic changes following AVF creation and the pivotal role of ECs in controlling the fate of vessel wall remodeling.

1.B) Native arteriovenous fistula failure biology

1.B1) *Failing AVF biology.*

Venous stenosis due to IH development is the first cause of failure in AVFs created for HD treatment. IH development can be divided into an inflammatory phase (hours to days), a granulation or cellular proliferation phase (days to weeks) and a phase of remodeling of the ECM and protein synthesis (3-18 months) (156). The aggressiveness of these processes is often not adequately compensated for by outward vessel remodeling, leading to AVF stenosis and failure (68, 157). Histological studies of stenotic tissues from AVFs undergoing early failure are characterized by an aggressive IH formed mainly by α-smooth muscle actin-positive, vimentin-positive and desmin-negative myofibroblasts (MFs) and some activated SMCs that migrate either from the adventitial and medial layers or derived from circulating progenitors (9, 158). They participate in neointimal formation due to their high ECM protein synthesis capacity and autocrine signalling mainly based on TGF-β (159, 160). The role of MFs in AVF failure is addressed in paragraph 1.B2

High levels of oxidative stress products (161), MMP-2 and MMP-9 were found in stenosed fistulas (86, 93, 162). ECM deposition is the major contributor to neointimal layer development and MMP-2 and -9 are involved in both beneficial AVF outward remodeling and stenosis induced by IH (94). MMP-2 and-9 up-regulation has been linked to endothelial denudation (163) while lower levels of MMP-2/TIMP-2 or MMP-9/TIMP-4 ratios were found to correlate with AVF stenosis (164). Decreased levels of MMP-1 and -3 together with MMP-9 (165) were also correlated with AVF failure. A recent study in mice showed that during AVF maturation a distinct temporal pattern regulates proteins such as MMP and TIMP and leads to the expression of structural proteins that potentially mediate ECM degradation and deposition to control AVF remodeling (162).

MMPs control ECM degradation whereas TGF-β is the major promoter of ECM protein synthesis and also the main regulator of activation of ECs, SMCs and FBs (166). This growth factor plays a central role in many pathways related to vascular dysfunction. Interestingly inhibition of TGF-β leads to decreased IH and MCP-1 expression (167). Due to its complex role in AVF failure this will be addressed in paragraph 1.B4.

Stenosed AVF tissue also shows macrophages infiltration (168) and elevated levels of VCAM (169), IL-6, IL-8 and MCP-1 (156, 169). These cytokines have chemoattractant properties that lead to monocyte recruitment and infiltration through the endothelium. Monocytes can also undergo differentiation toward macrophages that participate in ECM remodeling and inflammation. MCP-1 binding to chemokine receptor 2 (CCR2) appears to be central in the process of monocyte recruitment and macrophage accumulation within vascular lesions (170). Beyond MCP-1 chemotaxis of

monocytes, this cytokine leads to activation and migration of endothelial cells, proliferation and migration of SMCs and pro-coagulant signalling (142).

Another important molecule in vessel remodeling and angiogenesis is the vascular endothelial growth factor (VEGF) (171). VEGF has a complex, central role in many vascular related events. Blocking VEGF-A correlates with a negative regulation of IH and positive vessel remodeling, thus has a beneficial effect in AVF maturation (172). Finally, preexistent CKD may have a detrimental effect on AVF maturation since this condition has many negative effects on vascular tissues. A description of this relationship is reported in paragraph 1.B3.

IH occurs in AVF areas that experience oscillating and reciprocating WSS, in particular on the venous side of the anastomosis (juxta-anastomotic stenosis) (71, 72, 173, 174). Endothelial damage and denudation during AVF creation activate the pro-inflammatory cascade that should be downregulated within a few weeks in order to preserve vessel patency. However, abnormal WSS prevents functional re-endothelization and causes an increase in vascular interstitial flow that activates vessel cellular components (148). Damaged ECs promote a pro-oxidative environment within vessel wall, altering MMP regulation and ECM remodeling. WSS also deeply affects endothelial barrier integrity that is central to down-regulation of inflammation after AVF creation. Disturbed WSS can also induce up-regulation of adhesive molecules and expression of chemoattractant agents by ECs, facilitating monocyte recruitment and transendothelial migration, a phenomenon tightly related to vascular dysfunction (175, 176).

In conclusion, both primary and late AVF failures are related to altered cellular proliferation and matrix deposition not compensated for by vessel diameter increase (figure 6). Despite pre-existing risk factors, such as CKD, the role of inflammation and

regulation of vascular tone in AVF failure suggests EC function is central to successful AVF maturation. An environment that promotes MFs activation and impaired re-endothelization enhances the risk of IH development.

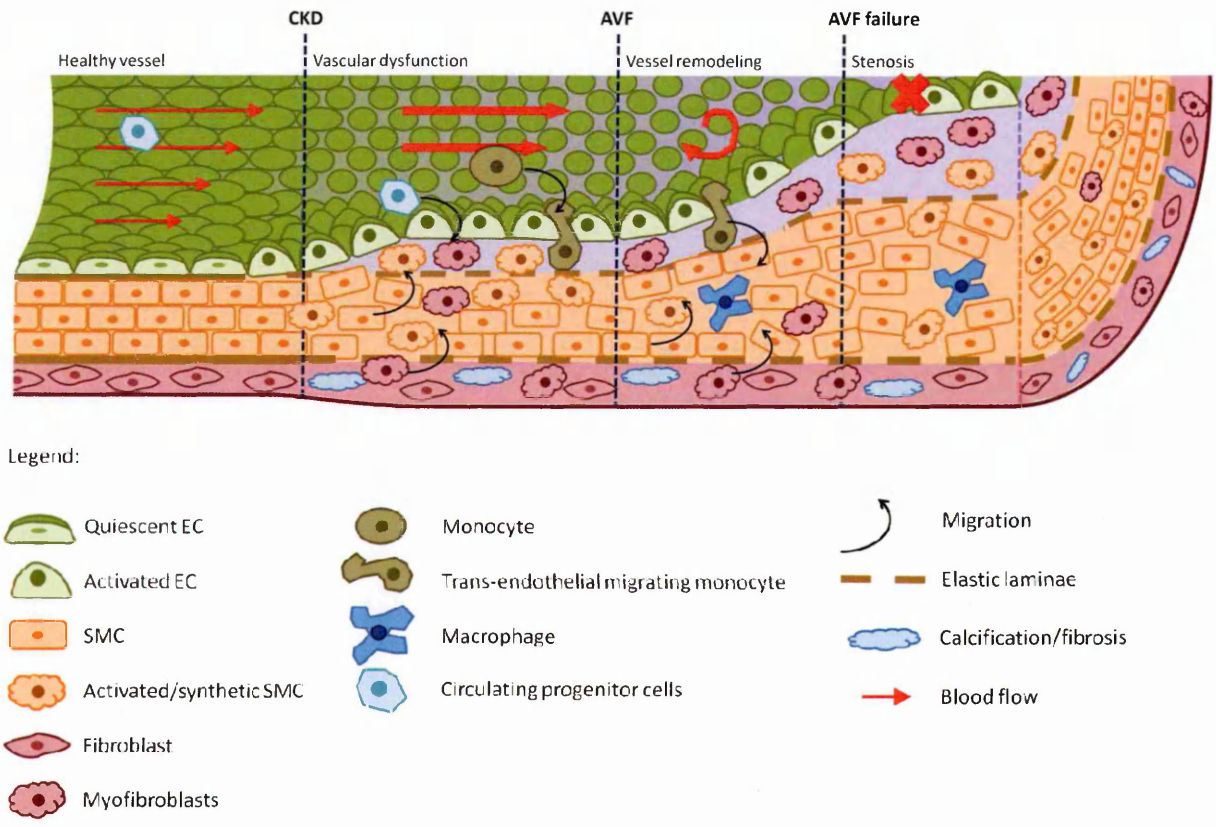

Fig.6: Potential mechanisms of AVF failure. The phases prior to AVF creation are similar to figure 4. In the later phases lack of equilibrium between the production of vascular tone active molecules and inflammation leads to fistula failure. Reciprocating WSS enhances endothelial ROS production that affects vasodilation. Furthermore reciprocating WSS prevents re-endothelization leading to a sustained inflammation and cell proliferation. The increased adventitial stiffness and sustained pro-inflammatory and chemoattractant signal production induced by reciprocating WSS, may cause vessel inward remodeling and sustain IH development in order to reduce WSS magnitude. This form of vessel remodeling is classed as fistula failure since it does not allow clinicians to use the AVF for HD treatment (68).

1.B2) Role of Myofibroblasts in AVF stenosis.

Myofibroblasts (MFs), also defined as "mesenchyme-like interstitia cells", are cells that contribute to tissue repair during wound healing by promoting tissue contraction. (177) MFs also participate in ECM remodeling, pro-inflammatory and pro-angiogenic signalling (178, 179). However, at the end of wound healing these cells should undergo massive apoptosis 2-3 days after injury, in order to reestablish quiescence in the vascular tissue (178). Despite in-vitro evidence showing the capability of MFs to reverse differentiation, in-vivo studies have not detected this phenomenon, leading to the assumption that apoptosis is the main process responsible for MF deactivation (180).

MFs can have multiple origins since they can derive from trans-differentiated SMCs, fibroblasts differentiated to proto-myofibroblasts then to MFs, ECs which have undergone a endothelial-mesenchymal transition (EndMT) (181), from circulating progenitors (fibrocytes) and others (182-185). The main source of MFs in AVF stenosis is still controversial. Furthermore some authors have suggested that MF markers identify a cellular functional status and not a specific cell type (182).

Activated MFs share many markers with SMCs, particularly α smooth muscle actin (α-SMA) which acts as a mechanosensor and is recruited to form stress fibers under mechanical tension (186). MFs form bundles of contractile microfilaments, integrin-mediated cell-to-matrix bonds and adherens junctions (AJs) and gap junctions (GJs) with surrounding cells (187), these ultrastructural features distinguish MFs from FBs and are responsible for wound contraction, cell migration and eventually cellular apoptosis.

Several external stimuli can activate MFs, including ECM stiffness, loss of cell-ECM interaction caused by surgical trauma and mechanical loading or altered TGF-β

signalling caused by pre-existing disease and altered hemodynamics (186, 188-190). As mentioned before, once recruited and activated, MFs contribute to wound healing by forming granulation tissue then disappear (178, 191).

A sustained activation of MF leads to ECM deposition that affects matrix stiffness and promotes MF activity (158). In-vivo evidence shows the adventitial layer of stenotic vessels exhibits an increased presence of fibrosis probably caused by the increase of oxidative stress (192). This increased fibrosis alters vessel stiffness and affects AVF maturation by limiting positive vessel remodeling and possibly inducing MF proliferation (188, 193, 194).

Sustained pro-inflammatory signalling, unbalanced mechanical loading on vessel tissues and lack of ECM stabilization may prevent MF apoptosis and lead to fibrosis. The fate of MFs at the end of the healing process may determine stable wall remodeling or excessive neointimal growth and negative remodeling leading to AVF failure (179, 195). This vicious cycle could be promoted via latent TGF-β mobilized by MF activity (196) or flow-induced EC signalling (197) leading to IH development (160, 172).

1.B3) *CKD as a risk factor in IH development.*

To address the biology of failing AVF due to IH development, it is not possible to avoid considerations of preexisting pathologies that affect the vasculature such as CKD (198), diabetes and hypertension. The degree of CKD, that is a prerequisite for AVF creation, is probably directly related to AVF non-maturation since its effects on the vasculature (199) could predispose to inward remodeling and IH development (69, 200).

The presence of IH in uremic patients even before AVF creation has been reported (201). However, this aspect is controversial since a study of over 50 uremic patients showed that IH was not present at the time of AVF creation but developed *de-novo* after surgery (157). Nevertheless it is a matter of fact that CKD induces vascular damage and endothelial barrier dysfunction in the earlier stages (199, 202, 203), possibly due the activation of the Notch intercellular communication pathway (204).

The Notch pathway is fundamental during embryonic development and is a key controller of vascular cell fate (differentiation, proliferation, survival and activation) (205-207). In mammals a large number of combinations of four Notch receptors (Notch1 -4) and five Notch ligands (Jagged 1 -2, Jag and Delta-like 1,3 -4, Dll) are possible. In addition other non-canonical ligands provide activation or inhibition of Notch activation (208). All vascular cells express specific patterns of Notch receptors and ligands, in a composition that depends on cell type and specific vascular locations.

Despite the complex and potentially opposite context-dependent effects, Notch signalling has emerged as a potential trigger of IH (209). It is involved in pro-inflammatory cytokine and chemokine release by EC or macrophages and it has multiple interactions with the main EC pro-inflammatory pathways (NF-κB, MAPK, NO/ROS and TGF-β) (210, 211). Some key aspects of Notch activation effects on ECs are related to the impairment of the endothelial barrier (209, 212). Notch affects Vascular Endothelial cadherin stability and promotes ECs to undergo EndMT (213). In contrast, Notch2 has anti-inflammatory effects on ECs by reducing VCAM expression and promoting EC apoptosis (214).

Notch1 and 3 receptors are also involved in SMC differentiation, probably via platelet derived growth factor (PDGF) modulation (206). Notch activation is required to

induce α-SMA expression in SMC and it has regulatory effects, which can enhance or inhibit the phenotypic switch due to Hes/Hey induction (215).

Notch 1 is involved in TGF-β-induced transition of lung FBs to MFs. Impaired Notch signalling has been shown to reduce MF differentiation in an animal model. (216)

The emerging concept focuses on tight spatial and temporal regulation of Notch activation pathways in the vasculature (209). Targeting of downstream Notch effects may positively or negatively regulate Notch-induced signalling, with important effects on IH development, CKD induced oxidation (217, 218)and Notch activation due to TGF-β up-regulation (219, 220). This activation may lead to endothelial dysfunction, EndMT, differentiation of SMCs and FBs, predisposing vessels to IH development (figure 7). Interestingly, the knockout of Recombinant binding protein-Jk (RBP-Jk) (221), the major transcription factor associated with Notch activation, in ECs of uremic mice, reduces CKD-dependant IH formation.

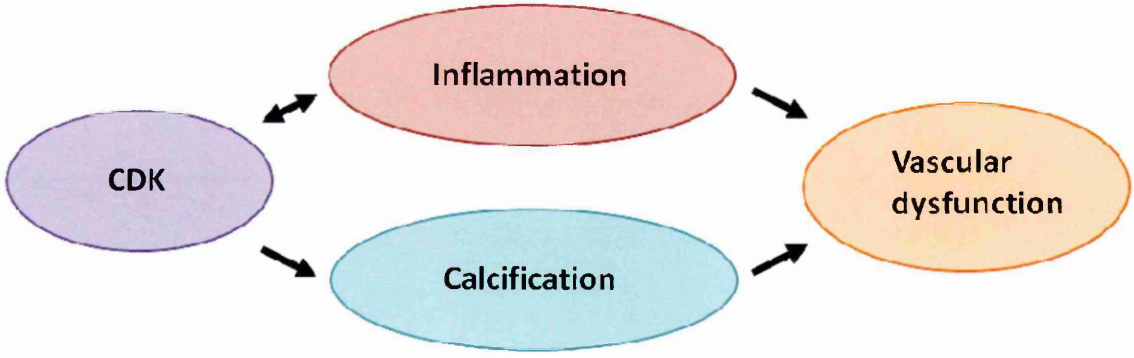

Fig.7: CKD relationship to vascular dysfunction.

1.B4) *TGF-β role in vascular homeostasis and disease.*

TGF-β superfamily signalling is fundamental in vasculogenesis, angiogenesis, vascular homeostasis and disease development (166, 222). TGF-β exerts its functions through complex pathways involving different small mother against decapentaplegic proteins (SMADs). Depending on the context, TGF-β elicits both cellular quiescence and proliferation (223).

Several extracellular mediators regulate the extent of the TGF-β binding effect (224). Downstream signalling effects depend on the expression level of ligands and receptor affinity. Ligand-trapping proteins or release mediators modulate the assembly of latent TGF-β and control cytokine availability and gradient formation (196).

The plethora of TGF-β superfamily ligand binding induces assembly of a complex composed of two type I (signal-propagating) and two type II (activator components) receptors that are serine/threonine-specific protein kinases. Ligand binding promotes type II receptors to phosphorylate type I receptors, which propagates the signal by phosphorylation of SMADs (225). The combination of receptors and accessory receptors (type III receptors) or ligand antagonists, regulate binding. All these factors interact to provide a fine tuning mechanism for TGF-β signalling (166, 226).

In addition to SMAD activation (225), TGF-β non-canonical signalling can activate other pathways that involve p38/MAPKs, NF-κB, Protein kinase B (AKT), ERK and JUN N-terminal kinase (JNK), Rho GTPases. These signals can have direct effects on cells or crosstalk with SMADs and mutually influence each other. Molecules such as Notch, WNT, Ras, Hedgehog, tumor necrosis factor (TNF) and interferons (IFs) can modulate both canonical and non-canonical TGF-β pathways (227).

Despite the complexity of these processes, TGF-β superfamily activity can be summarized in two main pathways. TGF-β binding promotes formation of TβRI (i.e.

activin receptor-like kinase 5, ALK-5), TβRII heteromeric receptor complex and induces receptor-regulated SMAD 2/3 (r-SMAD) phosphorylation that, in association with common-mediator SMAD 4 (co-SMAD), sustains cell quiescence through expression of different transcription factors (i.e. Plasminogen activator inhibitor-1, PAI-1) (228). On the contrary bone morphogenic proteins (BMPs) binding to ALK-1/2/3/6, BMPR2 complex phosphorylate r-SMAD 1/5/9(8) that, in association with co-SMAD 4, leads cells to a proliferative state due to synthesis of transcription factors such as DNA-binding protein inhibitor (229, 230).

Inhibitory SMAD 6/7 (i-SMAD) also participates in this process through blocking signalling induced by TGF-β or BMP (224). Moreover type III receptors like betaglycan and endoglin (Eng) control cytokine binding to different receptor complexes depending on cell type, senescence and possibly on mechanical loading.

ECs are involved with a distinct TGF-β pathway (231) (figure 8). ALK-1, typically involved in BMP signalling, can form a receptor complex with TβRII in ECs, becoming responsive to TGF-β induced r-SMAD 1/5/9(8) and eliciting ECs proliferation, migration and organization (222). In contrast, TGF-β-induced ALK-5 signalling leads EC to a quiescent state and regulates endothelial permeability. Although these receptors have divergent effects on ECs, they do interact. ALK-5 is required in ALK-1 activation and ALK-1 can directly antagonize ALK-5-related SMADs phosphorylation (232). Eng is considered to be the major regulator of preferential TGF-β binding to ALK-1 rather than ALK-5 (233, 234).

Eng exists in long (L-Eng, most expressed) and short (S-Eng) isoforms that are able to interact with both ALK-1 and ALK-5. Eng isoforms differ by receptor affinity, inducing different levels of phosphorylation and regulating TGF-β-dependent response (235).

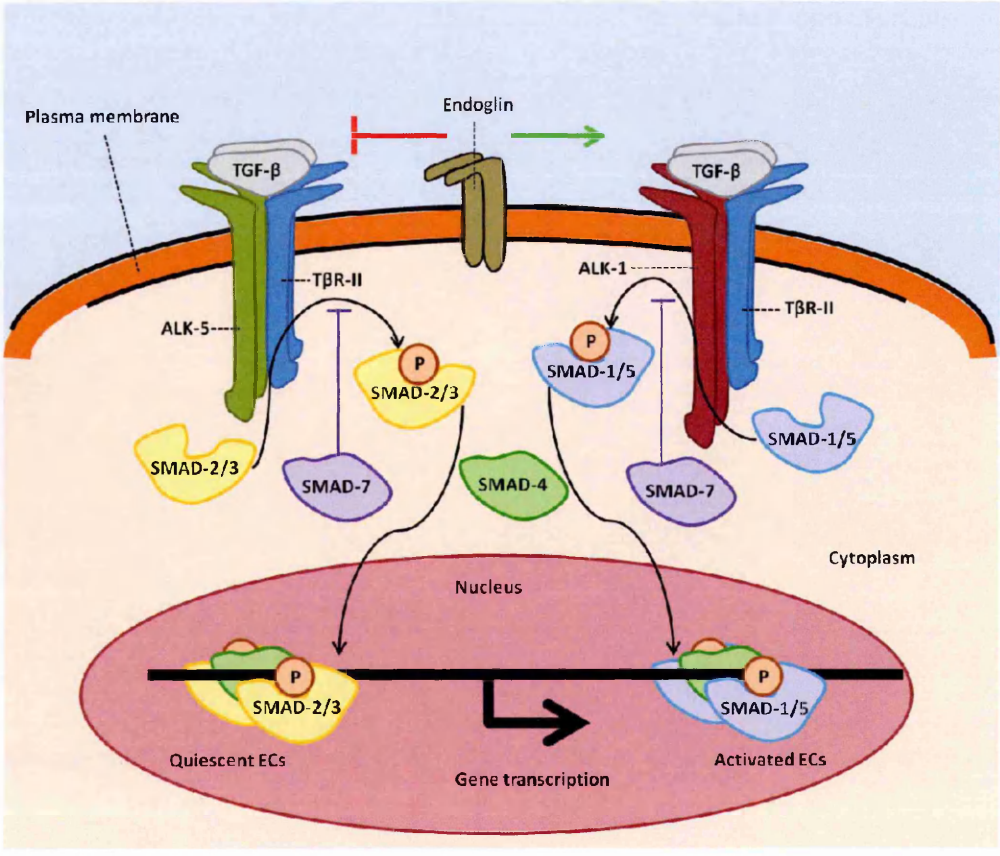

Fig.8: Possible role for endoglin in regulation of TGF-β pathway in ECs. Abbreviations: TGF-β transforming growth factor β, TβR transforming growth factor β receptor, ALK activin receptor-like kinase and SMADs small mother against decapentaplegic proteins (231, 235).

L-Eng have pro-angiogenic effects by inducing NOS expression otherwise S-Eng has anti-angiogenic effects. S-Eng is enhanced by EC senescence (236), leading to age-related vascular dysfunction (235). A soluble form of Eng, cleaved by MMP-14, is a biomarker for vascular dysfunction (237). However, Eng and ALK-1 function in TGF-β signalling are not completely understood (238) and increasingly the cellular context (developmental stage, receptor composition) is considered as a key regulator of TGF-β and other signalling in ECs (239-241).

Beyond the dramatic effects on ECs, TGF-β signalling also regulates SMC de-differentiation via SMAD-3 and p38/MAPK pathways (242). Furthermore, TGF-β enhances SMC activation, proliferation and migration and inhibits apoptosis (243).

TGF-β canonical and non-canonical pathways are also the main regulators of FB to MF transition (178). These phenotypic switches play a fundamental role in wound healing and vessel remodeling after AVF creation. Due to the synthetic nature and elevated motility, MF fate is pivotal in IH development. A clinical study (244) in patients with primary AVFs showed that polymorphism in the region encoding for TGF-β1 affects AVF outcome. In particular, patients with increased protein synthesis activity have a shorter AVF patency rate compared to those with a low synthesis activity. In conclusion the TGF-β pathway deeply affects vasculature biology and the consequent alterations in signalling may result in vascular defects and diseases.

1.C) Summary

After surgical creation of an AVF the vessel wall tissue undergoes a major remodeling process orchestrated to reduce WSS and tensile stress to within the physiological range (78). The complex cascade of events that involves vessel tone regulating molecules and inflammation, determines the balance between beneficial outward remodeling and detrimental IH development (as shown in figure 9) (68).

These two processes have some common features such as the role of MMPs in facilitating outward remodeling in the early stages of AVF maturation but also enhancing IH formation in the later stages. Furthermore, pro-inflammatory signals and such as MCP-1 and IL-8 are produced during initial inflammation to reestablish vessel continuity, but their sustained upregulation is also involved in the proliferative phase of IH (156).

Endothelium is probably the master regulator of these events and its integrity is functional to vasodilatation, luminal caliber preservation and thus long-term AVF patency since it prevents IH development (245). In the last decades hemodynamics has

emerged as a potent stimulus in regulating endothelial permeability and signalling. In particular, depending on the features of the flow waveform, WSS has been shown to induce EC phenotypes that can deeply affect AVF remodeling.

Beyond endothelial activities, to understand AVF biology it is necessary to consider pre-existing CKD. Several studies have shown that renal dysfunction can have a significant impact on the vasculature by enhancing inflammation and oxidative stress (202). Finally, both CKD and WSS have been shown to influence TGF-β signalling (246, 247) with potential effects on cellular components of the vessel such as EndMT (248) and myofibroblasts activation (223, 228).

In conclusion, CKD patient arteries and, although less investigated, veins have an increased stiffness that can predispose to inward remodeling and IH development after AVF creation. Despite this pre-existent vascular dysfunction, some fistulas adequately mature for HD treatment. Our hypothesis is that hemodynamics plays the ultimate role in deciding the fate of AVF remodeling and that EC mechanotransduction of WSS could make the difference between failure and maturation. This aspect is addressed in the next Chapter.

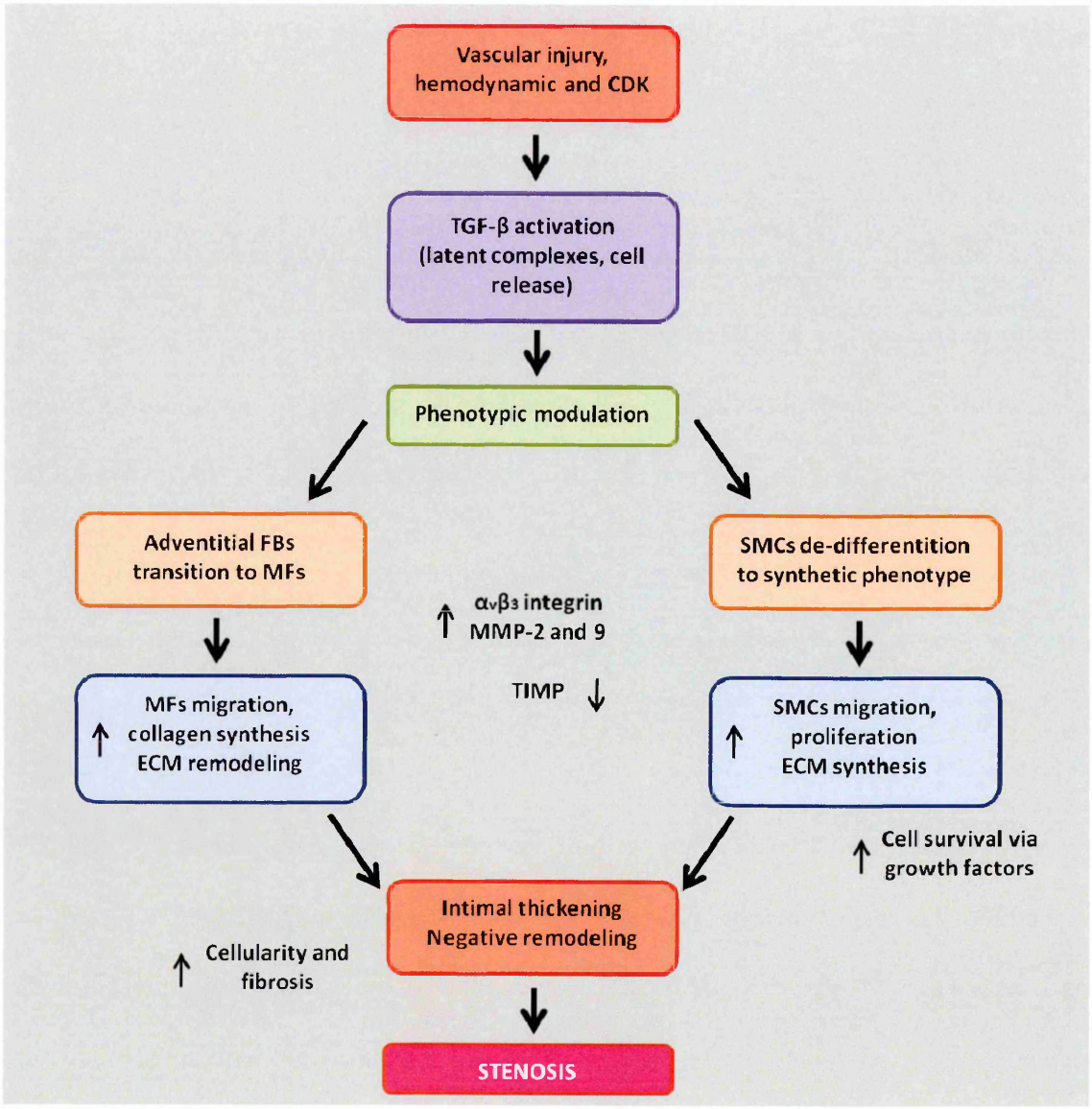

Fig.9: General mechanisms of AVF failure due to intimal hyperplasia-induced stenosis. Abbreviations: CDK chronic kidney disease, TGF-β transforming growth factor β, FBs fibroblasts, SMCs smooth muscle cells, MMP metalloproteinases, TIMP tissue inhibitor metalloproteinases and ECM extracellular matrix (166).

CHAPTER 2: Wall Shear Stress in AVF failure

This Chapter addresses the biological effects of Wall Shear Stress (WSS) on the endothelium. After a brief definition of analytical methods to evaluate WSS, a previously published idealized computational model of an End-to-Side Arteriovenous Fistula is presented, used to calculate the WSS waveforms investigated in vitro in the present work. The second part of the Chapter focuses on the literature findings related to WSS effects on endothelial cells that are potentially involved in Fistula stenosis and failure.

2.A) Wall shear stress effects on endothelial function.

2.A1) *Wall shear stress definition.*

WSS is the frictional force per unit area exerted by blood flow on the surface of the endothelium. The average physiological levels of WSS range from 1 to 6 dyn/cm^2 and from 10 to 70 dyn/cm^2 (76) in the venous and in the arterial vasculature network respectively (10 dyn/cm^2 = 1 Pa). WSS magnitude and direction depend on blood flow rate and vessel geometrical features. According to *Poiseuille's* law (249) the WSS generated by a laminar flow in a straight a cylinder (figure 10) is

$$WSS = \tau = \frac{6 * Q * \mu}{\pi * R^3}$$

where τ is wall shear stress (Pa), Q is the blood flow (m^3s^{-1}), μ is blood dynamic viscosity (Pa·s) and R is the vessel radius (m) (250).

During the cardiac cycle, the endothelium experiences rapid changes in WSS magnitude and direction. Features of vascular geometry such as branches and curvature

force the blood to create zones of recirculation and flow separation. Studies by Caro and colleagues (251) on atherosclerosis localization identified a correspondence between low WSS and areas of the vasculature most exposed to lesion development. Ku and Giddens (259) proposed in addition that marked oscillations in the direction of WSS may lead to atherogenesis. Subsequent studies have shown how shear stress deeply affects EC morphology, gene expression and biochemical signal productions depending on the features of the WSS waveform.

Despite the fact that *Poiseuille's* law is widely used to provide a simple method to calculate WSS, this formula assumes a steady, fully developed flow in a rigid cylinder. However, the AVF physiological conditions differ from these assumptions, since blood flow is unsteady and the vessels are elastic and present curvatures.

In 1955, *Womersley* considered the unsteady blood flow components by introducing a non-dimensional parameter that is the ratio between the transient inertial effect and the viscous effect of blood according the following definition

$$Wo = R_0 \sqrt{\omega/\nu}$$

where Wo is the *Womersley* number, R_0 is the vessel radius, ω is a frequency component of the blood flow ($\omega = 2 \cdot \pi / T$ where T is typically the fundamental period of the unsteady flow) and ν is the kinematic viscosity of blood (252, 253). Physiological values of Wo vary from ≈ 20 at the aorta level to values ≈ 1 at the terminal part of arteries, and became <1 in arterioles, capillaries and veins (254). Using this parameter it is possible to determine the blood velocity profile within vessels and to estimate the phase lag between the oscillating pressure and the correspondent flow. Furthermore, for higher values of α, several authors found dramatic differences in blood flow profiles

with respect to those calculated with *Poiseuille's* law. In particular the blood inertia effect causes zones of backward flows near the vessel wall despite an overall forward flow within the vessel (figure 10). Many previous studies have shown that considering *Womersley* number in calculating blood velocity and WSS, increases the accuracy of results compared to those obtained with non-linear numerical approaches (255, 256).

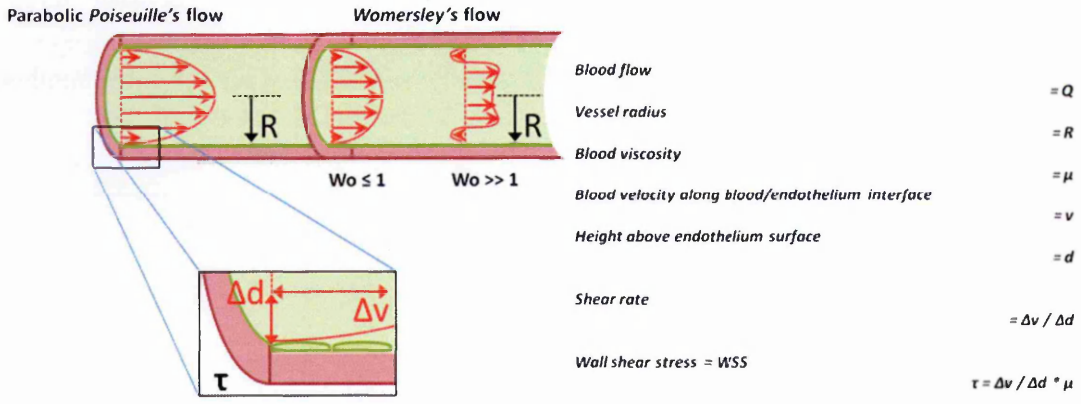

Fig.10: Wall Shear Stress (WSS) in a cylinder according *Poiseuille's* law or corrected with *Womersely* number.

An even better estimation of WSS generated by unsteady blood flows in realistic vessel geometries (i.e. tapered or stenosed vessels) can be achieved by considering the *Strouhal* number (also referred as reduced velocity) defined as

$$St = \frac{1}{U_{red}} = \frac{2}{\pi} \frac{Wo^2}{Re_D}$$

where St is the Strouhal number, U_{red} is the reduced velocity, Re is Reynolds number of the characteristic diameter D and Wo is the Womersley number (257).

Furthermore, to take into account vessel curvatures and branches, the *Dean* number can be used together with other parameters, while to model vessel elasticity

numerical approaches based on the fluid-structure interactions are required (257, 258). A detailed description of the above mentioned approaches is beyond the purpose of this study.

2.A2) *Wall shear stress in side-to-end AVFs.*

CFD simulations were performed in an idealized side-to-end AVF geometry, created between the radial artery and the cephalic vein, by Ene-Iordache et al. (79). Flow simulations were performed with an 8 core, 64 bit computer using the OpenFOAM 2.3.1. code, a multipurpose CFD tool based on the finite volume method (OpenFOAM team, 2014, The OpenFOAM Foundation, http://www.openfoam.org). A three-dimensional parametric model (figure 11) of the volume inside the AVF geometry was built using the GAMBIT 2.3 mesh generator software (Fluent Inc., Lebanon, NH, USA). The internal volume, corresponding to the fluid domain, was meshed with a structured grid consisting of 131,443 hexaedral cells (figure 12). Blood density was assumed constant (1.045 g/cm3) and blood viscosity was considered non-Newtonian. The result of simulation was post-processed and visualized using ParaView 4.2 software (Kitware Inc. Sandia National Laboratories, Albuquerque, NM, USA). For the purpose of this study only the WSS vector components parallel to the mean flow direction were considered.

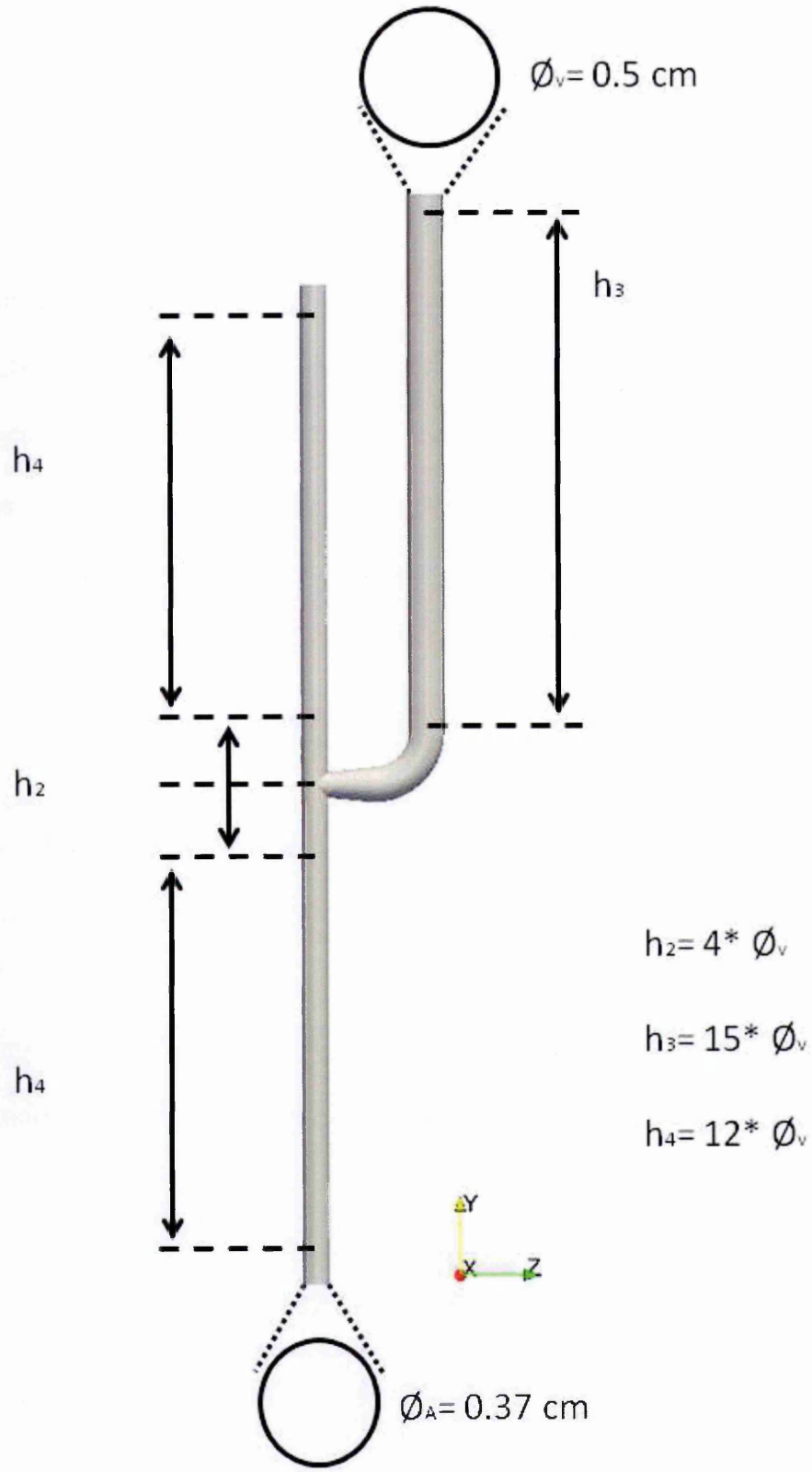

Fig.11: Parametric model of AVF used in flow simulations. $ø_A$ is the arterial diameter and $ø_V$ is the venous diameter(79).

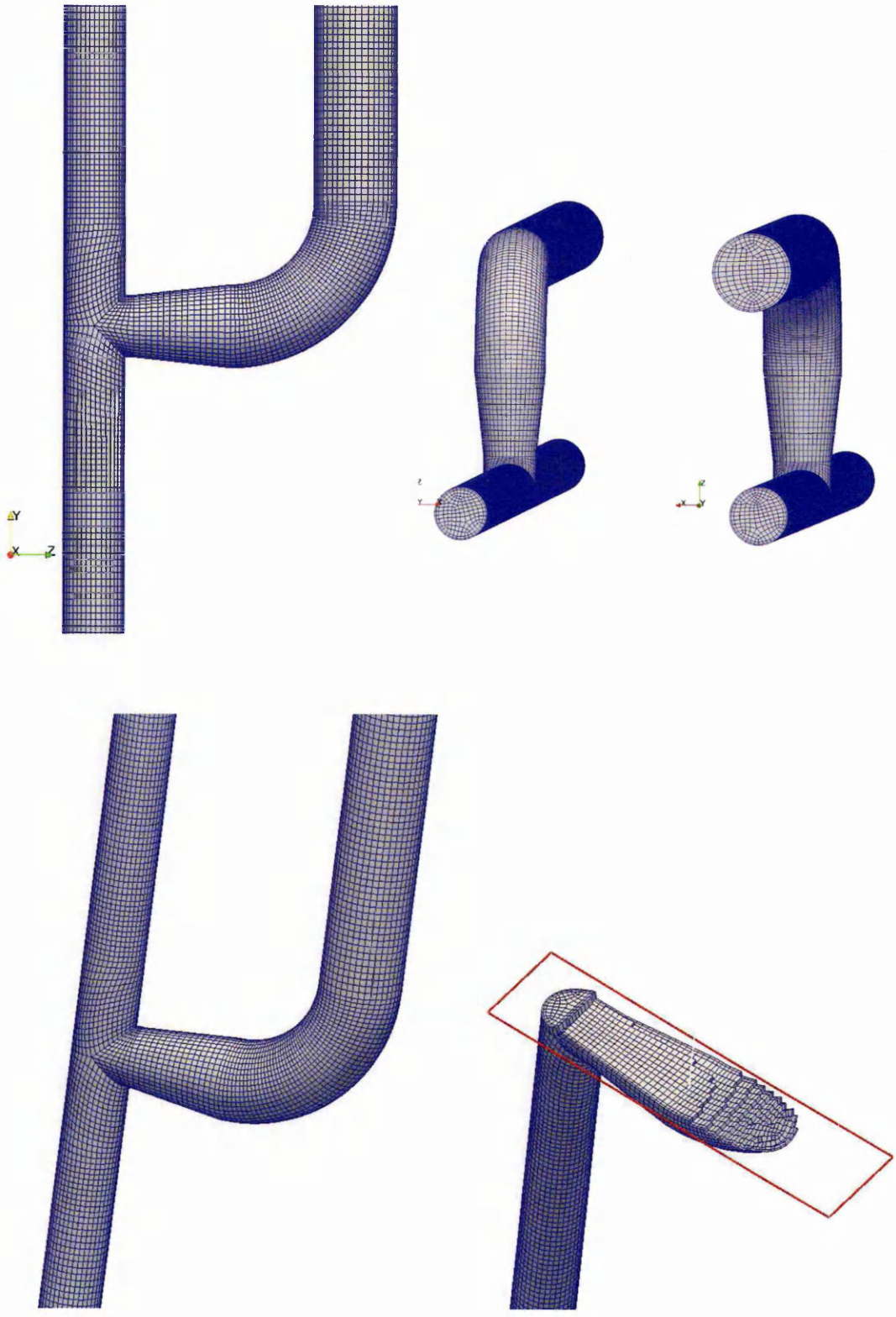

Fig.12: Structured mesh of AVF model (79).

In the present work, four WSS patterns have been tested (table 6, figures 13 and 14):

- ✓ The radial artery WSS calculated before the AVF surgical creation (PUL_A).
- ✓ The cephalic vein WSS calculated far from the disturbed area (PUL_V).
- ✓ The distal radial artery WSS, downstream of the AVF on the anastomosis floor (REC_A).
- ✓ The venous side of the anastomosis WSS (REC_B).

PUL_A represents the lower WSS measured in the radial artery before the AVF creation. PUL_V derived from the cephalic vein, downstream the anastomosis, where the flow re-acquires a laminar and unidirectional waveform, after the disturbances introduced by the anastomosis curvature. Both these waveforms demonstrate pulsatile behavior and are distinguished by the suffix PUL.

REC_A and REC_B were calculated downstream of the AVF on the anastomosis floor and at the anastomosis on the inner side of vein curvature respectively. These two areas have been previously identified as common sites for IH development (71).

Waveforms	PUL_A	PUL_V	REC_A	REC_B
Mean [dyn/cm^2]	3.35	15.78	0.08	0.07
STD [dyn/cm^2]	6.58	3.16	7.53	9.55
Max absolute WSS [dyn/cm^2]	26.67	22.76	16.51	26.03
WSS step [dyn/cm^2]	30.03	10.32	29.67	37.08
OSI	0.06	0	0.49	0.49

Tab.4: Main features of investigated WSS waveforms. Mean is the mean value of WSS during the 1 second cycle, STD is the standard deviation of WSS values during the cycle, Max absolute WSS is the highest value of WSS modulus, WSS step is defined as the difference between the maximum and minimum WSS values and OSI is the Oscillatory shear index (259).

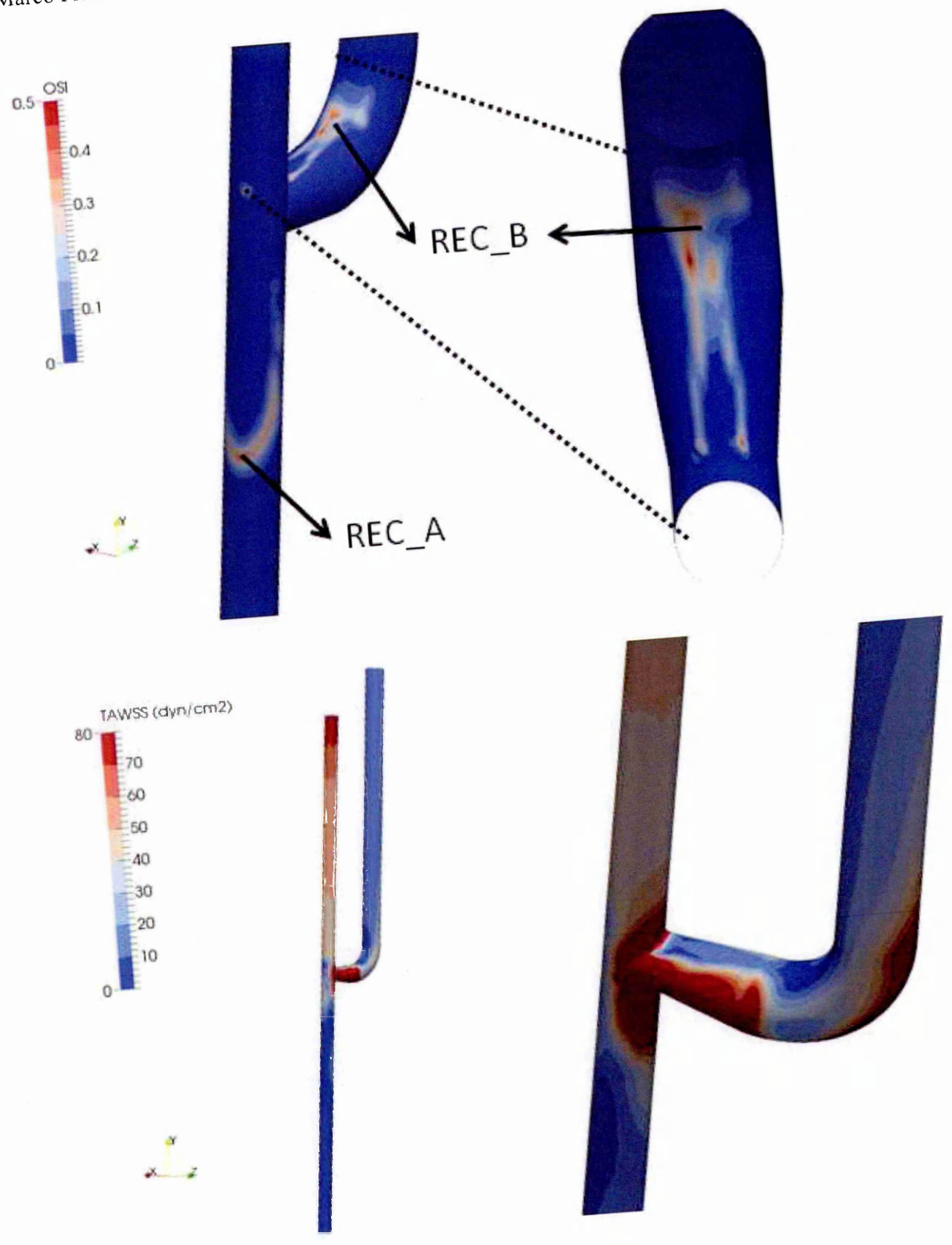

Fig.13: OSI and time averaged WSS (TAWSS) distribution in the AVF model (79).

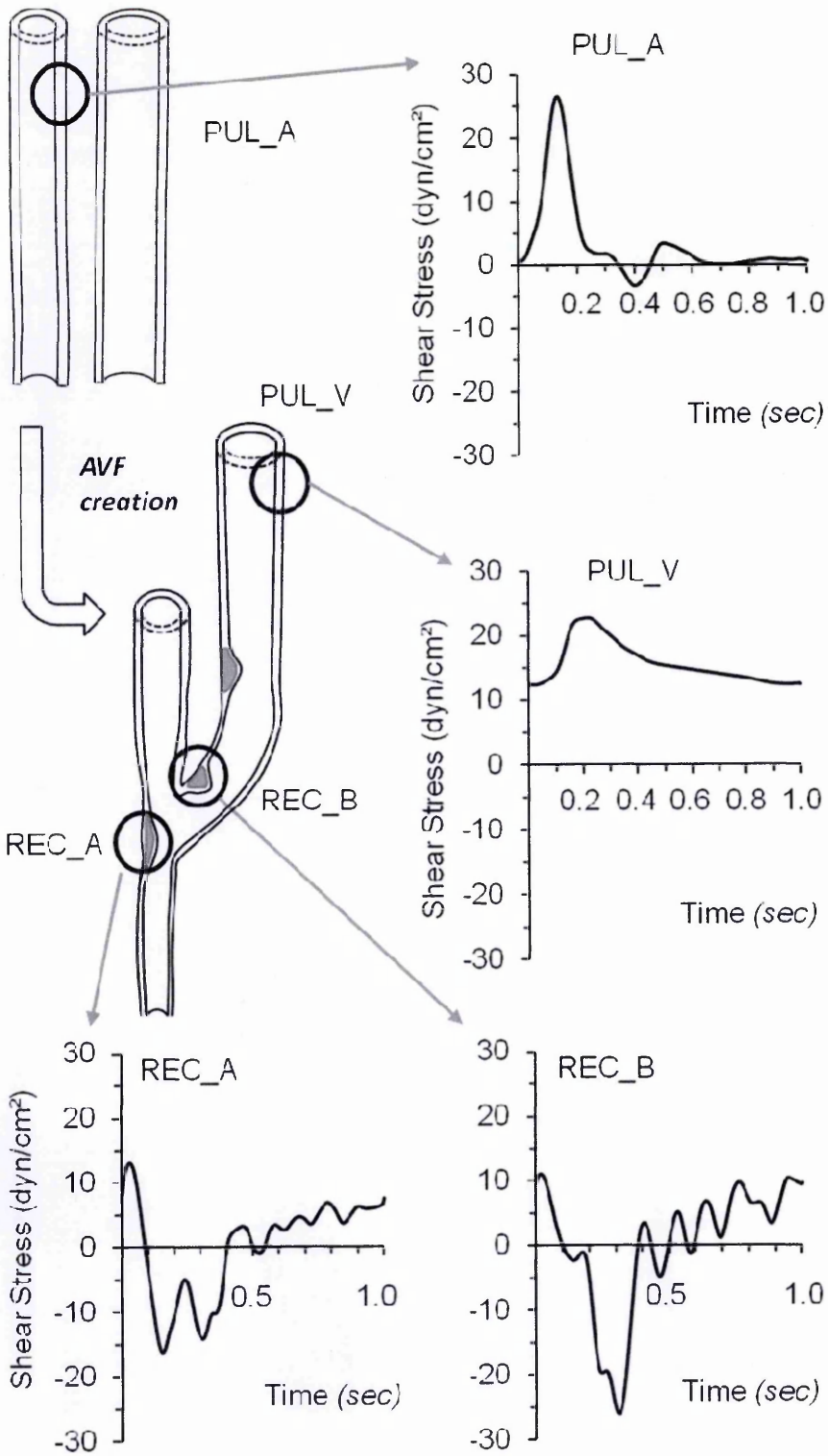

Fig.14: Origin and profile of WSS waveforms selected for the present study (79). This image has been published in "Am. J. Physiol. Heart Circ. Physiol. 2015 Oct 23. doi: 10.1152/ajpheart.00098.2015".

2.B) Endothelial WSS mechanotransduction.

2.B1) *Endothelial wall shear stress mechanotransduction.*

Evidence emerging in the last three decades of *in-vivo* and *in-vitro* experimental studies focused on atherosclerosis, has shown that WSS waveforms can be divided into two classes named "*Atheroprone*" or "*Atheroprotective*", depending on their capacity to elicit or prevent vascular dysfunction (260). According to this classification, the WSS waveforms calculated from the AVF CFD model were divided into two groups. As shown in figure 15, unidirectional and pulsatile waveforms with a relatively high magnitude and low frequency oscillations have been shown to be protective for endothelium (261) by eliciting a quiescent ECs phenotype that results in vessel homeostasis and antioxidant effects (262). On the contrary, as shown in figure 16, reciprocating or disturbed WSS, characterized by a relative low magnitude and/or important reverse flow phases with high frequency oscillations, elicits an activated state in ECs that results in an overall pro-inflammatory, proliferative paracrine signalling and in pro-oxidant state (263). Continuous exposure to oscillating WSS stimuli deeply affects EC morphology, gene expression and biochemical signals and results in an endothelial loss of continuity and altered permeability (77).

Mechanotransduction of WSS in ECs is exerted by a plethora of sensors (102). Immediately after WSS onset, activation of surface potassium channels leads to membrane hyperpolarization (264). Subsequent recovery and membrane depolarization depend on chloride channel activation. Moreover the WSS onset leads to a net influx of Ca^{2+} (265, 266) and causes NO production (267, 268). Other membrane structures such as G-coupled protein receptors (269) and tyrosine kinase receptors are also activated by

WSS (110). Finally, WSS affects the balance between caveolae-mediated NO release and ROS (270, 271).

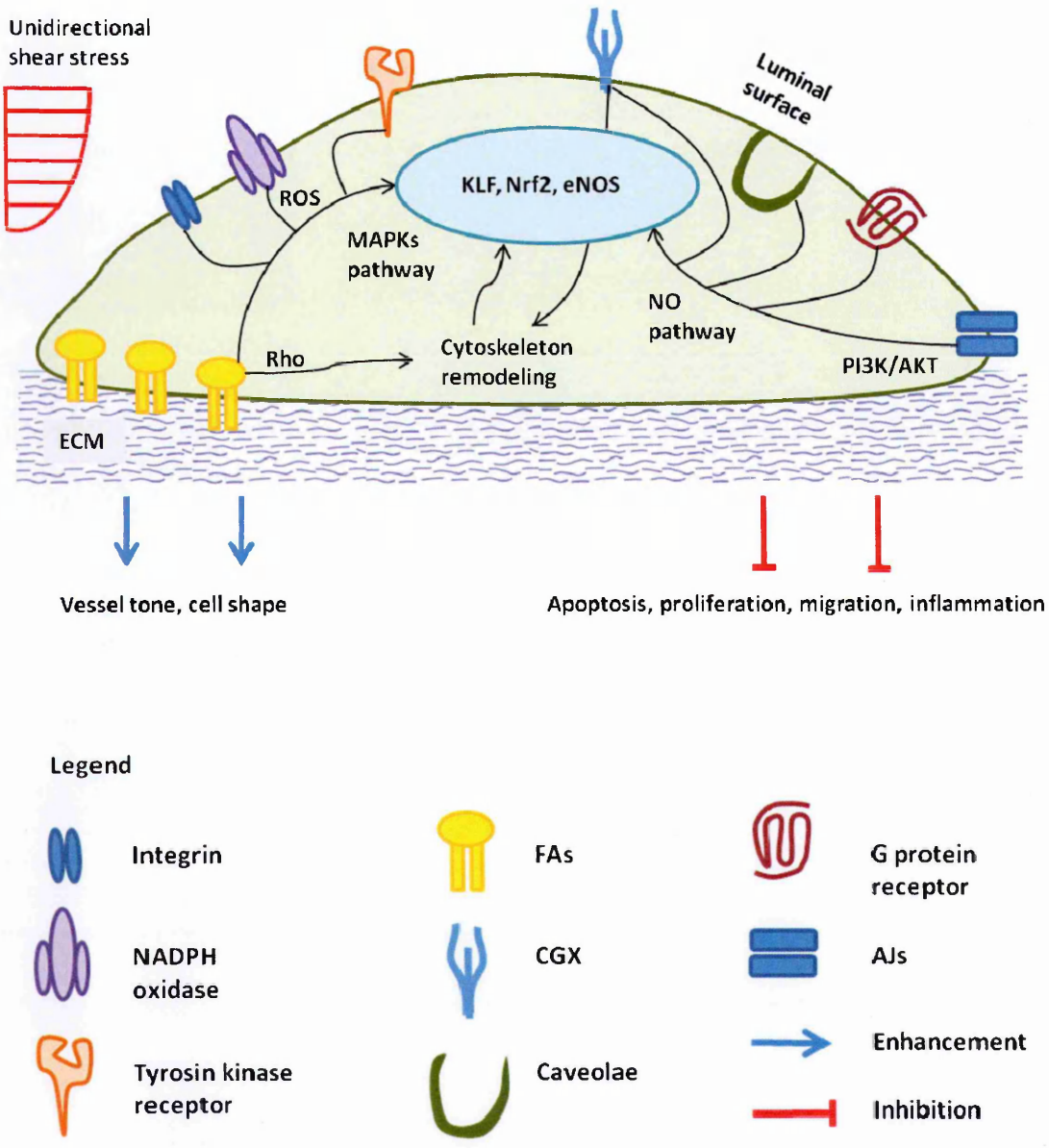

Fig.15: Schematic representation of unidirectional WSS signalling in ECs. Abbreviations: ROS reactive oxygen species, MAPKs mitogen activated protein kinases, KLF Krüppel like factor, Nrf2 nuclear factor-erythroid 2-like 2, eNOS endothelial nitric oxide synthase, NO nitric oxide, PI3K phosphatidylinositol-3-kinases, AKT protein kinase B, ECM extracellular matrix, NADPH nicotinamide adenine dinucleotide phosphate, FAs focal adhesions, AJs adherns junctions (263).

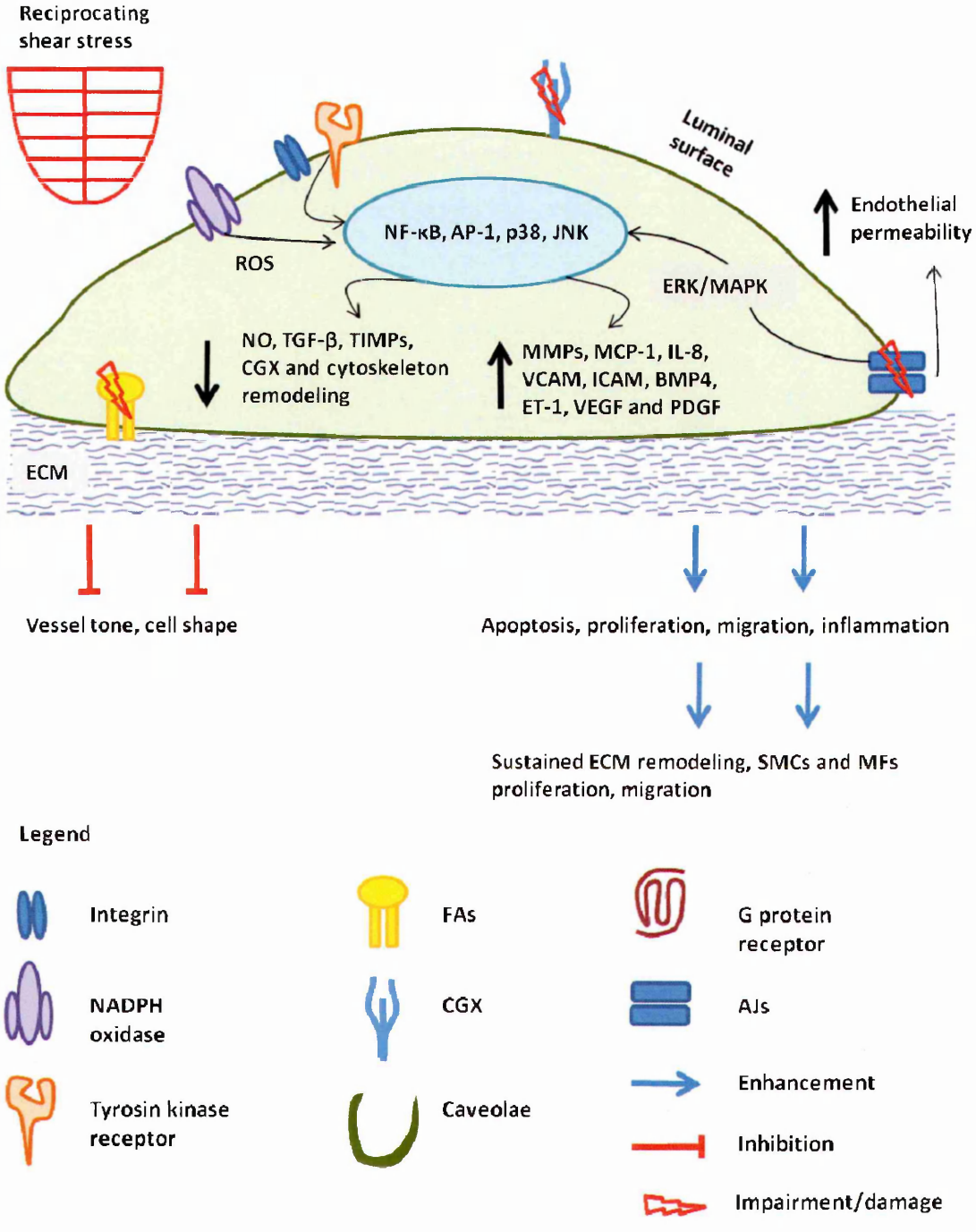

Fig.16: Schematic representation of reciprocating WSS signalling in ECs. Abbreviations: ROS reactive oxygen species, NF-κB nuclear factor κB, AP-1 activator protein 1, JNK jun n-terminal kinase, ERK extracellular-signal-regulated kinase, MAPKs mitogen activated protein kinases, NO nitric oxide, TGF-β tumor growth factor β, TIMPs tissue inhibitor metelloproteinases, GCX

glycocalyx, MMPs metalloproteinases, MCP-1 monocyte chemoattractant protein 1, IL-8 interleukin 8, VCAM vascular adhesion molecule, ICAM intracellular adhesion molecule, BMP-4 bone morphogenic protein 4, ET-1 endothelin 1, VEGF vascular growth factor, PDGF platelet derived growth factor, ECM extracellular matrix, NADPH nicotinamide adenine dinucleotide phosphate, FAs focal adhesions, AJs adherns junctions (75).

Depending on WSS waveform features, flow-induced transcription factors elicit gene expression on a time scale of 24-72 (125) hours controlling EC morphology, proliferation, migration, inflammation and apoptosis, thus promoting wall remodeling induced by mechanical stress. These pathways synergistically act to modulate EC transcription factors including NF-κB, AP-1 (75).

Activation of EC surface receptor molecules induces activation of several downstream pathways within seconds to hours (104). Key molecules regulating these pathways are MAPKs (ERKs, JNKs), kinases involved in the cell cycle and proliferation (272).

EC activation is only transitional if elicited by physiological/unidirectional WSS onset (273). On the contrary sustained signalling is generated by disturbed/reciprocating WSS stimuli (274, 275). The temporal regulation of these pathways is mainly exerted by functional ECs morphological adaptation to flow that involves structures such as the glycocalyx (GCX) and cytoskeleton (135, 276).

WSS-induced cytoskeleton remodeling is related to EC quiescence or activation by transmitting and producing intracellular forces with direct effects on several EC structures. The structural tensegrity (277, 278) model provides a description for the mechanical properties of ECs. In this model the cell is considered as a prestressed

tensegrity structure due to the ability of the cytoskeleton to absorb the mechanical loading applied to its surface.

The cytoskeleton elements are very flexible and can adapt to variations in mechanical stress. The interconnected structures of the cytoskeleton balance the internal forces of tension originated by microfilaments and compression forces exerted on microtubules in order to reach equilibrium (figure 17). Changes in mechanical loading, such as those elicited by AVF creation, induce EC cytoskeleton remodeling as described by the "bumper-car" model (279).

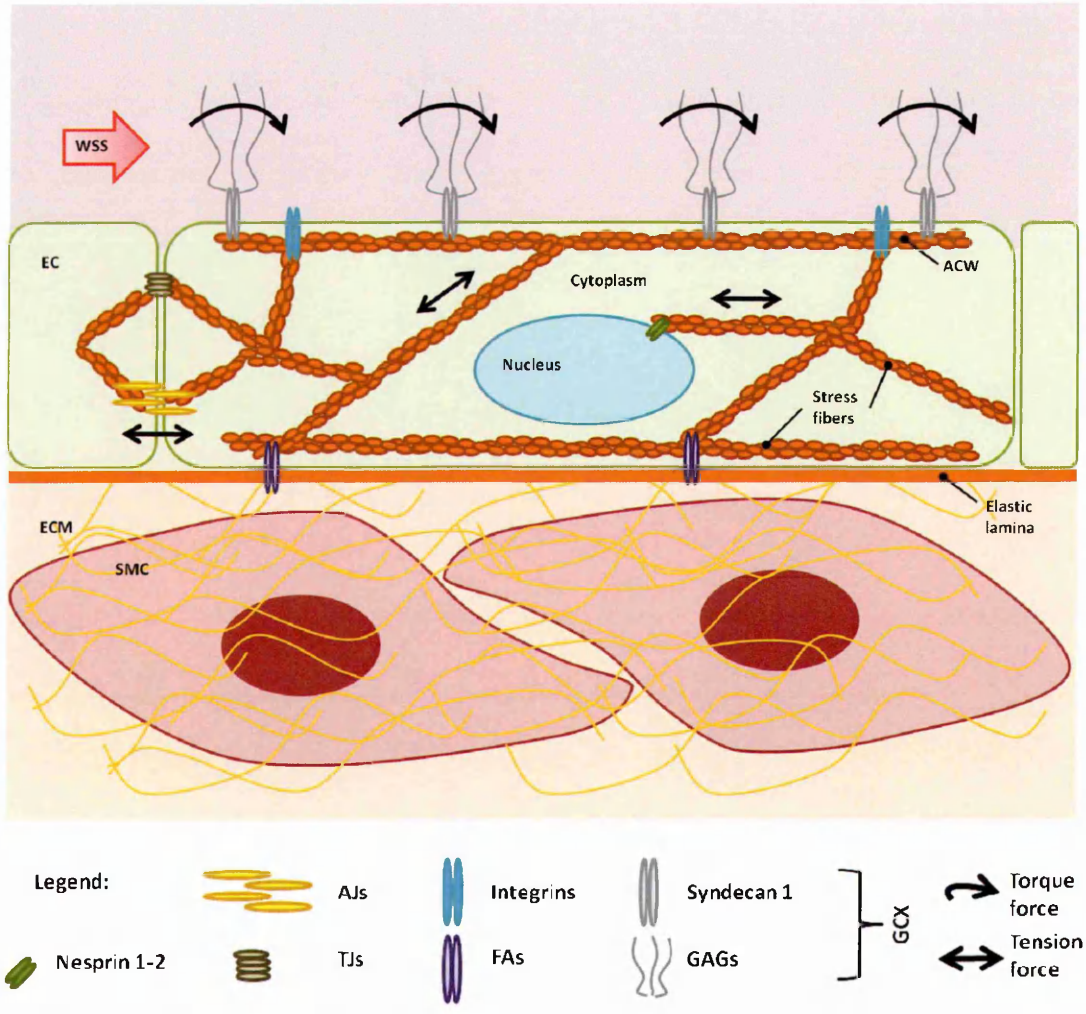

Fig.17: Schematic representation of endothelial cytoskeleton and its connections with mechanosensitive structures. Abbreviations: WSS wall shear stress, EC endothelial cell, ACW actin cortical web, SMC smooth muscle cell, ECM extracellular matrix, adherens junctions AJs, tight junctions TJs, focal adhesions FAs, glycosaminoglycans GAGs, glycocalyx GCX (279).

2.B2) *"Bumper-car" model of endothelial cells mechanotransduction.*

The "bumper-car" model (279) provides a hierarchical description of mechanical downstream events induced by WSS that result in signalling transfer from the cell apical surface to the cytoskeleton, then to junction complexes, to basement integrins and to the cell nucleus.

The normal endothelial surface is covered by a thick (0.5 -10 μm) (293) structure called the glycocalyx. This is composed of several transmembrane (syndecans) and membrane bonded (glypicans) core proteglycans carrying a complex network of glycosaminoglycan (GAG) chains that can bind to circulating molecules such as growth factors to form the endothelial surface layer (ESL) (280-282). Under physiological conditions, an extended endothelial CGX arises from endothelial surface and, by forming the ESL, provides a filter at the blood/EC interface, both steric and electrochemical due the net negative charges conferred to endothelial surface (283). A fully formed CGX may be able to completely shield the EC surface from WSS stimuli, preventing direct WSS activation of EC surface structures (284).

The GCX structure has a quasi-periodic highly dynamic structure (276). Several factors including the surrounding microenvironment, diseases such as CDK (285, 286) and local hemodynamics (276), regulate GCX composition and extent. Furthermore, ECs can provide active regulation of physicochemical properties and content of GAGs as a result of a continuous metabolic turnover orchestrated in order to adapt the CGX to changes in the local environment (287).

The most abundant GAG in human endothelium is heparan sulfate (HS, 50-90%), the rest is composed by chondroitin/dermatan sulfate and hyaluronic acid or hyaluronan. GAGs chains are covalently attached to specific sites on proteoglycans (288).

Human ECs express different proteoglycans. Transmembrane syndecan-1, -2 and -3, emerge from the cell surface with a very regular pattern and provide 3 to 5 attachment sites for GAGs in the extracellular domain, which bind preferentially, but not exclusively, to HS (289). The syndecan cytoplasmic domain is associated with the cytoskeleton via a hexagonally arranged actin filament cortical web (ACW) and participates in its organization through molecules such as α-actinin and tubulin. Simultaneously, syndecan-binding properties can be modulated by intracellular signals (290, 291).

Glypican-1 is also expressed by human ECs and localized to lipid rafts at the caveolae level that are involved in NO release. Glypican-1 is directly bound to the cell membrane through a C-terminal glycosylphosphatidylinositol anchor and presents 3 to 4 attachemnt sites for HS (292).

Recent studies have revealed the structure of the GCX (293) participates in EC mechatransduction of WSS (294). Alternatively, knockout of sydecan-1 or glypican-1 causes lack of cytoskeletal remodeling and a reduction in NOS synthesis respectively in ECs exposed to fluid flow (295). Similar effects were observed after enzymatic removal of HS (296).

WSS exposure causes torsion of GCX core proteins and initiates an integrated signalling in which cytoskeletal elements, such as ACW, transduce apical forces at basement attachment sites and at junction complexes (297). WSS also induces major cytoskeletal remodeling that affects the type and structure of connections and can lead to changes of a specific ECs phenotype (289, 298).

Actin filaments (F-actin) are the most abundant and proximal to cell membrane, among the three polymers that compose cytoskeleton (299). They are directly connected to β-integrin tails, by talin and filamin, and to cadherins, by vinculin and catenins. In EC

cultures under static conditions, F-actin is organized in dense peripheral bands (DAPBs) localized at the cell border and connected to neighborhood cells DAPBs by weak VE-cadherin linkages (279). As soon as ECs are exposed to unidirectional WSS, DAPBs disassemble and F-actin fibers undergo remodeling to form stress fibers connecting the cell basement and apical surface, several hours later (24-46 hrs) (300).

The Ras superfamily of GTPases and in particular, the GTPases RhoA, Rac1, and Cdc42 are known to regulate cell shape changes through effects on the cytoskeleton, cell polarity and transcription factor activity, in response to WSS (134). The primary regulation of GTPase operates similar to GEFs, GAPs control binding to GDP/GTP (139).

The first effect of WSS onset is probably the conversion of Ras-GDP to Ras-GTP that induces the activation of ERK and JNK pathways (301, 302). Flow onset induces immediately a structurally identifiable Rac-1 mediated formation of ruffles/lamellipodia in the direction of flow (303). WSS-induced activation of Rac-1 and its effector Serine/threonine-protein kinase (PAK) is required at the front of the cell to regulate actin polymerization and membrane protrusion (304). The activation of Rac-1 has to be spatially restricted in order for cells to polarize and align and/or migrate in the direction of flow. Localization of activated Rac-1 is induced by WSS through a PKA-dependent alpha4 integrin phosphorylation at the downstream edge of ECs and directs cytoskeletal alignment in response to shear stress (305, 306). Rac-1 is also required to induce NF-κβ transcription and nuclear translocation in response to WSS (307).

Rho activity regulates stress fibers and focal adhesions via the Rho-associated protein kinase (ROCK) pathway (308). Rho activity is also required for the initial alignment of EC and for WSS-induced polarization and (309) migration (310). It has

also been proposed that subcellular localizations of RhoA activation is linked to endothelial barrier integrity and barrier function. Indeed Rho participates to AJs, TJs and FAs regulation and is necessary to induce WSS-mediated increase of endothelial permeability (309). A potential inhibitor of RhoA activity is the tyrosine phosphorylation of p190RhoGAP GTPase activating protein (311-313). In ECs, integrin-mediated adhesion provides a binding site for p120RasGAP (314), displacing it from the complex with p190RhoGAP and hence contributes to the decrease in RhoA activity (315, 316). CDC42 is known to promote formation of filopodia and controls cell polarity (317, 318). Despite the fact that CDC42 is not required in ECs to control stress fibers formation or permeability (309), its fundamental role has been established in the polarization of the microtubule-organizing centre (MTOC) to a position on the downstream side of the nucleus relative to the direction of flow (319). A correct spatial activation of CDC42 rather than activity *per-se* is essential for localization of the MTOC after shear stress.

A tight spatial and temporal regulation is essential in GTPase orchestrated activation and deactivation of cytoskeletal activities and can be modulated by external agents such as thrombin, VEGF or WSS (133, 320). The hallmark of these processes is the elongation of ECs in the flow direction in order to distribute the mechanical loading and to control endothelial barrier function. The optimization of stress fibers architecture and cell shape orientation in the flow direction, rather than merely an increased amount of polymerized F-actin, are necessary in ECs to maintain adhesion to the substrate when chronically stimulated with WSS (321).

2.B3) *Adherens junctions in endothelial mechanotransduction.*

Remodeling and stabilization of the cytoskeleton promotes formation of AJ complexes with several downstream effects on ECs. AJs, along with TJs, directly control endothelial permeability and intracellular signals (322). Many molecules with different functions form AJs (323, 324). VE-cadherin is the regulator of complex formation and provides the link between neighbouring cells (325). Platelet-endothelial cell adhesion molecule (PECAM) is a mechanosensor situated at the cell-to-cell interface and it may be responsible for the signalling that controls AJ formation in response to the pulling force transmitted by the cytoskeleton after WSS onset (326). A main AJs component is vascular endothelial growth factor receptor 2 (VEGFR-2) (327), a receptor tyrosine kinase that mediates the angiogenic effect of VEGF. VEGFR downstream effects strongly depend on AJ complex formation and context. VEGFR-VEGF binding in an intact endothelial monolayer controls proliferation contact inhibition by promoting pro-survival AKT signalling (328). On the contrary VEGFR-VEGF binding in damaged endothelium promotes proliferation via ERK/MAPK signalling. Many other molecules have functional interactions with AJ complexes (329). p120 β-catenin is the link between AJs and the cytoskeleton and promotes VE-cadherin stabilization (330). AJs also interact with TGF-β, hepatocyte growth factor (HGF or MET), VEGF, epithelial growth factor and fibroblast growth factor (FGF) possibly leading to signalling dysfunction (331).

2.B4) *Tight and Gap junctions in endothelial mechanotransduction.*

Similar to AJs, TJs are also junctional complexes that regulate endothelial permeability and leukocyte trafficking (332, 333). TJs consist in protein complexes where occludins, claudins and junctional adhesion molecules are connected to F-actin

fibers through zonula occludens (ZO-1, 2, 3) (334). Upon VEGF, MCP-1 or WSS stimulation, occludin is phosphorylated on multiple serine and threonine residues leading to increased endothelial permeability (335). Furthermore ZO-1 expression is also modulated by WSS with important effects on EC signalling and leukocyte transmigration (336).

Gap junctions (GJs) provide passage for ions and small molecules between adjacent cells (337). GJs are formed by connexin proteins and even if they may have a secondary role in mechanotransduction, they do participate in WSS-induced signalling (338-341).

2.B5) *Focal adhesion complexes in endothelial mechanotransduction.*

As mentioned above, the cytoskeleton transmits mechanical stress from the apical membrane to ECs basal laminae. At this level, the mechanical stress is equal and opposite in direction to the stimulus at apical level. This is necessary to avoid catastrophic endothelial delamination (279). Beyond cell-to-cell adhesion complexes, WSS causes major redistribution of proteins involved in FA formation (342). These complexes provide anchorage for ECs to the elastic laminae underneath the endothelium and promote linkage of F-actin to extracellular matrix via transmembrane integrins such as $\alpha_v\beta_3$ and transmembrane syndecan-4 (343-345). A short time after WSS onset, FAK are recruited to form complexes involving, among others, vinculin, paxilin and talin (346). According to the "bumper car" model (279), ECs assume an unstable configuration during the transitional remodeling phase. To avoid EC delamination, new FAs are formed together with actin stress fibers at the basal EC margin due to vinculin migration. Once the new configuration is stable, DAPBs are reformed and vinculin is dispersed.

Phosphorylation and relocalization of FAs caused by mechanical stimuli are deeply involved in ECs mechanotransduction. Modulation of FA activity is involved in EC migration, proliferation and apoptosis. FAs are also involved in the regulation of endothelial permeability and inflammation (347-349). Conformational activation of integrins, caused by activated VEGFR-2 recruitment and activation of PI3K, induce formation of new binding sites on the ECM that promote activation of small GTPases, such as Rho and Rac (272). Furthermore, downstream effects of integrin activation involve up-regulation of proinflammatory transcription factors such as NF-κB, MAPK or adhesion molecules that affect vascular permeability (350, 351). Interestingly, blocking integrins with specific antibodies inhibits WSS-induced EC remodeling (352).

The tension exerted on integrins by physiological flows however, is lower than that necessary for direct activation and it is more likely that the force generated by the cytoskeleton (272) causes integrin activation. Latent TGF-β (353, 354), possibly activated by integrin signalling (355), plays the most important role in matrix deposition due to its ability to induce synthetic phenotypes in vascular cells, regulating IH development.

2.B6) *Primary cilia in endothelium mechanotransduction.*

The primary cilium is a non-motile apical membrane structure involved in mechanotransduction (356, 357). It protrudes from the EC membrane as a single structure with functions of an antenna able to transduce both mechanical (WSS, pressure) and chemical (PDGF) signals within the cell (358). Primary cilia are involved in Ca^{2+} influx induced by WSS and cilia defects are related to several pathologies. (359) A recent study showed that lack of primary cilium induce ECs to undergo EndMT due

to TGF-β signalling and repression of KLF-4, while cilium rescue or KLF-4 overexpression prevent the transition (360).

2.B7) *Nucleus transmembrane complexes in endothelial mechanotransduction.*

The EC cytoskeleton structure can directly bind to the cell nucleus membrane and nuclear laminin (361). Actin filaments form a nesprin/SUN/laminin complex that binds nuclear chromatin and can transmit mechanical forces to the nucleus karyoskeleton. This evidence suggests that, beyond biochemical pathways activation, WSS can directly control gene expression through cytoskeletal mechanotransduction (362).

2.B8) Hemodynamics in AVF maturation and failure.

Previous studies have shown that low/reciprocating WSS has many detrimental effects on ECs leading to pathologies such as atherosclerosis and aneurysms. Low/reciprocating WSS waveforms have been defined as athero-prone due their ability to lead to atherosclerotic lesion development (274). WSS waveforms in the high risk stenosis area of AVFs have a generally higher magnitude with higher frequency oscillations and possibly several reverse flow phases compared to those investigated in atherosclerosis development (260). Since atherosclerosis development is a major focus of research interest, the affect of AVF-specific WSS waveforms on ECs has been poorly addressed.

As mentioned before, AVF creation induces a significant increase in blood flow while the rise in WSS acting on the endothelium is limited by the vessel diameter increase induced by NO release. The high sensitivity of endothelium to WSS is further confirmed in-vivo. A previous study showed that radial artery remodeling after AVF

creation is able to provide an increased blood flow maintaining an almost constant peak WSS during the cardiac cycle (82).

An effective remodeling process provides an increased blood flow through the AVF with limited effects on WSS. In high risk AVF areas, WSS has been shown to be reciprocating with non-physiological high frequency oscillations. Since physiological unidirectional WSS is a determinant in inducing EC quiescence (figure 9), reciprocating WSS in the AVF may lead to altered EC permeability and chemoattractant signalling, responsible for IH development.

As described above, many upstream events may be responsible for IH development and lack of positive remodeling, such as surgical handling, damage to the adventitia and other vessel layers, increased oxidative stress levels and inflammation. Since these events affect all the areas of AVF vessels but IH-induced stenosis occurs in those areas exposed to reciprocating WSS, it is reasonable to hypothesis this force is the ultimate regulator of IH development.

This hypothesis is strongly supported by further experimental evidence focused on atherogenesis, which have emerged in the last three decades (figure 10) (110). Reciprocating flows cause a down-regulation of KLF-2 expression (140). KLF2 is highly expressed in-vivo by endothelium but not in areas of the vasculature characterized by curvature and branches that are exposed to reciprocating WSS (363). ECs exposed to reciprocating WSS show a lack of cytoskeletal remodeling and elongation, related to cell quiescence (364). Reciprocating WSS affects vascular remodeling mainly by the down-regulation of NO release and up-regulation of the vasoconstrictor ET1 (365). Disturbed WSS also prevents CGX formation (366) and affects cytoskeleton remodeling and stabilization. The unstable cytoskeleton promotes AJ destabilization that prevents contact inhibition and induces EC proliferation. Also

FA formation and distribution is affected by cytoskeletal remodeling (279). Disturbed WSS also affects integrin interaction with ECM and EC nuclei (361).

Furthermore, WSS has been shown to control EC adhesion molecule expression such as VCAM and ICAM. The expression of these molecules along with overexpression of IL-8 and MCP-1 is fundamental in promoting monocyte adhesion and infiltration (75, 76). Reciprocating WSS also causes an increase in MMP-2 and 9 syntheses that, along with impaired TIMP expression, sustains ECM remodeling inducing SMC migration and proliferation (367). ECM remodeling can also activate latent TGF-β complex inducing vascular cells activation and IH (354).

2.C) Summary

Wall Shear Stress is a fundamental mechanical stimulus in vascular biology. Several analytical and computational approaches have been developed in order to calculate *in-vivo* WSS profiles during the cardiac cycle in the different areas of vasculature. To address this problem in the Arteriovenous Fistula for hemodialysis vascular access, our group have developed an idealized model to calculate WSS waveforms in AVF areas more frequently affected by neointimal hyperplasia (72). From previously published simulations, four WSS profiles are reported here to be used in the present *in vitro* study (79). These profiles were classified according their temporal behaviour as Pulsatile or Reciprocating. Pulsatile WSS was computed in AVF areas relatively protected from IH development while Reciprocating WSS was computed in areas that previous studies identified as more exposed to IH and stenosis. This classification is similar to that proposed by several authors to define the atherogenicity of WSS that develops in the carotid bifurcation (260).

To explore the hypothesis that local disturbed hemodynamic, and the consequent reciprocating WSS, in the AVF affects EC phenotype and signalling, enhancing IH development, an experimental set-up, based on a cone-and-plate geometry was designed as described in the next chapter.

To investigate the cellular effects generated by these AVF-specific WSS waveforms, later chapters describe observation of EC morphology after flow exposure and quantification of F-actin fiber distribution to assess cytoskeletal remodeling. This is complemented with further evaluation of KLF-2 m-RNA differential expression elicited by WSS stimuli and the expression of genes involved in RhoGTPase downstream effects. Measurement of the flow-induced production of IL-6, IL-8 and MCP-1 is also reported along with the evaluation of the paracrine proliferative effect on SMCs of medium conditioned by HUVECs during flow exposure experiments. Finally, flow-induced CCR2 and CK1-α mRNA expression was quantified.

CHAPTER 3: Cone-and-Plate device

This Chapter provides a review of the currently available cell shearing devices used in biomedical research and the design and construction of the real-time controlled Cone-and-Plate device used in the present work. In the second part of the Chapter, results obtained with analytical and numerical methods to evaluate the capability of the device to generate tightly controlled, highly unsteady Wall Shear Stress stimulations over the cell monolayer culture are reported.

3.A) In-vitro exposure to WSS

3.A1) Cell shearing devices.

The last thirty years have seen an enormous increase of interest towards in-vitro models to evaluate the effect of mechanical stimulation on different tissue and cell types. Despite the attempt to reproduce the complex in-vivo environment, the reductionist approach implicit in in-vitro models was introduced to study the effects of a single mechanical parameter. To investigate the effect of in-vitro shear stress on cell cultures many devices have been developed (figure 18), these include;

- Square Capillary tube (A);
- Parallel plates flow chamber (B);
- Parallel plates viscometer (C);
- Cone-and-plate viscometer (D).

Each of the systems has both positive and negative aspects (368). The capillary tube (Fig.18A) presents difficulties in cell seeding, it does not allow observation of

seeded cells under the microscope and it also requires a system to generate the flow inside the tube (e.g. constant pressure head, syringe or peristaltic pump). Indeed, it offers a simple geometry, similar to physiological conditions.

The parallel plates chamber (figure 18B) is capable of providing a wide range of WSS stimuli, however it does not allow control of WSS magnitude and waveform over a continuous range. Flow is usually produced with a pressure generating system similar to those reported for the capillary tube. WSS rise time depends on chamber geometrical parameters and fluid viscosity, thus a time delay occurs between a change of inlet pressure and consequent WSS variation. Among the advantages are the easiness of cell seeding and the opportunity to observe cell behaviour under a microscope during the experiment.

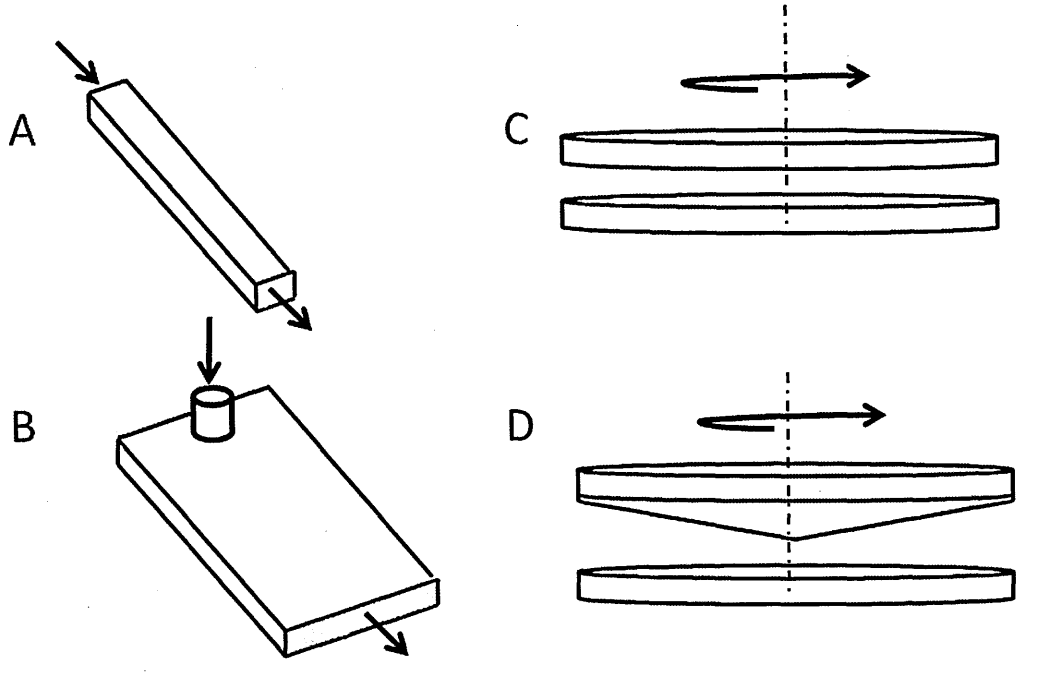

Fig.18: Examples of cell shearing systems. A) Capillary tube, B) parallel plates chamber, C) parallel plate viscometer and D) cone and plate viscometer.

The two viscometer configurations were originally developed to measure fluid viscosity. Basically they consist in an element rotating over a fixed plate. The test fluid fills the gap and it is dragged by the rotating element. The fluid viscosity is evaluated from measurements of torque necessary to maintain a constant rotation.

The two viscometers have been used to stimulate cell monolayer cultures since the 1980's and present similar advantages. The main improvement over other devices relates to the fluid drive system. The flow is regulated by rotation of the viscometer upper element provided by an electrical engine. This system allows a continuous control of WSS delivered to the culture surface and no pumping system is required. Similarly, both systems require a time of development necessary to achieve the new shear stress value on the culture surface due a change of rotation velocity. This aspect limits the maximum acceleration and deceleration, which can be correctly transferred across the gap.

The main difference between these systems relates to the rotating element and the geometry of the surface that moves the fluid. Due to the geometrical configuration, the parallel plates apparatus (figure 18C) fails to create a uniform shear stress stimulus on the entire culture surface. The fluid tangential velocities generated by a certain cone angular velocity increase along the radius from the plate centre to the periphery. This limitation was overcome by introducing the cone-and-plate geometry (figure 18D) that compensates for the radial increase in velocity with the increase of gap between the two elements due to the cone angle. A detailed description of cone-and-plate geometry (cone-and-plate device, CPD) and fluid dynamics is provided in next paragraphs.

3.A2) Cone-and-plate device.

Introduced by *Mooney* and *Ewart* in 1934 (369) as a tool to measure fluid viscosity, the device was firstly used by *Dewey* and colleagues (1981) (370) as device for cell shear loading (371). Since then many groups have used devices analogous to the cone-and-plate viscometer to study in-vitro effects of shear stress on monolayer cell culture, platelet adhesion or red blood cell mechanical damage.

For applications in cell biology, the CPD is usually operated to obtain laminar flow (termed primary flow), which generates concentric fluid streamlines, thus a uniform shear stress field on the entire culture surface. To match such conditions, the cone angle must be small (0.5°-3°) and the cone rotation velocity has to be low. However, different studies have addressed the CPD problem for larger cone angles as well as higher velocities

Using dye visualization techniques, *Cox* and others in 1962 (372), observed the development of circulatory secondary flows when the centrifugal forces become significant. *Pelech* and *Shapiro* in 1964 (373), proposed the ratio between fluid centrifugal forces and inertial forces (the so-called modified *Reynolds* number, Re, very similar to the *Reynolds* number used to evaluate turbulence inside pipes) as the parameter which governs the secondary flow onset in CPD geometry.

Fewell and *Hellums* in 1977 (374), provided a complete theoretical description of CPD internal flows. They reported how secondary flows are always present within the fluid, but are negligible for low angular velocities.

Bussolari in 1982 (375) and *Sdougos* in 1984 (371), proposed a simple formulation, based on CPD geometry simplifications, to calculate WSS on the plate surface. This approach is accurate only when CPD flow is primary. The authors successfully used Re as a threshold to avoid secondary flows within the CPD (371). For

Re→0, (Re<0.5) it is possible to consider the CPD internal flow as primary with fully developed concentric streamlines (figure 19). For higher Re values (0.5<Re<1) the secondary flows increase but remain negligible. Secondary flows start to disturb CPD internal flow for *Reynolds* number greater than 1 (1<Re<4), in this condition the fluid streamlines deviate from their concentric path by an angle which is a function of Re itself, forming a helix around the plate centre (figure 19). Finally for Re>4 the flow becomes fully turbulent and numerical methods are necessary to evaluate the shear stress field inside the CPD.

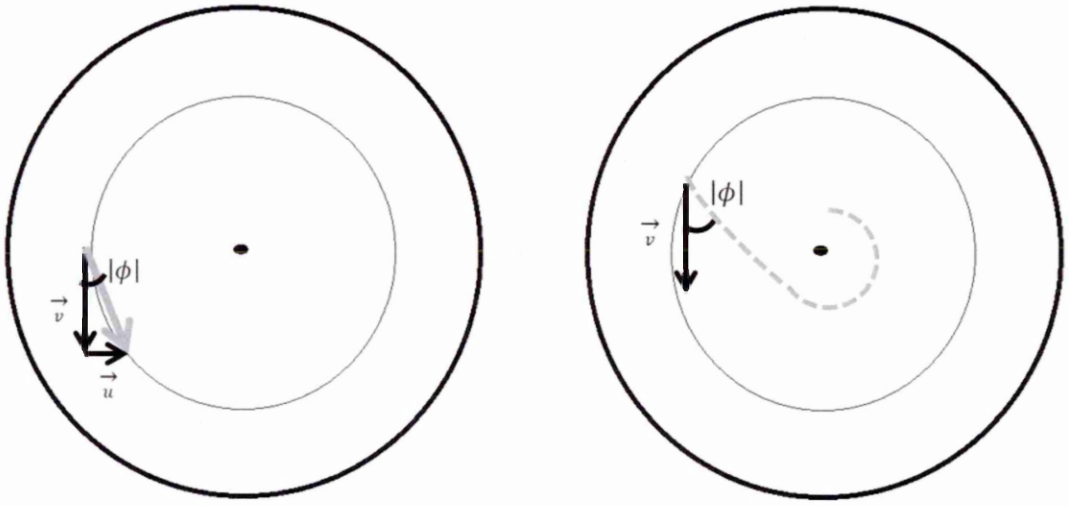

Fig.19: Effect of secondary flows within a cone-and-plate viscometer. Azimuthal (v) and radial (u) components of velocity near the plate surface, showing the angle ϕ. The dotted line represents the surface streamline and the angle between azimuthal and the surface directions (371).

Although numerical evaluations are necessary to calculate WSS on the plate for high Re values, macroscopic observations have reported recirculation of fluid along the radial direction. In this condition the fluid at the cone surface experiences outward

centrifugal forces, while an inward motion due to the recirculation forces characterizes fluid motion at the plate level.

Together with the increase of Reynolds number, other aspects ignored under primary flow conditions, become relevant. The formation of transient eddies, caused by fluid turbulence and the irregularities of the cell coated plate surface, affect the CPD internal fluid dynamics. Nevertheless, *Couette* flow is observed in the peripheral fluid volume present in the outer plate region, outside the cone area. These aspects however, were not addressed for the present study purpose.

The *Sdougos'* formulation (371) provides a valuable tool to estimate shear stress values on the plate surface. However, it is based on an idealized CPD geometry with no gap between the cone apex and the plate centre. Real experimental set-ups maintain a certain distance between the two elements of the device, which strongly affects the shear stress field underneath the cone, at the plate level.

Buschmann and his group (376) proposed a new formulation to overcome this limitation. The new approach introduces gap height as a parameter to calculate WSS delivered to the cell monolayer. The WSS evaluated with this method varies with radius, losing shear stress field uniformity. The proposed formula is accurate for realistic CPD configurations and agrees with CFD simulations performed by *Spuell* at al. (377).

The majority of reported experiments apply steady flow to stimulate the cell culture. However many cellular events rely on transient signals following the onset of unsteady flows. Several groups have reported the important role played by the form of the shear stress waveform in inducing disease progression. Together with the emerging importance of unsteady flows, research interest has moved to waveform features such as the level of mean shear stress, the magnitude and the frequency content.

These studies require dynamic control of cone rotation through a motor connected to a programmable interface. *Blackman* and colleagues (378) have proposed such a device that enabled the group to accurately handle complex shear stress stimulation. However, to accurately apply a realistic shear stress waveform it is necessary to evaluate the effect of inertial forces on CPD internal flow and the resulting effect on WSS delivered to the plate surface.

The steady flow condition provides an easy control for cell loading after the transitional phase at the beginning of a stimulus. In contrast, time-dependant stimulations require the evaluation of the time lag between variation in cone rotation speed and the subsequent change of WSS magnitude at the plate level. The goal is to avoid undesired loss of stimulus frequency components.

According to *Malek* and others (379), the analytical solution for a suddenly accelerated plane wall in a semi-infinite Newtonian fluid allows evaluation of the development time necessary to obtain a deviation of the velocity profile from the asymptotic linear distribution less than 1%. A frequency threshold is introduced to achieve an accurate replication of shear stress waveform on the culture plate. The next section describes the CPD developed for the present study and the evaluation of the internal flows for the experimental test conditions.

3.B) CPD development

3.B1) Design of a compact cone-and-plate device.

The project aim was to test in-vitro effects of realistic fluid shear stress stimuli on HUVEC monolayers. Computational studies of in-vivo wall shear stress reported a wide range of physiological values and patterns depending on the vessel tree area examined. WSS values range from 0 to 70 dyn/cm^2 with either unidirectional or

reversing patterns (76), while oscillations at frequencies much higher than heart rate resulted from CFD simulations.

To deliver such highly unsteady flows, the cell shearing device had to match two main requirements: the capability to accurately generate both unidirectional and oscillating/reversing flow patterns, in a time dependant manner and to ensure a wide range of almost uniform stimulation on the entire culture surface at any given instant.

Among the different in-vitro systems currently available to expose cell monolayers to fluid shear stress, only the cone-and-plate device meets the project requirements. To achieve the study aims, a compact CPD, suitable for use in a standard cell incubator, was designed and constructed together with the *Mechatronic Laboratory* of *Bergamo University* (figure 20).

The system is composed of an AISI-316 stainless steel cone with a radius, r, of 67 mm and an angle, α, of 0.5° deg, coupled with a standard tissue culture Petri dish (disposable P-150, Falcon, BD Biosciences, Franklin Lakes, NJ, USA) used as a plate (figure 21).

The cone apex and plate are very close to each other, but they are not in contact, maintaining a gap h_0 of 0.1 mm (figure 22). The basement of the device is aluminium coated to prevent any corrosion phenomena. The base is shaped to provide a lodge for the plate. A vacuum was created underneath the plate through a pipe connected to a pump to ensure the correct position of the plate. This solution provides a strong bond to the plate that remains fixed in position. At the end of experiment however the bond is easily removed by turning off the pump. The cone is connected to a gear that is moved by a pinion (figure 23A) driven by a brushless electrical engine (Mavilor, Barcelona, Spain) operated by a dedicated programmable driver. The cone and gear rotate on a

circular guide thanks to three runners (figure 23B). By changing the rectified spacers between the cone and the plate it is possible to modify the gap h_0 (figure 23C).

The described system ensures quick and simple assembly/disassembly processes. By removing the engine from the CPD base (figure 24), the system is compact and easy to handle. Cell culture plates loading and unloading, culture medium change, are performed under a laminar flow hood, ensuring sterile and quick procedures. Furthermore, the CPD size and the reduced engine heat production, make the system suitable for use in a regular cell incubator chamber, ensuring proper culture conditions for long-term experiments. Finally a dedicated electrical circuit in compliance with legal electrical safety requirements provides the CPD power supply.

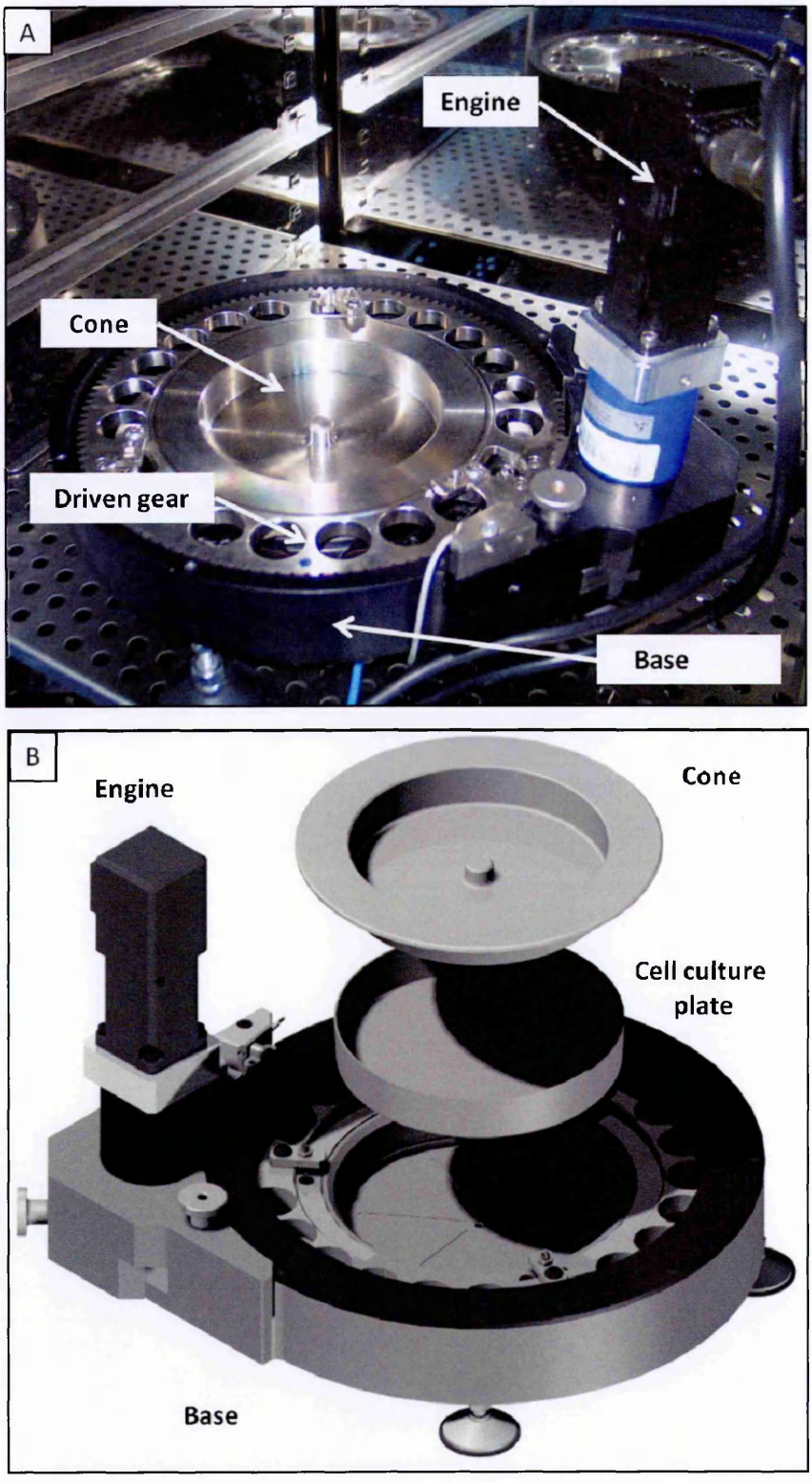

Fig.20: A) A picture of the CPD system within the cell incubator. B) Exploded view of the CPD system. This image has been partially published in "Am. J. Physiol. Heart Circ. Physiol. 2015 Oct 23. doi: 10.1152/ajpheart.00098.2015".

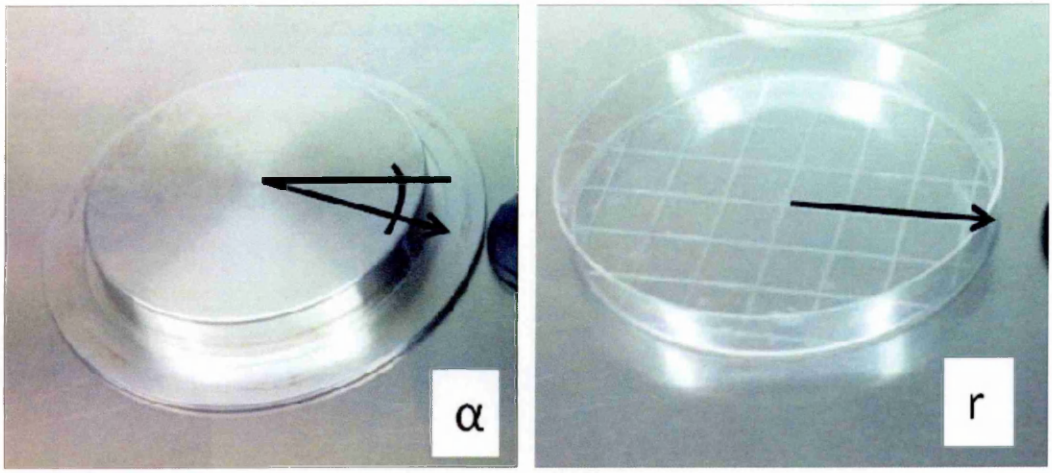

Fig.21: Images of the cone and its angle α and the plate with its radius r.

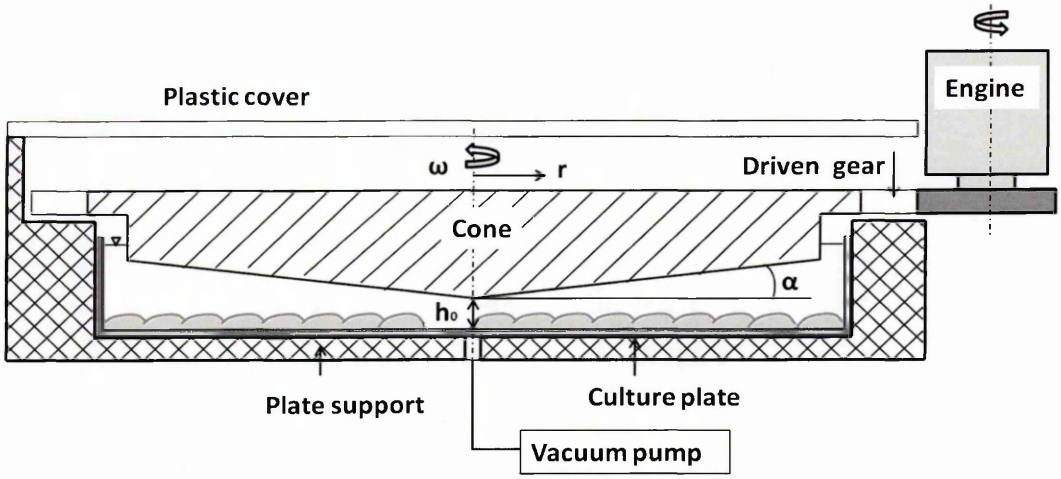

Fig.22: Schematic representation of the CPD geometrical features. Abbreviations: ω cone angular velocity, r radius, h0 gap between cone apex and plate and α cone angle. This image has been published in "Am. J. Physiol. Heart Circ. Physiol. 2015 Oct 23. doi: 10.1152/ajpheart.00098.2015".

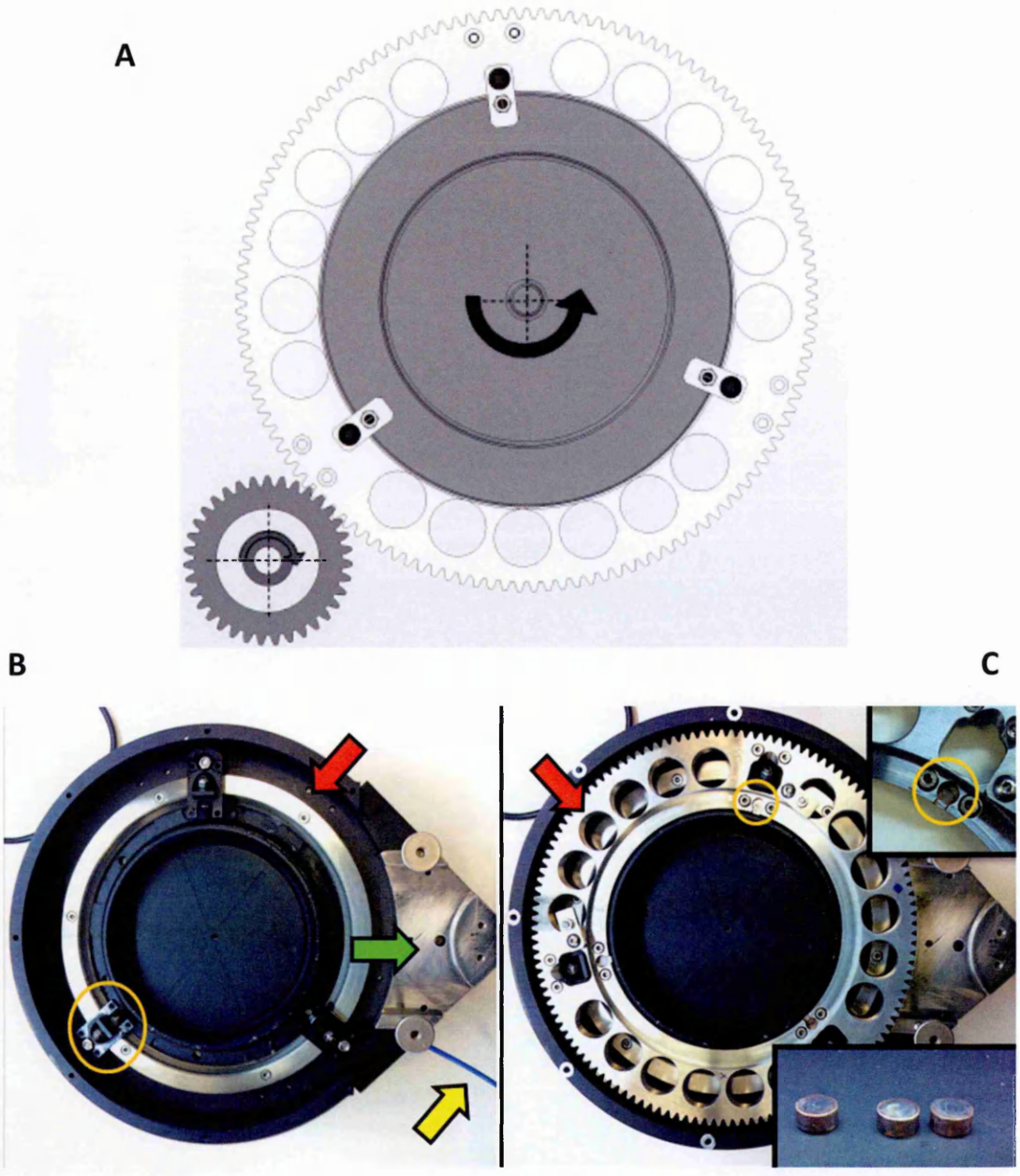

Fig.23: A) Schematic representation of the operating principle of the CPD. B) The circular guide (red arrow), the space for the engine (green arrow), the vacuum line (yellow arrow) and the runners (orange circle). C) The driven gear (red arrow) the lodge (orange circle) of the rectified spacers (in the box).

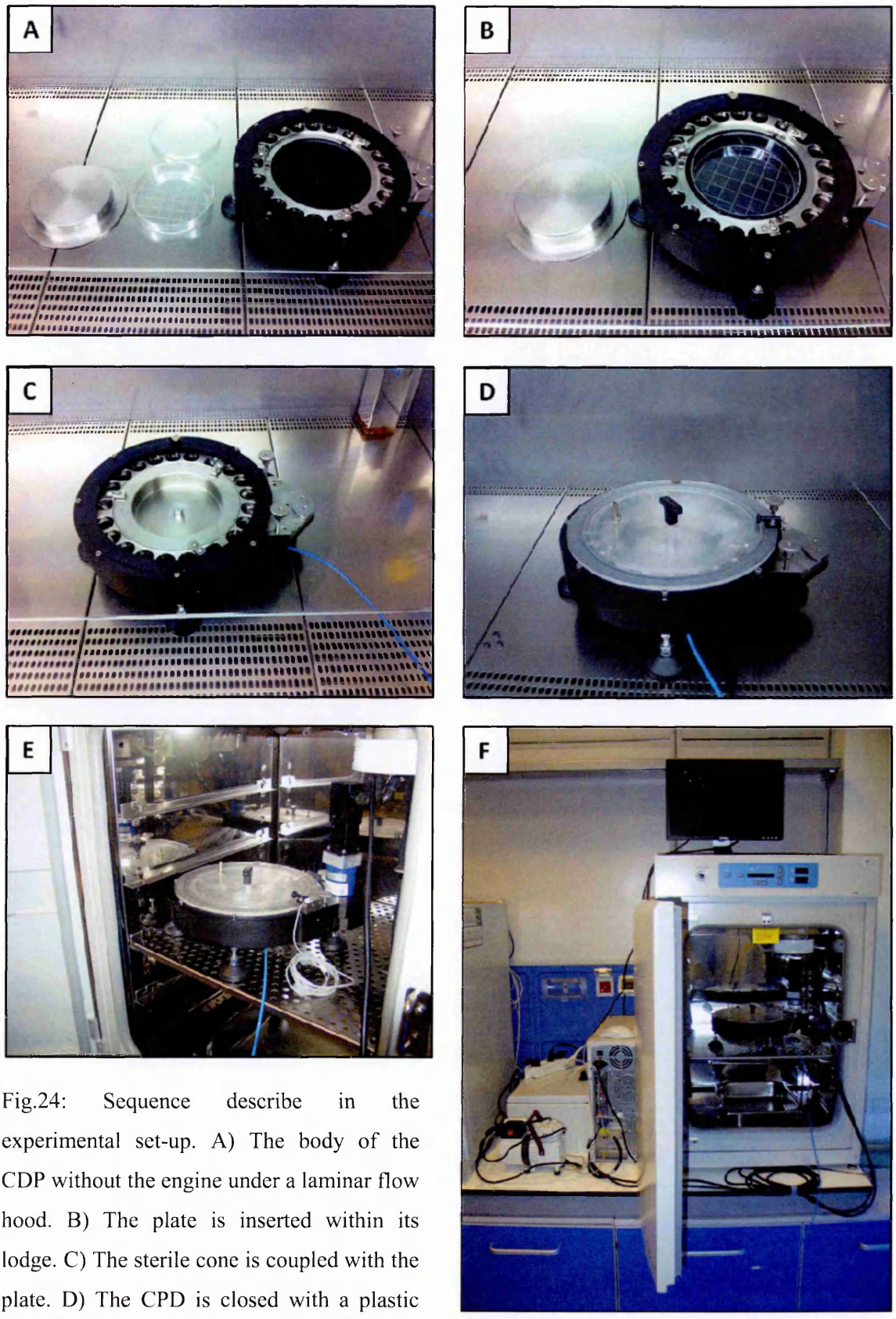

Fig.24: Sequence describe in the experimental set-up. A) The body of the CDP without the engine under a laminar flow hood. B) The plate is inserted within its lodge. C) The sterile cone is coupled with the plate. D) The CPD is closed with a plastic cover. E) The CPD is positioned within the incubator and mounted with the engine. F) An overview of the set-up.

The motion control of the cone is provided by a PC-based platform, equipped with a Linux-based Real-Time Application Interface that enables the control loop to be closed with a 1 kHz sample frequency through a hard-real time thread. An acquisition data board or NIB (NI-6229, National Instruments Corp, Austin, TX, USA) supporting the COMEDI collection of drivers for data acquisition is used as the interface between the device and the control unit (figure 25A). An encoder embedded with the engine (E) produces a signal based on engine angular velocity ω_p (t). This signal is acquired by the control unit that generates a torque control voltage signal (V) to pilot the engine and two digital signals that enable power and logic driver switches. A graphical user interface, developed with Linux IDE (Qt Creator), allows the user to upload the motion law that sets the cone rotation velocity set-point ω_s (t) and the cone acceleration, each millisecond. Furthermore the user interface provides a real-time visualization of cone rotation velocity, engine torque and cone position. The user can easily create motion laws since they are based on ASCII text files

In order to perform highly unsteady WSS stimulations, a proportional-integral controller (PID) with an anti wind-up element for the integral component, closed on the cone velocity, provides tight control and fast cone rotation dynamics (Figure 25B). The PID is a low-pass filter that reduces high frequency noise while the integral component guarantees the tracking of steady state conditions. To compensate for cone and gear inertial effects during fast acceleration, important for realistic WSS waveforms, a feed-forward block (FF) was introduced to compensate for such effects and to increase the dynamic behavior of the system. Finally, the device performance was evaluated for reproduction of highly unsteady waveforms. Different waveforms were replicated in the

laboratory and the correspondence of engine angular velocity ω_p (t) to velocity set-point ω_s (t) was verified.

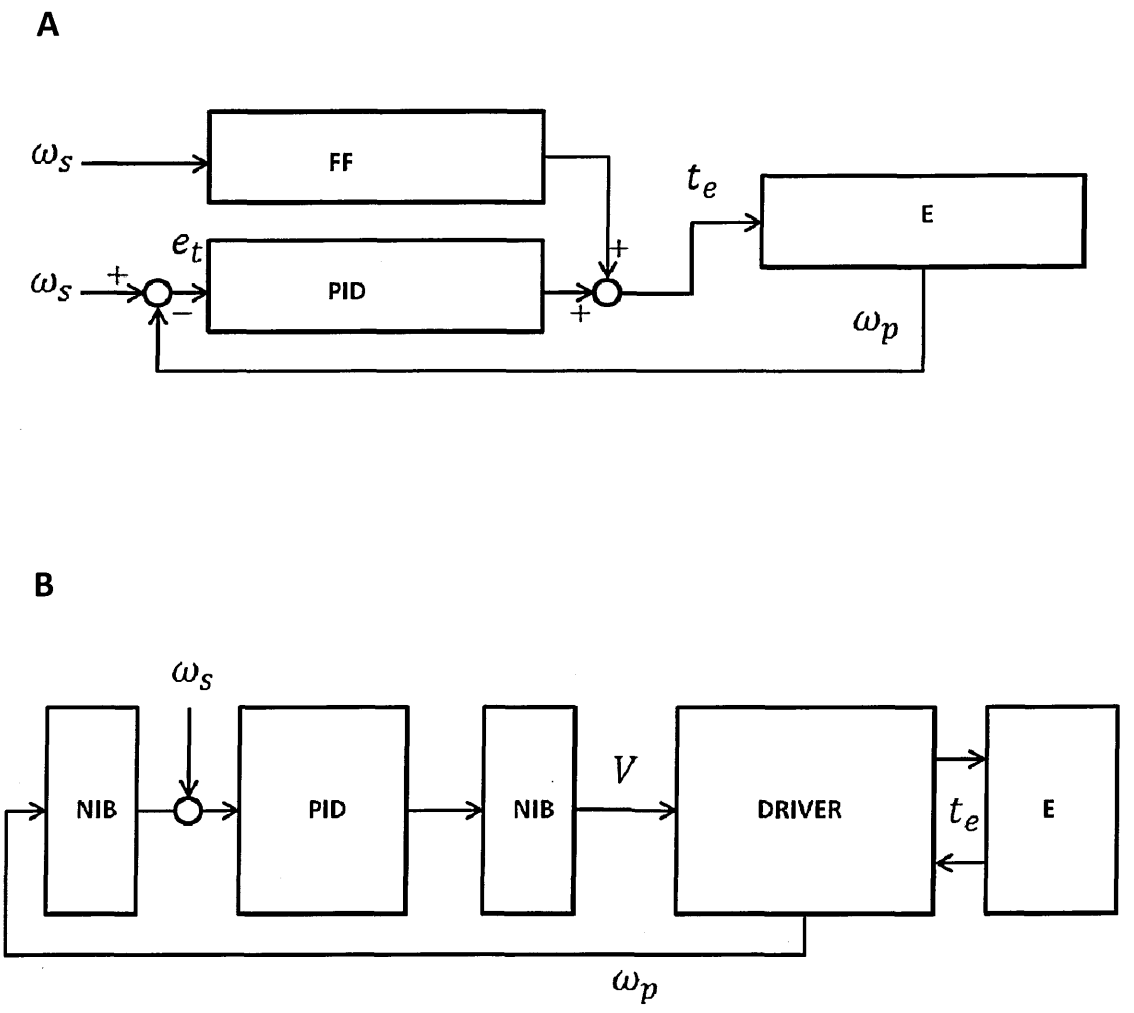

Fig.25: Schematic representations of the CPD control system. A) The set-point velocity (ω_s) is coupled with the engine velocity (ω_p) and the difference (et) is used by the proportional-integral controller (PID) together with the correction generate by the feed-forward component (FF) to generate the torque signal (t_e) to pilot the engine. B) The signal generated by PID is transformed into a voltage signal (V) by the acquisition data board (NIB) and transferred to the engine driver. The driver generates also the voltage signal that is used as feedback for the PID control loop.

3.B2) Analytical evaluation of cone-and-plate fluid dynamics.

The main advantage in choosing the cone-and-plate geometry consists in an almost uniform shear stress filed over the entire culture surface due to the linear increase of both gap width h_r and azimuthal cone surface velocity v_r, thus a radius independent shear rate $\delta_v / \delta_z = v_0 / h = const$. Despite the complexity of the device internal fluid dynamics, a simple formulation is commonly used to estimate shear stress values generated on the plate surface. By assuming low velocities, small cone angle $\alpha < 5°$, thus $\tan \alpha \approx \alpha$, and considering the axial-symmetry of the device geometry, it is possible to calculate the WSS on the plate surface (371)

$$\tau = \mu * \partial v / \partial z = \mu * \left(\frac{v_0}{h}\right) = \mu * \left(\frac{\omega r}{r} tan\alpha\right) = \mu * \frac{\omega}{\alpha} \qquad 1]$$

where τ is wall shear stress on the plate, μ is dynamic viscosity of the fluid in the gap, and δ_v / δ_z is the variation of velocity v in the z direction, ω is cone angular velocity, r is the radius and α is the cone angle in radians. This formula has been validated with computational and experimental studies and shown to be accurate when negligible secondary flow exists and the gap h_0 is negligible.

To ensure negligible secondary flows, it is necessary to respect the threshold for the modified *Reynolds* number specific for the cone-and-plate geometry, proposed in (371) , where υ is kinematic viscosity

$$Re = \frac{r^2 \omega \alpha^2}{12\upsilon}. \qquad [2]$$

Similar to the traditional *Reynolds* number, this formula evaluates the ratio between centrifugal forces and viscous forces acting on the fluid at any radius from the cone centre. Low *Reynolds* value (Re < 0.5) ensures optimal conditions for cell shear loading. Below this threshold the viscous forces dominate, the centrifugal forces are negligible and secondary flows are small over the entire plate surface

Although good agreement of this approach has been shown with experimental results, this formulation considers an ideal configuration with no gap between the plate and the cone apex. Realistic experimental set-ups maintain a certain gap, thus to calculate WSS on the plate it is necessary to consider a formulation which takes into account this parameter.

Sucosky et al. (380) addressed this issue and proposed the following formula where h_0 is the gap between cone and plate at the centre

$$\tau = (\mu * \omega) * (r/(h_0 + r\alpha)). \quad [3]$$

This approach introduces a radius dependence for the WSS value over the plate (figure 26A), which goes from 0 at the plate centre and increases along the radial direction up to approximately 85% of WSS value obtained with the previous formulation (figure 26B). The approach differences for WSS patterns tested in the present work will be discussed in the next paragraph.

Although many studies used *Sdougous* approach, considering a constant WSS on the entire plate surface, *Dardik* et al. (381) measured differences in WSS generated at the centre and the periphery of a cone-and-plate device, which affect both cell proliferation and morphology. Bovine aortic ECs (BAEC) seeded at the two different locations after 24 hrs and 5 days of exposure to laminar shear stress (210 rpm cone

rotation velocity, resulting in a stimulation of 4.8 dyn/cm^2 at the centre and 11.1 dyn/cm^2 at the periphery) revealed significant cellular alignment at the periphery but cells at the centre showed a polygonal shape, increased proliferation and apoptosis, similar to effects observed after reciprocating flow exposure.

The gap h_0 together with the cone angle α, are fundamental parameters to minimize the radius dependence of WSS on the plate. *Spruell* and *Baker* (377) simulated the effect of different device configurations by changing angle α from 0.5° to 2° and gap h_0 from 1 to 100 μm. The effect of different angles and gaps on WSS, reported by other authors, are similar to those obtained by the *Sucosky* analytical approach [3] (380). Increasing cone angle increases the non-uniformity of WSS delivered at plate level (figure 27A). By increasing the gap h_0, the WSS generated at plate level decreases dramatically (Figure 27B).

Even though a gap of 100 μm strongly affects the shear stress field uniformity, this was adopted in the experiments of this thesis in order to preserve the integrity of the EC monolayer. The adherent EC thickness in the central perinuclear region is approximately 3 μm while the covering glycocalyx layer (measured in-vitro for BAEC) was found to be thicker than 10 μm (293). From these considerations it is possible that irregularities in the cultured monolayer alters the flow field and influence WSS at the plate level.

According to these considerations we considered the plate outer ring (from 2 cm radius to the external edge at 6.7 cm radius) as exposed to a controlled and rather uniform shear stress. We defined this area of the plate region of interest since WSS calculated with [3] varies from 65% to 85% with respect to that calculated with [1].

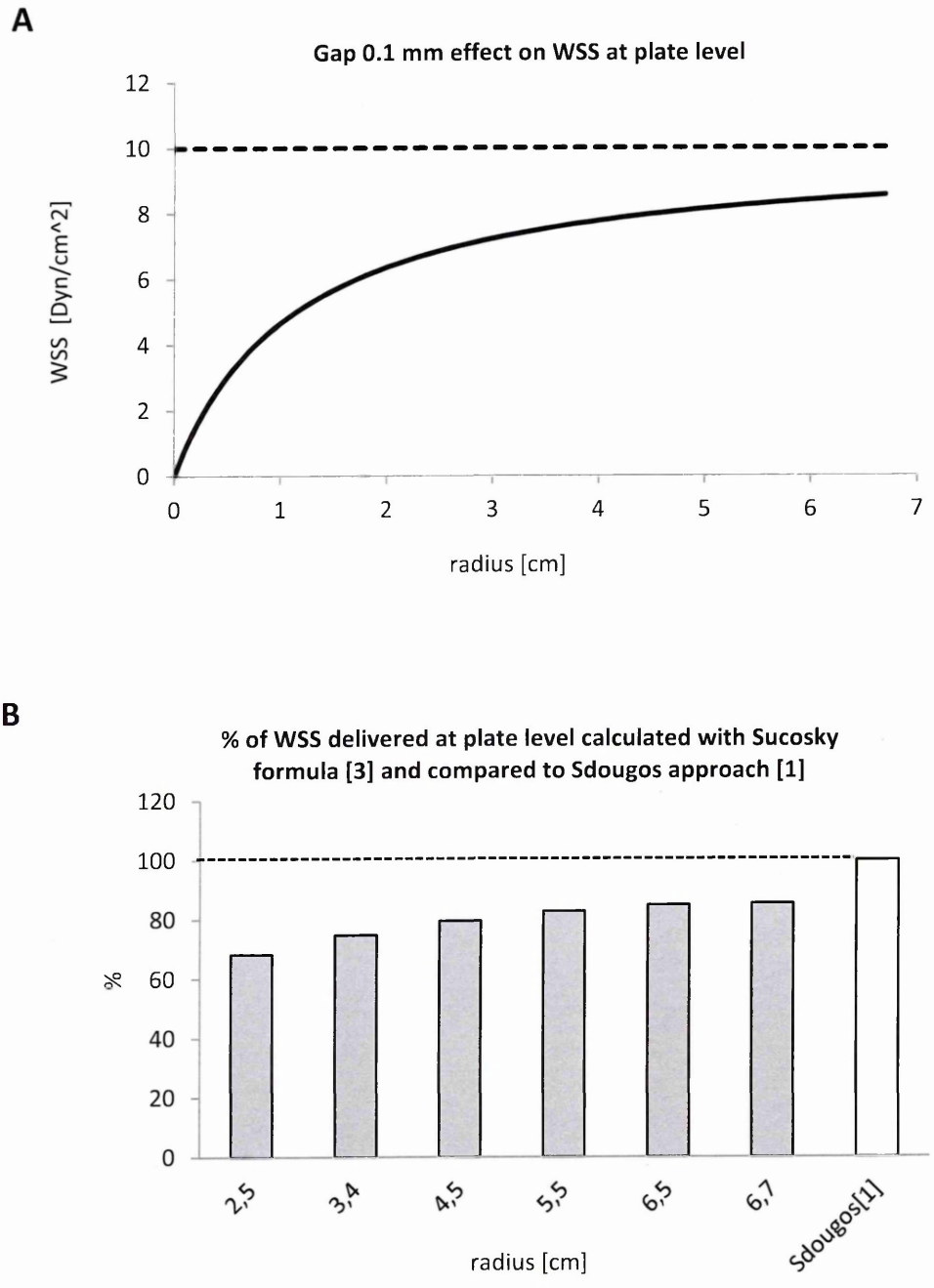

Fig.26: Comparison of WSS at plate level calculated by eq. [1] and eq. [3]. A) The effect of the gap of 0.1mm on WSS (continuous line) calculated by eq. [3] for an angular velocity ω of 2.46 rad/s. Eq. [1] (dotted line) does not consider the gap and the result is a constant WSS along the plate radius. B) The comparison of WSS calculated by eq. [1] and eq. [3] in the plate region of interest were HUVECs are seeded.

The second device requirement was to perform highly unsteady WSS stimulation, requiring rapid change of cone rotation velocity or even change in rotation direction. Despite fine control of cone rotation velocity, a time delay occurs between cone rotation and WSS generated on the plate (376). According to *Sutera* and colleagues (382), it is possible to estimate the wave development time in the gap between the cone and the plate with the suddenly accelerated plate formula,

$$t_d < 0.25 * \frac{h_r^2}{\upsilon} \qquad [4]$$

where h_r is the gap along the plate radius, υ is the fluid dynamic viscosity and t_d is the time required to get a difference between cone velocity and it's asymptotic value less than 1%. This approach limits the cone maximum acceleration to ensure complete motion transmission across the gap, achieving precise WSS stimulus at the plate level. The time lag of the device used in this study is < 50 ms at any radius (figure 27C), ensuring full WSS development for any WSS waveform with frequency components up to 10 Hz.

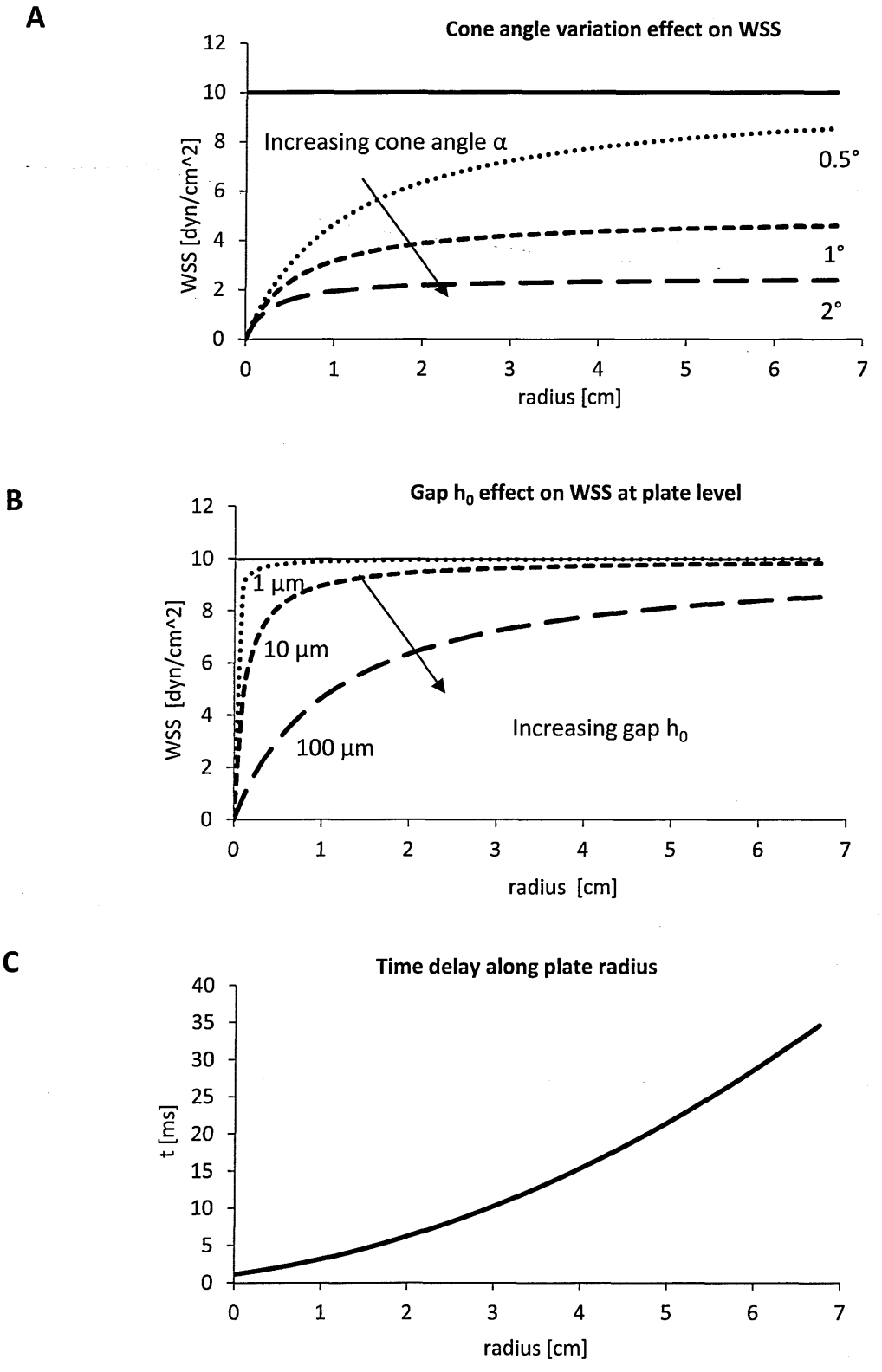

Fig.27: A) The effect of different cone angle (0.5°, 1°, 2°) on WSS at plate level for ω of 2.46 rad/s and a gap of 0.1mm. B) The effect of different gaps (1, 10, 100 μm) on WSS at plate level for ω of 2.46 rad/s and cone angle of 0.5°. C) The time delay between cone accelerations and the 99% development of correspondent WSS at plate level, estimated by eq. [4].

3.B3) Computational evaluation of CPD fluid dynamics.

To evaluate the accuracy of these analytical methods in describing CPD fluid dynamics, numerical simulations of CPD transient flows were performed using the OpenFOAM code (383). BlockMesh is a mesh generator tool included in OpenFOAM v. 2.3.1 suite. The mesh represents the fluid domain inside the CPD and consists of the upper conical surface and a bottom plane surface representing the cells, connected with an exterior vertical wall. After a mesh sensitivity test (see appendix A), the volume was meshed using a structured grid consisting of 138,000 hexahedral cells (figure 28).

Newtonian fluid with a dynamic viscosity, μ, of 3.54 cP and a density ρ of 0.9544 g/cm^3 was considered. Geometrical parameters were the same as the experimental set up (cone angle, α, of 0.5°, cone radius, r, of 67 mm and a central gap, h_0, of 0.1 mm). The variable angular velocity $\omega(t)$ in rad/s during the cycle was imposed as the boundary condition on the upper conical surface according to the CPD motion laws of the different WSS profiles. No-slip (i.e., zero velocity) conditions were imposed on the bottom surface (the cell monolayer) and on the vertical wall. The unsteady Navier-Stokes equations were solved using pimpleFoam, a transient solver for incompressible flows employing the PIMPLE (merged PISO-SIMPLE) algorithm and first order Euler time integration scheme. One period of the cycle (T = 1 s) was divided in 1,000 fixed time steps (dt = 1 ms) and the results were saved for post-processing in 1,000 time steps for each cycle. Four complete cardiac cycles were solved in order to damp the initial transients of the fluid and only the results of the fourth cycle were considered for data processing. The results of simulations were post-processed and visualized with ParaView software. In the next section the results are compared between the CFD model and analytical approaches [1] and [3].

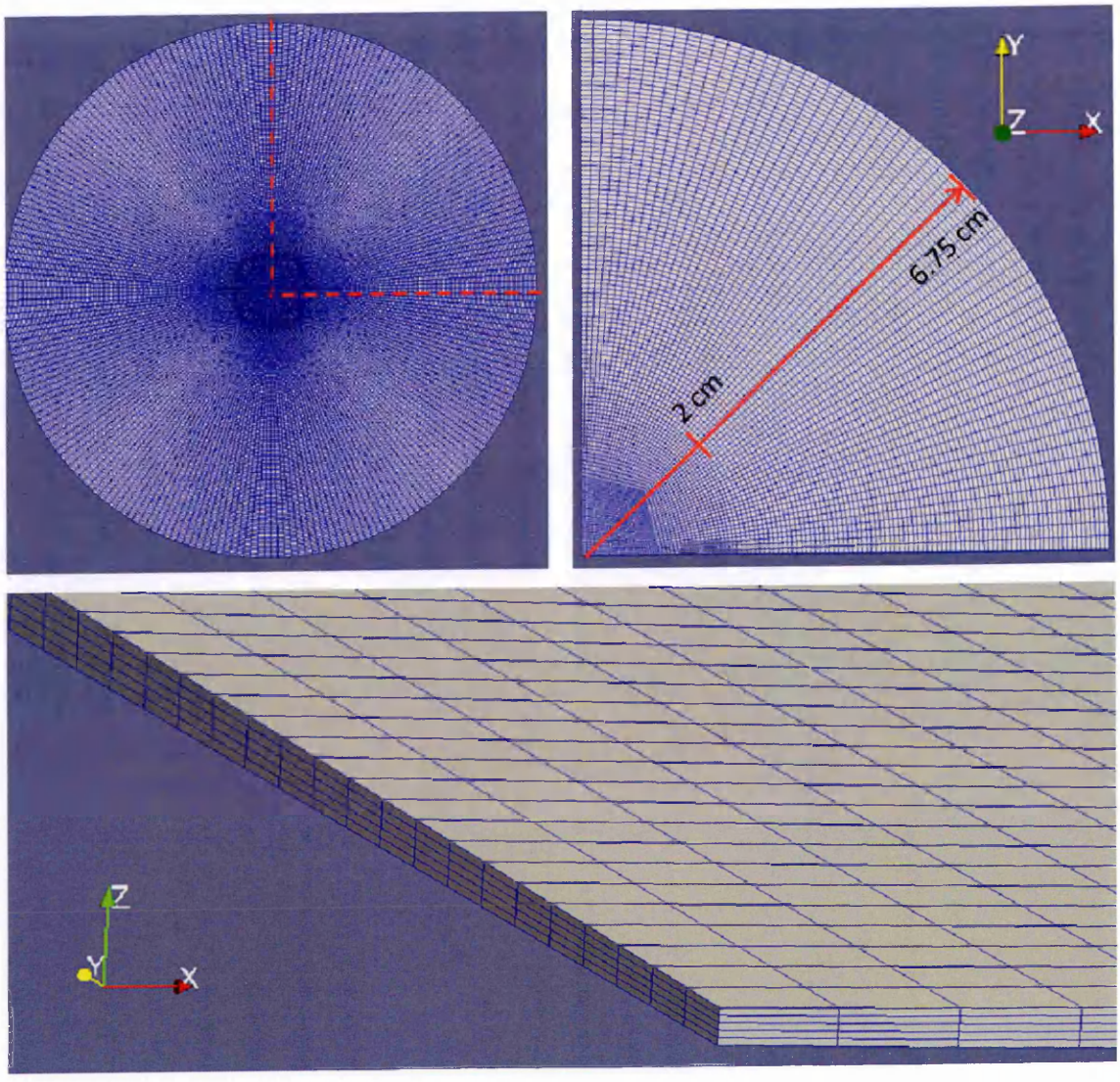

Fig.28: 138'000 elements structured grid created to mesh internal fluid volume of CPD and used to simulate the different flows.

3.C) Comparison of different methods to evaluate WSS at plate level

The effect of gap h_0 on WSS generated at plate level was computed. Using equation [3] a difference of WSS peak value with respect to that calculated with [1] ranged from 68.3% to 84.8% from radius 2.5 to 6.5 cm (figures 29A, 32A, 35A, 38A). This result is independent of the velocities and accelerations of the single WSS waveform since it depends uniquely on the medium viscosity and on the gap dimension.

According to the results of CFD simulations (figures 29B, 32B, 35B, 38B), the Sucosky approach accurately describes the gap effect on WSS generated at plate level (figures 30, 33, 36, 39). The WSS peak values calculated with equation [3] with respect to that calculated using CFD methods, in the region of interest, ranges from 96.2 to 100.2% in PUL_A waveforms, from 95.5 to 95.8% in PUL_V, from 96.3 to 99.8% in REC_A and from 96.2 to 99.6% in REC_B (figure 31A, 34A, 37A, 40A).

A significant difference emerged from the comparison of the results obtained at the outer edge of the plate. At a radius of 6.7cm the WSS peak calculated with equation [3] is 85.4% of that calculated with [1]. In the CFD model the presence of the fixed plate outer edge introduces border effects that strongly reduce WSS magnitude in all the waveforms. WSS peaks calculated with equation [3] are the 138.1, 133.6, 144.3 and 137.3% of those reported by the simulation for PUL_A, PUL_V, REC_A and REC_B waveforms respectively (figure 31A, 34A, 37A, 40A).

The td for WSS peak with equation [1] and CFD simulations was also computed. Equation [1] depends exclusively on medium viscosity and the distance between the rotating cone surface and the plate. td ranges from 9 to 37 ms for radii 2.5 and 6.7cm respectively (figures 31B, 34B, 37B, 40B). As expected the simulations showed a reduced delay with respect to that evaluated for the instantaneously accelerated plane. The td of PUL_A and PUL_V was 5 ms at radius 2.5cm and 20 ms at 6.5cm. REC_A

had td increasing from 5 to 18 ms. REC_B td ranged from 4 to 17 ms (figures 31B, 34B, 37B, 40B). Maximal td was found at radius 6.5cm. On the outer edge the lowest WSS magnitude calculated by simulations was reached 1 ms earlier.

These results make the selected limit of 10 Hz a reasonable threshold for frequency components of WSS waveforms. A 10 Hz oscillation completes its cycle in 100 ms, one order of magnitude higher that the td found in the tested cases.

3.C1) Arterial Pulsatile waveform (PUL_A).

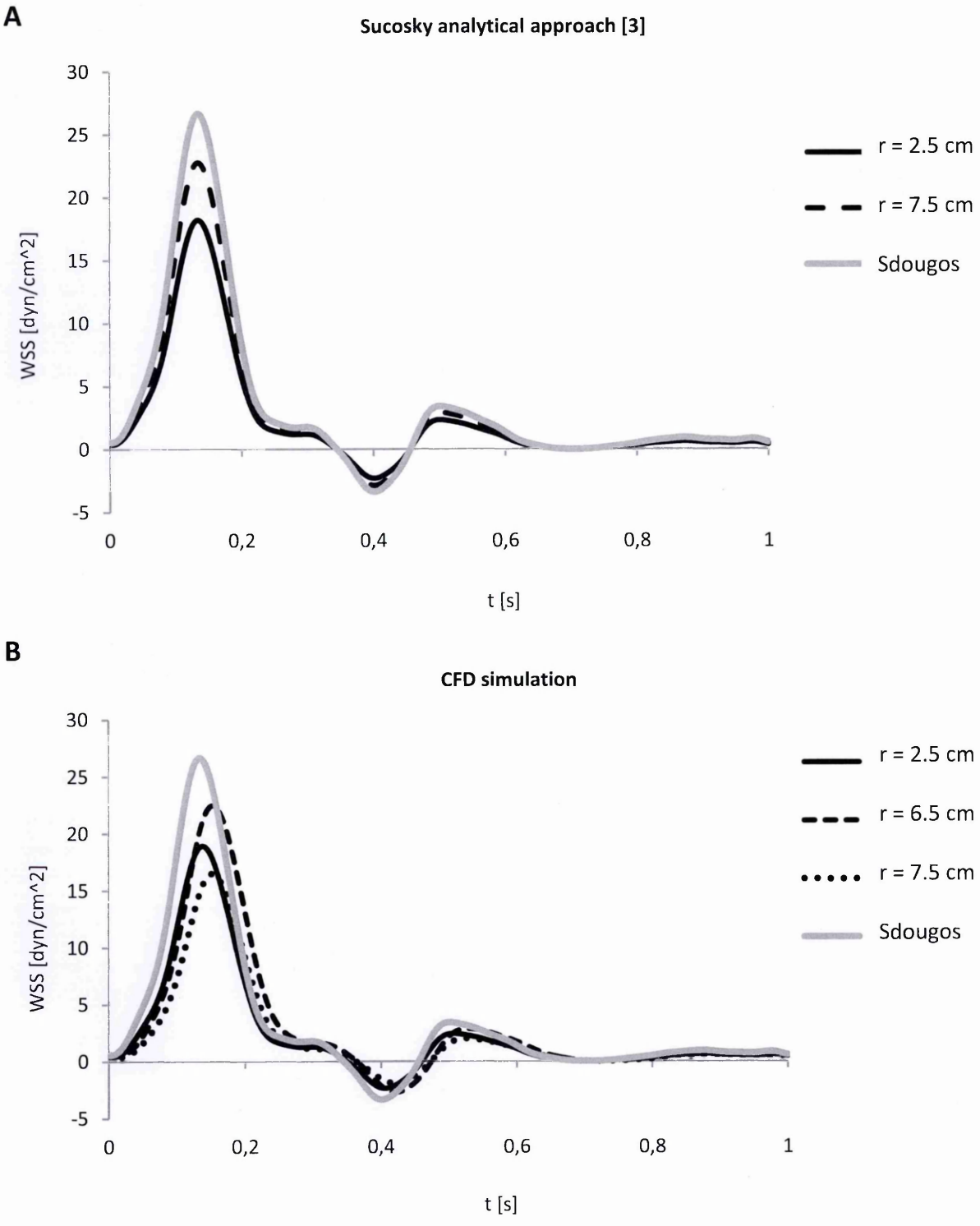

Fig.29: PUL_A WSS stimuli at plate level. A) WSS calculated by eq. [3] and eq. [1] (Sdougos). B) WSS calculated by CFD methods and eq. [1] (Sdougos).

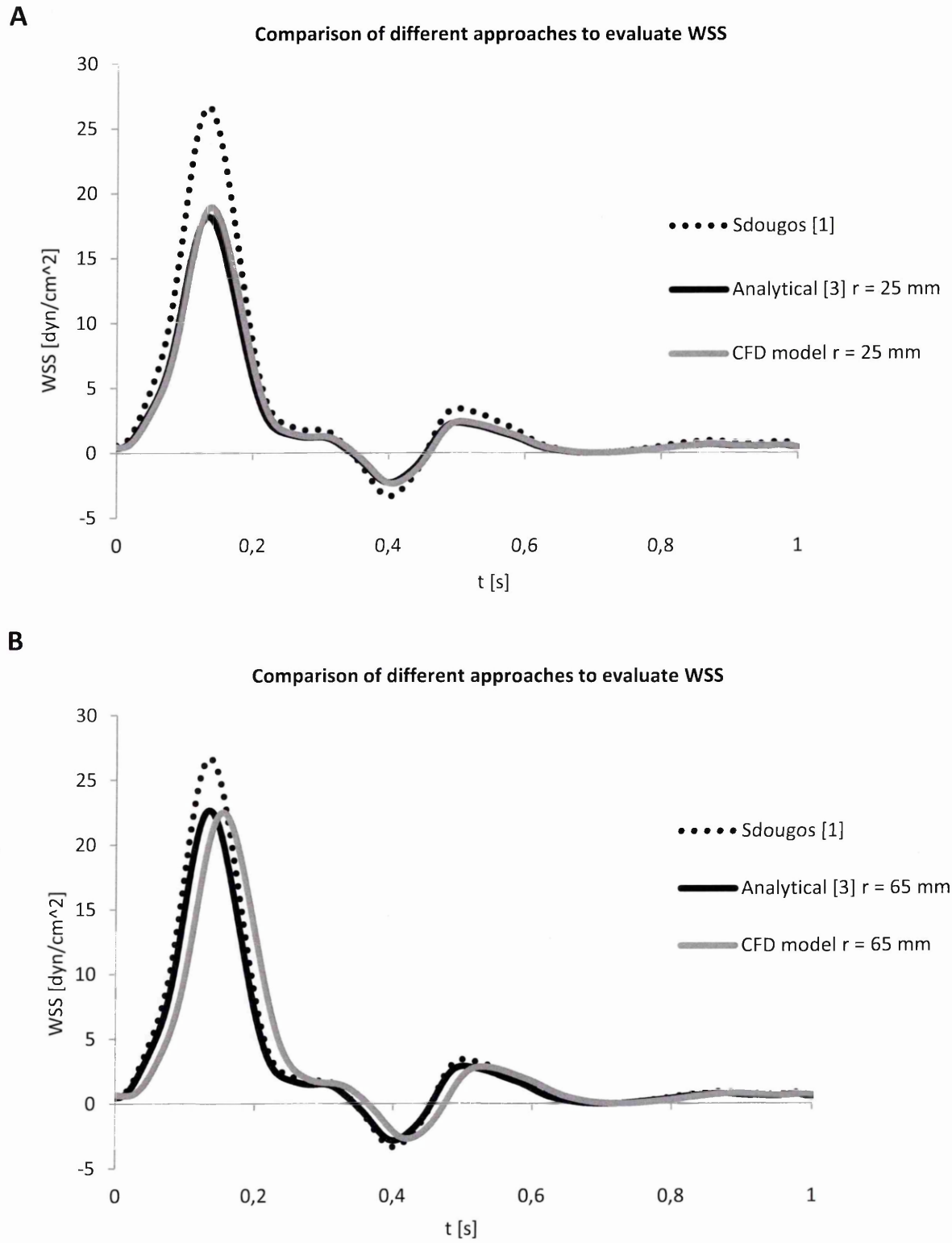

Fig.30: PUL_A WSS stimuli at plate level. A) WSS calculated by eq. [1] (Sdougos), eq. [3] and CFD method at 2.5 cm radial position. B) WSS calculated by eq. [1] (Sdougos), eq. [3] and CFD method at 6.5 cm radial position.

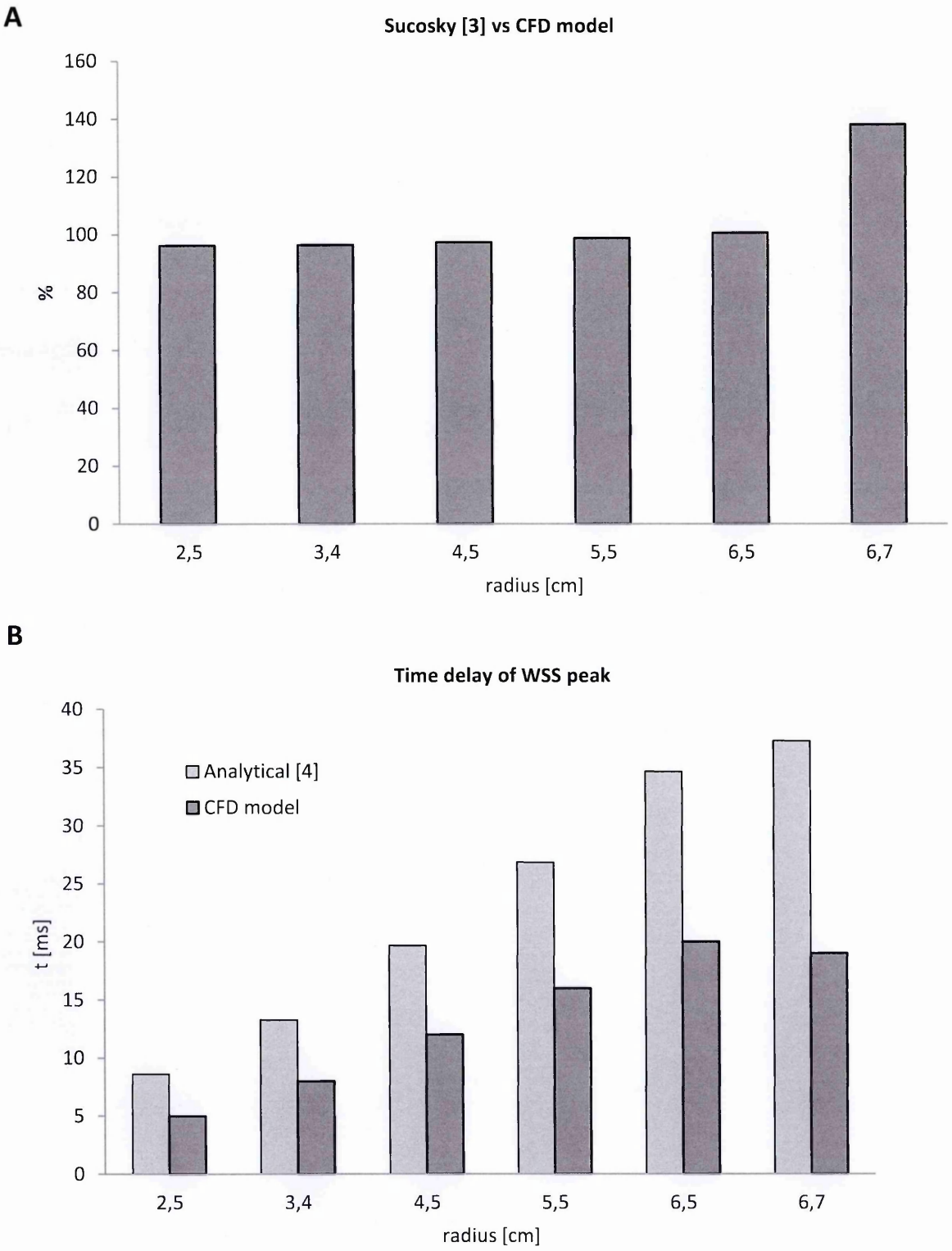

Fig.31: A) Comparison of WSS calculated by eq. [3] vs. eq. [1] in the plate region of interest. B) Time delay estimated by eq. [4] and calculated by CFD in the plate region of interest.

3.C2) Venous Pulsatile waveform (PUL_V)

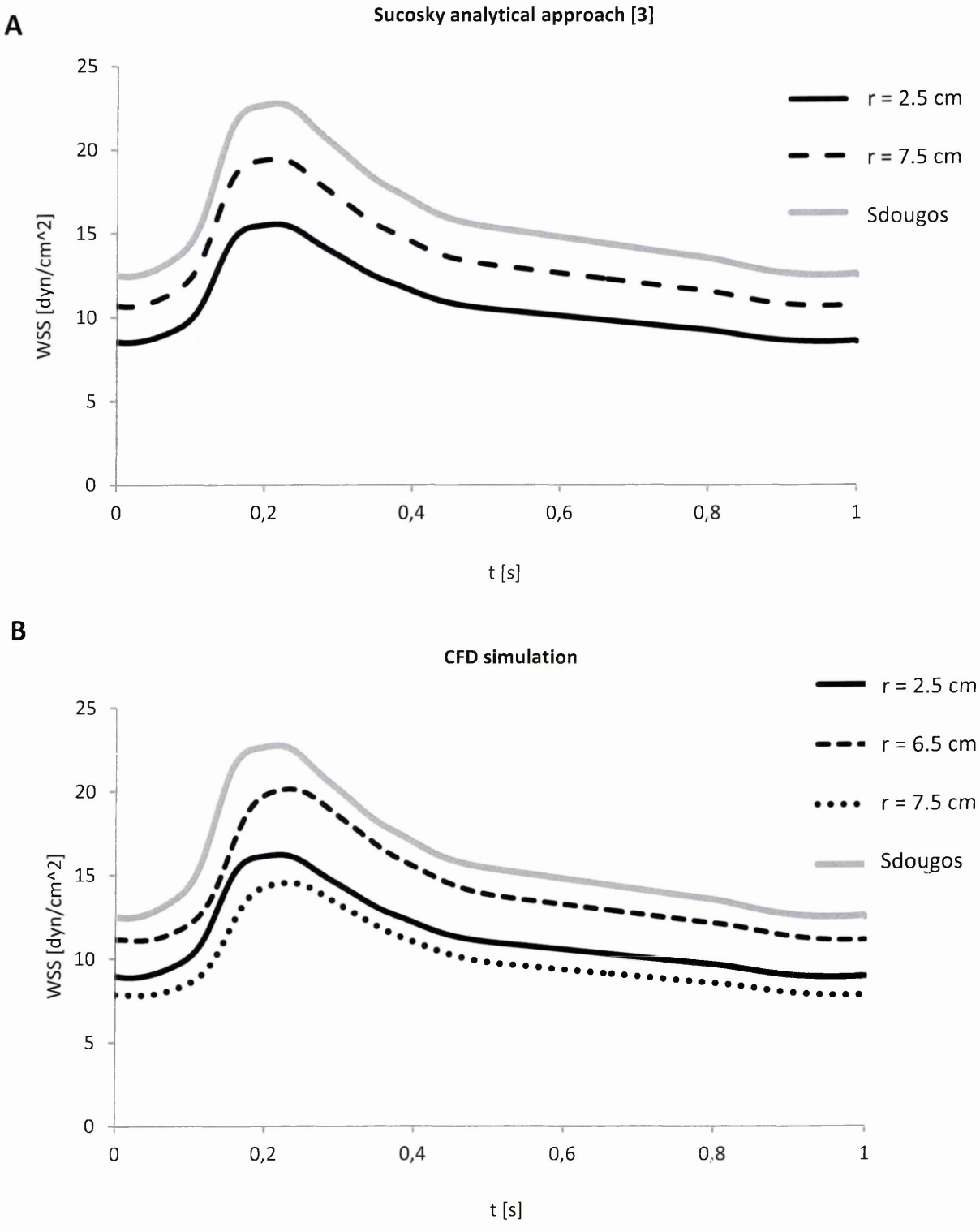

Fig.32: PUL_V WSS stimuli at plate level. A) WSS calculated by eq. [3] and eq. [1] (Sdougos). B) WSS calculated by CFD methods and eq. [1] (Sdougos).

A

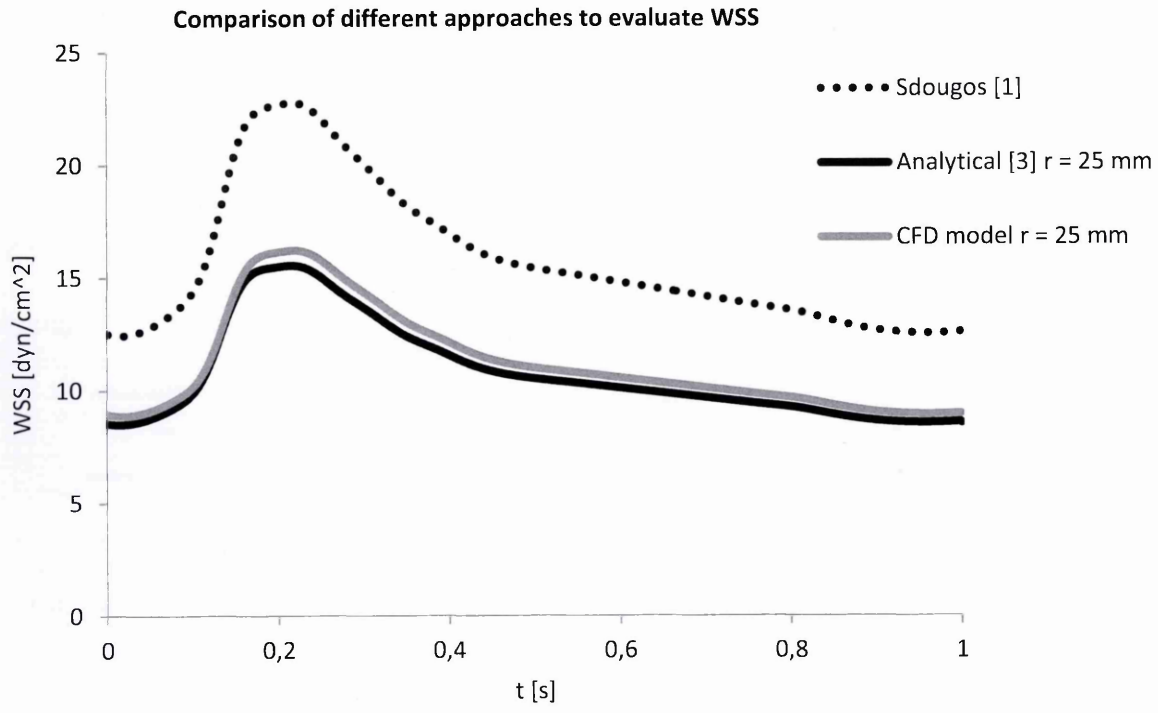

B

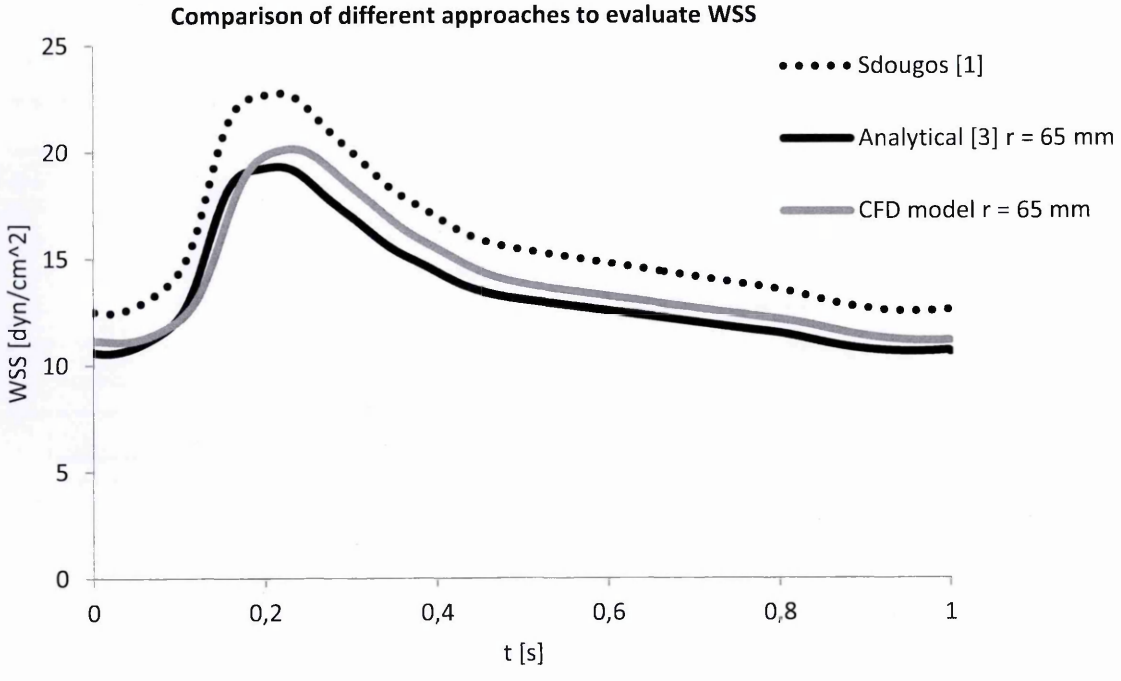

Fig.33: PUL_V WSS stimuli at plate level. A) WSS calculated by eq. [1] (Sdougos), eq. [3] and CFD method at 2.5 cm radial position. B) WSS calculated by eq. [1] (Sdougos), eq. [3] and CFD method at 6.5 cm radial position.

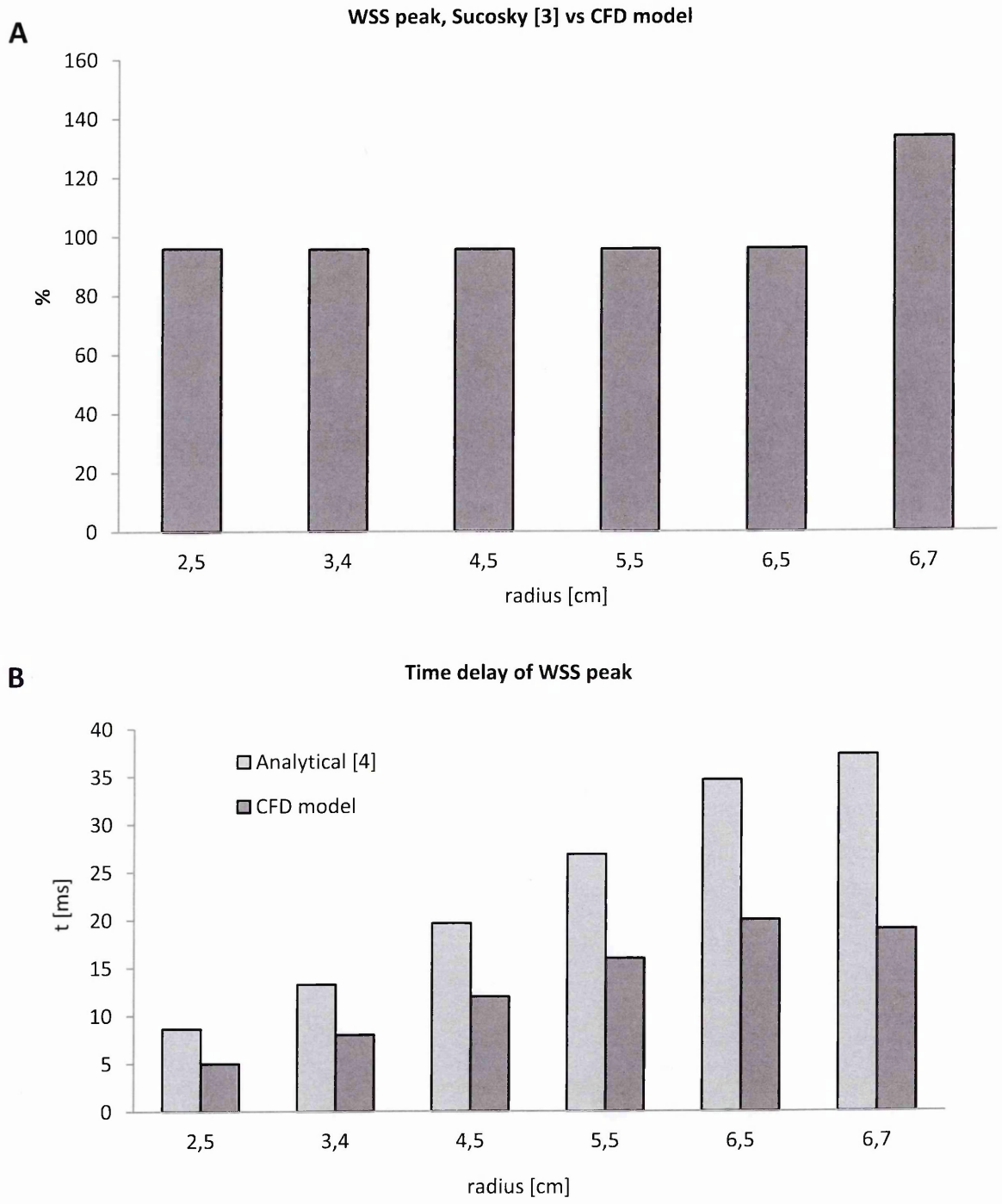

Fig.34: A) Comparison of WSS calculated by eq. [3] vs. eq. [1] in the plate region of interest. B) Time delay estimated by eq. [4] and calculated by CFD in the plate region of interest.

3.C3) Anastomosis floor Reciprocating waveform (REC_A)

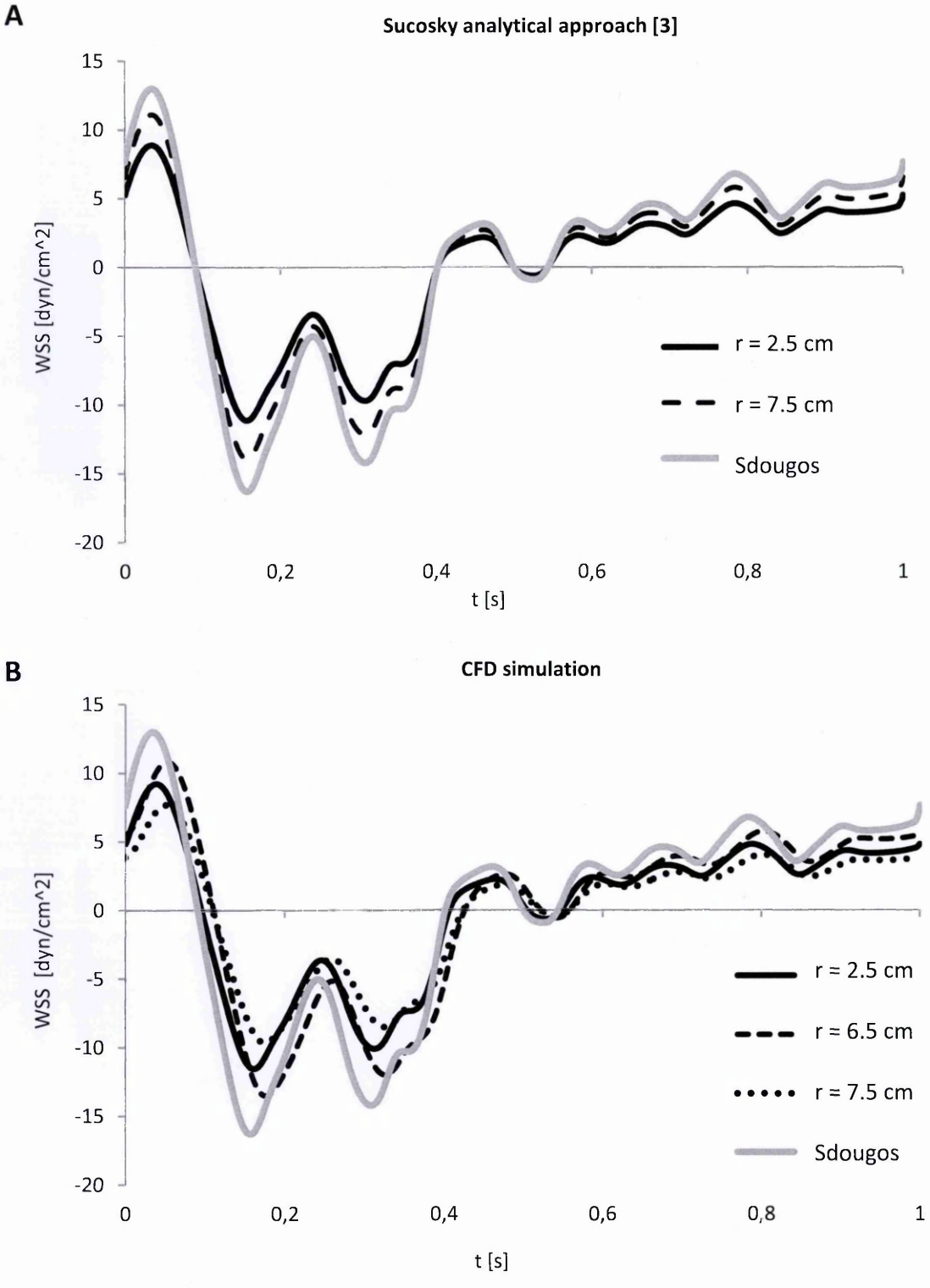

Fig.35: REC_A WSS stimuli at plate level. A) WSS calculated by eq. [3] and eq. [1] (Sdougos). B) WSS calculated by CFD methods and eq. [1] (Sdougos).

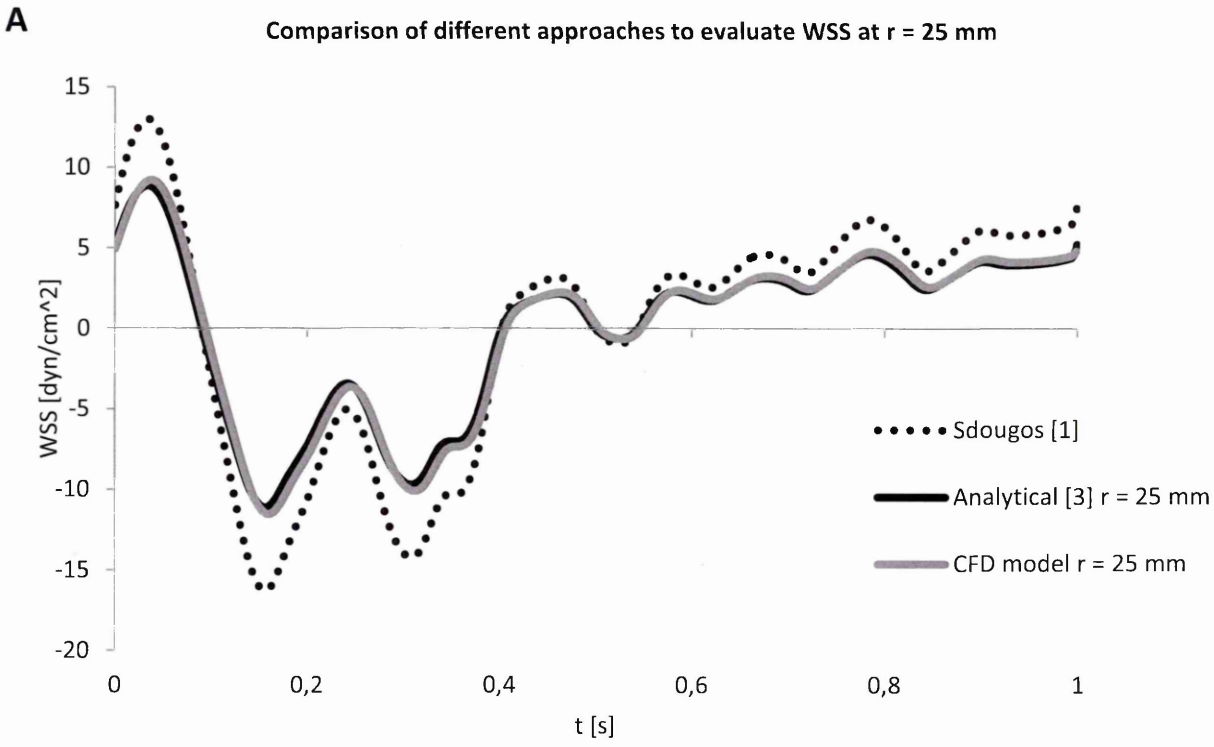

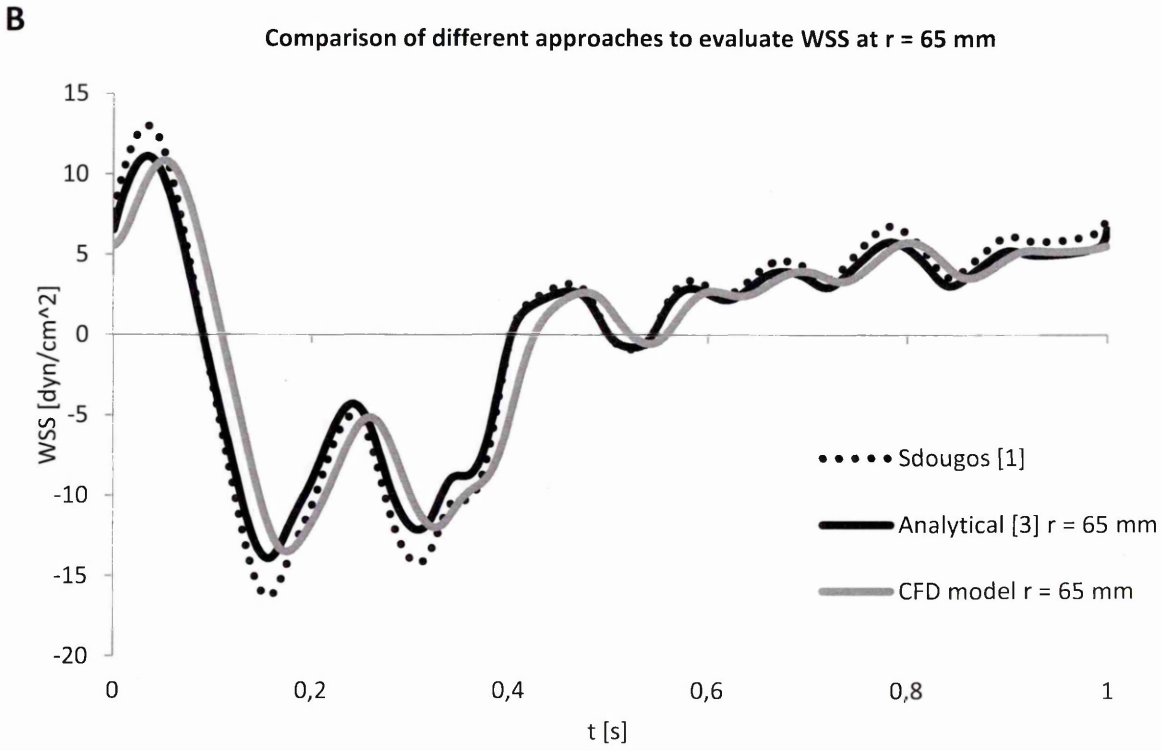

Fig.36: REC_A WSS stimuli at plate level. A) WSS calculated by eq. [1] (Sdougos), eq. [3] and CFD method at 2.5 cm radial position. B) WSS calculated by eq. [1] (Sdougos), eq. [3] and CFD method at 6.5 cm radial position.

A

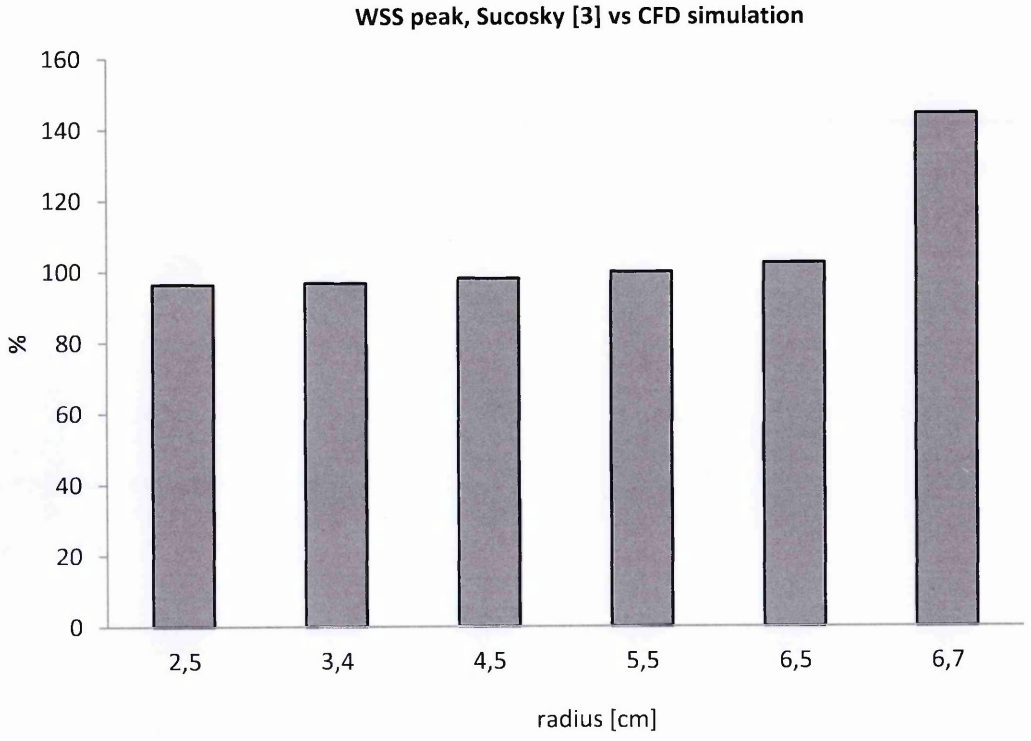

B

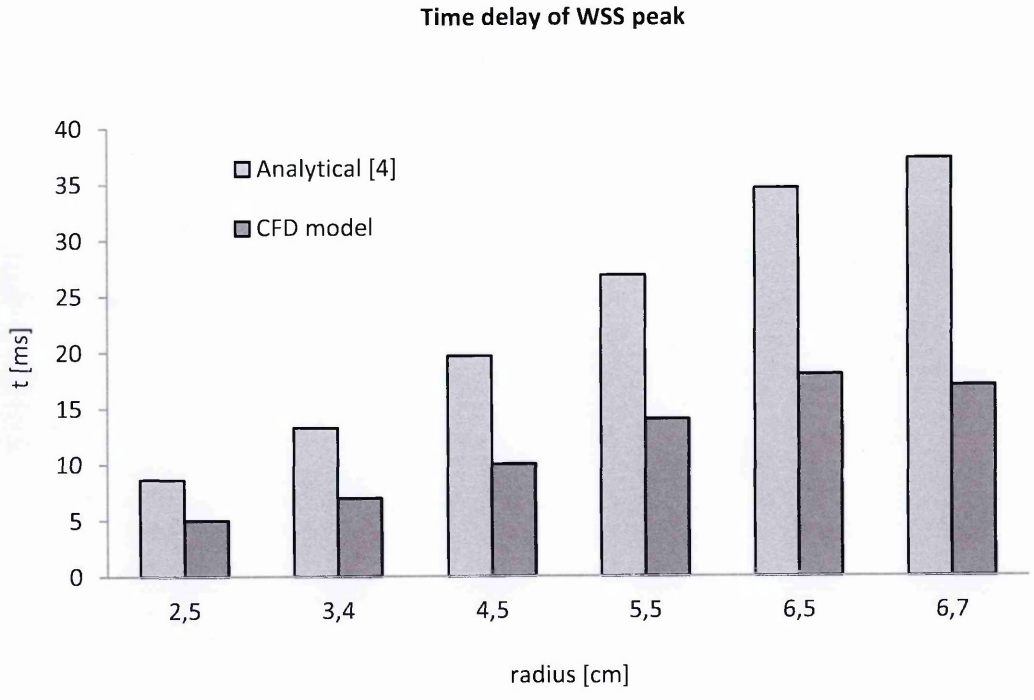

Fig.37: A) Comparison of WSS calculated by eq. [3] vs. eq. [1] in the plate region of interest. B) Time delay estimated by eq. [4] and calculated by CFD in the plate region of interest.

3.C4) Anastomosis angle Reciprocating flow (REC_B)

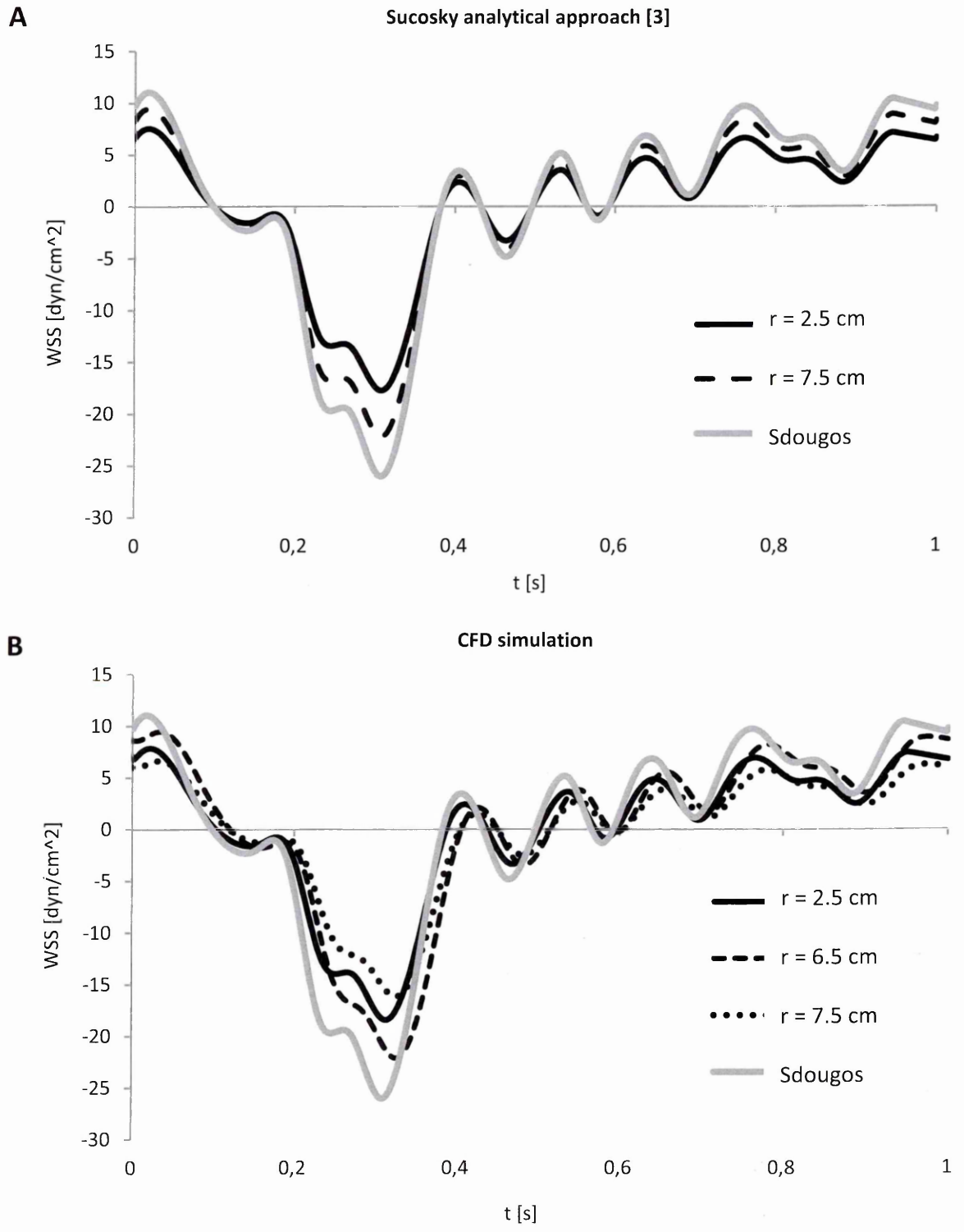

Fig.38: REC_B WSS stimuli at plate level. A) WSS calculated by eq. [3] and eq. [1] (Sdougos). B) WSS calculated by CFD methods and eq. [1] (Sdougos).

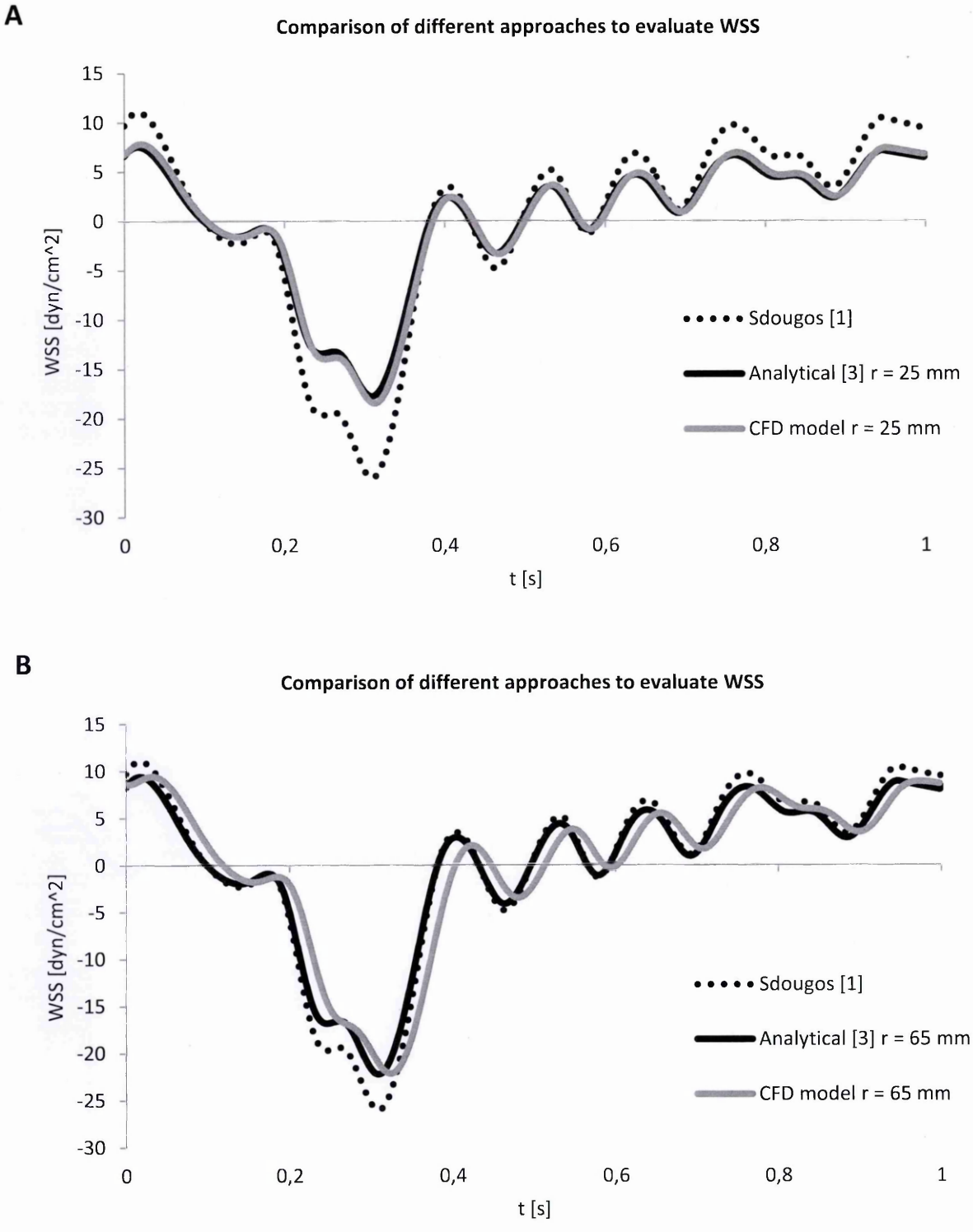

Fig.39: REC_B WSS stimuli at plate level. A) WSS calculated by eq. [1] (Sdougos), eq. [3] and CFD method at 2.5 cm radial position. B) WSS calculated by eq. [1] (Sdougos), eq. [3] and CFD method at 6.5 cm radial position.

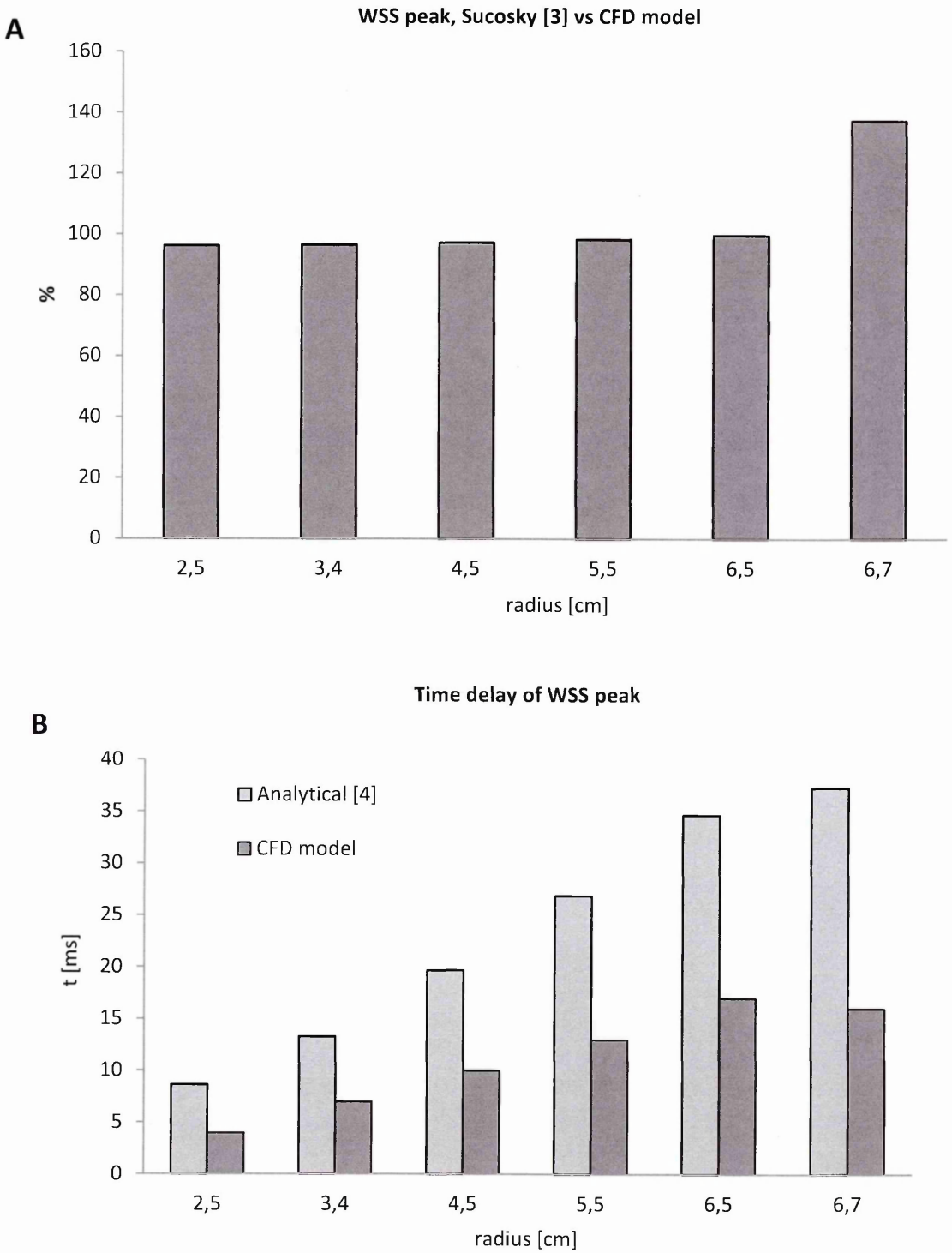

Fig.40: A) Comparison of WSS calculated by eq. [3] vs. eq. [1] in the plate region of interest. B) Time delay estimated by eq. [4] and calculated by CFD in the plate region of interest.

3.D) Summary

Due to the fundamental importance of Wall Shear Stress in endothelial biology, several systems have been developed and used in biomedical research to reproduce flows over cell cultures. Despite the fact that each system presents some advantages, in order to obtain controlled, highly unsteady WSS stimulation over a cell monolayer culture a compact, real-time controlled Cone-and-Plate device was designed and constructed, suitable for use within a standard cell incubator. The device is controlled by dedicated software and a proportional-integral controller able to accurately pilot the cone rotation in a time dependant manner. In order to verify the correspondence between cone velocity and WSS at plate level, published analytical methods and a computational model were used. In line with previous studies, the results showed that the device produces a WSS stimulus that increases from the centre to the periphery and that the vertical edge of the plate strongly reduces the magnitude at the border. Furthermore, to guarantee a coherent stimulus over the entire plate, it is necessary to introduce a threshold for the frequency components of WSS waveforms since medium inertial effects cause a time lag between cone accelerations and the correspondent WSS variations. In conclusion, the stimulus was considered to be uniform in the outer ring of the plate (for radius > 20mm, referred as region of interest) and for WSS waveforms with frequency components < 10Hz.

CHAPTER 4: Endothelial cell culture and exposure to AVF-specific transient WSS

This Chapter addresses the methods used to isolate Human Umbilical Endothelial Vein Cells (HUVECs) and to culture them in order to obtain the cell monolayers used in the flow exposure experiments. Isolated cells were characterized and the content of smooth muscle cells was quantified to ensure that these cultures were composed of HUVECs. Further evaluation is reported of the cell culture plate coating and the experimental set-up of the Cone-and-Plate device. The investigations performed to evaluate HUVECs morphological adaptation to flow are reported in the second part of the Chapter. After a qualitative analysis based on contrast phase microscopy and scanning electron microscopy images, specific structural features were stained, F-actin fibers and tight junctions ZO-1 protein, for cells exposed to different culture conditions and these features were quantified with a software-based image analyzer tool.

4.A) HUVEC isolation and characterization

4.A1) HUVECs isolation.

HUVEC were freshly isolated from the umbilical cord according to (384). Briefly, cords were carefully washed with warm physiologic solution twice to remove blood from the vein. The cords, filled with collagenase solution or COLLS composed by 47,6 mg of collagenase (Sigma-Aldrich, St. Louis, USA) in 100 mL of Phosphate Buffered solution (DPBS, refers to *Dulbecco's* phosphate buffered solution. The solution is composed by distilled filtered water added with 132 mg/L of CaCl2 (Merck KGaA, Darmstadt, Germany), 100 mg/L MgCl2 (Carlo Erba reagents, Milan, Italy), 440 mg/L Na2HPO4 (Carlo Erba), 200 mg/L KH2PO4 (Sigma), 8 g/Ml NaCl (Sigma), 200

mg/L KCl (Carlo Erba) warmed to 37°C, were incubated for 13 minutes at 37°C. COLLS containing isolated HUVECs plus red blood cells, was collected in a backer with New Born Calf Serum (NBCS, Life Technologies, Milan, Italy), to block collagenase activity. The cell suspension was centrifuged for 8 minutes at 1200 rpm. The pellet was re-suspended with growth medium (GM), composed by culture medium (M199 Biowest, Nauillé, France) added with 10% of NBCS, 10% of Human Serum (HS, directly separated in our laboratory from human plasma), 1% Penicillin and Streptomycin (PenStrep, Life Technologies), 1% Amphotericin B (Fungizone, Life Technologies) and 0.1% Heparin (TEVA, Petah Tikva, Israel) and seeded in a cell culture plate (disposable P55, Falcon) coated with bovine gelatine at 1% (Sigma).

After cell adhesion, the medium was removed and the dish surface was washed twice with warm physiologic solution to remove red blood cells. Finally GM added with and 0.02% endothelial cell growth supplement (ECGS, Tebu-Bio, Offenbach, Germany, referred also as complete GM) was added to the dish. HUVEC were expanded until 3rd passage and then frozen in GM added with 5% Dimethyl Sulfoxide (DMSO, Sigma).

Six days before the experiment, the HUVEC were thawed in GM, then seeded on a Petri dish P150 (BD Bioscience, Franklin Lakes, NJ, USA), coated with bovine gelatine at 0.2% (Sigma) grown until confluence and used in flow exposure experiments at 4th or 5th passage.

4.A2) Isolated HUVEC characterization.

To characterize cells collected from umbilical cords, we incubated samples of isolated cells with rabbit anti human *von Willebrand* factor (vWF, 1:100, Sigma) primary antibody for two hours at room temperature, and with Fluorescein isothiocyanate-labeled (FITC) goat anti-rabbit secondary antibody (1:25, Jackson

Immunoresearch) for 45 minutes at 37°C. Counterstaining with 4',6-diamidin-2-fenilindolo (DAPI) (1μg/ml, Sigma) for 10 minutes at 37°C was performed for cell nuclear staining.

To further evaluate contaminations of isolated HUVECs with SMCs we performed FACS analysis to evaluate percentage of cells positive for α smooth muscle actin (α-SMA). Cells were detached from the culture plate after 3 minutes incubation with trypsin (EDTA trypsin 0.05%, Sigma) at 37°C. Cells were then fixed with 2% solution of paraformaldehyde (Società Italiana Chimici, Rome, Italy). The cells were washed twice with PBS buffer solution then permeabilized with 0.1% triton X-100 (Fluka) for 3 minutes and incubated in 3% BSA (Sigma) for 10 minutes at room temperature. The sample was incubated with Cy3-labeled anti-human α-SMA antibody (1:250, Sigma) for 30 minutes at room temperature, suspended in 500 μL of PBS solution and analyzed with FACSCanto II system (BD Biosciences).

4.A3) Results.

Cells collected after collagenase digestion of the umbilical cord vein endothelial layer may be contaminated with SMCs. In order to evaluate this contamination and the effective phenotype of isolated cells we performed imunofluorescence staining for endothelial marker vWF (figure 41A). Images showed that almost all isolated cells were positive for this marker. We further confirmed this result by counting the SMC specific marker α-SMA positive cells with Fluorescence-activated cell sorting (FACS). The result confirmed a low contamination of 4.6% α-SMA positive cells within the pool that was then used in flow exposure experiments (figure 41B).

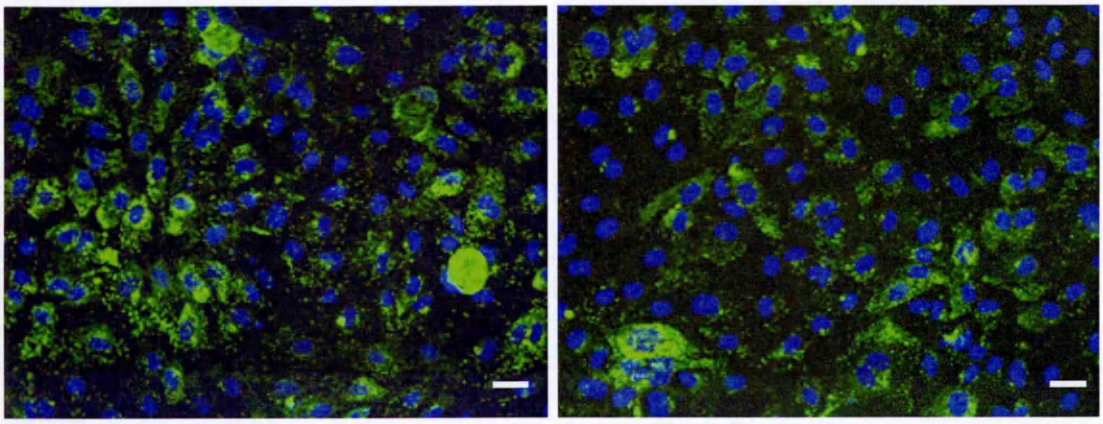

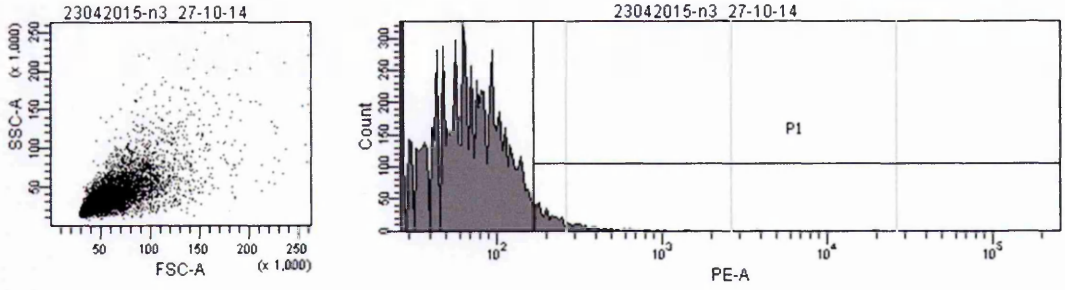

Population	#Events	%Parent	PE-A Mean
All Events	10,000	####	71
P1	460	4.6	316

Fig.41: A) HUVECs stained for vWf (green) and counterstained for nuclei (blue). Magnification 20x, scale bar 20µm. B) FACS result for HUVECs incubated with anti-α-SMA antibody.

4.B) Culture plate gelatine coating evaluation

4.B1) Cell cultures time-lapse.

A well of a 6-well plate (Falcon) was coated with different percentage bovine gelatine (Sigma) solutions, 0.2%, 0.6%, 1% respectively, for one hour at 37°C. After the coating process, the well was seeded with $3 \cdot 10^5$ /cm^2 HUVEC and 2mL of complete growth medium was added to each well. HUVEC motility and proliferation was observed for 24 hours using an Axio Observer.Z1 microscope equipped with a Slide-in module standard XLMultiS1, a heating module and a CO2 module (Carl Zeiss, Jena, Germany). Images were taken at a rate of one frame per minute. Cell movement analysis was performed using Axio Vision software (Carl Zeiss). Each percentage solution was tested three times. Motility was reported as the average cell velocity in um/s and proliferation was reported as the % of cells, which underwent mitosis during the 24 hours period.

4.B2) Results.

Gelatine coating evaluation did not show statistically significant differences in HUVECs motility (figure 42A). Furthermore a slight increase in the number of mitotic cells (figure 42B), from 15% to 25%, was observed in plates coated with decreasing concentration of gelatine. Based on these results plates for the flow exposure experiment were coated with 0.2% gelatine solution.

4.B3) Statistic methods

To evaluate the statistic significance of results obtained during the research activities, we performed one-way ANOVA test and the post-hoc Bonferroni multiple

comparisons test was used to establishe differences among groups. Tests were performed using PRISM 6.0f software (GraphPad Software Inc., La Jolla, CA, USA).

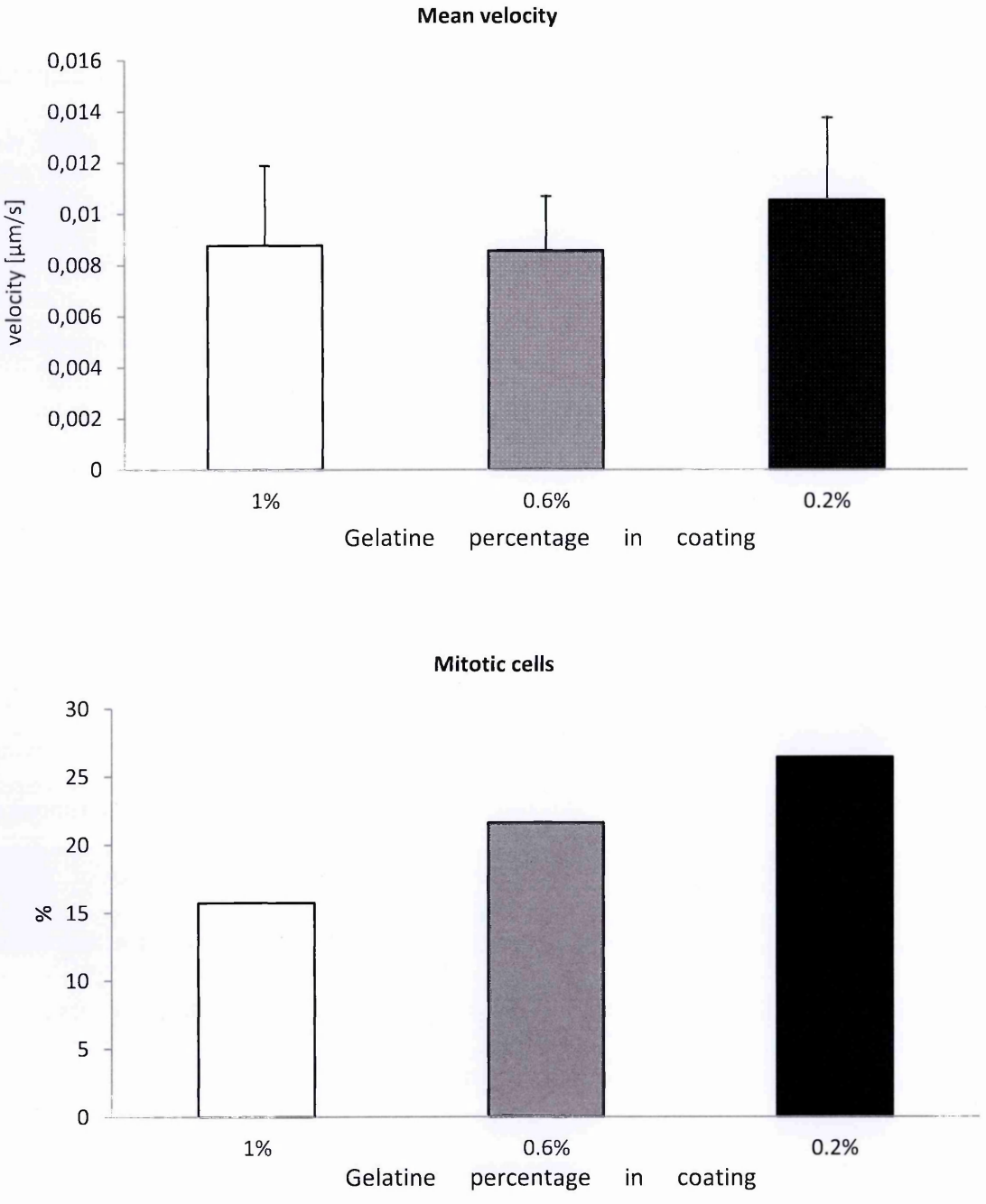

Fig.42: A) Mean velocity of HUVEC seeded on different gelatine percentage (1%, 0.6%, 0.2%) coated plates. B) Percentage of mitotic cells counted in plates coated with different percentage gelatine solutions.

4.C) Flow exposure experiments

4.C1) Experimental set-up.

Confluent EC monolayers were exposed to four different WSS patterns, derived from previous CFD analysis of an idealized AVF (79) as reported in chapter 2. The day of the experiment, under a laminar flow hood, the GM was changed with experimental medium (EM, composed by GM, added with 4% of high molecular weight Dextran (Dextran from Leuconostoc spp, 450-650 kDa, Sigma) (385). The plate was fixed in position with a vacuum pump and closed with the cone. The CPD, described in chapter 3, was then transferred to the incubator and mounted with the engine. The cone rotation speed was slowly increased to the desired value over approximately 1 hour, experimental medium was changed twice a day and stored at -80°C for further analysis. Contrast phase microscopy images where taken at the beginning, during and at the end of each experiment. Each condition was tested ten times. A control cell sample underwent the same process as the cells exposed to flow, without transfer to the CPD device.

4.C2) SEM sample preparation.

Since contrast phase microscopy images provide only limited information on cells morphology and are not indicated to evaluate the three dimensional shape, we wanted to develop a protocol to be able to perform SEM images of cells attached to the plate of our system. Thus after 48 hrs of flow exposure, the cell culture plate was removed from the device. Using a circular hollow punch (0.6 mm of diameter), we removed pieces of the plate from the area of interest of the dish. These samples were fixed in 2.5% glutaraldehyde in 0.1M sodium cacodilate for 1 hour, then postfixed with osmium tetroxide and dehydrated with a series of passage in increasing ethanol baths.

Cell monolayers on samples were dried in pure hexamethyldisilazane (HDMS, Fluka Chemie AG, Buchs, Switzerland), sputter-coated with gold and examined using scanning electron microscope (SEM, 1540 EsB, Carl Zeiss GmbH, Oberkochen, Germany).

4.C3) Results.

Contrast phase microscopy images showed that HUVECs exposed to unidirectional stimuli have deep morphological changes compared to the static control (figure 43). As shown in figures 44 and 45, cells exposed to PUL_A and PUL_V waveforms were elongated and aligned in the flow direction. A major alignment was observed in HUVEC exposed to PUL_V (figure 45) WSS waveform while cells exposed to PUL_A (figure 44) presented a lower rate of alignment especially in the outer part of the plate. HUVECs exposed to both REC_A (figure 46) and REC_B (figure 47) WSS waveforms did not elongated or aligned and presented a cobblestone shape similar to that observed in HUVECs maintained in static condition (figure 48).

Finally, in order to evaluate the three dimensional shape of HUVECS, we developed a SEM sample preparation protocol that allowed us to obtain images of the cell culture monolayers after 48 hours of exposure to PUL_V WSS waveforms and after 48 hours of static culture, as shown in figure 49.

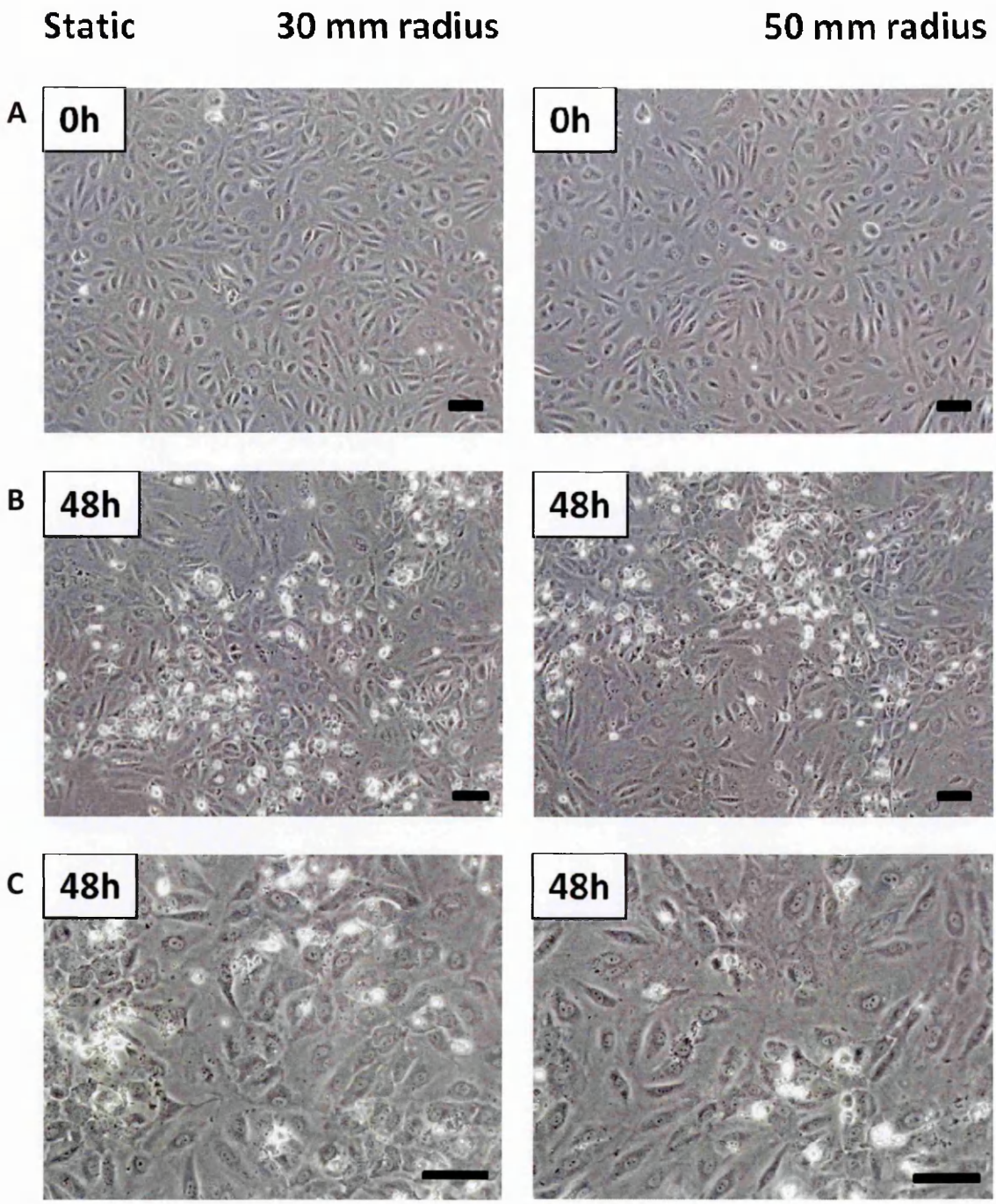

Fig.43: Contrast phase microscopy images of HUVECs at different plate radial positions, maintained in static conditions. A) HUVECs at the beginning of experiment, magnification 10x, scale bar 50μm. B) HUVECs after 48 hours, magnification 10x, scale bar 50μm. C) HUVECs after 48 hours, magnification 20x, scale bar 50μm.

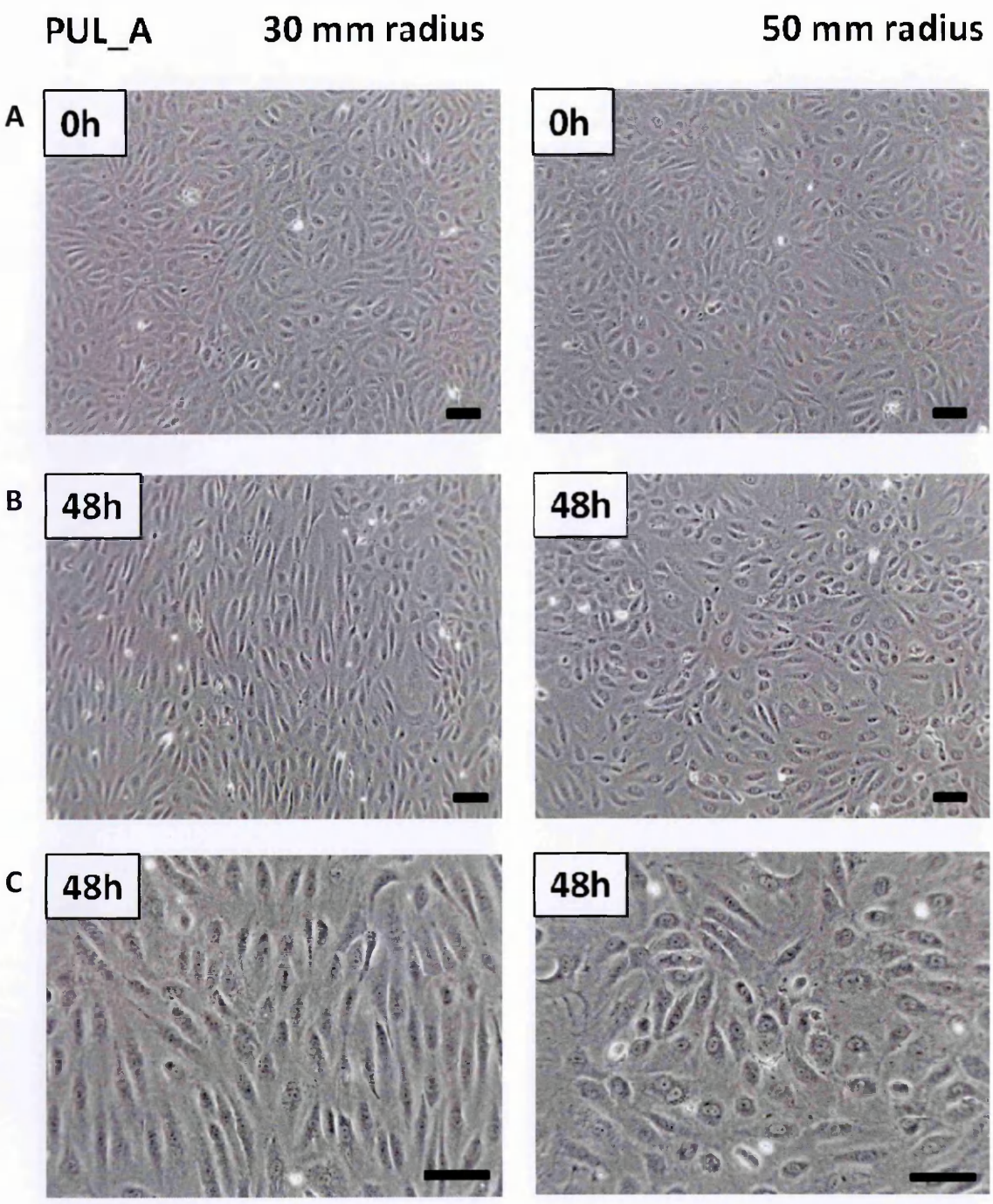

Fig.44: Contrast phase microscopy images of HUVECs at different plate radial positions, exposed to PUL_A waveform. A) HUVECs at the beginning of experiment, magnification 10x, scale bar 50µm. B) HUVECs after 48 hours, magnification 10x, scale bar 50µm. C) HUVECs after 48 hours, magnification 20x, scale bar 50µm.

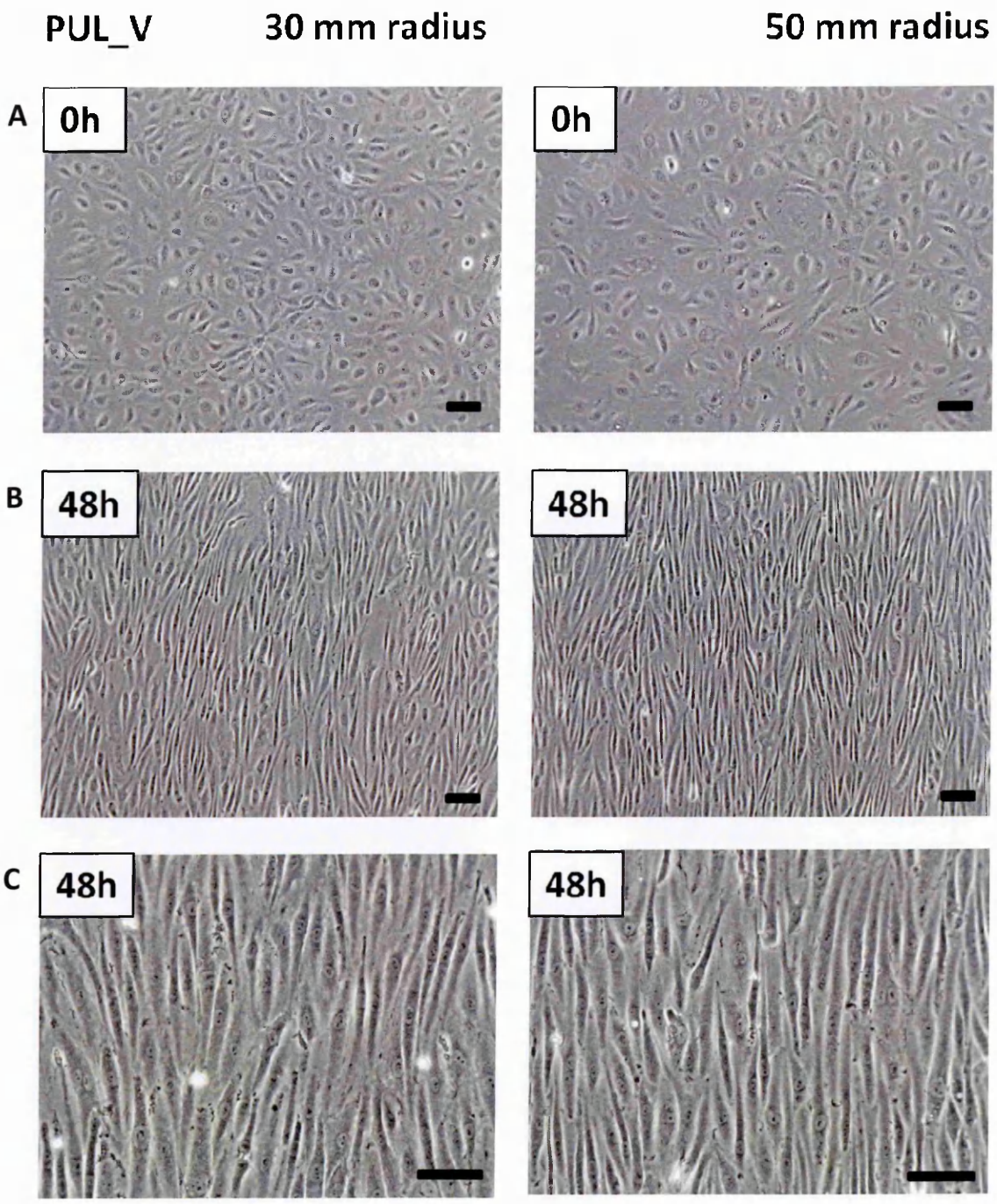

Fig.45: Contrast phase microscopy images oh HUVECs at different plate radial positions, exposed to PUL_V waveform. A) HUVECs at the beginning of experiment, magnification 10x, scale bar 50μm. B) HUVECs after 48 hours, magnification 10x, scale bar 50μm. C) HUVECs after 48 hours, magnification 20x, scale bar 50μm.

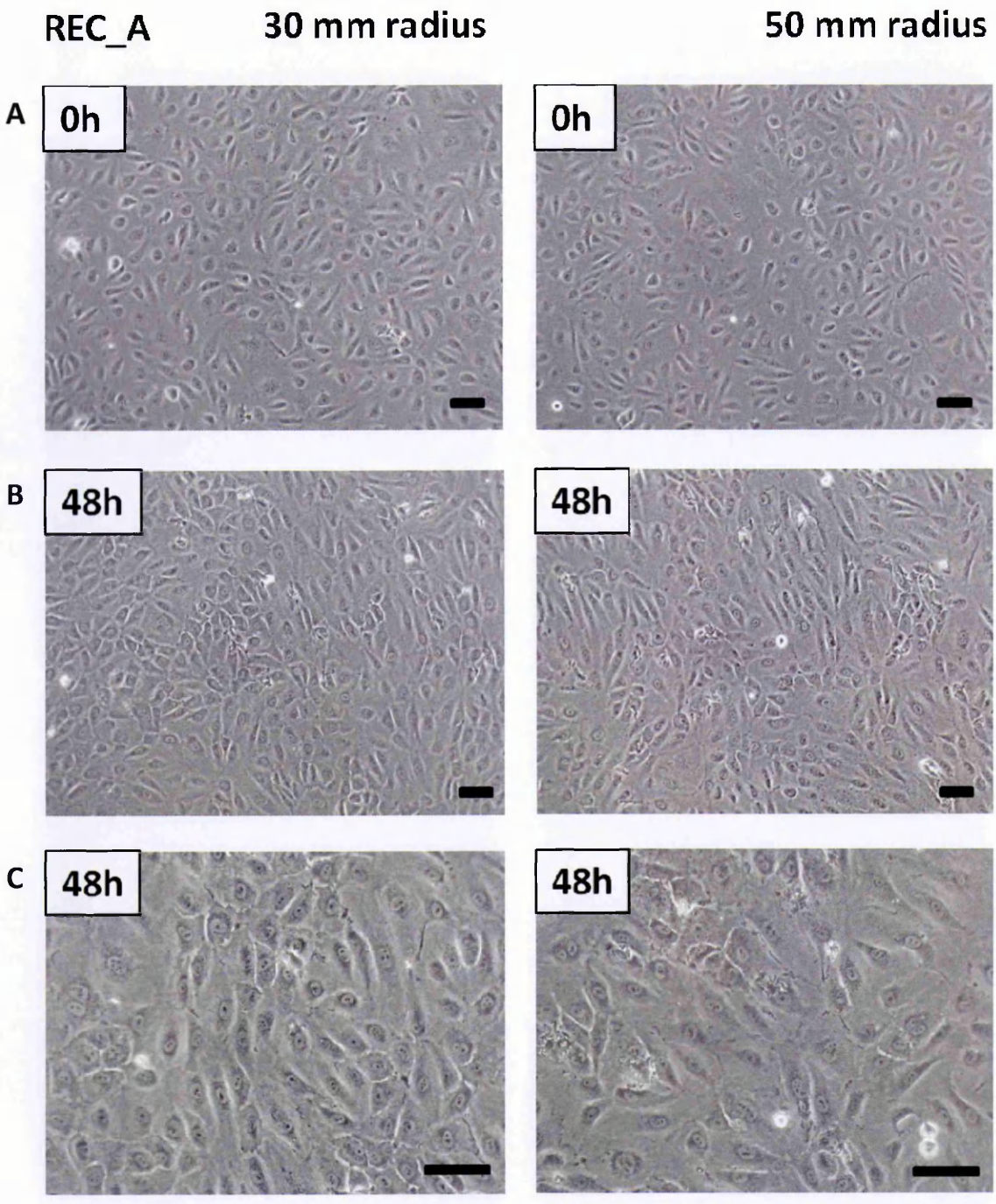

Fig.46: Contrast phase microscopy images of HUVECs at different plate radial positions, exposed to REC_B waveform. A) HUVECs at the beginning of experiment, magnification 10x, scale bar 50μm. B) HUVECs after 48 hours, magnification 10x, scale bar 50μm. C) HUVECs after 48 hours, magnification 20x, scale bar 50μm.

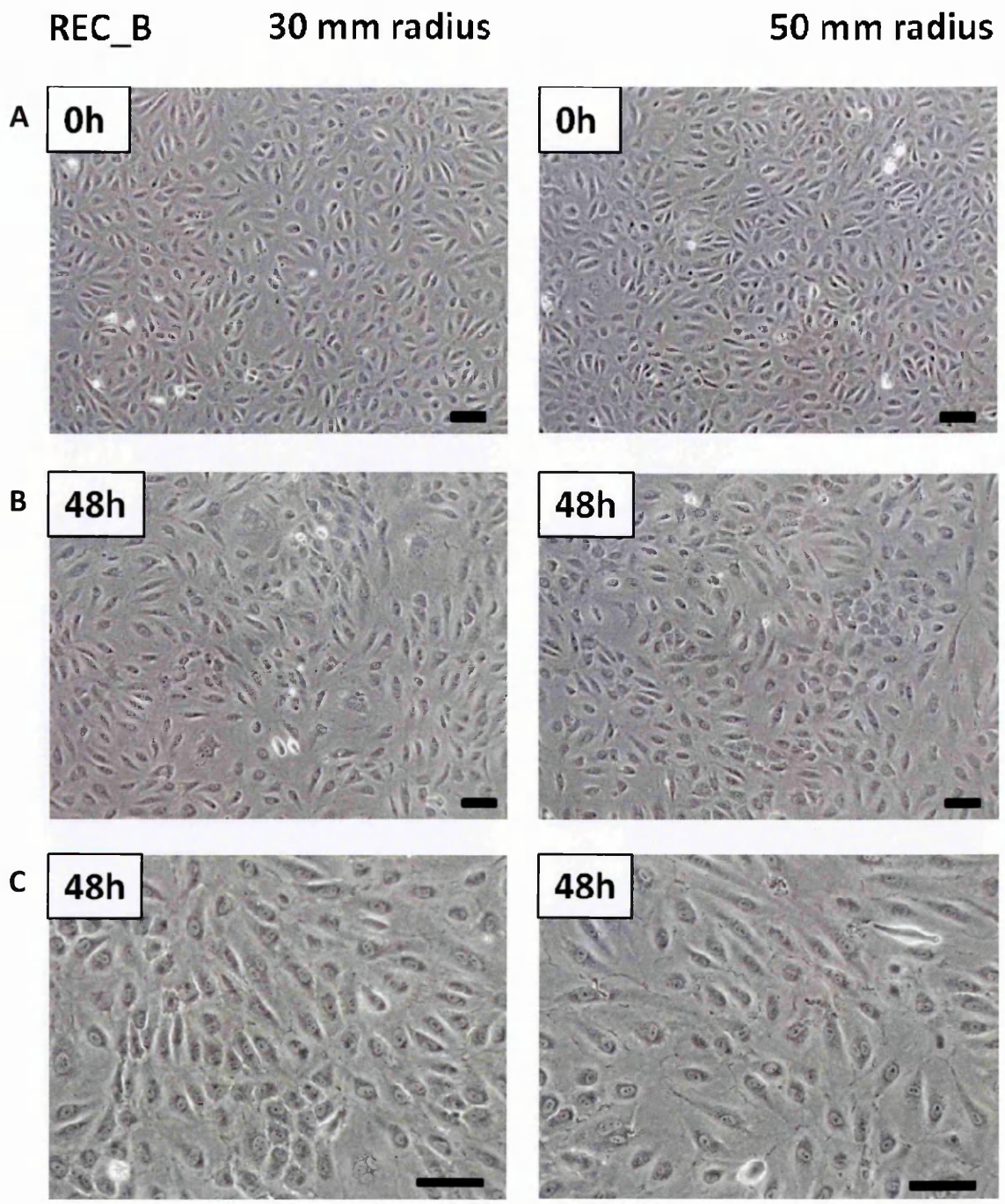

Fig.47: Contrast phase microscopy images of HUVECs at different plate radial positions, exposed to REC_B waveform. A) HUVECs at the beginning of experiment, magnification 10x, scale bar 50μm. B) HUVECs after 48 hours, magnification 10x, scale bar 50μm. C) HUVECs after 48 hours, magnification 20x, scale bar 50μm.

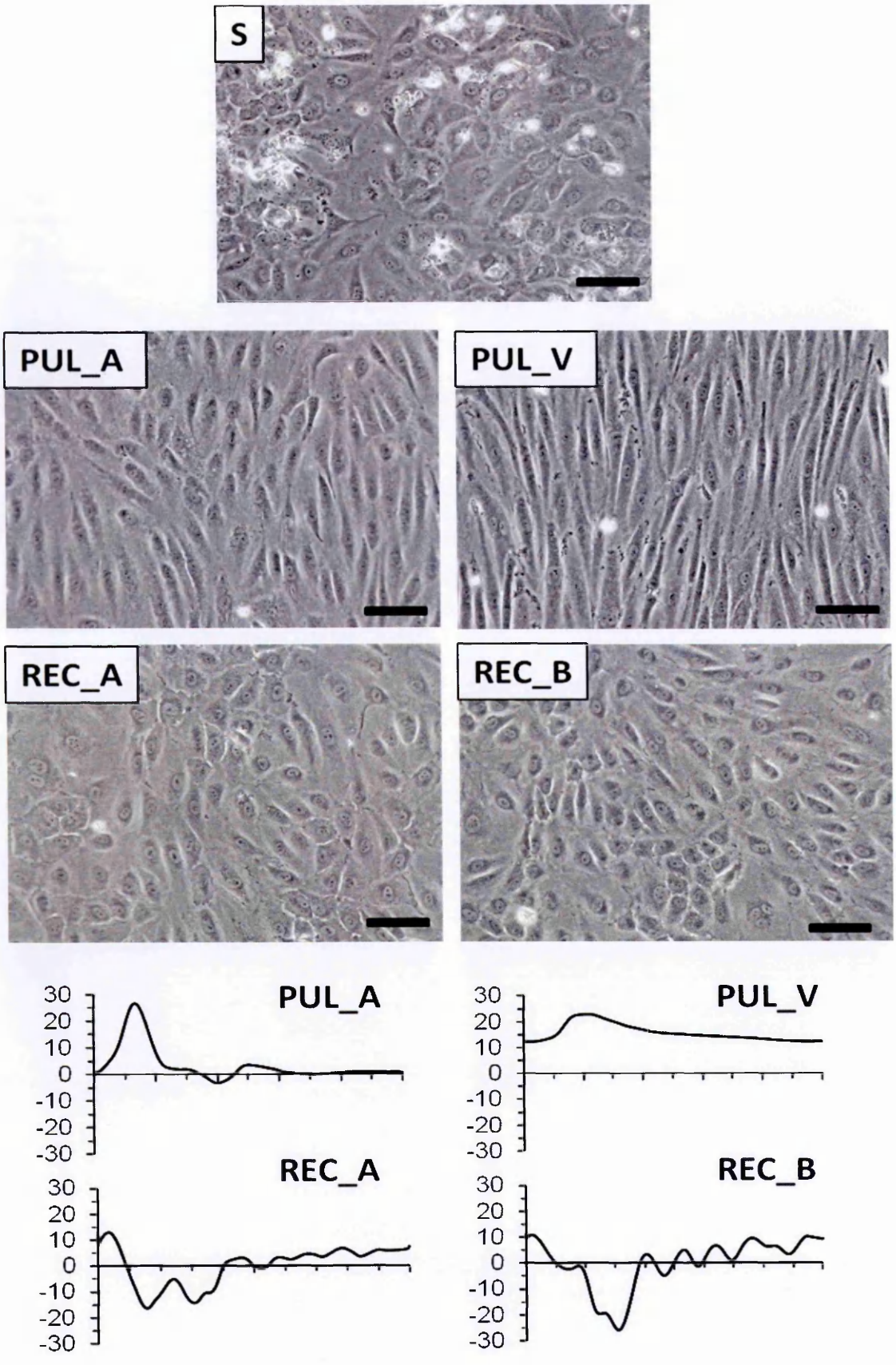

Fig.48: Contrast phase microscopy images oh HUVECs kept static (S) or exposed to different WSS conditions for 48 hours. Magnification 20x, scale bar 50μm.

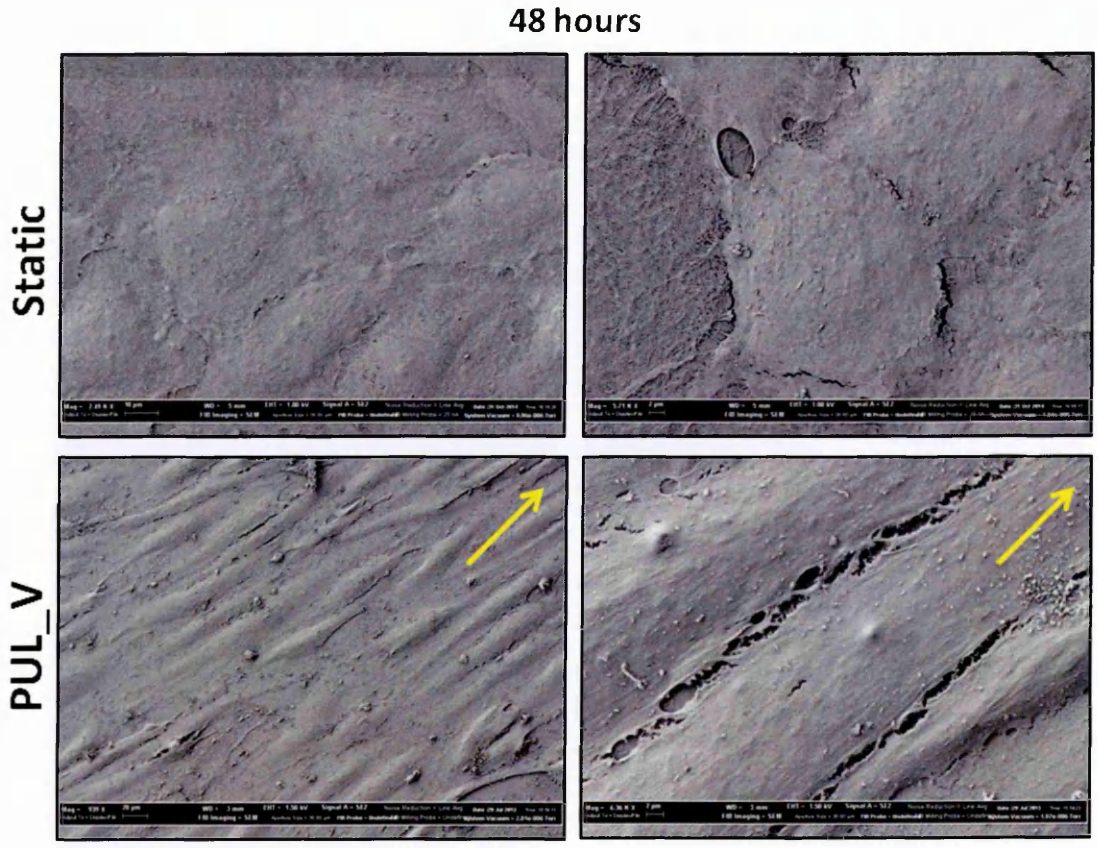

Fig.49: SEM images of HUVEC exposed to 48 hours of PUL_V WSS stimulation or kept static.

4.D) HUVEC morphology evaluation

4.D1) Immunofluorescence staining.

At the end of each experiment the cell monolayer on the Petri dish P150, was fixed in 2% paraformaldehyde (Società Italiana Chimici) in 4% sucrose (Sigma) solution, for 10 minutes at room temperature. Cells were then permeabilised in 0.1% triton X-100 (Fluka) for 3 minutes and incubated in 3% BSA (Sigma) for 30 minutes at room temperature. HUVEC were incubated with rabbit anti-ZO-1, 1 µg/mL (Sigma) overnight at 4°C as a primary antibody. HUVEC were then incubated with a FITC-conjugated goat anti-rabbit (1:25) antibody (Jackson Immunoresearch, West Grove, PA) for 45 minutes at 37°C followed by incubation with rhodamine-labeled phalloidin

(Invitrogen, Paisley, UK) (1:40) for 45 minutes at room temperature. Counterstaining with DAPI (1 mg/ml, Sigma) for 20 minutes at 37°C was performed for cell nuclear staining. The slides were finally mounted with a fluorescent mounting medium (Dako Cytomation, Carpinteria, CA) and examined by ApoTome microscopy (Axio Imager.Z2, Carl Zeiss). Each condition was tested three times.

4.D2) Immunofluorescence image analysis.

To quantify F-actin fibers distribution the ImageJ plug-in OrientationJ (EPFL, Lausanne, Switzerland) was used, as described in a previous study (386). Briefly, immunofluorescence images were acquired and split into RGB components. The R (red) channel image was then transformed to an 8-bit image and processed by the plug-in to return the distribution of fibers according their direction. The complete procedures and settings are reported in Appendix B1.

To evaluate the elongation of HUVECs exposed to different WSS waveforms, the open source software CellProfiler (v2.1.0, Broad Institute, Cambridge, USA) was used to perform automatic recognition of cells in immunofluorescence images obtained after ZO-1 protein staining. The software allows the user to define a sequence of modules, or pipeline, that processes images and identifies single cells. After nuclei (primary objects) and cell (secondary objects) recognition an additional module allow manual correction of mismatched objects. Finally, a dedicated module quantifies geometrical parameters of cells, returning axes dimensions and orientation of the major axis. Two pipelines, reported in appendix B2, were defined to differentiate between elongated and polygonal cell shapes.

4.D3) Statistic methods

To evaluate the statistic significance of results obtained during the research activities, we performed one-way ANOVA test and the post-hoc Bonferroni multiple comparisons test was used to establish differences among groups. Tests were performed using PRISM 6.0f software (GraphPad Software Inc., La Jolla, CA, USA).

4.D4) Results.

As shown in figure 50B, HUVEC monolayers maintained in static condition showed random distribution of F-actin fibers, mostly organized in dense peripheral actin bands, with a few fibers crossing the cellular body. HUVECs exposed to the PUL_A WSS waveform showed a loss of peripheral actin bands and greatly increased number and thickness of F-actin stress fibers across the cell body (figure 51B). This flow-dependant organization was even more evident in EC exposed to the PUL_V WSS waveform (figure 52B). In HUVECs exposed to REC_A (figure 53B) and REC_B (figure 54B) WSS waveforms, F-actin fibers remained mostly peripheral with fibers not oriented in the flow direction, showing a pattern similar to that of cells maintained in static condition (figure 50).

Automatic cell shape evaluation performed on tight junction-associated ZO-1 protein staining images (figure 50C, 51C, 52C, 53C, 54C), allowed computation of the mean ratio of the major/minor axis for cells exposed to different WSS waveforms. In figure 55 is provided the comparison of immunofluorescence images obtained from cell monolayers exposed to different flow conditions.

Automatic detection of the direction of F-actin fibers using digital image processing was carried out as described in Appendix B. As shown in figure 56A, in HUVECs exposed to the PUL_V waveform, 59.5% of F-actin fibers were aligned with

the flow (within ±15° of flow direction) with only 3.6% of fibers perpendicular to flow (± 15°). Interestingly HUVEC exposed to the PUL_A waveform did not show a similar orientation of F-actin distribution since only 23.2% of fibers were aligned with the flow (± 15°), with 13.6% of fibers perpendicular to flow (± 15°). In HUVEC exposed to the REC_A and REC_B waveforms, 21.3% and 28.7% of F-actin fibers were aligned with the flow (± 15°) and 17.9% and 9.9% of F-actin fibers were perpendicular to flow (± 15°), respectively. In conclusion only the PUL_V WSS waveform elicited a strong alignment of F-actin stress fibers with the flow direction (figure 56B).

HUVEC exposed to PUL_A and PUL_V stimuli have a ratio of 2.56±1.32 and 5.10±1.67 respectively, significantly (figure 57, $p < 0.01$ PUL_A and PUL_V vs. Static, REC_A and REC_B, n=3) higher than that calculated in cells exposed to the REC_A and REC_B waveforms, in which the elongation ratio averaged only 1.58 ±0.36 and 1.57±0.37, respectively. These values were comparable to those calculated for cells maintained in static conditions (1.54 ±0.37). Cell alignment was also quantified by measurement of cell major axis direction (figures 58). 35.1 % of cells exposed to PUL_A and 73.4% of HUVEC exposed to the PUL_V waveform had major axes oriented between ±20° of the flow direction. Only 21.2% and 22% of cells exposed to the REC_A and REC_B WSS waveforms respectively were aligned between ±20° of the flow direction, similar to the 28.8% of HUVEC maintained static which had this orientation.

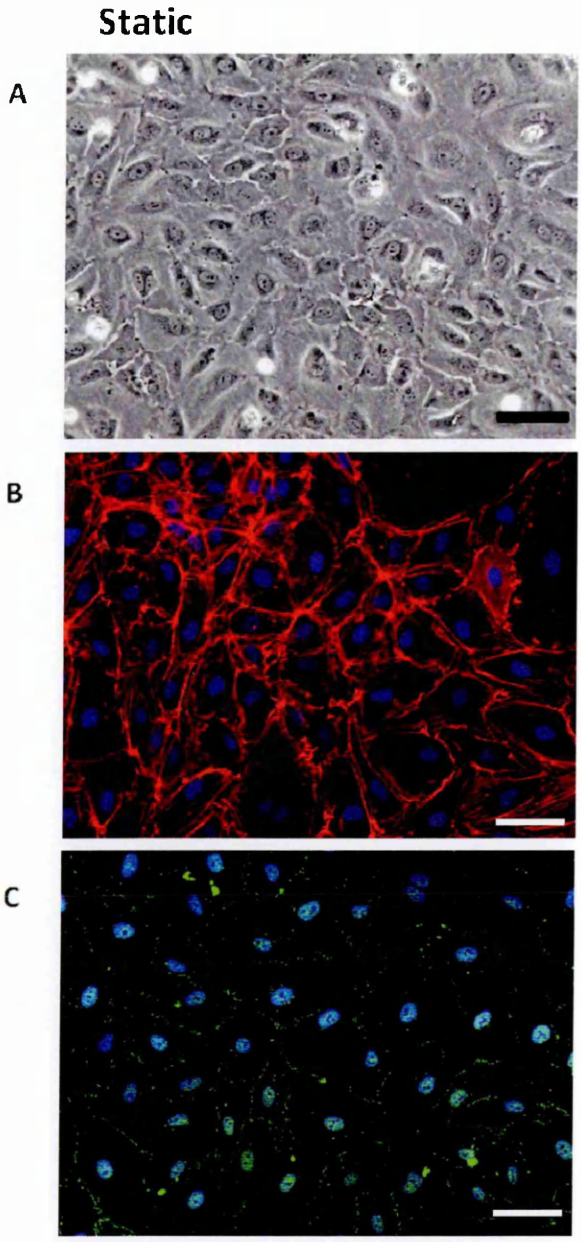

Fig.50: Images of HUVECs maintained in static conditions for 48 hours. A) Contrast phase microscopy image, magnification 20x, scale bar 50μm. B, C) Immunofluorescence images of HUVECs stained for F-actin (red), ZO-1 (green) and nuclei (blue), magnification 20x, scale bar 50μm.

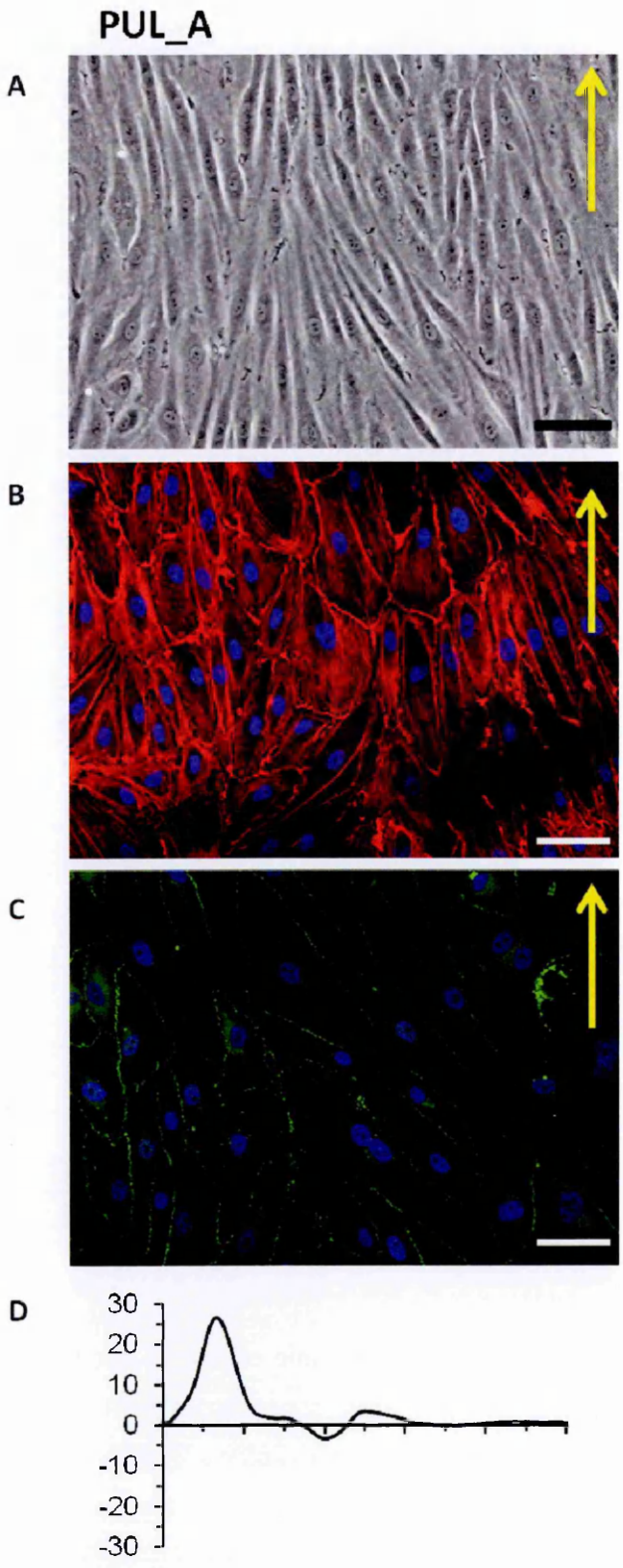

Fig.51: Images of HUVECs exposed to PUL_A WSS waveform (the yellow arrows indicate the flow direction) conditions for 48 hours. A) Contrast phase microscopy image, magnification 20x, scale bar 50μm. B, C) Immunofluorescence images of HUVECs stained for F-actin (red), ZO-1 (green) and nuclei (blue), magnification 20x, scale bar 50μm. D) WSS profile PUL_A.

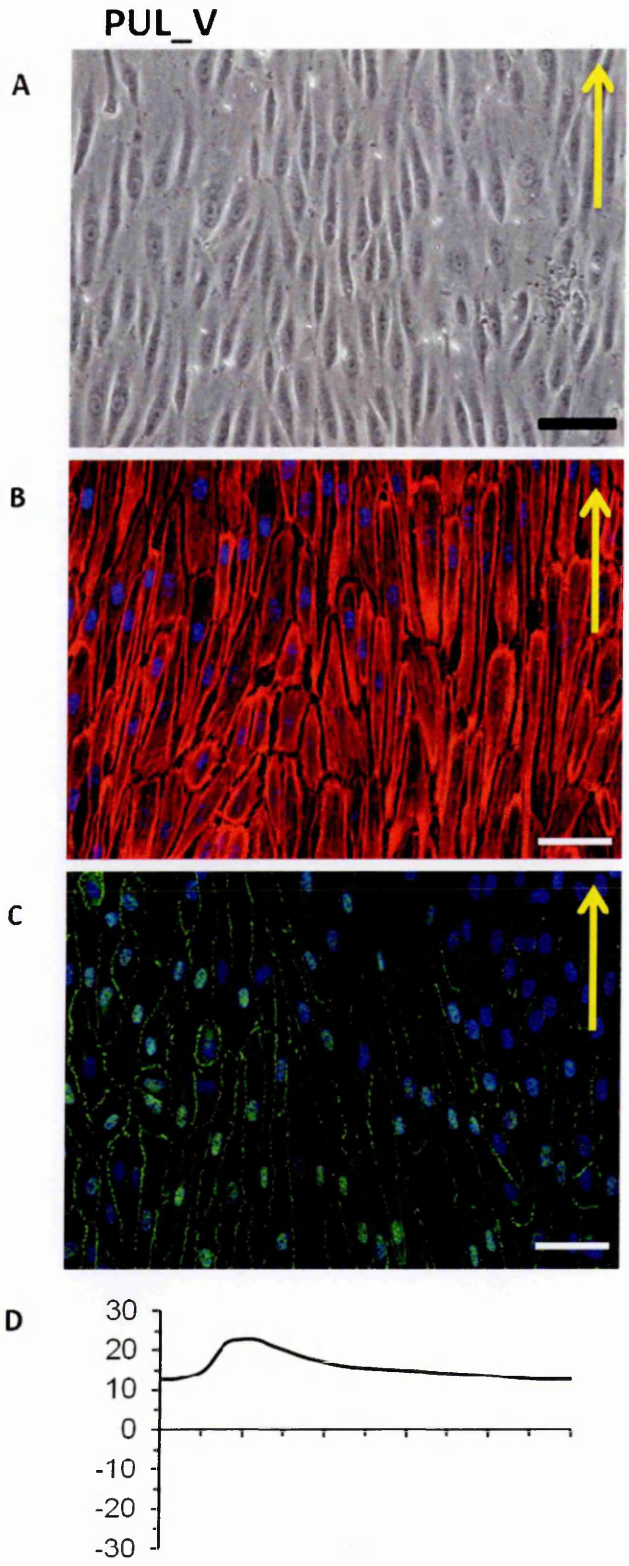

Fig.52: Images of HUVECs exposed to PUL_V WSS waveform (the yellow arrows indicate the flow direction) conditions for 48 hours. A) Contrast phase microscopy image, magnification 20x, scale bar 50µm. B, C) Immunofluorescence images of HUVECs stained for F-actin (red), ZO-1 (green) and nuclei (blue), magnification 20x, scale bar 50µm. D) WSS profile PUL_V.

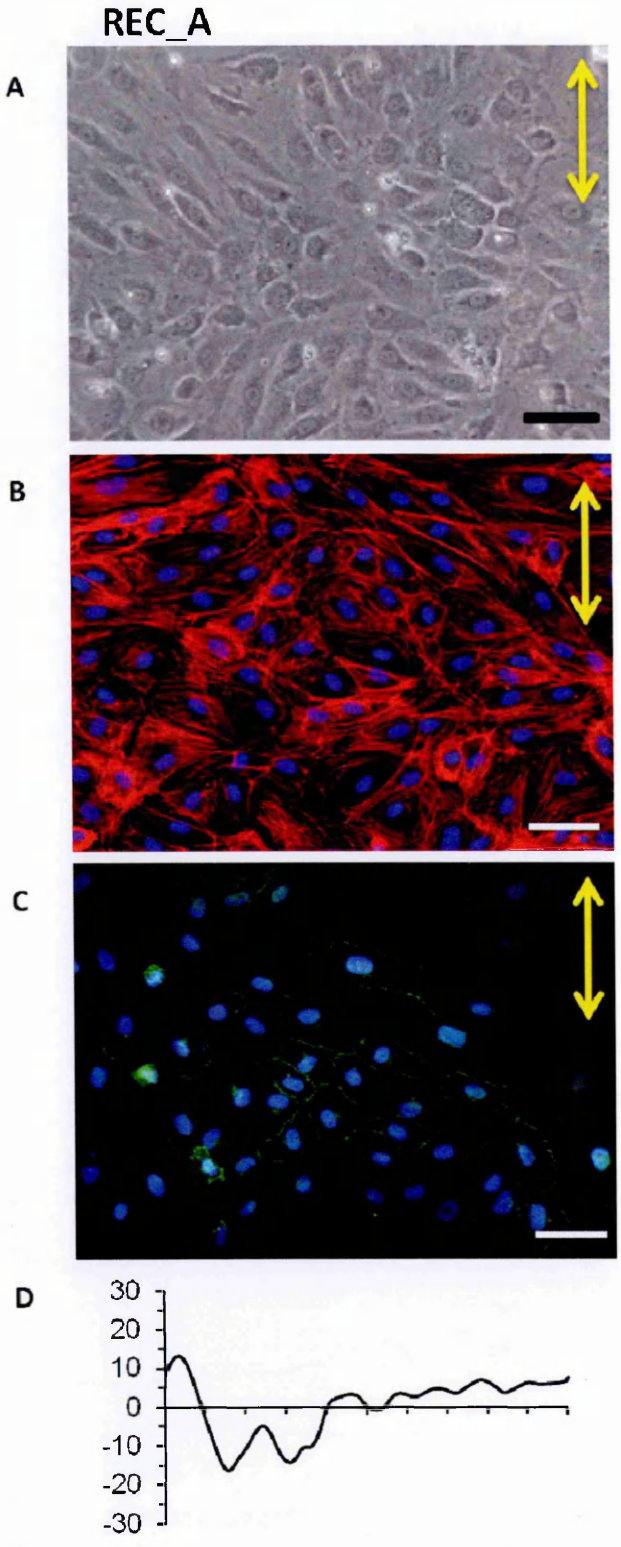

Fig.53: Images of HUVECs exposed to REC_A WSS waveform (the yellow arrows indicate the flow direction) conditions for 48 hours. A) Contrast phase microscopy image, magnification 20x, scale bar 50μm. B, C) Immunofluorescence images of HUVECs stained for F-actin (red), ZO-1 (green) and nuclei (blue), magnification 20x, scale bar 50μm. D) WSS profile REC_A.

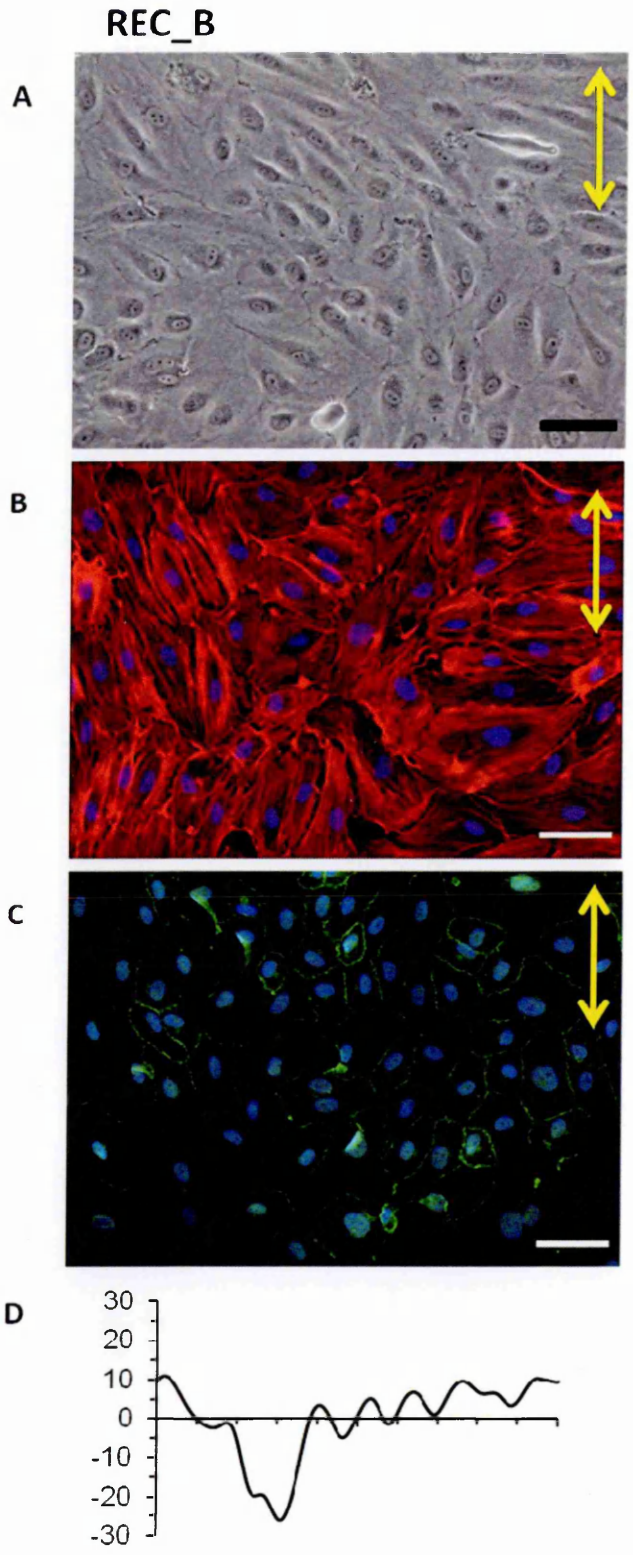

Fig.54: Images of HUVECs exposed to REC_B WSS waveform (the yellow arrows indicate the flow direction) conditions for 48 hours. A) Contrast phase microscopy image, magnification 20x, scale bar 50µm. B, C) Immunofluorescence images of HUVECs stained for F-actin (red), ZO-1 (green) and nuclei (blue), magnification 20x, scale bar 50µm. D) WSS profile REC_B.

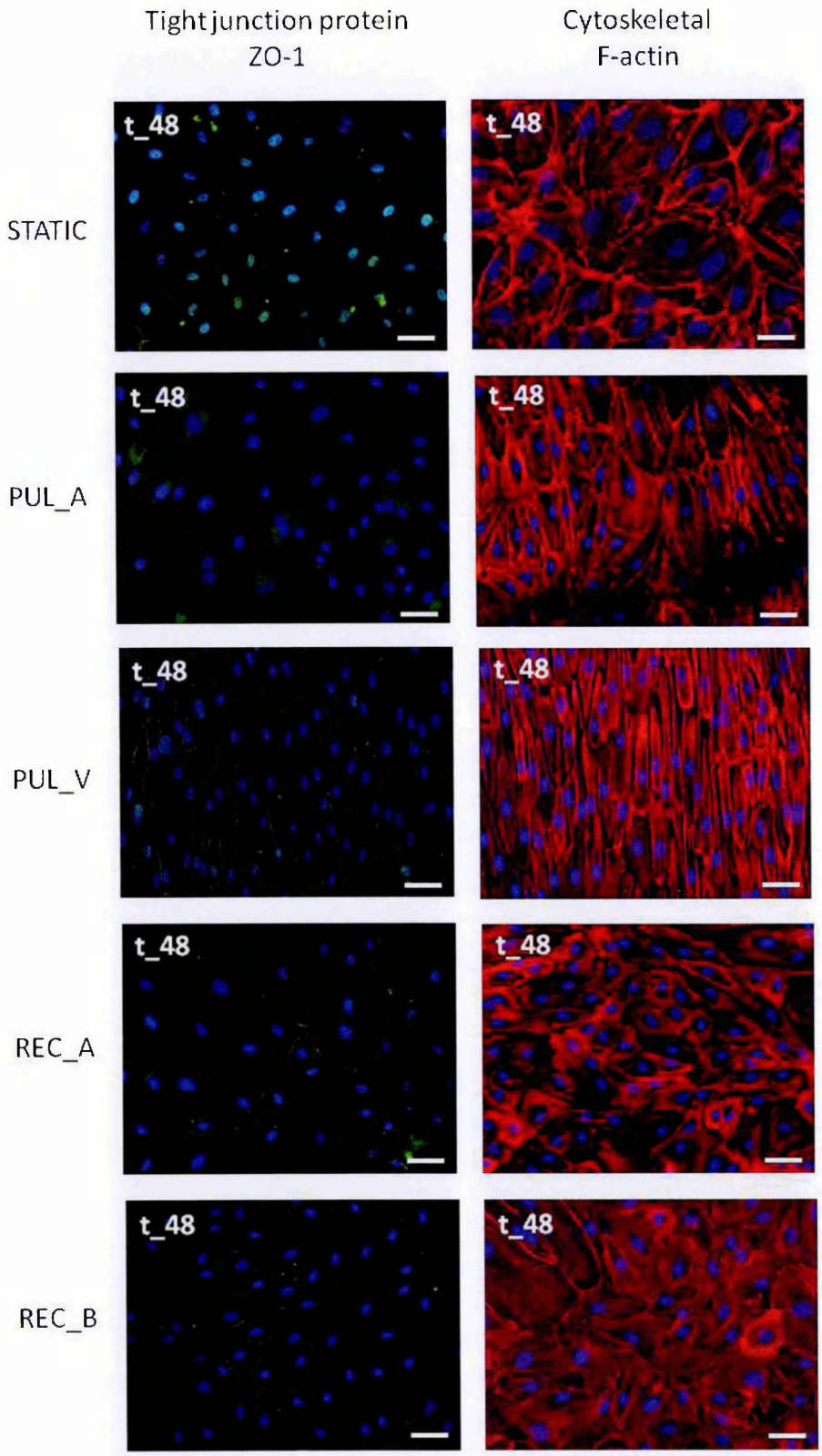

Fig.55: Immunofluorescence images of HUVECs after 48 hours of different culture conditions. Staining for ZO-1 (green), F-actin (red) and nuclei (blue). Magnification 20x, scale bar 50µm. This image has been published in "Am. J. Physiol. Heart Circ. Physiol. 2015 Oct 23. doi: 10.1152/ajpheart.00098.2015".

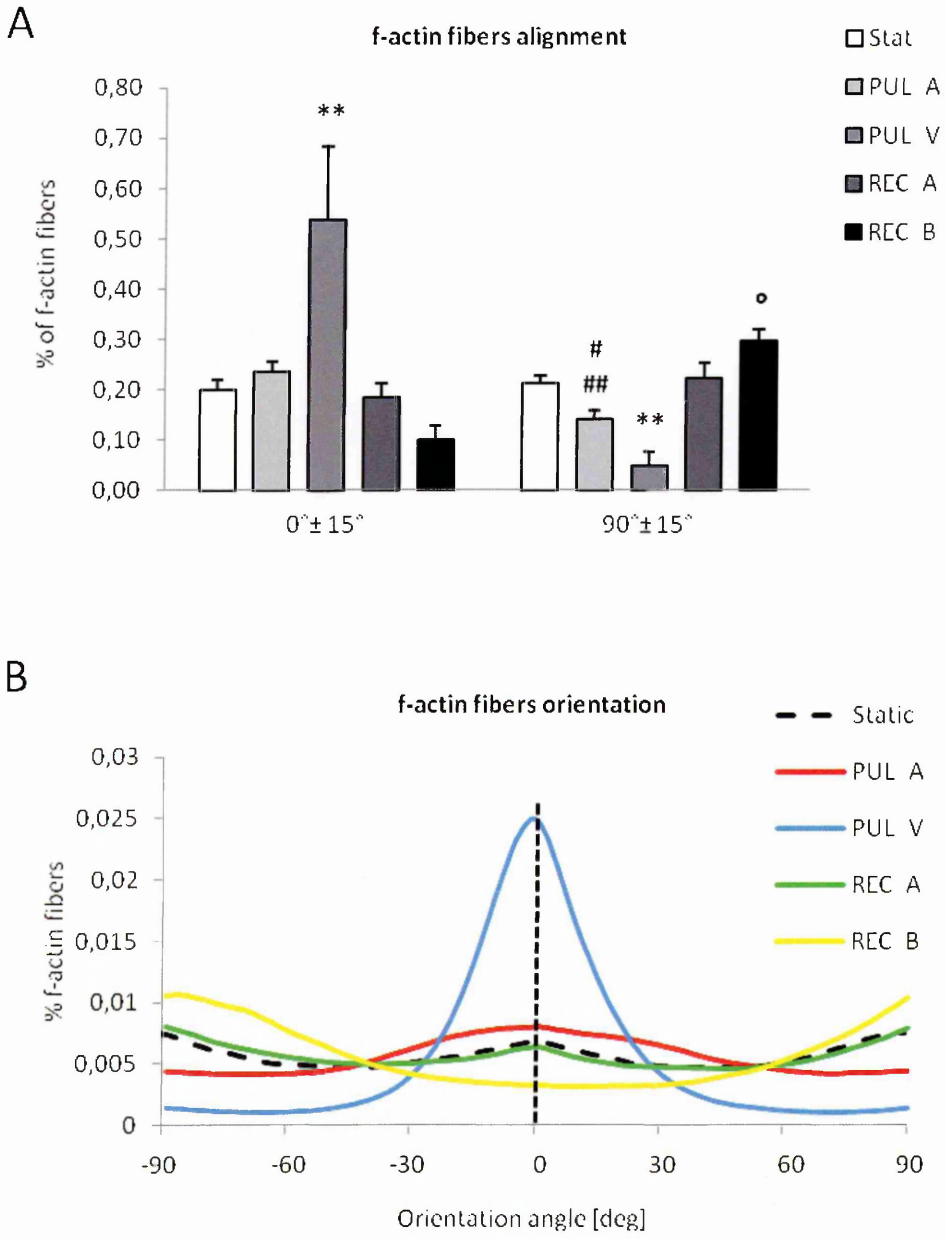

Fig.56: F-actin fibers distribution after 48 hours of exposure to flows or static conditions. A) Percentage of fibers aligned to the flow (0°±15°) or perpendicular to it (90°±15°). ** $p<0.01$ PUL_V vs. all, # $p<0.05$ PUL_A vs. Static and REC_A, ## $p<0.01$ PUL_A vs. REC_B and ° $p<0.05$ REC_B vs. static and REC_A, n =3. B) Percentage of fibers oriented to any angle. This image has been partially published in "Am. J. Physiol. Heart Circ. Physiol. 2015 Oct 23. doi: 10.1152/ajpheart.00098.2015".

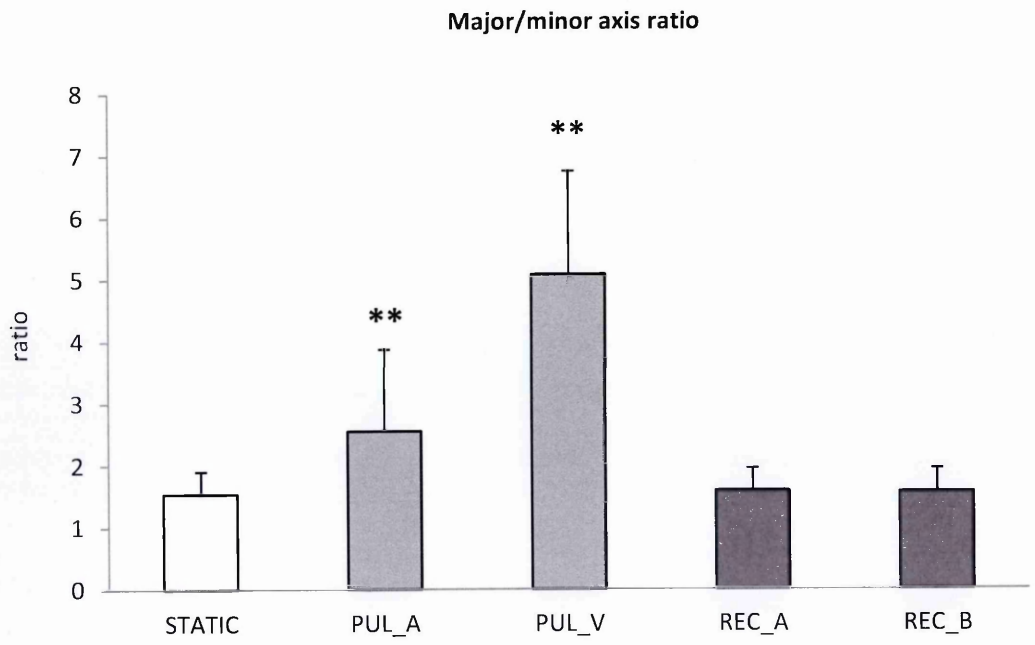

Fig.57: Ratio of major and minor axes of HUVECs exposed to different conditions of WSS. ** $p < 0.01$ vs. static, REC_A and REC_B, n=3. This image has been published in "Am. J. Physiol. Heart Circ. Physiol. 2015 Oct 23. doi: 10.1152/ajpheart.00098.2015".

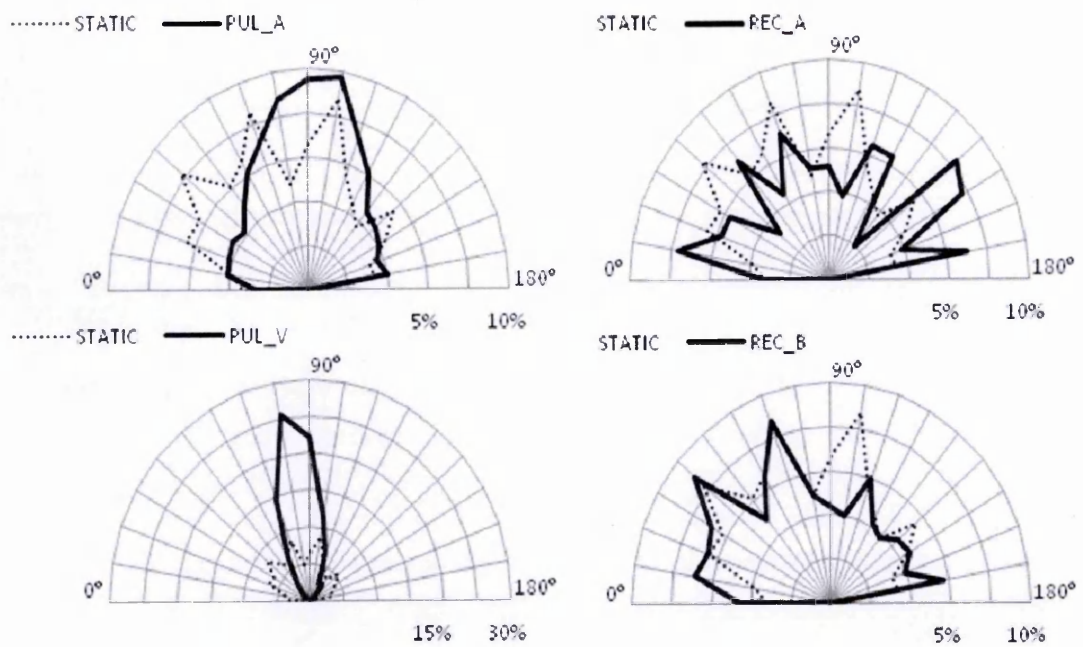

Fig.58: Distribution of HUVEC major axes respect to flow direction (90°) after 48 hours of exposure to different WSS waveforms compared to static.

4.E) Discussion

HUVECs derived freshly from umbilical cord are widely used and investigated. However if the collagenase digestion of endothelial layer is too long or if the tissues are damaged, the cord basement membrane may be dissolved and the endothelial cells suspension will be contaminated with smooth muscle cells or fibroblasts (387). The described HUVECs isolation procedure allowed us to obtain homogenous endothelial cells culture as showed by vWF staining and α-SMA FACS analysis.

Furthermore it is known that HUVECs growth substrate have deep effects on cell growth and cell culture plate coatings are considered necessary for ECs cultures (388, 389). Based on previous experiences of our laboratory (365, 390, 391), the use of different percentage gelatine solutions coating on cell motility and proliferation has been evaluated. No major statistical differences were found in the investigated conditions and according to these results we used a 0.2% gelatine solution for flow exposure experiments.

The previously described experimental set-up ensured adherent HUVECs after 48 hours of flow exposure. The strength of the procedure relies on the easiness of Cone-and-Plate handling in sterile conditions and on the disposable and removable culture plate that provides a cost-effective solution and allows the user to remove the plate at the end of experiment for further analysis. Furthermore the device is sized to be placed within a standard cell incubator in order to avoid the use of other components to control temperature and gas composition of CPD environment.

The cells morphological adaptations to different flow conditions were evaluated with different techniques. As expected (260, 392) HUVECs morphology was diversely affected by the WSS waveforms calculated in AVF high or low stenosis risk areas (figures 48 and 55), in line with previous works (260). ECs exposed to PUL_V WSS

waveform aligned and elongated in the flow direction. PUL_A waveform induced a reduced elongation and orientation respect to PUL_V. On the contrary, exposure of HUVECs to REC_A and REC_B profiles did not elongate nor aligned, and maintained cobblestone shape similar to cells in static condition.

The cell elongation induced by PUL_V was also visualized by SEM imaging. Even though this technique was not further explored, the developed protocol may provide information on the three dimensional shape of cells after flow exposure thus allows investigating the force acting on cells with different morphology.

HUVEC monolayers maintained in static condition showed a random distribution of F-actin fibers, mostly organized in DPABs, with a few fibers crossing the cellular body. HUVECs exposed to PUL_V WSS waveform showed a loss of peripheral actin bands and greatly increased number and thickness of F-actin stress fibers across the cell body. These fibers were markedly orientated towards the flow direction. PUL_A waveform again induced a less tightly spatial organized distribution of stress fibers. In HUVECs exposed to REC-1 and REC-2 WSS waveform F-actin fibers remained mostly peripheral with fibers not oriented in the flow direction, showing a pattern similar to that of cells maintained in static condition.

The HUVECs dramatic changes in shape and reorganization of cytoskeletal structure, induced by PUL_A and PUL_V, is involved in several protective effects of unidirectional WSS. Cytoskeleton reorganization and optimization is involved in endothelial barrier functions as well as in ECs quiescence due its tight relation with expression of transcription factors involved in cell proliferation (322).

4.F) Summary

After HUVEC isolation and characterization, the experimental conditions necessary to maintain cells adherent to the system plate in long term flow exposure experiments have been evaluated. Thus the culture plate coating, the timing of flow onset and the medium change frequency have been tested. The described set-up allowed us to perform 48 hours of exposure to different WSS waveforms, maintaining an adequate number of cell attached to the plate thus enabled us to perform further investigations on the exposed HUVEC monolayers.

The results of cell morphology evaluation were in line with previous investigations and showed a significant elongation and alignment of cells exposed to pulsatile WSS waveforms as compared to those exposed to reciprocating WSS or maintained in static conditions. F-actin fibers showed a dramatic reorganization in the flow direction in HUVECs exposed to PUL_V profile, while cell exposed to PUL_A presented a less markedly reorganization. HUVECs exposed to reciprocating WSS profiles showed randomly distributed F-actin fibers, similar to those observed in cell maintained in static conditions.

These morphological adaptations of cells are involved in the beneficial effect induced by unidirectional WSS on endothelium. To further demonstrate this effect, the HUVECs flow-induced gene expression has been evaluated, methods and results are provided in the next Chapter.

CHAPTER 5: Quantification of endothelial cell gene expression following exposure to AVF-specific WSS waveforms

This Chapter addresses the mRNA expression elicited in endothelial cells exposed to different flow conditions as described in Chapter 4. We initially evaluated the expression of KLF2, a very well known WSS-related transcription factor, deeply involved in cell quiescence as described in Chapter 2. Furthermore, since WSS-induced cytoskeleton reorganization is involved in cell shape changes, in endothelium barrier function as well as in forces transmission necessary to resist to WSS increase after fistula creation, we performed a gene array analysis to evaluate the differential expression of more than 80 genes involved in cell motility, induced by the tested flow conditions. mRNA of genes that resulted differentially expressed was further quantified by traditional RT-PCR in order to confirm the data of the assay and to provide the statistical significance of this altered expression.

5.A) KLF-2 mRNA expression.

5.A1) RT-PCR.

Following exposure of the HUVEC to the four WSS waveforms described in chapter 2, total RNA was extracted from HUVECs using Trizol reagent (LifeTechnologies) according to the manufacturer's instruction. Contaminating genomic DNA was removed by RNase-free DNase (Promega) for 1h at 37°C. Two μg of purified RNA was reverse transcribed using a mix of random-examers/oligoT and 200U of SuperScript II RT (Invitrogen) for 1h at 42°C. No enzyme was added for reverse transcriptase-negative controls.

To amplify cDNA, we used TaqMan Universal PCR Master Mix (Applied Biosystems) according to the manufacturer's instructions and inventoried TaqMan assays of Kruppel-like factor2 (KLF2 Hs00360439_g1 FAM/MBG probe), and an endogenous control (hHPRT1 Hs99999909_m1 FAM/MBG probe). The PCR was performed on a 7300 Real Time PCR System (Applied Biosystems). The amplification profile consisted of 2 min at 50°C for and 10 min at 95°C, the samples were cycled 40 times at 95°C for 15 s and 60°C for 60 s. We used the DDCt technique to calculate cDNA content in each sample using the cDNA expression in static control HUVEC as calibrator. Each condition was tested five times.

5.A2) Results.

HUVEC exposed to unidirectional PUL_A and PUL_V WSS stimulation showed an increased expression of KLF2 compared to the static control (figure 59). KLF2 mRNA showed a 4.7±2.4 and 3.7±2.2 fold increase in the two conditions respectively. It was further observed that both REC_A and REC_B WSS waveforms did not affect KLF2 expression, resulting in a 1±0.3 and 1.5±0.3 fold increase respectively over the level expressed by HUVECs maintained in static conditions.

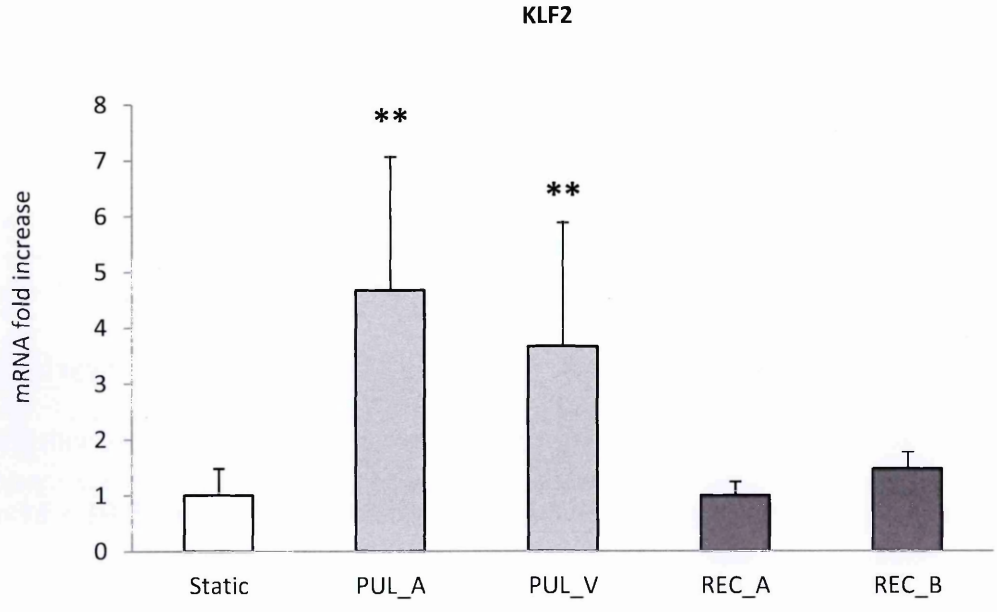

Fig.59: KLF2 mRNA expression elicited by different WSS waveforms relative to the static control. ** $p < 0.01$ vs. static, REC_A and REC_B, n=5. This image has been published in "Am. J. Physiol. Heart Circ. Physiol. 2015 Oct 23. doi: 10.1152/ajpheart.00098.2015".

5.B) Rho GTPase effectors mRNA analysis.

5.B1) Gene array.

To study the differentially expressed genes in HUVEC exposed to different WSS, the Human Cell Motility RT2 Profiler PCR Array (PAHS-128ZC; SABioscience, Qiagen, Frederick, MD, USA) was used. Since PUL_V induced a more elongated and organized HUVECs structure, the effect of this stimulus was compared to that induced by REC_A and REC_B. Total RNA was extracted using Trizol (LifeTechnologies) and was cleaned by RNeasy MinElute Cleanup kit according to the manufacturer's protocol (Qiagen). RNA from three experiments of each group was pooled and quantified spectrophotometrically (NanoDrop ND-1000, Thermo Scientific, Wilmington, DE, USA). The first-strand cDNA (1μg) was synthesized with RT2 First Strand Kit and was analyzed by quantitative Real-Time PCR. Data analysis was performed using the online SABioscience software. The boundary (fold regulation cut off) was set to 2-fold change between the different groups compared to static control. Those genes that were found to have a 2 or more fold increase relative to the static control were considered to be positively regulated and those that were found to have a 0.5 or less fold increase relative to the static control, negatively regulated.

5.B2) Results.

The PCR array allowed investigation of the expression of 84 genes involved in cytoskeletal remodeling and cell movement, which may be modulated by different conditions of WSS (tables 5a and 5b). Three different WSS waveforms were considered (PUL_V, REC_A and REC_B) as well as on HUVEC maintained static as control. Among these, 23 genes were identified as regulated by WSS. Some of these genes code for proteins that have been related to vascular dysfunction. Another 30 genes were

identified to be regulated below the 2-fold threshold. It is worthy of note that Rho GTPases RhoA and Rac1 resulted not regulated by the tested conditions. On the contrary we observed that other gene expression, deeply involved in IH development such as ROCK1, MMP-14 and -9 were downregulated by PUL_V if compared to REC_A.TIMP-2 expression was mostly down-regulated by REC_A while VEGFA was slightly up-regulated by PUL_V.

In conclusion we found that PUL_V caused the downregulation of mRNA expression of genes involved in Rho GTPases downstream pathways and in cell motility. On the contrary reciprocating flows and especially REC_A caused a generalized upregulation of these genes.

Gene name	PUL_V	REC_A	REC_B	Rho GTPase effectors	Cellular projections	Chemotaxis	Cell adhesion molecules	Integrin receptors
ACTR2	0.66	1.52	1.41	X	X			
ACTR3	0.55	1.49	1.41	X	X			
ARHGDI	1.61	1.84	1.79	X				
BAIAP2	3.85	1.71	1.69	X	X			
CDC42	1.44	3.32	1.31	X	X			
CFL1	0.84	1.27	1.09	X				X
CRK	0.59	1.13	0.69	X				
MSN	1.01	2.01	1.65	X				
PLCG1	2.97	2.39	1.44	X				
LYM	0.41	1.71	0.48	X				
MYL9	0.48	0.95	0.56	X				
PAK1	0.34	0.76	0.53	X				
PLD1	0.24	1.33	1.04	X	X	X		
PRKCA	1.84	1.8	1.74	X				
PTEN	0.17	0.50	0.42	X			X	
PTPN1	0.61	1.52	1.42	X				
RAC1	0.83	0.96	0.72	X	X			
RHOA	0.86	0.84	0.93	X	X		X	
ROCK1	0.75	1.71	0.93	X	X		X	
STAT3	0.96	1.36	1.12	X				
VIM	0.44	0.49	0.50	X				
WASF1	0.31	0.55	0.42	X	X			
WASF2	0.67	0.60	0.85	X	X	X		
WASL	0.5	0.58	0.72	X	X			
ARF6	1.46	1.97	1.38		X			
CAPN1	2.16	1.54	0.84		X		X	
DPP4	1.51	1.38	0.64		X		X	

Tab.5a: Gene array analysis result. In the table are reported those genes that were expressed by HUVECs afetr 48 hours of exposure to different flow conditions. Gees that were downregulated beyond the 2-fold threshold as compared to static control are highlighted in green, gene that resulted upregulated are highlighted in red. Red boxes indicate those genes that were selected for RT-PCR. This table has been published in "Am. J. Physiol. Heart Circ. Physiol. 2015 Oct 23. doi: 10.1152/ajpheart.00098.2015".

Gene name	PUL_V	REC_A	REC_B	Rho GTPase effectors	Cellular projections	Chemotaxis	Cell adhesion molecules	Integrin receptors
ENAH	0.59	1.48	0.86		X		X	
EZR	2.85	2.11	1.69		X		X	
DIAPH1	1.6	1.73	2.03		X			
MYH9	0.77	1.47	1.13		X	X	X	X
MYL10	0.21	0.76	0.45		X	X		
MMP2	0.66	0.98	0.85		X			
MMP14	0.63	1.06	0.62		X		X	
MSN	1.01	2.01	1.65		X		X	
PTK2	2.43	1.73	1.3		X		X	X
PXN	0.72	1.08	0.62		X		X	
RASA1	0.43	0.78	0.7		X		X	
RDX	0.59	1.49	1.03		X			
TLN1	0.79	1.67	1.16		X		X	
VCL	0.50	1.16	0.81		X		X	
VEGFA	1.21	0.82	0.88		X	X		
WIPF1	1.20	0.65	0.75		X	X		
TGFB1	0.78	1.45	1.71			X	X	
CAPN2	1.73	1.47	1.66				X	
CAV1	1.04	1.85	1.04				X	
CSF1	0.58	0.85	0.56				X	
ILK	0.98	1.75	0.91				X	X
ITGA4	0.23	1.38	0.83				X	X
ITGB1	0.34	1.28	0.66				X	X
ITGB3	0.72	1.25	1.04				X	X
MET	0.41	2.61	1.47					X
TIMP2	0.71	0.57	0.82					X

Tab.5b: Gene array analysis result. In the table are reported those genes that were expressed by HUVECs afetr 48 hours of exposure to different flow conditions. Gees that were downregulated beyond the 2-fold threshold as compared to static control are highlighted in green, gene that resulted upregulated are highlighted in red. Red boxes indicate those genes that were selected for RT-PCR. This table has been published in "Am. J. Physiol. Heart Circ. Physiol. 2015 Oct 23. doi: 10.1152/ajpheart.00098.2015".

5.C) Selected genes RT-PCR

5.C1) RT-PCR

Following exposure to flow or static control, total RNA was extracted from HUVECs using Trizol reagent (LifeTechnologies) according to the manufacturer's instructions. Contaminating genomic DNA was removed by RNase-free DNase (Promega, Milan, Italy) for 1h at 37°C. Two μg of purified RNA was reverse transcribed using a mix of random-examers/oligoT and 200U of SuperScript II RT (Invitrogen) for 1h at 42°C. No enzyme was added for reverse transcriptase-negative controls. To amplify cDNA, TaqMan Universal PCR Master Mix (Applied Biosystems, Monza, Italy) was used according to the manufacturer's instruction and inventoried TaqMan assays of hCDC42 (Hs00918044_g1), hITGA4 (Hs00168433_m1), hPLD1 (Hs00160118_m1) and hRASA1 (Hs00963554_m1) probe and an endogenous control (hHPRT1 Hs99999909_m1 FAM/MBG) probe. The PCR was performed on a 7300 Real Time PCR System (Applied Biosystems), as previously described (393, 394). After initial hold for 2 min at 50°C and for 10 min at 95°C, the samples were cycled 40 times at 95°C for 15 s and 60°C for 60 s to reach the plateau. The ΔΔCt technique was used to calculate cDNA content in each sample using the cDNA expression in static HUVECs as a calibrator.

5.C2) Results.

Among the four genes that were selected, expression of three of them was found to be significantly increased by the REC_A and REC_B WSS waveforms. In particular, PLD1 mRNA expression was 0.69±0.32, 1.71±1.16 and 2.17±0.54 in HUVECs exposed to PUL_V, REC_A and REC_B respectively compared to HUVEC kept in static conditions 1±0.1 (figure 60A). ITGA4 levels were 0.43±0.3, 2.36±0.71 and 1.51±0.48

in HUVEC exposed to PUL_V, REC_A and REC_B respectively compared to the static control 1±0.3 (figure 60B). RASA1 mRNA expression levels were 0.66±0.31, 1.63±1.11 and 2.1±0.51 in HUVEC exposed to PUL_V, REC_A and REC_B respectively as compared to the static control 1±0.31 (figure 61A). Finally CDC42 mRNA expression levels were 1.28±0.29, 1.75±0.87 and 0.98±0.14 fold increased in HUVEC exposed PUL_V, REC_A and REC_B respectively compared to the static control 1±0.35. These levels were not statistically different (figure 61B).

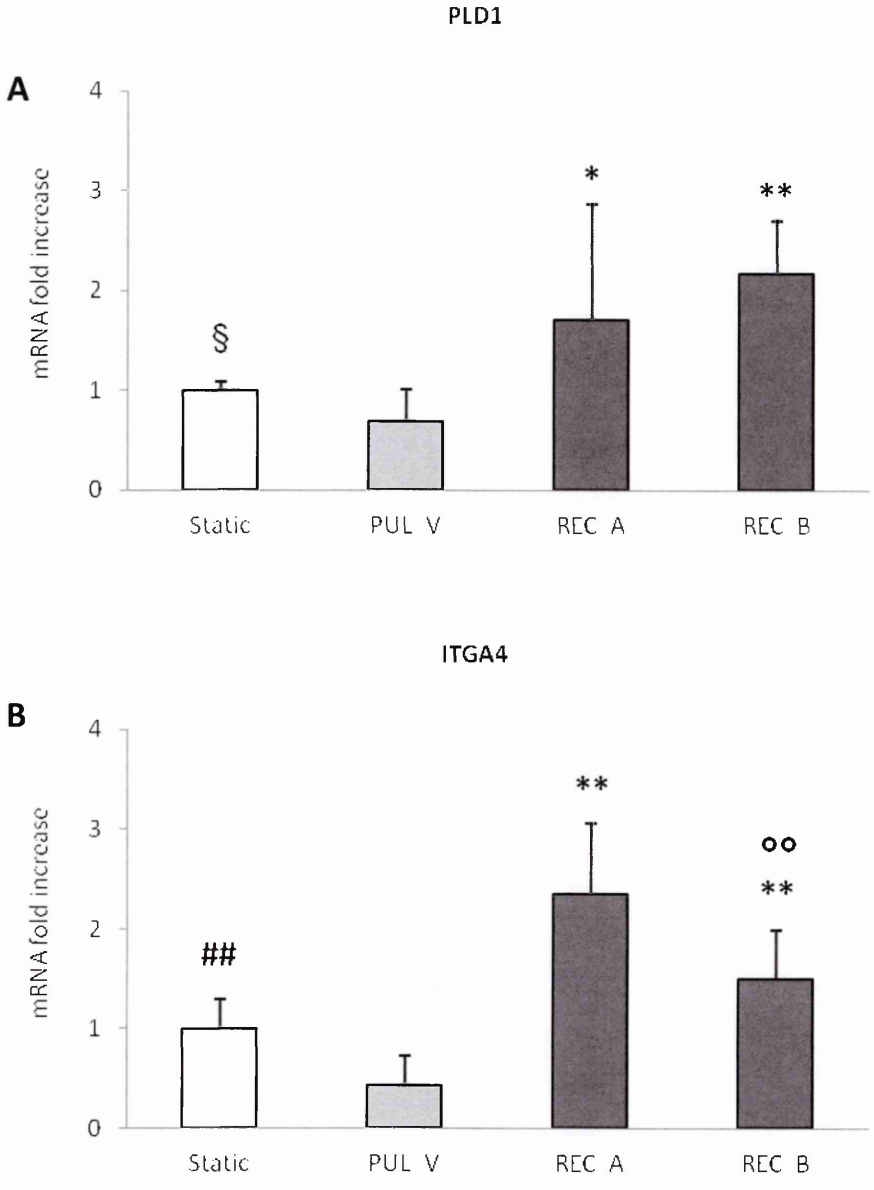

Fig.60: A) PLD1 mRNA expression elicited by different culture conditions. § $p < 0.01$ vs. REC_B, * $p < 0.05$ vs. PUL_V and ** $p < 0.01$ vs. PUL_V. B) ITGA4 mRNA expression elicited by different culture conditions. ## $p < 0.01$ vs. REC_A, ** $p < 0.01$ vs. PUL_V and ^{oo} $p < 0.01$ vs. REC_A. This image has been published in "Am. J. Physiol. Heart Circ. Physiol. 2015 Oct 23. doi: 10.1152/ajpheart.00098.2015".

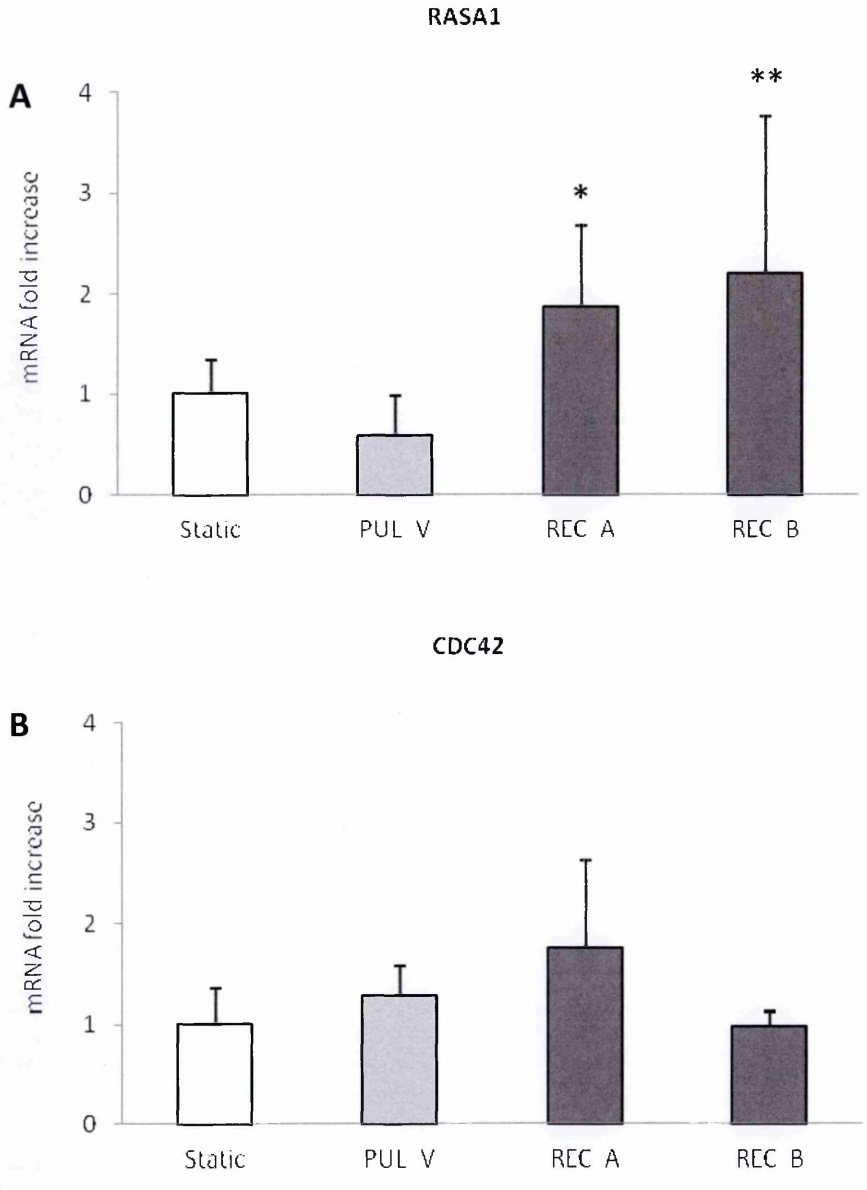

Fig.61: A) RASA1 mRNA expression elicited by different culture conditions. * $p < 0.05$ vs. PUL_V and ** $p < 0.01$ vs. PUL_V. B) CDC42 mRNA expression elicited by different culture conditions. No statistical differences were found. This image has been published in "Am. J. Physiol. Heart Circ. Physiol. 2015 Oct 23. doi: 10.1152/ajpheart.00098.2015".

5.D)Discussion

KLF2 mRNA expression of HUVECs was differently elicited by tested flow conditions. As expected (260, 395), both PUL_A and PUL_V waveforms induced HUVECs up-regulation of KLF2 mRNA expression after 48 hours of flow exposure (figure 59). PUL_A KLF2 levels where even higher despite a reduced spatial organization. This up-regulation was significant respect to REC_A, REC_B and static conditions that showed similar KLF2 expression. KLF2 has been deeply investigated by several authors and its protective function in ECs relies on the anti-inflammatory, antithrombotic, antioxidant and anti-fibrotic effects (396) (146) (397).

We further performed the gene assay analysis in order to quantify the mRNA expression of genes involved in cytoskeletal remodeling and cell motility that were potentially regulated by different WSS waveforms (tables 5a and 5b). Rho GTPases (RhoA, Rac1) mRNA resulted not differentially expressed by HUVECs exposed to 48 hours of different stimuli. The downregulation of these proteins, after the initial transitional activation, is consistent with previous studies and may indicate that the long-term effect of WSS-induced cytoskeletal conformation could rely others signals (398).

Despite no statistical significance can be derived from this evaluation, it provides much information in a time/cost effective manner. To further verify these results and to provide the statistical significance, we quantified the selected genes with traditional RT-PCR. With this aim we further selected 4 genes involved in cell motility and differentially expressed by HUVECs exposed to different stimuli. We verified that PLD1, RASA1 (coding for p120 RasGAP), ITGA4 but not CDC42 levels were statistically increased after 48 hours of exposure to REC_A and REC_B stimuli (figures 60 and 61). This up regulation has potential detrimental effects on ECs.

PLD1 gene codes for phospholipase D1, an enzyme known to mediate phosphatidylcholine (PC) to the second messenger signalling lipid phosphatidic acid (PA) (399). The physiological significance of PLD activation is not well understood, but, as shown in figure 62, it has been implicated in mitogenesis, cytoskeletal reorganization, chemotaxis, protein trafficking and secretion (462). Despite some controversies linked to the strategy used to block PLD activity, a differential role has emerged for PLD1 and PLD2 the two most common mammalian isoforms of PLD (400). PLD2 shows a higher activity and it localized at the cell membrane while PLD1 has a lower activity and is generally localized to intracellular compartments (401). PLD1 however can be activated depending on the several stimuli and participates in vWF secretion (402). vWF is a potent pro-coagulant agent and an inducer of SMCs non-canonical activities (403).

ITGA4 gene codes for integrin α4 or CD49d, a protein that, together with integrin β1 forms the Integrin alpha4beta1 (Very Late Antigen-4, VLA4) dimer (404). VLA4 is expressed in monocytes and causes adhesion to adhesive molecule VCAM expressed by the endothelium promoting monocyte arrest and transendothelial migration. CD49d however can be expressed also in ECs. Localization of CD49d phosphorylation inhibits the assembly of CD49d-paxillin–Arf-GAP complex at the driving edge of migrating cells imposing a spatial restriction on Rac activation and leading to an adhesion-dependent activation of Rac. As shown in Figure 63, a previous study showed that localized phosphorylation of CD49d control WSS-induced EC alignment (405). Within 5 minutes of exposure to physiological level of WSS a PKA-dependant phosphorylation of CD49d in the downstream edge of microvascular EC promotes localized activation of Rac1 and cytoskeletal alignment and cell elongation. According to the authors CD49d informs the cell about the direction of the flow (406).

We observed no alignment or elongation in EC exposed to both REC_A and REC_B WSS profiles and that elongated EC exposed to PUL_V have significant lower level of ITGA m-RNA. The upregulation of this gene could be related to a continuous attempt of the cell to establish a preferential direction for elongation and alignment that is prevented by reciprocating flows.

RASA1 is the gene coding for Ras GTPase activating protein 1 (p120-RasGAP). This protein is traditionally considered protective for endothelium since it showed to inhibit Ras activity by hydrolysis of GTP to GDP, and to couple with p190-RhoGAP to form an integrin-activated membrane bound complex that can block Rho activity (Figure 64) (314). These two functions seem to be opposed to detrimental effects induced by oscillating WSS in EC. However, since persistent RASA1 upregulation was not elicited by PUL_V, we hypothesis that ECs up-regulate this gene to limit RhoA activity despite a lack in cytoskeletal reorganization and cell elongation. A possible upstream event that can cause EC RASA1 regulation is MET signalling. MET alternatively induces both activation and quiescence in EC. Physically associate amplifier and co-receptor such as GRB2-associated-binding protein 1 (GAB1) can modulate MET signalling strength, duration and versatility (407). GAB1 deactivation involves the tyrosine phosphatase SHP2, which dephosphorylates the p120-RasGAP binding site on GAB1 and prevents the recruitment of p120 RasGAP (Figure 64). Interestingly we found that MET was upregulated by REC_A and REC_B. Finally, miRNA-221/222 and miRNA-132 have been shown to be shear stress sensitive and to limit RASA1 and p120-RasGAP function respectively (463-466). To our knowledge, no previous data are available on the WSS-induced modulation of RASA1 expression. Further studies on the spatial and temporal regulation of flow-induced RASA1 and p120

RasGAP regulation are required to elucidate the role of this protein in EC WSS transduction.

In conclusion we verified that reciprocating flows elicited a sustained expression of genes involved in cytoskeleton remodeling and cell motility as compared to that caused by PUL_V. This up-regulation together with the not upregulated KLF2 expression indicate that cells exposed to reciprocating flows fails to functionally stabilize the morphology. The lack of stabilization may cause an altered endothelial permeability and reendothelization after AVF creation, leading to IH development.

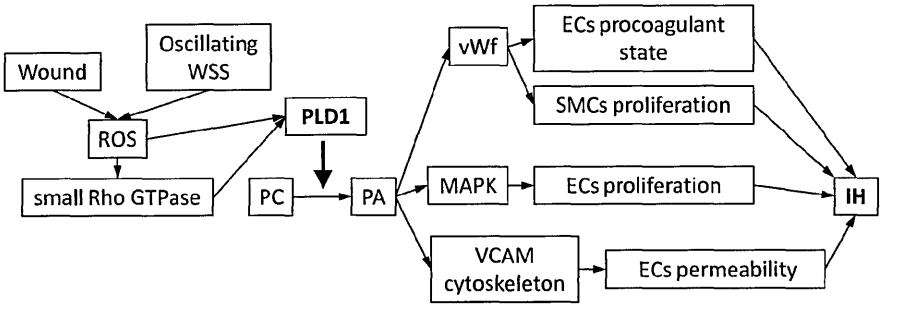

Fig. 62: Possible mechanism of flow-induced IH development induced by PLD1 upregulation. Abbreviations: ROS reactive oxygen species, GTPase guanosine triphosphate hydrolase enzyme, PLD1 phospholipase D1, PC phosphatidylcoline, PA phosphatidic acid, vWf von Willebrand factor, MAPK mitogen activated protein kinase, VCAM vascular cell adhesion molecule, ECs endothelial cells, SMCs smooth muscle cells and IH intimal hyperplasia (399, 402, 461, 462).

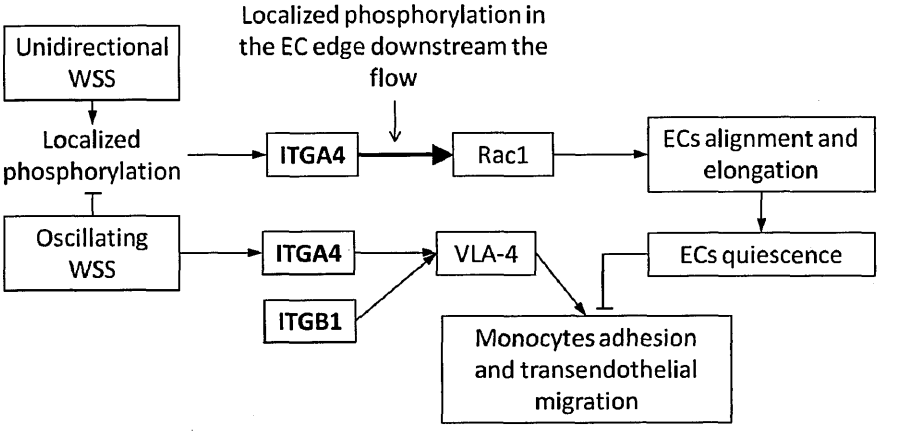

Fig. 63: Possible mechanism of flow-induced IH development induced by ITGA4 upregulation. Abbreviations: WSS wall shear stress, ITGA4 Integrin-alpha 4, ITGB1 Integrin-beta 1, EC endothelial cell and VLA-4 very late antigen 4 (404-406).

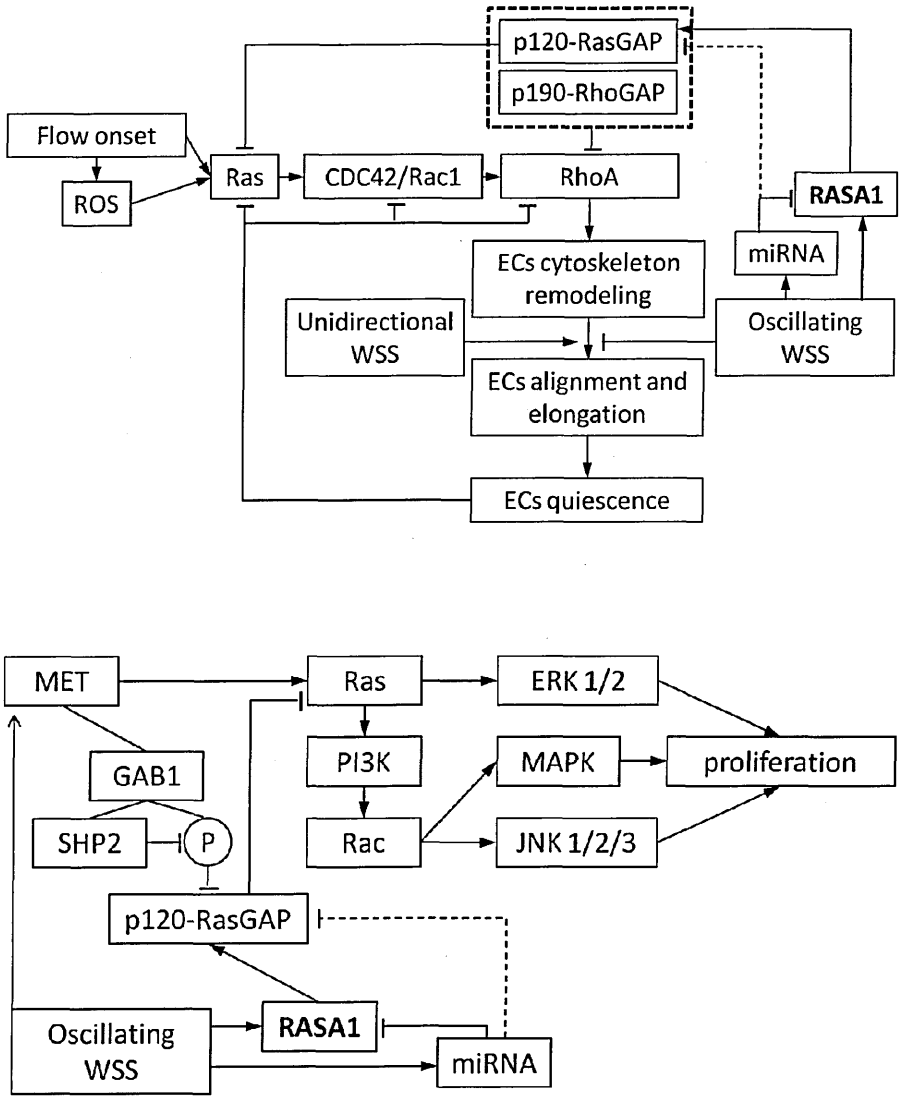

Fig. 64: The possible roles of Oscillating WSS in RASA1 pathway. Abbreviations: ROS reactive oxygen species, CDC42cell division control protein 42, RASA1 gene coding for RasGAP Ras GTPase activating protein, RhoGAP Rho GTPase activating protein, Rho A Ras homolog A, ECs endothelial cells, WSS wall shear stress, MET hepatocyte growth factor receptor, PI3K phosphatidylinositol-3-kinase, Rac Ras-related C3 substrate, ERK extracellular-signal-regulated-kinase, MAPK mitogen activated protein kinase, JNK JUN n-terminal kinase and mRNA micro-RNA (314, 407, 463-466).

5.E)Summary

Differential gene expression elicited by different WSS waveforms in HUVECs after 48 hours of exposure was quantified. The results showed that PUL_V and PUL_A elicited an upregulation of the protective gene KLF2. On the contrary reciprocating flows and especially REC_A did not affect KLF2 expression as compared to static conditions but caused an upregulation of mRNA expression of genes involved in cytoskeletal remodeling and cell motility. In addition, Rho GTPases (RhoA, Rac1 and CDC42) ECs expression resulted not affected by WSS after 48 hours of exposure. This further confirms that WSS onset induced a transient activation of these proteins. All these evidences indicate that reciprocating flows-induced morphological adaptations are not functional to ECs quiescence and that this sustained cell activation may be involved in vascular dysfunctions. A consequence of this different activation state induced by WSS may be an alteration of ECs paracrine signalling. Thus the production of cytokines known to be involved in the proliferative phase of IH, has been quantified. Methods and results are addressed in the next Chapter.

CHAPTER 6: Quantification of cytokine release in response to AVF-specific WSS waveforms

This Chapter addresses the production of cytokines involved in intimal hyperplasia development caused by different wall shear stress waveforms. As reported in Chapter 2, IL-6, IL-8 and MCP-1 showed to be involved in arteriovenous fistula stenosis possibly due their pro-inflammatory and chemoattractant properties. Here it is reported the average production of these cytokines and the production time course of those differently induced by the tested conditions.

6.A) Cytokines production elicited by WSS

6.A1) Milliplex assay

The production of MCP-1, IL-8, Il-6, IL-10 and IL-1β was compared between HUVECs exposed to flow or in a static control group by measuring concentration in samples of conditioned medium using a Milliplex Map Human kit (Millipore, Billerica, MA, USA), according to the manufacturer's instructions. Briefly, test samples were incubated with beads coated with specific antibodies overnight at 4°C, and with a biotinylated detection antibody for one hour at room temperature. The resulting mixture was finally incubated with a streptavidin phycoerythrin solution for 30 minutes at room temperature. A Bio-Plex 200 plate reader (Bio-Rad, Milan, Italy) was used to detect the fluorescence signal. All specimens were tested in duplicate to assess inter-assay variability. Cytokine concentration in the multiplex assay was calculated from calibration curves using recombinant protein as a reference and expressed as ng/h/10^6cells. Each condition was tested five times.

6.A2) ELISA

ELISA to evaluate MCP-1 and IL-8 produced by HUVEC was performed to investigate the time course of cytokine production in cells exposed to PUL_V, REC_A and REC_B or kept in static condition, during T_1 (0-12 hrs), T_2 (12-24 hrs), T_3 (24-36 hrs) and T_4 (36-48 hrs) periods of flow exposure. MCP-1 concentration was determined using a commercially available kit (Booster Technology Ltd, Fremont, CA, USA) according to manufacturer's instructions. IL-8 concentration was determined using a specific kit (Thermo Scientific) according to manufacturer's instructions. Infinite m200-pro (Tecan Group Ltd, Männedorf, Switzerland) was used to measure absorbance. All specimens were tested in duplicate to assess inter-assay variability. Cytokine concentrations in the multiplex assay were calculated from calibration curves using recombinant protein as a standard and expressed as ng/h/10^6cells. Each condition was tested five times.

6.A3) Results

The Milliplex assay results showed differential production of MCP-1 and IL-8 cytokines induced by different flow conditions (as shown in figure 65). In particular, MCP-1 production was 2.25±1.75, 2.49±1.14, 2.3±1.21, 3.37±1.6 and 4.72±1.88 ng/h/10^6cells under static conditions or by PUL_A, PUL_V, REC_A and REC_B WSS waveforms respectively. MCP-1 production elicited by REC_A was higher compared to PUL_A and PUL_V stimuli while production elicited by REC_B was statistically higher than PUL_A, PUL_V and static stimuli (figure 65A).

IL-8 production was 0.51±0.13, 0.73±0.49, 0.68±0.44, 1.26±0.76 and 1.31±0.7 ng/h/ 10^6cells under static conditions or by PUL_A, PUL_V, REC_A and REC_B WSS

waveforms, respectively. Both REC_A and REC_B waveforms induced a statistically significant increase in IL-8 production (figure 65B).

IL-6 production was 0.09±0.03, 0.08±0.05, 0.1±0.03, 0.1±0.04 and 0.12±0.04 ng/h/ 10^6cells under static conditions or by PUL_A, PUL_V, REC_A and REC_B WSS waveforms, respectively (figure 65C). None of the different conditions induced statistically significant differences in IL-6 production. Finally, production of IL-10 and IL-1β was undetectable in the medium for all conditions.

ELISA was performed on medium conditioned during the flow exposure experiments to evaluate the time course of cytokine production. Experiments included three different conditions (PUL_V, REC_A and REC_B) as well as a static control. The results showed a time-dependent production of both MCP-1 and IL-8.

HUVECs MCP-1 production (figure 66) elicited by the PUL_V WSS stimulus (0.87±0.61, 1.16±0.6, 1.26±0.63 ng/h/10^6 cells during T_1, T_2 and T_4 periods respectively) or under static conditions (0.83±0.61, 1.08±0.35, 2.44±0.94 ng/h/10^6 cells) was lower than those elicited by both REC_A (2.80±1.71, 2.30±0.6, 2.82±1.03 ng/h/10^6 cells) and REC_B (4.99±1.65, 3.07±2.74, 3.71±1.74 ng/h/10^6 cells) waveforms (figures 66A and B). MCP_1 production elicited by reciprocating WSS was higher compared to that induced by PUL_V. In particular the initial (T_1) increase elicited by the REC_B WSS waveform was statistically significant compared to that elicited by the PUL_V waveform or static conditions (REC_B vs. PUL_V and Static, $p<0.01$, $n=5$). It is of interest that MCP-1 production elicited under static culture conditions showed a tendency to increase at T_4.

HUVECs IL-8 production (figure 67) elicited by the PUL_V WSS stimulus (0.91±0.39, 1.2±0.66, 0.8±0.4, 0.63±0.31 ng/h/10^6 cells during T_1, T_2, T_3 and T_4 periods respectively) or under static conditions (0.67±0.26, 0.7±0.27, 0.92±0.47, 0.72±0.3

ng/h/10^6 cells) was lower than hat elicited by both REC_A (1.1±0.6, 1.61±0.95, 1.75±0.68, 1.88±1.17 ng/h/10^6 cells) and REC_B (1.45±0.79, 1.53±0.92, 1.78±0.6, 1.68±0.9 ng/h/10^6 cells) waveforms (figures 67A and B). In particular after an initial increase elicited by all WSS stimuli compared to the static control, REC_A and REC_B sustained long-term HUVEC IL-8 production compared to that measured in medium conditioned by HUVEC exposed to PUL_V waveform or maintained in static condition. The increase became statistically significant in medium collected during the T_4 period of flow exposure (REC_A and REC_B vs. PUL_V or Static, $p<0.01$ and $p<0.05$ respectively, n=5).

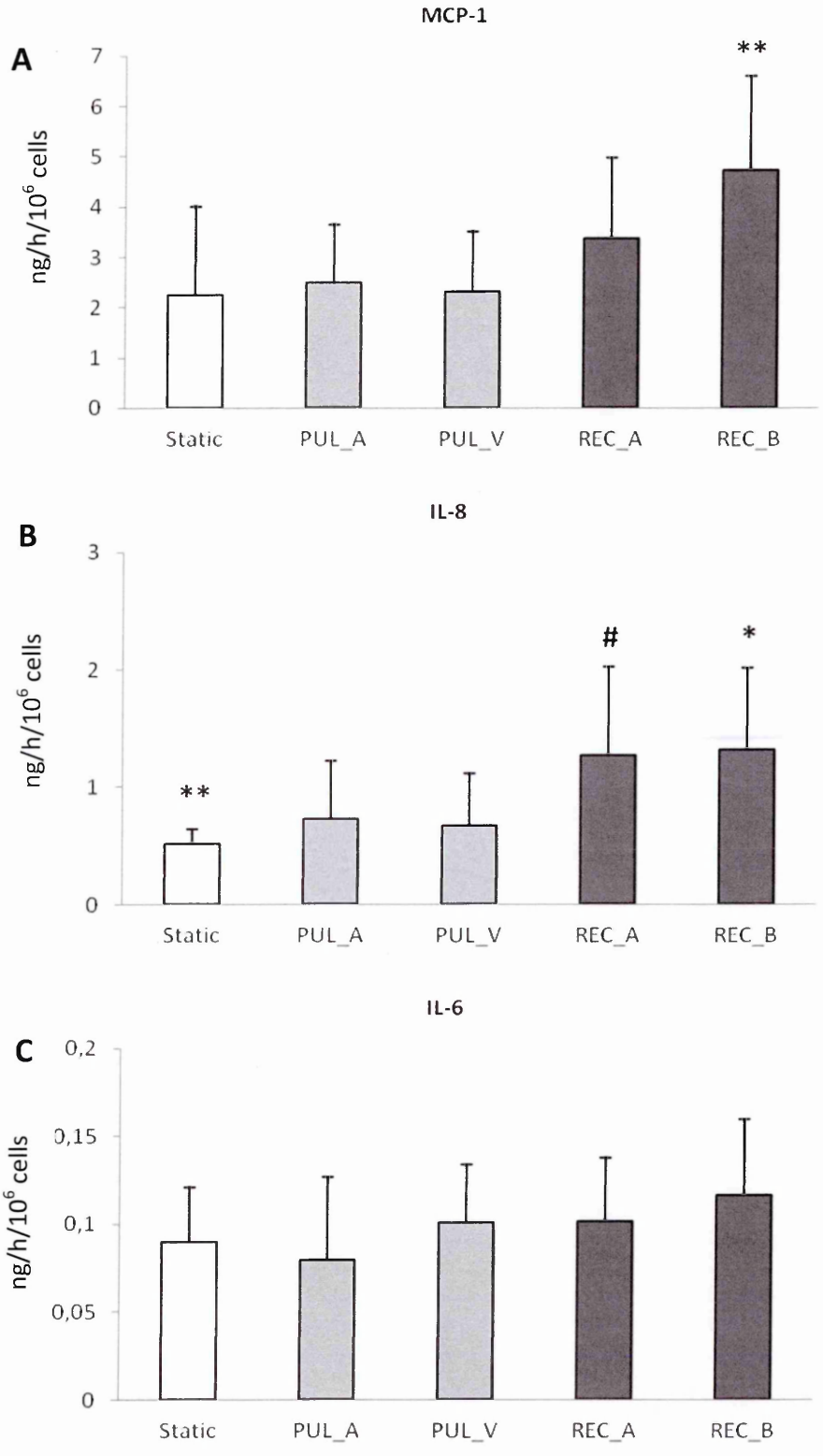

Fig.65: A) MCP-1 production induced by different culture conditions. ** p <0.01 vs. static, PUL_A and PUL_B. B) IL-8 production induced by different culture conditions. ** p <0.01 vs. REC_A and REC_B, # p <0.05 vs. PUL_V and * p <0.05 vs. PUL_A and PUL_V. C) IL-6 production induced by different culture conditions.

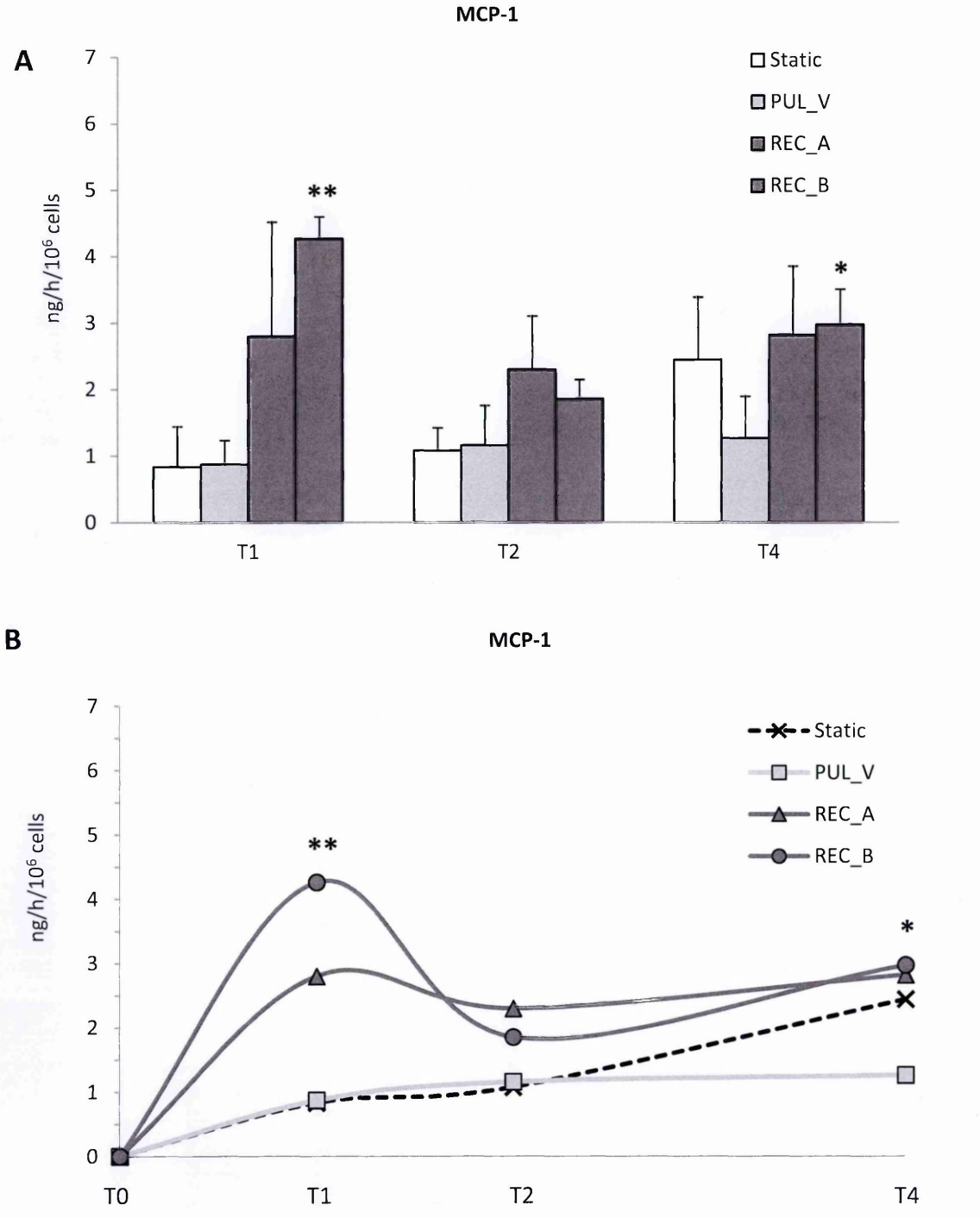

Fig.66: A, B) Time course of MCP-1 production during T_1, T_2 and T_4 periods of HUVECs flow exposure. ** $p < 0.01$ vs. static and PUL_V. This image has been partially published in "Am. J. Physiol. Heart Circ. Physiol. 2015 Oct 23. doi: 10.1152/ajpheart.00098.2015".

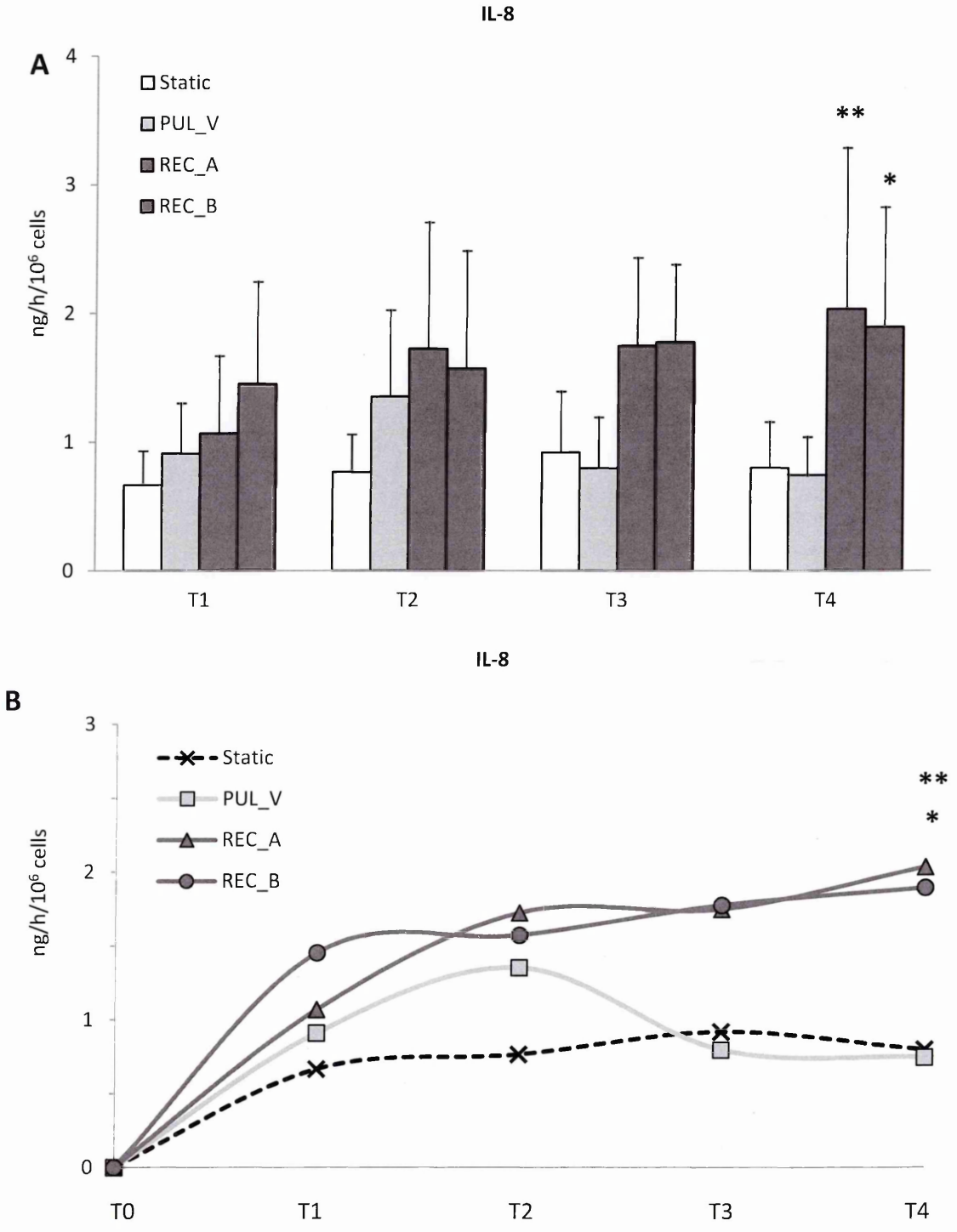

Fig.67: A, B) Time course of IL-8 production during T1, T2, T3 and T4 periods of HUVECs flow exposure. ** $p < 0.01$ vs. static and PUL_V, * $p < 0.05$ vs. static and PUL_V. This image has been partially published in "Am. J. Physiol. Heart Circ. Physiol. 2015 Oct 23. doi: 10.1152/ajpheart.00098.2015".

6.B) Discussion

Cytokines are deeply involved in vascular remodeling and inflammation. In particular we focused on cytokines known to be involved in vascular dysfunctions such as IL-6, IL-8, MCP-1, IL-1β and IL10.

Previous studies showed that IL-6, IL-8 and MCP-1 are produced during the proliferative phase of IH development (156). IL-6 is a pro-inflammatory cytokine that induce other inflammatory cytokines and matrix metalloproteinases. Studies focused on the atherosclerosis development have shown that IL-6 promotes endothelial dysfunction, the proliferation and migration of SMCs, the recruitment of inflammatory cells and the atherosclerotic plaques destabilization (408, 409).

MCP-1 and IL-8 exert their pro-inflammatory functions mainly by inducing monocytes adhesion to the endothelium and by promoting the transmigration of immune cells underneath the endothelium into the intima (142, 410).

Furthermore IL-1β is a potent vascular pro-inflammatory signals induced by infection, trauma or immunological challenge. The downstream effects of this protein include the modulation of endothelial inflammatory response (411,412).

IL-10 is an anti-inflammatory cytokine and it is considered vasculo-protective since it attenuates vessel superoxide levels during inflammation and attenuates expression and/or production of pro-inflammatory cytokines, which impair endothelial functions (413, 414).

In line with previous studies (260, 415), we found that WSS elicited an increased production of IL-8 and MCP-1 in a time dependant manner (figure 66 and 67). In particular MCP-1 levels resulted higher in culture medium conditioned by HUVECs exposed to reciprocating WSS. Both REC_A and REC_B caused an increased production of MCP-1 during the first 12 hours of exposure that resulted statistical

significant for REC_B. After this initial increase, MCP-1 levels return to values similar to those observed in medium conditioned by HUVECs exposed to PUL_V or maintained static. Furthermore, MCP-1 concentrations measured in medium derived from the last period, from 36 to 48 hours of flow exposure, showed a increasing tendency in medium derived from reciprocating flow exposure experiments as compared to that derived from PUL_V experiments, that again resulted significant for REC_B condition. It is worth to note that also HUVECs maintained in static conditions, displayed increased levels of MCP-1 respect to those measured in previous periods of flow exposure.

IL-8 showed a time course production very similar to that reported by Dai and colleagues, who investigated the effects of realistic WSS waveforms derived by carotid bifurcation areas differentially exposed to atherosclerosis. In particular all WSS waveforms onset caused the upregulation of IL-8 levels into culture medium. However, PUL_V elicited IL-8 production decreased in the last 24 hours of flow exposure, on the contrary, reciprocating flows sustained the increased production that was found even higher in the last 48 hours of HUVECs flow exposure. Finally IL-8 levels were statistically higher in the 36-48 hours period of the experiment.

Finally we found that IL-6 produced by HUVECs exposed to different culture conditions was similar and that neither IL-1β nor IL-10 was detectable in conditioned mediums. These results are probably caused by the limitations of our system, thus the lack of leukocytes and the absence of surrounding tissues, since in-vivo studies showed that these cytokines do participate to WSS- induced vessel remodeling and intimal thickening (408, 409, 416).

In conclusion our results clearly demonstrate that reciprocating flows sustained the ECs pro-inflammatory signals involved in IH development.

6.C) Summary

As reported in Chapter 2, ECs produce a plethora of signals that modulate inflammation and vascular tone after AVF creation. Based on these evidences we wondered if WSS, calculated in areas of AVF differentially exposed to IH development, diversely modulate ECs IL-1β, IL-6, IL-8, IL-10 and MCP-1 productions into the culture medium. Our results have shown that reciprocating flows elicited an increased production of IL-8 and MCP-1. IL-6 resulted not affected by different WSS stimuli and IL-1β and IL-10 production resulted below detection level in any conditions.

IL-8 and MCP-1 production time course showed that WSS onset induced an increase of these cytokines production that resulted higher in ECs exposed to reciprocating flows, as compared to static control. Furthermore reciprocating WSS sustained this higher cytokines production while pulsatile WSS-induced cytokine production is only transiently increased and returns to basal levels within 48 hours.

Beyond the chemoattractant functions, IL-8 and MCP-1 may be involved in the ECs paracrine proliferative signalling. To evaluate this aspect we cultured human smooth muscle cells with medium conditioned by HUVECs during flow exposure experiments as described in Chapter 4. The methods and results are reported in Chapter 7.

CHAPTER 7: Quantification of smooth muscle cell proliferation induced by HUVECs exposed to WSS stimuli.

In the previous Chapter it has been shown that reciprocating WSS stimuli caused an increased production of pro-inflammatory cytokines known to be involved in intimal hyperplasia development. Beyond the proinflammatory effects of these cytokines, they may also be involved in cell proliferation. In this Chapter the potential WSS-induced proliferative paracrine effect of ECs was evaluated by incubating human aortic smooth muscle cells with medium conditioned by HUVECs exposed to different flow waveforms as described in Chapter 4.

7.A) Smooth muscle cell proliferation

7.A1) Cell proliferation assay.

Human aortic smooth muscle cells (HAOSMCs, Cell Applications Inc. San Diego, CA) were grown in culture flasks in smooth muscle cell growth medium specifically designed by the manufacturer (Cell Applications) to promote attachment, spreading and proliferation. The cells were incubated at 37°C in a humidified 5% CO_2 atmosphere. HAOSMC were subcultured when the cells reached approximately 80% confluence. Cells at the fifth passage were used for proliferation experiments. Cell proliferation was measured by a 3-(4,5-dimethylthiazol-2-yl)-5-(3-carboxymethoxyphenyl)-2-(4-sulfophenyl)-2H-tetrazolium (MTS) assay. HAOSMC were seeded at a density of $8x10^3$ cells/well on 96-well plates. The cells were incubated for 24h with 100 µl of T_1 (0-12 hrs), T_2 (12-24 hrs), T_3 (24-36 hrs) and T_4 (36-48 hrs) conditioned medium collected from experiments of HUVEC exposure to PUL_V, REC_A and REC_B WSS waveforms as well as from HUVEC kept as static control. After incubation, 20 µl of MTS (1.9 mg/ml, Promega Italia S.r.l, Milano, Italy) were added into each well and incubated for 90 minutes at 37°C. HUVEC testing medium,

HAOSMC growth medium and HAOSMC basal medium were used as controls. Four wells per treatment were used for the assay. The plate was read spectrophotometrically by measuring the absorbance of the dye at a wavelength of 490 nm using Infinite m200-pro (Tecan Group Ltd, Männedorf, Switzerland). Spectrophotometric readings were normalized using HAOSMC cell-free media as a blank. Results were normalized with respect to absorbance of cells exposed to the medium from HUVEC static control and expressed in arbitrary units. Each condition was tested three times.

7.A2) Results

The MTS assay showed that medium conditioned after T_1, T_2, T_3 and T_4 periods of HUVECs maintained under static conditions induced no significant differences in proliferation of HAOSMCs after 24 hours of incubation (figure 68). HAOSMC proliferation induced by medium collected following PUL_V stimulation of HUVECs was significantly higher for the T_1 and T_2 periods compared to the T_3 ($p < 0.01$ vs. T_1 and $p < 0.05$ vs. T_2, $n=3$) and T_4 ($p < 0.01$ vs. T_1 and T_2) periods of flow exposure. Medium conditioned by HUVECs exposed to the REC_A waveform showed a statistically significant increase in HAOSMC proliferation at T_2 ($p < 0.01$ vs. all). Medium derived following the T_2 period of HUVEC exposure to the REC_B waveform resulted in proliferation that was higher but not statistically significant (figure 68).

Comparing proliferation induced by medium collected following the same period of exposure to different waveforms (figure 69) verified that the proliferation of HAOSMCs incubated with medium collected following the T_1 period of flow exposure was statistically lower only for SMCs exposed to medium derived from REC_A experiments compared to the static control. Medium collected following the T_2 period of REC_A and REC_B flows exposure and of static control, induced a significant

increase in SMC proliferation compared to PUL_V condition ($p < 0.01$ REC_A and REC_B vs. PUL_V, and $p < 0.05$ static vs. PUL_V). T_3 medium elicited proliferation is statistically lower in those conditioned by HUVECs exposed to PUL_V and REC_A conditions as compared to static control ($p < 0.01$ PUL_V vs. static, $p < 0.05$ REC_A vs. static). T_4 medium derived from REC_A and REC_B flow experiments and from static control, elicited much proliferation similar to that observed following exposure for period T_2 ($p < 0.01$ REC_A and REC_B vs. PUL_V, and $p < 0.01$ REC_A and PUL_V vs. static). Finally, the controls showed strong effects of medium serum content on SMC proliferation. HAOSMC medium without serum elicited decreased proliferation compared to other controls ($p < 0.01$ vs. all).

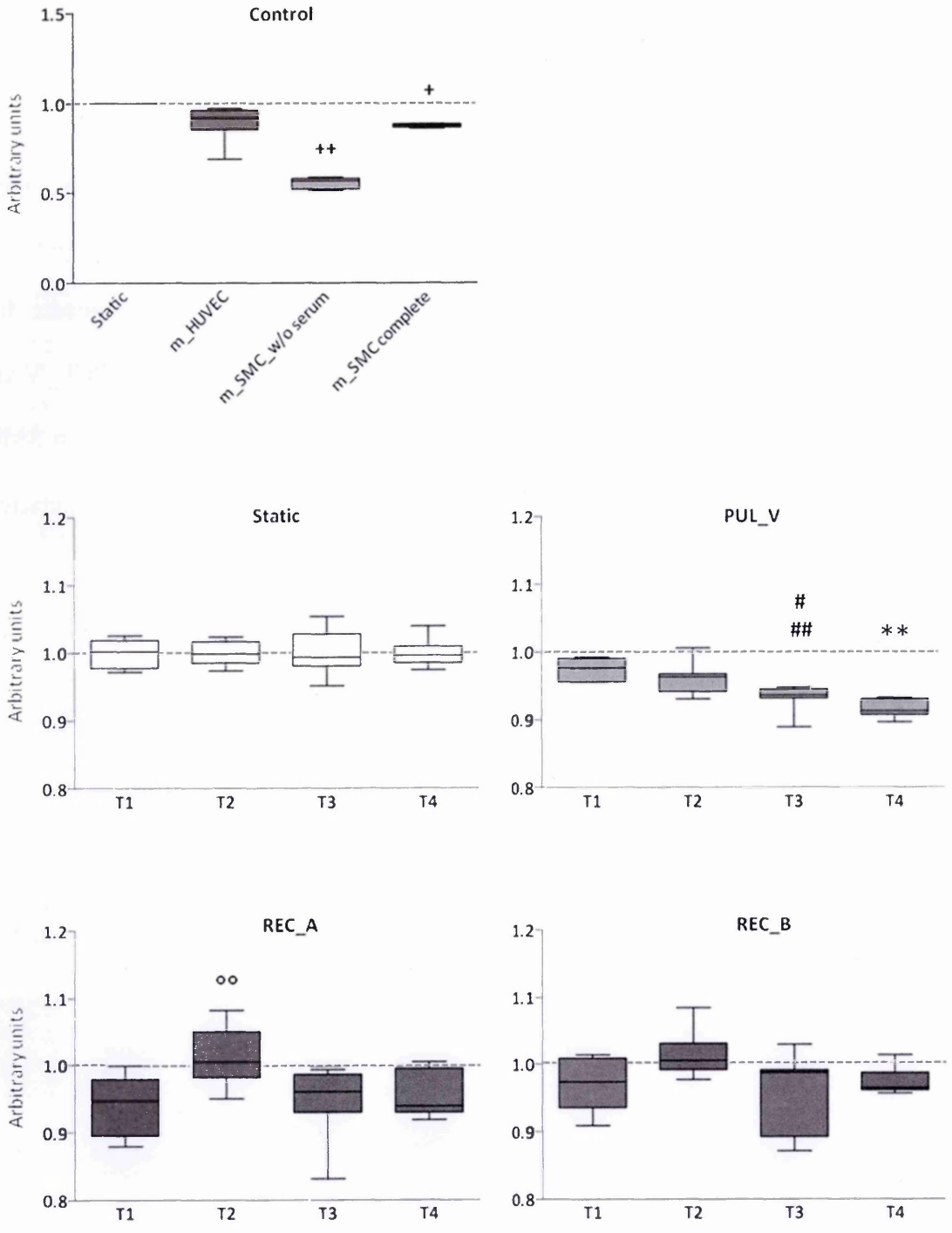

Fig.68: Comparison of HAOSMC proliferation elicited by medium conditioned by HUVEC exposed to different flow conditions. ++ $p < 0.01$ vs. all, + $p < 0.05$ vs. mSMC_complete, # $p < 0.05$ vs. T_2, ## $p < 0.01$ vs. T_1, ** $p < 0.01$ vs. T_1 and T_2, ^{oo} $p < 0.05$ vs. all.

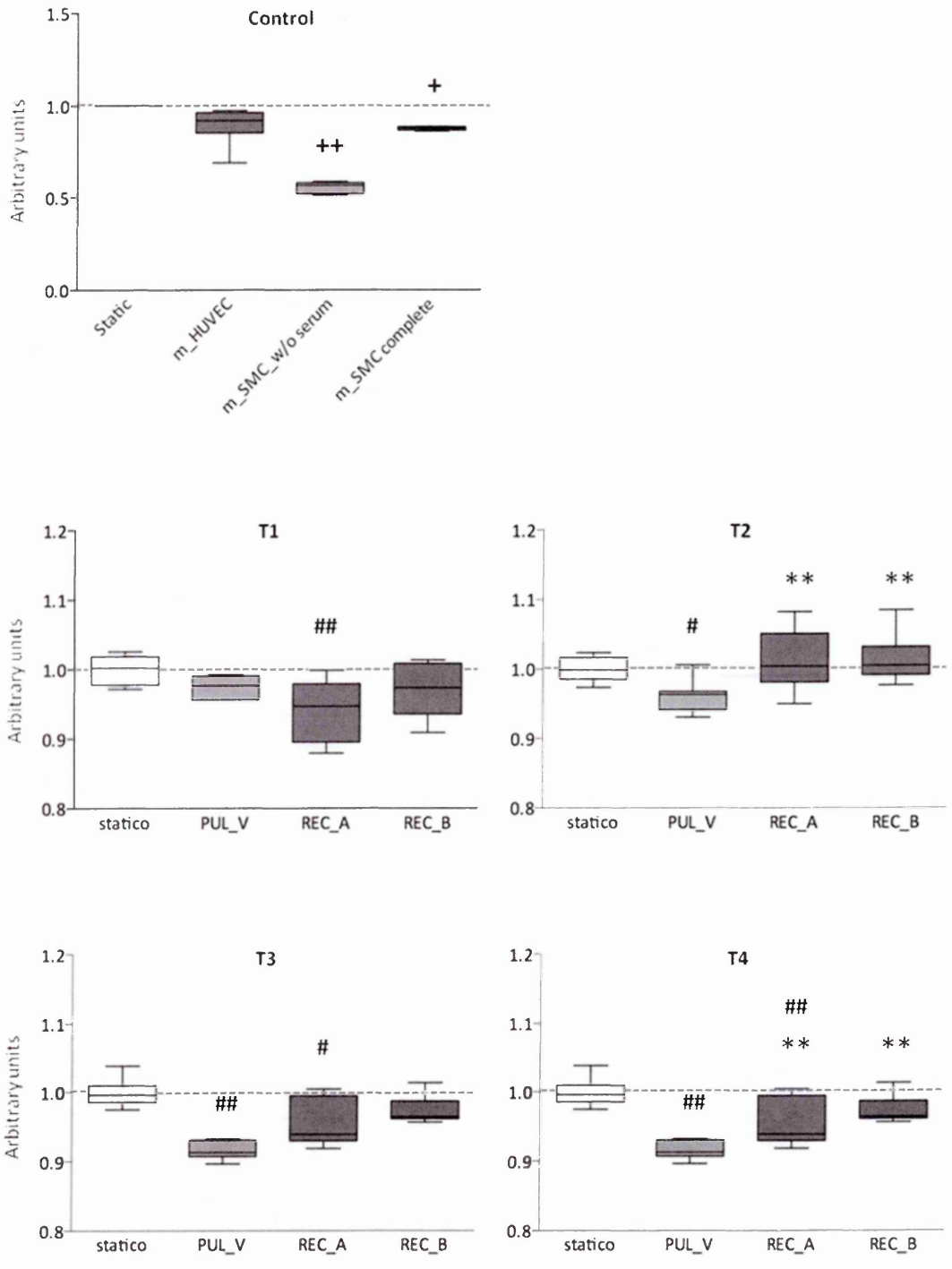

Fig.69: Comparison of HAOSMC proliferation elicited by medium conditioned by HUVEC exposed to different flow conditions. ++ p <0.01 vs. all, + p <0.05 vs mSMC_complete, ## p <0.01 vs. static, # p <0.05 vs. static and ** p <0.01 vs. PUL_V. This image has been partially published in "Am. J. Physiol. Heart Circ. Physiol. 2015 Oct 23. doi: 10.1152/ajpheart.00098.2015".

7.B) Discussion

Several studies have shown that ECs convert hemodynamic stimuli into biochemical signals that modulate vascular cell components functions (275, 417-419). After AVF creation, ECs synthesize and secrete many molecules that control proliferation, migration, phenotypic transformation and apoptosis of SMCs and fibroblasts that participate in wall remodeling in order to re-establish tissue integrity and physiological mechanical stress. In particular reciprocating or disturbed WSS has been shown to induce ECs to produce signals such as MCP-1, that have been related to SMC proliferation (420).

This chapter investigated the potential proliferative paracrine effects of ECs exposed to different WSS waveforms using an experimental set-up that is much more idealized than in-vivo (421, 422) or coculture models (423-425). However, despite the simplicity of the system, the results show that medium conditioned by HUVECs exposed to different flows has different effects on SMC proliferation. As expected (Figure 68), medium derived from the T_3 and T_4 periods of PUL_V experiments, elicited a lower SMCs proliferation compared to the previous periods. On the contrary, reciprocating WSS derived mediums elicited a different trend in SMCs proliferation respect to that induced by PUL_V derived mediums. SMCs proliferation induced by incubation with mediums collected following T_3 and T_4 periods of HUVEC exposure to reciprocating flows remained similar to that induced by medium collected following T_1 period. Interestingly, medium collected during the T_2 period of REC_A and REC_B flow exposure had an increased effect on proliferation that was statistically significant in SMCs incubated with medium derived from REC_A T_2 period (Figure 68).

By comparing the effects of medium collected during the same time periods for different experiments (Figure 69), the proliferation of SMCs incubated with REC_A

and REC_B medium collected during T_2 and T_4 periods, was significantly higher than proliferation elicited by medium conditioned during PUL_V flow exposure. Furthermore, medium conditioned by HUVECs maintained in static conditions and collected after the different periods, induced similar levels of SMC proliferation. It should be noted that, despite the lower content of MCP-1, the medium derived from T_3 and T_4 periods of static HUVEC cultures showed a higher proliferative potential compared to medium derived from flow exposure experiments and collected following the same periods (Figure 69). Finally, the increase in SMC proliferation induced by medium collected after static cultures, resulted statistically higher as compared to T_2, T_3 and T_4 periods of PUL_V flow exposure (Figure 69).

These results are in line with previous studies but are only partially consistent with the observed concentration of MCP-1, shown in Chapter 6. This indicates that the WSS waveforms modulated other proliferative molecules beyond MCP-1. Further studies are required to evaluate the production of other molecules, potentially induced by WSS and involved in SMC proliferation, such as platelet-derived growth factors, insulin growth factor and transforming growth factor.

In conclusion, despite the experimental conditions of SMCs culture are very different from the physiological environment, it was found that reciprocating flows induced HUVECs to produce paracrine signals that elicited a limited but statistically significant higher proliferation rate in SMCs.

7.C) Summary

In this chapter it has been shown that reciprocating flows elicited HUVEC production of paracrine signals that caused SMCs to proliferate more than their counterparts incubated with medium conditioned during PUL_V exposure. The increase

in proliferation resulted in a limited but statistically significant change for medium collected at the end of T_2 and T_4 periods of flow exposure. Furthermore, HUVECs maintained in static conditions showed even higher proliferative paracrine signal production that should be further investigated. This evidence further confirms the role of reciprocating WSS in inducing vascular cell proliferation and thus intimal hyperplasia.

CHAPTER 8: CK1α and CCR2 expression following exposure to AVF-specific WSS waveforms

Several pathways have been related to intimal hyperplasia development but their possible WSS-induced modulation has not been investigated. Casein kinase alpha-LS has been shown to participate in vascular cell proliferation by inducing the hydrogen peroxide mitogenic pathway. Furthermore, despite the fact that the MCP-1/CCR2 axis is central to inflammation and monocyte recruitment, adhesion and transmigration at endothelial level, the possible endothelial autocrine role of CCR2 and its relationship with WSS remain largely unknown. This Chapter addresses this by focussing on the possible differential induction of the casein kinase alpha family and CCR2 mRNA expression induced by different WSS waveforms in HUVECs, as described in Chapter 4.

8.A) CK1α and CCR2 mRNA expression

8.A1) HUVEC flow exposure and Il-1β stimulation.

HUVEC were seeded as described in paragraph 4.C1 and exposed to different WSS stimuli as described in 4.E1 paragraph. A single HUVEC culture was also incubated with EM added with 20ng/mL IL-1β (Sigma). This culture was maintained in static conditions and medium was replaced every 12 hours.

8.A2) RT-PCR.

Total RNA was extracted from HUVEC using Trizol reagent (LifeTechnologies) according to the manufacturer's instructions. Contaminating genomic DNA was removed by RNase-free DNase (Promega) for 1h at 37°C. Two μg of purified RNA was reverse transcribed using a mix of random-examers/oligoT and 200U of SuperScript II RT (Invitrogen) for 1h at 42°C. No enzyme was added for reverse transcriptase-negative controls.

The TaqMan Universal PCR Master Mix (Applied Biosystems) was used to amplify cDNA according to the manufacturer's instruction and inventoried TaqMan assays of Casein Kinase1 alpha1 (CSNK1A1 Hs00793391_m1) C-C chemokine receptor type 2 (CCR2 Hs00356601_m1), and a endogenous control (hHPRT1 Hs99999909_m1 FAM/MBG probe). The PCR was performed on a 7300 Real Time PCR System (Applied Biosystems). The amplification profile consisted of 2 min at 50°C for and 10 min at 95°C, the samples were cycled 40 times at 95°C for 15 s and 60°C for 60 s. The ΔΔCt technique was used to calculate cDNA content in each sample using the cDNA expression of control HUVECs as calibrator. Each condition was tested 5 times with the exception of CCR2 expression by HUVEC incubated with Il-1β that was tested once.

8.A3) Results.

RT-PCR data showed that CK1-α was not up-regulated by reciprocating WSS. Surprisingly only PUL_A induced a significant up-regulation with respect to other conditions (figure 70A, ** $p < 0.01$ vs. static, PUL_V and REC_A).

CCR2 mRNA levels were at the lower limit of detectability with no differential expression in HUVECs exposed to different flow conditions or maintained static (figure 70B). Adding IL-1β to culture medium was also shown to increase the level of HUVEC CCR2. However, this test was performed only once and thus no statistical analysis data are available.

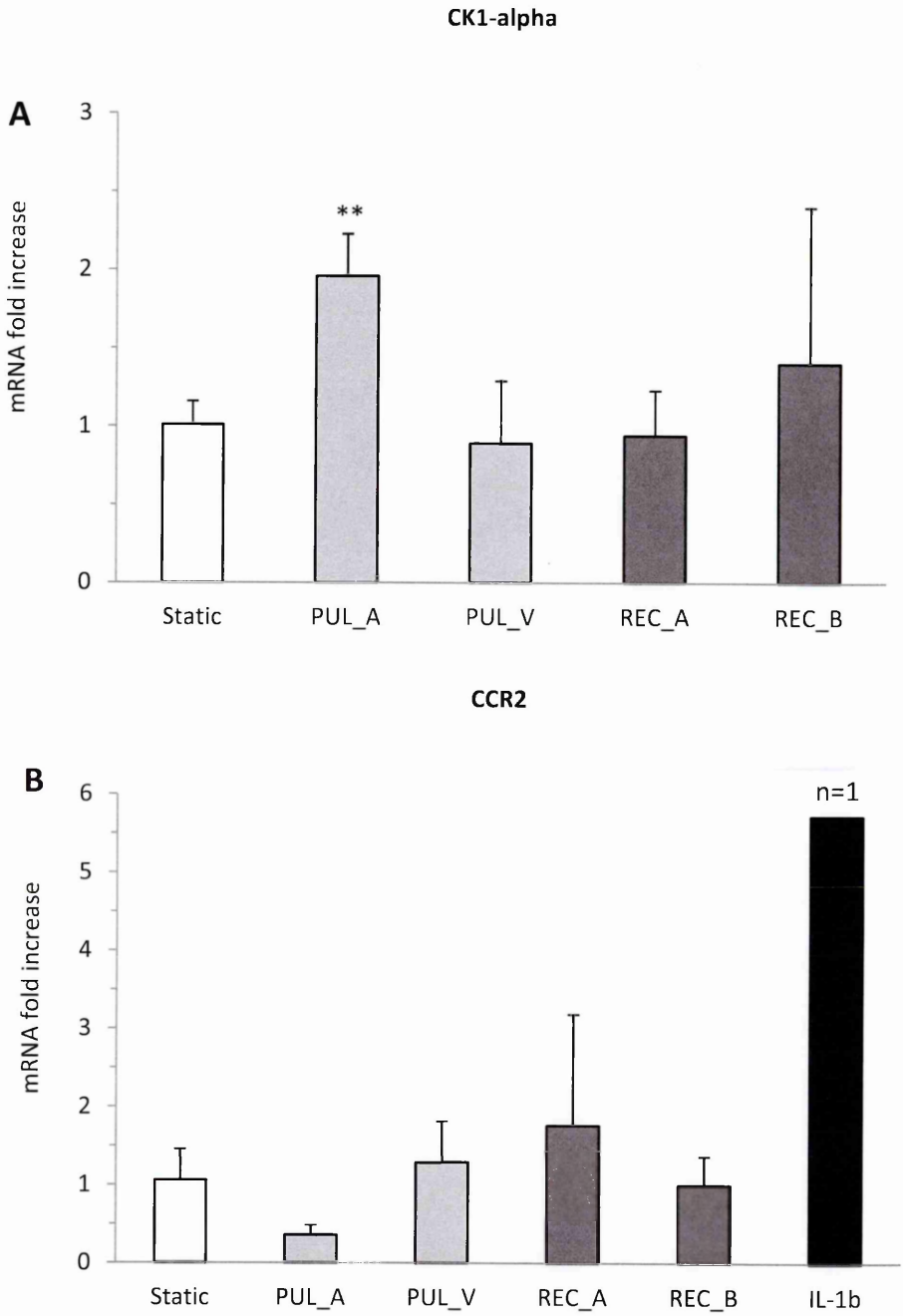

Fig.70: A) CK1α mRNA expression elicited by different flow conditions, ** $p < 0.01$ vs. static, PUL_V and REC_A. B) CCR2 mRNA expression elicited by different flow conditions or by incubation with 20 ng/mL of IL-1β .

8.B) CCR2 visualization and quantification

8.B1) IL-1β incubation and flow exposure experiments

HUVECs were seeded as described in paragraph 4.C1. In the first experiment two HUVECs cultures were incubated in EM with or without addition of 20ng/mL of IL-1β (Sigma). This culture was maintained under static conditions and medium was replaced every 12 hours.

A second experiment incubated two samples of HUVECs with 20ng/ml of IL-1β, one was kept under static conditions, the other was exposed to the REC_B WSS waveform as described in paragraph 4.E1. A third cell culture was maintained under static conditions and no IL-1β was added. Culture medium was replaced every 12 hours.

A third experiment reduced the time of HUVEC incubation with IL-1β and the time of flow exposure. Three cell culture monolayers were seeded. One culture was maintained under static conditions without the addition of IL-1β and used as negative control, the second was maintained static but culture medium was added with 20ng/mL of IL-1β and the third was incubated with 20ng/mL of IL-1β and exposed to the REC_B waveform as described in paragraph 4.E1. Culture medium of all cultures was replaced after 8 hours with EM without IL-1β. The experiment was ended after 24 hours. Contrast phase microscopy images were taken at the beginning and at the end of the experiment.

8.B2) Immunofluorescence staining

At the end the experiment the cell monolayer was fixed in 2% paraformaldehyde (Società Italiana Chimici) in 4% sucrose (Sigma) solution, for 10 minutes at room temperature. Cells were then permeabilized in 0.1% triton X-100 (Fluka) for 3 minutes and incubated in 3% BSA (Sigma) for 30 minutes at room temperature. HUVEC were incubated with goat anti-human CCR2 FITC (1:50 in 3% solution of BSA) overnight at

4°C. Counterstaining with DAPI (1 mg/ml, Sigma) for 20 minutes at 37°C was performed for cell nuclear staining. The slides were finally mounted with a fluorescent mounting medium (Dako Cytomation) and examined by ApoTome microscopy (Axio Imager.Z2, Carl Zeiss).

8.B3) CCR2 positive cells FACS analysis

Cells were detached from the culture plate by 3 minutes incubation with trypsin (EDTA trypsin 0.05%, Sigma) at 37°C and washed twice. Cells were then fixed with 2% solution of paraformaldehyde (Società Italiana Chimici, Rome, Italy) at 4°C. Cells were then permeabilized in 0.1% triton X-100 (Fluka) for 3 minutes and incubated in 0.5% BSA (Sigma) for 10 minutes at 4°C. Cell were washed twice with PBS buffer solution. Samples were incubated with FITC rabbit anti-human CCR2 (1:50, Santa Cruz Biotechnology, Inc, Dallas, TX, USA) for 30 minutes at 4°C. The sample was then suspended in 500 µL of PBS solution and analyzed with FACSCanto II system (BD Biosciences).

8.B4) Results.

In the first experiment we verified that high dose IL-1β induced an increased number of HUVECs positive for CCR2 (figure 71) compared to those not incubated with the cytokine (66% vs. 52%, figure 72). Furthermore, the presence of the stimulus induced also changed the HUVECs shape, which appears more elongated after 24 and 48 hours of stimulation (figure 73).

The presence of IL-1β affects also the HUVECs adhesion to the plate. In the REC_B flow exposure experiment, the repeated addition of the stimulus induced significant cell detachment at 24 hours with complete detachment after 48 hours (figure 74).

To overcome this problem the time of incubation of HUVECs with IL-1β was reduced to 8 hours (figure 75). This ensures the permanence of cells over the plate. After 24 hours of exposure to the REC_B WSS waveform the number of cells positive for CCR2 was the same as the static control (29.8% vs. 29.4%) and only slightly increased with respect to the negative control (20.6%) (figure 76). Interestingly, the intensity of the mean fluorescence was higher in the positive control respect to other conditions.

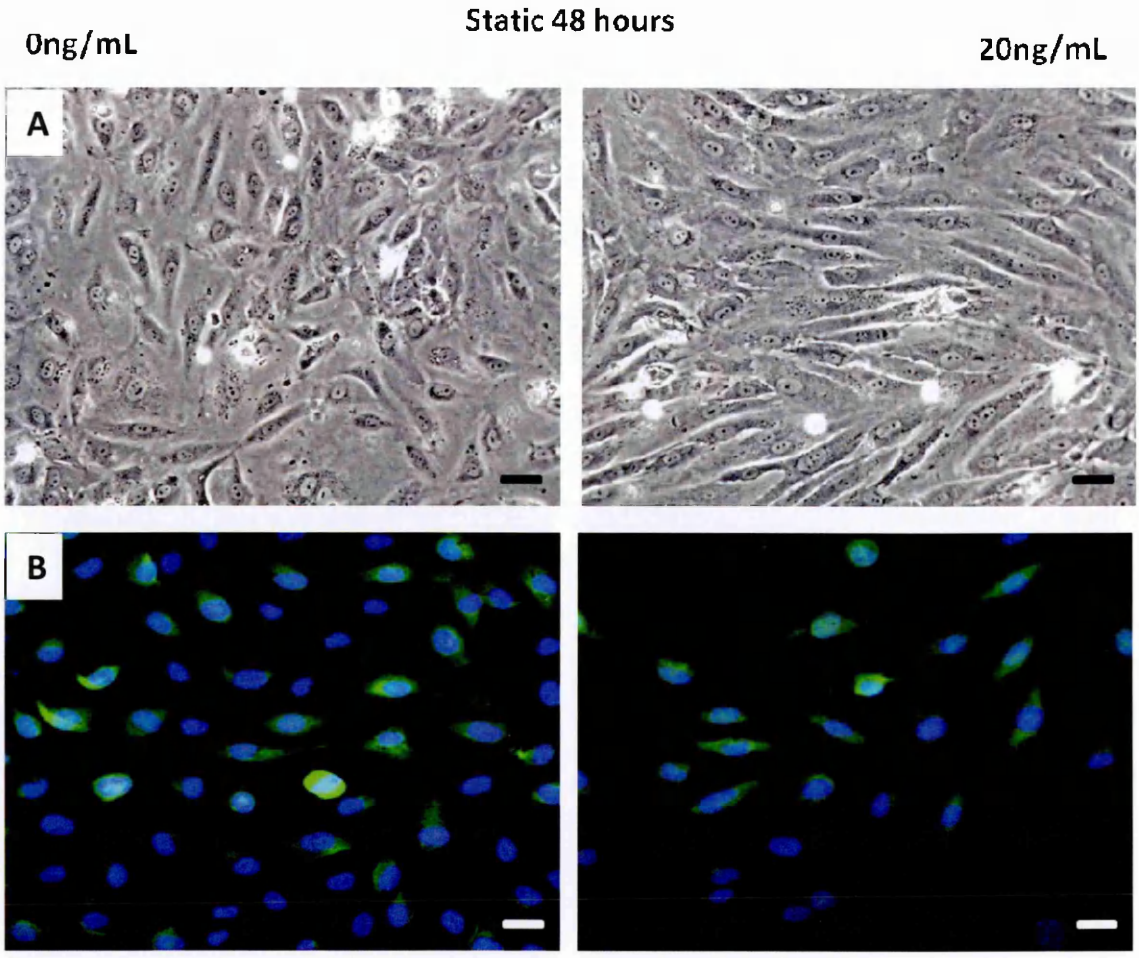

Fig.71: A) Contrast phase microscopy images of HUVECs treated with or without 20 ng/mL of IL-1β for 48 hours. Magnification 20x, scale bar 10μm. B) Immunofluorescence images of HUVECS treated with or without 20 ng/mL of IL-1β for 48 hours. HUVECs were stained for CCR2 (green) and nuclei (blue). Magnification 20x, scale bar 10μm.

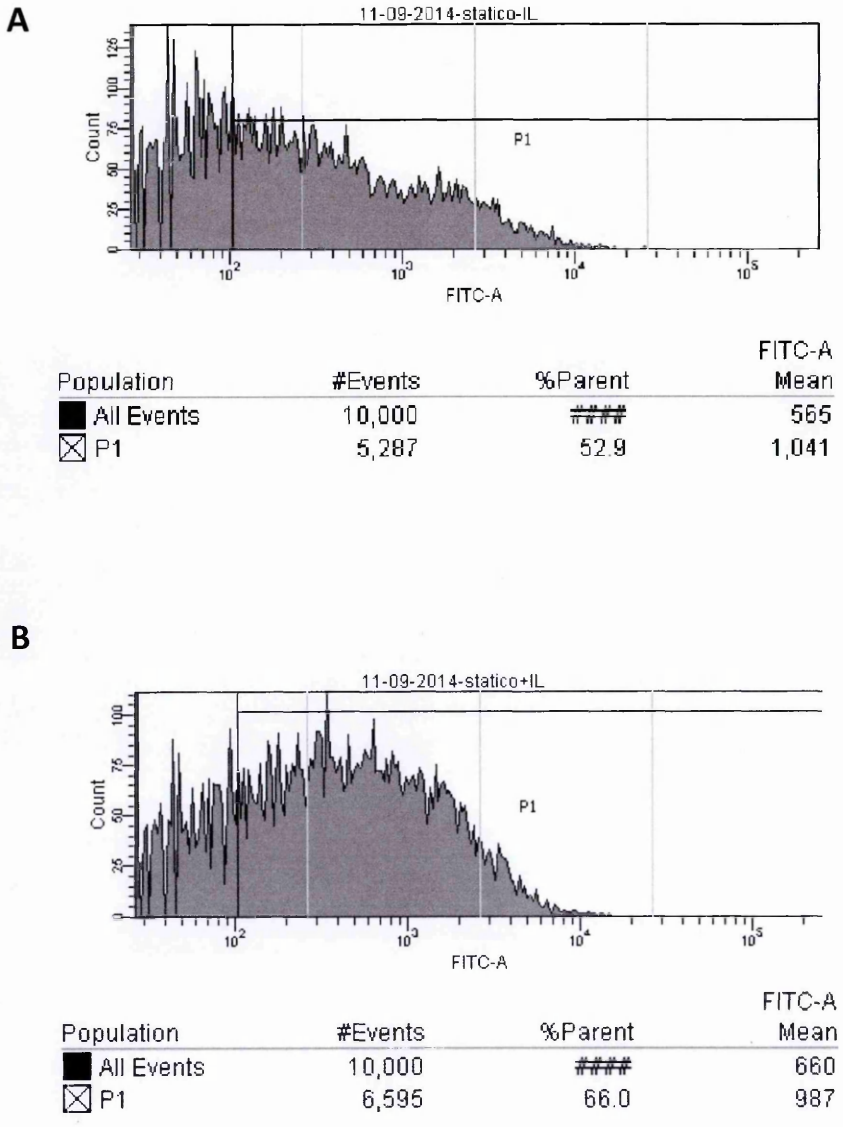

Fig.72: FACS analysis of CCR2 positive HUVECs. A) Basal level of CCR2 positive cells. B) Positive cells after treatment with 20 ng/mL of IL-1β for 48 hours.

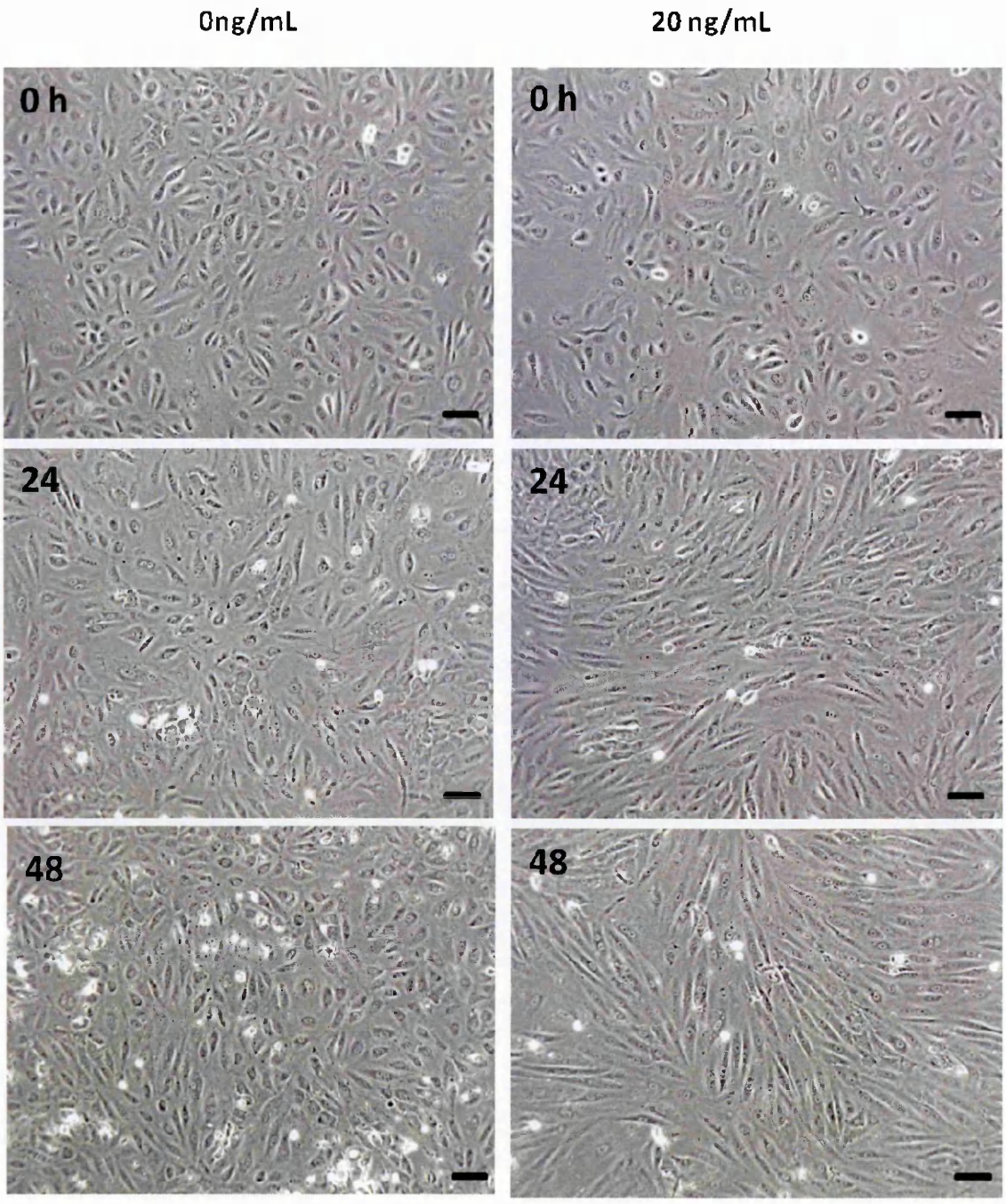

Fig.73: Contrast phase microscopy images of HUVECs treated with or without 20 ng/mL of IL-1β at 0, 24 and 48 hours of incubation. Magnification 10x, scale bar 20μm.

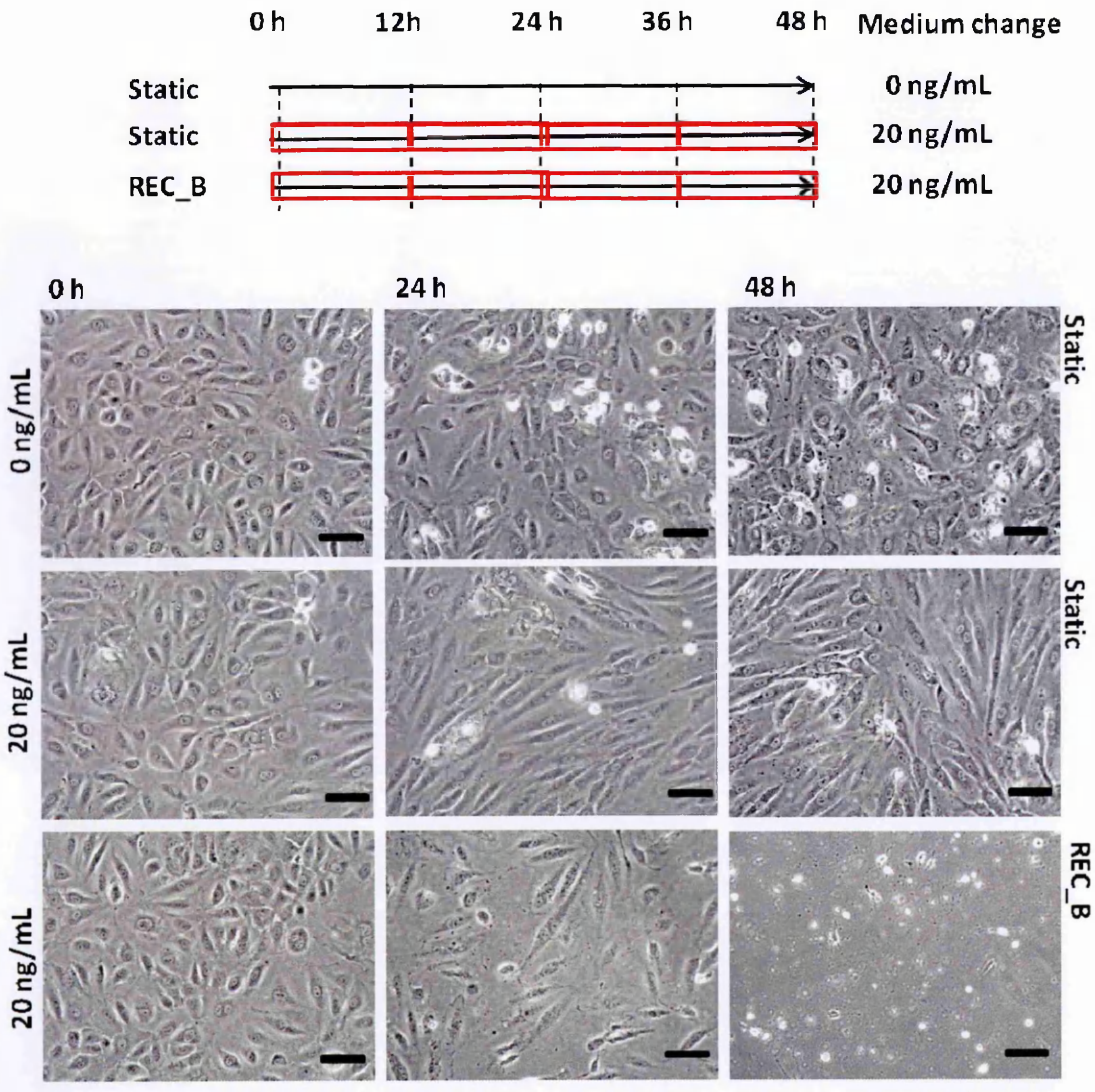

Fig.74: Experimental design and contrast phase microscopy images of HUVECs treated with or without 20 ng/mL of IL-1β and exposed to REC_B WSS profiles or maintained static for 48 hours.

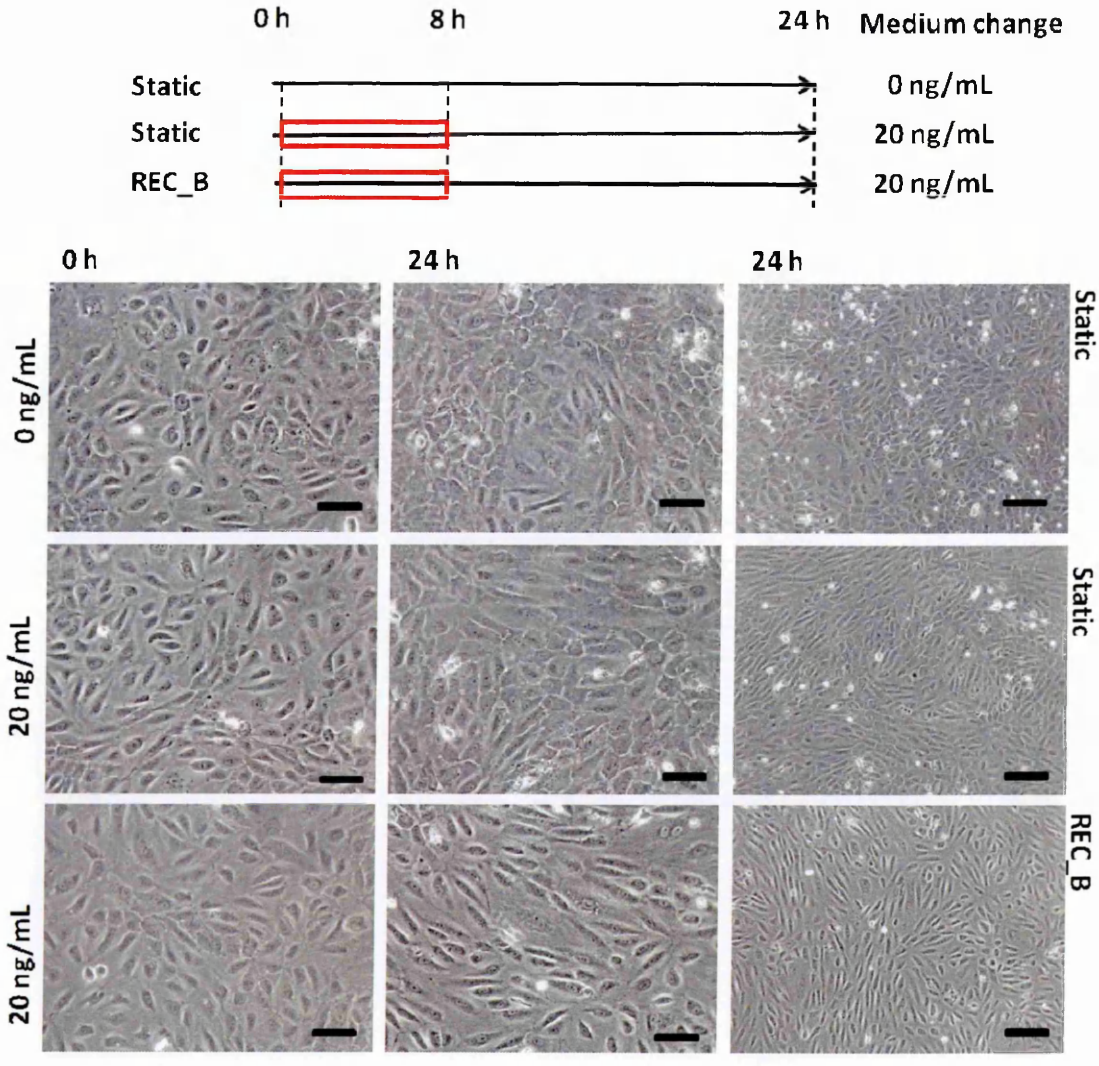

Fig.75: Experimental design and contrast phase microscopy images of HUVECs treated with or without 20 ng/mL of IL-1β for 8 hours and exposed to REC_B WSS profiles or maintained static for 24 hours.

Static 0 ng/mL

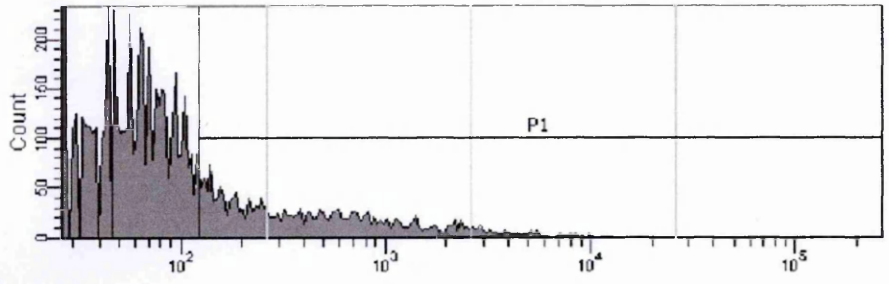

Population	#Events	%Parent	FITC-A Mean
All Events	10,000	####	195
P1	2,057	20.6	806

Static 20 ng/mL

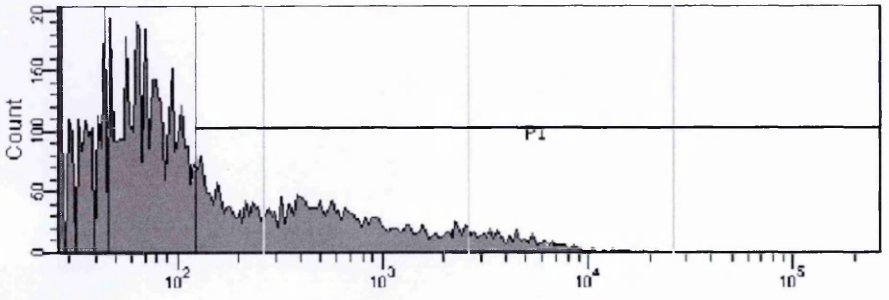

Population	#Events	%Parent	FITC-A Mean
All Events	10,000	####	361
P1	2,942	29.4	1,132

REC_B 20 ng/mL

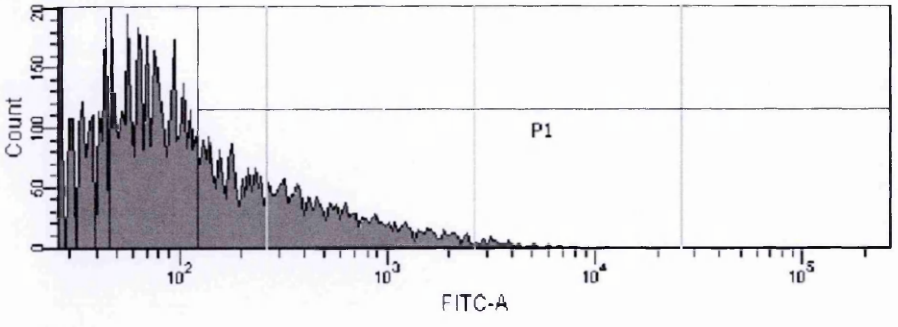

Population	#Events	%Parent	FITC-A Mean
All Events	10,000	####	193
P1	2,975	29.8	548

Fig.76: FACS analysis of CCR2 positive HUVECs. A) Basal level of CCR2 positive cells after 24 hours. B) Positive cells after treatment with medium added 20 ng/mL of IL-1β for 8 hours then incubated with medium not added with IL-1β. C) Positive cells exposed to 24 hours of REC_B WSS, cells were treated with 20 ng/mL of IL-1β for 8 hours, and then medium was replaced with medium not added with IL-1β.

8.C) Discussion

Despite their role in IH development (114,426), these results confirm that neither CK1α nor CCR2 mRNA levels were upregulated by reciprocating WSS (figure 70). The CK1 family is involved in numerous ECs stress-activated pathways. CK1αLS phosphorylation may promote H_2O_2-stimulated cell growth (113, 427). However cytosolic forms of CK1α (CK1α and CK1αS) play important roles in the inhibition of key proliferative signalling (428). Future studies could reveal a role for WSS in modulating CK1α isoforms (429, 430).

CCR2 is mostly investigated for its role as a MCP-1 receptor in monocytes (431). Its potential role in the EC autocrine pathway is generally addressed in cancer (432). ECs produce low levels of CCR2 mRNA that can be increased by incubation with IL-1β (433). The treatment however had dramatic effects on HUVECs resistance to WSS. To solve this issue we implemented a new protocol that successfully combined the effects of chemical and mechanical stimuli.

8.D) Summary

To assess the influence of different WSS waveforms in inducing CK1α and CCR2 in HUVECs, the mRNA expression of genes coding for these proteins was evaluated after 48 hours of exposure to different flow conditions as reported in Chapter 4. The results confirm that mRNA levels were not affected by different culture conditions compared to the static control. In particular CCR2 basal levels were very low and almost undetectable, in line with the literature. Furthermore, since IL-1β is known to induce CCR2 expression in HUVECs, a protocol was developed to successfully investigate the combined effects of this cytokine and WSS stimuli. However,

preliminary results showed that the REC_B profile did not change the expression of CCR2 elicited by stimulation with IL-1β.

CHAPTER 9: Conclusion and discussion

9.A) General conclusion

In order to stimulate ECs with highly unsteady WSS waveforms, a real-time controlled CPD system was designed and constructed. The system resulted in reproducible unsteady WSS stimulation of cell monolayer cultures. The compact design of the system and the removable engine allow the user to easily handle the CPD base under a laminar flow hood ensuring the sterility of cell cultures when inserted into the device or during culture medium changes. Furthermore, the device is sized to allow placement within a standard cell incubator to avoid the use of other components to control temperature and gas composition of the CPD environment.

The distribution of WSS generated by cone rotation on the culture monolayer surface was assessed by comparing results obtained with analytical and computational methods. The results showed a very good agreement between different approaches. The maximum time delay that occurs between the cone acceleration and the WSS variation in the tested waveforms was determined. These results led to definition of a threshold of 10 Hz for WSS frequencies correctly delivered at plate level in the CPD. Below this frequency threshold, the WSS is coherent at different plate radial positions and can be described as a function of the angular velocity (ω) calculated by equation [3].

In line with literature findings (260) it was verified that WSS waveforms derived from AVF areas generally protected from IH development, PUL_A and PUL_V, elicited HUVEC morphological adaptations that led to cells elongating and aligning with the flow direction. Furthermore, these waveforms caused an organized cytoskeletal remodeling where F-actin stress fibers were preferentially orientated in the flow

direction. In addition, the beneficial effect of pulsatile WSS stimuli was confirmed by the upregulation of KLF2, a transcription factor known to induce quiescence in ECs. On the contrary, HUVECs exposed to reciprocating WSS waveforms derived from AVF areas exposed to IH development, REC_A and REC_B, have shown no elongation nor alignment and a lack of cytoskeletal organization compared to HUVECs maintained in static culture. These reciprocating waveforms also failed to induce KLF2 mRNA expression but sustained the expression of genes involved in cytoskeleton reorganization.

To investigate the potential role of WSS in sustaining inflammation and promoting monocyte recruitment, the production of cytokines known to be involved in IH proliferative phase and vessel inflammation was evaluated (156, 415). Milliplex analysis showed an increased MCP-1 and IL-8 average production of HUVECs exposed to REC_A and REC_B WSS compared to the production induced by PUL_A and PUL_V waveforms or by static condition. The time course of cytokine production showed that MCP-1 medium content was significantly higher in the T_1 period of REC_B flow exposure compared to PUL_V or a static condition and IL-8 resulted in significant up-regulation in REC_A and REC_B using T_4 medium compared to PUL_V or a static control (figure 58). These results demonstrate that AVF specific WSS waveforms modulate HUVEC chemoattractant signaling.

To further explore the paracrine proliferative potential elicited by flow, human SMCs were incubated with medium conditioned by HUVECs exposed to different WSS waveforms. Thus the increase in SMC proliferation was quantified after 24 hours incubation with HUVECs EM collected during different periods of HUVEC exposure to PUL_V, REC_A and REC_B flow experiments or static. The results have shown that mediums collected during the T_2 and T_4 periods of exposure to REC_A and REC_B

elicited a limited but statistically significant increase in SMC proliferation. These results are only partially consistent with the cytokine production time course (figure 60) since medium conditioned by static cultures induced a generally higher proliferation despite lower contents of MCP-1 and IL-8.

Finally, despite their probable role in IH development (114, 426), neither CK1α nor CCR2 mRNA levels were up-regulated by reciprocating WSS. In conclusion, *in-vitro* HUVECs exposed to reciprocating/disturbed WSS of AVF high-risk stenosis areas showed an activation state and a pro-inflammatory signaling that is coherent with neointimal growth. This results leads to acceptance of the initial working hypothesis, that reciprocating WSS waveforms are a determinant of intimal hyperplasia development influencing AVF maturation and outcome.

9.B) Discussion

To provide adequate renal replacement therapy to the increasing number of end-stage renal disease patients is an open challenge. The lack of kidney donors causes an increase of demand for dialysis. However to perform efficient and effective dialysis treatment it is necessary to create a vascular access (VA) that provides an adequate blood flow to the filtration system with low complication rates.

Despite the fact that VA surgical placement has been performed for many years, the associated complications are the main cause of hospitalization among hemodialysis patients (9). Even the autologous arteriovenous fistulas (AVFs), considered the best VA modality choice, have high failure rates due to stenosis induced by neointimal formation (100). In this context, the aim of this work was to assess the influence of mechanical stress, and in particular the Wall Shear Stress (WSS) that may develop in the AVF geometry after creation, on endothelial cell monolayers in *in-vitro* culture.

For many years it has been known that WSS has profound effects on EC phenotype (75). AVF creation introduces hemodynamics changes that go far beyond the normal physiological range (78). Very high frequency fluctuations and very high velocities create unique hemodynamics that vessel remodeling should accommodate to reestablish WSS and pressure to physiological values. The specific WSS patterns can interfere with the restoration of a functional endothelium after AVF creation and prevent AVF maturation.

CFD methods are currently widely used to study hemodynamics in realistic vasculature geometries. There is an increasing body of evidence that challenges traditional paradigms to evaluate WSS effects on the endothelium. The analysis of multidirectional WSS in locating atherosclerosis seems more accurate than considering just the OSI value. Furthermore, a study focused on internal carotid artery aneurysms revealed strong flow instabilities and periodic vortex shedding at 100 Hz frequency (434). In a recently published study of our group, it has been shown that high frequency oscillations developed in patient-specific AVF geometries and that new hemodynamic index such as the transverse WSS or transWSS (460) provides more information than OSI regarding localization of AVF areas most exposed to IH development (435). The magnitude of WSS waveforms frequency components has recently emerged as a determinant in controlling EC state (446). In this context, the CPD developed in this study provides a valuable tool to investigate the effect of a wide variety of realistic WSS waveforms. However, new designs in cell shearing devices are necessary to investigate the effects of planar multidirectional stimulation. Furthermore, a limitation of CPD use emerged during the experimental activity concerning the device engine heat production. For high velocity rotation (necessary to obtain WSS higher than 30 dyn/cm^2), an increase of temperature within the cell incubator above 37°C was measured. This is

caused by the insulation of the incubator environment that prevents heat exchange. To solve this issue it would be necessary to develop a refrigerating system, which could affect the ease of the experimental procedure and the compactness of the device that were required by the project.

The biological determinations performed on HUVEC monolayers exposed to different flows, have led to acceptance of the working hypothesis, identifying WSS as central to AVF maturation and failure. This study corroborates the idea that disturbed WSS in the AVF has the potential to trigger IH.

In recent years many pharmacological and surgical treatments have been proposed to ameliorate AVF outcomes. However, the results have been disappointing, since none of the proposed methods induced an increase in AVF usability and patency. Statin treatment is a meaningful example of promising pharmacological approaches to protect EC function that has failed in preventing AVF failure, despite the promising results obtained in a murine model. These vasoprotective molecules are widely used in clinical practice due their effect on the endogenous cholesterol metabolism and anti-inflammatory properties. These molecules are also known to induce KLF2 and eNOS expression in ECs and to exert a protective function on the endothelium (436). Recent studies however, showed that statins might have a negative effect on EC structure (437) by preventing stress fibers and focal adhesion formation. Furthermore statins induce the over-expression of adhesion molecule expression in ECs (438). In this context, *Florescu* and *Birch* suggested that statins anti-inflammatory effects are likely to be insufficient in AVF remodeling due the ESRD context (439). Recently it has been showed that statins beneficial effects are amplified by combination with laminar unidirectional WSS (147, 438, 440). On the contrary, reciprocating WSS reduces EC sensitivity to statin treatment (440, 441). The precise role of reciprocating WSS in impairing statins protective effects

in ECs remains to be elucidated (441), but it indicates once more the importance of hemodynamics in vascular disease.

Since no treatments are currently available to reduce native vascular accesses stenosis and failure and despite the complete mechanism of intimal hyperplasia growth is not established yet, the hemodynamics that develop in a newly created AVF has a role in vessel tone regulation and inflammation, thus it is a potential target to ameliorate AVF outcome.

In line with these observations, computer-assisted pre-surgical planning emerges as the main available method to prevent or reduce disturbed hemodynamics that develops in AVF. The shape of a side-to-end anastomosis is commonly established with an angle between the artery and the vein. Our group has shown that reduced AVF angles minimize areas exposed to reciprocating shear stress (79) and clinically encouraging results were also obtained using a narrow-angle anastomosis technique in AVF creation (442). Further studies must be performed to determine the best clinical and surgical procedures to ensure functional vascular access in hemodialysis patients.

9.C) Future perspective

Since the definition of the role of WSS in vascular pathologies is still an open question, many groups around the world are currently producing data in this field.

The most recent findings have led to definition of major areas that should be developed in order for knowledge to advance and to provide clinical solutions for the many vascular dysfunctions where WSS is potentially involved.

The first area concerns the development of new tools to stimulate cell culture with conditions as close as possible to physiological conditions. Since in *in-vivo* investigations it is difficult to assess the exact mechanical forces that act on living

tissues, *in vitro* studies remain fundamental to develop concepts that then have to be tested in animal models or clinical tests. As previously reported, new emerging evidence directs theories of WSS effects to turn toward the study of multidirectional WSS (443). To investigate the effects of this complex hemodynamic condition a new cell shearing device has been developed by *Wang* and colleagues (444, 445). The system is based on a plate, seeded with cells, that can rotate in a uniform flow field generated by a parallel flow chamber. This device has significant potential and the results may define once for all the relative importance of magnitude and direction in atherosclerosis development but also in other vascular dysfunctions such as AVF failure.

Another feature of WSS waveforms that has shown to be important in establishing endothelial phenotype is the WSS profile frequency components. As previously reported (446), by changing the magnitude of higher frequency components it is possible to dramatically change the effect of WSS stimulation. In this field of research, our system has the potential to provide useful information on the effects of changing WSS frequency and magnitude, despite the limitations previously described.

Beyond the tools necessary to investigate the effect of WSS on endothelium, new biological focus is emerging from different areas of research such as cancer therapy, transplant and molecular biology. As reported in Chapter 1, TGF-β seems to be central in the events that elicit cell proliferation and migration, as well as in matrix deposition, leading to IH development.

A recently addressed downstream signal of TGF-β in endothelium is based on the induction of the matricellular proteins that belong to the CCN family, via AP-1 (447-449). CCN1 and CCN2 have been shown to be pro-fibrotic and to promote angiogenesis (449-451). On the contrary CCN3 seems to be protective and to prevent

IH formation possibly via the downregulation of NF-κB activity (453). In a CCN3-ko mice model IH development was dramatically increased. Furthermore CCN3 has been shown to reduce EC VCAM expression and to prevent monocyte adhesion (454, 455).

CCN family member activation relies on the TGF-β signalling pathways, thus on binding to the different TGF-β receptors and WSS has been shown to regulate this binding, thus the role of WSS in modulating CCN has been addressed. The results showed that CCN3 can be induced by laminar WSS (455) but no data are available of the role of WSS features in inducing this molecule. In this context the CPD system has potential to investigate the role of AVF-specific WSS stimuli on TGF-β receptors and the downstream activation of SMAD pathways and CCN.

Another recently emerging field where the effects of WSS stimuli remain poorly understood is *microRNA* (miRNA) regulation and function (456). miRNA has been shown to participate in the transcriptional and post-transcriptional modification of mRNA. Different flow-induced miRNAs are involved in inflammation as well as in the protection of vessel tissues (110, 457-459). However no data are available on the effects of realistic WSS waveforms on miRNA transcription and activation and the possible downstream regulation caused by flow onset or long term exposure. Since miRNAs have been shown to participate in most intimate cell functions, the comprehension of these mechanisms could provide new therapeutic strategies in order to improve AVF outcomes.

References

1. Lozano R, Naghavi M, Foreman K, *et al.* Global and regional mortality from 235 causes of death for 20 age groups in 1990 and 2010: a systematic analysis for the Global Burden of Disease Study 2010. *Lancet* 2012; **380:** 2095-2128.

2. Foundation NK. NKF-DOQI clinical practice guidelines for vascular access. National Kidney Foundation-Dialysis Outcomes Quality Initiative. *Am J Kidney Dis* 1997; **30:** S150-191.

3. Foundation NK. NKF-DOQI clinical practice guidelines for chronic kidney disease. National Kidney Foundation-Dialysis Outcomes Quality Initiative. *Kidney Int Suppl* 2013; **3:** 1-150.

4. Jha V, Garcia-Garcia G, Iseki K, *et al.* Chronic kidney disease: global dimension and perspectives. *Lancet* 2013; **382:** 260-272.

5. Italian Health Ministry website. Kidney transplantation activity report 2013-2014. http://wwwtrapiantisalutegovit. 12 March 2015.

6. Quinn RR, Ravani P, Zhang X, *et al.* Impact of modality choice on rates of hospitalization in patients eligible for both peritoneal dialysis and hemodialysis. *Perit Dial Int* 2014; **34:** 41-48.

7. Williams VR, Quinn R, Callery S, *et al.* The impact of treatment modality on infection-related hospitalization rates in peritoneal dialysis and hemodialysis patients. *Perit Dial Int* 2011; **31:** 440-449.

8. Lee T, Roy-Chaudhury P. Advances and new frontiers in the pathophysiology of venous neointimal hyperplasia and dialysis access stenosis. *Adv Chronic Kidney Dis* 2009; **16:** 329-338.

9. Riella MC, Roy-Chaudhury P. Vascular access in haemodialysis: strengthening the Achilles' heel. *Nat Rev Nephrol* 2013; **9:** 348-357.

10. Kumar VA, Sidell MA, Jones JP, *et al.* Survival of propensity matched incident peritoneal and hemodialysis patients in a United States health care system. *Kidney Int* 2014; **86:** 1016-1022.

11. Vilar E, Farrington K. Emerging importance of residual renal function in end-stage renal failure. *Semin Dial* 2011; **24:** 487-494.

12. Griva K, Kang AW, Yu ZL, *et al.* Quality of life and emotional distress between patients on peritoneal dialysis versus community-based hemodialysis. *Qual Life Res* 2014; **23:** 57-66.

13. Griva K, Yu Z, Chan S, *et al.* Age is not a contraindication to home-based dialysis - Quality-of-Life outcomes favour older patients on peritoneal dialysis regimes relative to younger patients. *J Adv Nurs* 2014; **70:** 1902-1914.

14. Palmer SC, de Berardis G, Craig JC, *et al.* Patient satisfaction with in-centre haemodialysis care: an international survey. *BMJ Open* 2014; **4:** e005020.

15. Robinson BM, Bieber B, Pisoni RL, *et al.* Dialysis Outcomes and Practice Patterns Study (DOPPS): its strengths, limitations, and role in informing practices and policies. *Clin J Am Soc Nephrol* 2012; **7:** 1897-1905.

16. Allon M. Fistula first: recent progress and ongoing challenges. *Am J Kidney Dis* 2011; **57:** 3-6.

17. Schinstock CA, Albright RC, Williams AW, *et al.* Outcomes of arteriovenous fistula creation after the Fistula First Initiative. *Clin J Am Soc Nephrol* 2011; **6:** 1996-2002.

18. Santoro D, Benedetto F, Mondello P, *et al.* Vascular access for hemodialysis: current perspectives. *Int J Nephrol Renovasc Dis* 2014; **7:** 281-294.

19. Spergel LM, Ravani P, Asif A, *et al.* Autogenous arteriovenous fistula options. *J Nephrol* 2007; **20:** 288-298.

20. Al-Jaishi AA, Oliver MJ, Thomas SM, *et al.* Patency rates of the arteriovenous fistula for hemodialysis: a systematic review and meta-analysis. *Am J Kidney Dis* 2014; **63:** 464-478.

21. Fokou M, Teyang A, Ashuntantang G, *et al.* Complications of arteriovenous fistula for hemodialysis: an 8-year study. *Ann Vasc Surg* 2012; **26:** 680-684.

22. Huijbregts HJ, Bots ML, Wittens CH, *et al.* Hemodialysis arteriovenous fistula patency revisited: results of a prospective, multicenter initiative. *Clin J Am Soc Nephrol* 2008; **3:** 714-719.

23. Ethier J, Mendelssohn DC, Elder SJ, *et al.* Vascular access use and outcomes: an international perspective from the Dialysis Outcomes and Practice Patterns Study. *Nephrol Dial Transplant* 2008; **23:** 3219-3226.

24. Pisoni RL. Vascular access use and outcomes: results from the DOPPS. *Contrib Nephrol* 2002: 13-19.

25. Polo JR, Vazquez R, Polo J, *et al.* Brachiocephalic jump graft fistula: an alternative for dialysis use of elbow crease veins. *Am J Kidney Dis* 1999; **33:** 904-909.

26. Khadra MH, Dwyer AJ, Thompson JF. Advantages of polytetrafluoroethylene arteriovenous loops in the thigh for hemodialysis access. *Am J Surg* 1997; **173:** 280-283.

27. Roy-Chaudhury P, Kelly BS, Miller MA, *et al.* Venous neointimal hyperplasia in polytetrafluoroethylene dialysis grafts. *Kidney Int* 2001; **59:** 2325-2334.

28. Salimi J. Patency rate and complications of vascular access grafts for hemodialysis in lower extremities. *Saudi J Kidney Dis Transpl* 2008; **19:** 929-932.

29. Stehman-Breen CO, Sherrard DJ, Gillen D, *et al.* Determinants of type and timing of initial permanent hemodialysis vascular access. *Kidney Int* 2000; **57:** 639-645.

30. Davidson I, Gallieni M, Saxena R, *et al.* A patient centered decision making dialysis access algorithm. *J Vasc Access* 2007; **8:** 59-68.

31. Gallieni M, Brenna I, Brunini F, *et al.* Dialysis central venous catheter types and performance. *J Vasc Access* 2014; **15 Suppl 7:** S140-146.

32. Bellinghieri G, Ricciardi B, Costantino G, *et al.* Exhaustion of vascular endowment in hemodialysis: proposal for a permanent inlet access. *Int J Artif Organs* 1998; **21:** 201-204.

33. Ash SR. Advances in tunneled central venous catheters for dialysis: design and performance. *Semin Dial* 2008; **21:** 504-515.

34. McGee DC, Gould MK. Preventing complications of central venous catheterization. *N Engl J Med* 2003; **348:** 1123-1133.

35. Kusminsky RE. Complications of central venous catheterization. *J Am Coll Surg* 2007; **204:** 681-696.

36. Spergel LM, Ravani P, Roy-Chaudhury P, *et al.* Surgical salvage of the autogenous arteriovenous fistula (AVF). *J Nephrol* 2007; **20:** 388-398.

37. Nagler EV, Webster AC, Bolignano D, *et al.* European Renal Best Practice (ERBP) Guideline development methodology: towards the best possible guidelines. *Nephrol Dial Transplant* 2014; **29:** 731-738.

38. Smith GE, Gohil R, Chetter IC. Factors affecting the patency of arteriovenous fistulas for dialysis access. *J Vasc Surg* 2012; **55:** 849-855.

39. Robbin ML, Chamberlain NE, Lockhart ME, *et al.* Hemodialysis arteriovenous fistula maturity: US evaluation. *Radiology* 2002; **225:** 59-64.

40. Malovrh M. Non-invasive evaluation of vessels by duplex sonography prior to construction of arteriovenous fistulas for haemodialysis. *Nephrol Dial Transplant* 1998; **13:** 125-129.

41. Khavanin Zadeh M, Gholipour F, Naderpour Z, *et al.* Relationship between Vessel Diameter and Time to Maturation of Arteriovenous Fistula for Hemodialysis Access. *Int J Nephrol* 2012; **2012:** 942950.

42. Brunori G, Ravani P, Mandolfo S, *et al.* Fistula maturation: doesn't time matter at all? *Nephrol Dial Transplant* 2005; **20:** 684-687.

43. Saran R, Dykstra DM, Pisoni RL, *et al.* Timing of first cannulation and vascular access failure in haemodialysis: an analysis of practice patterns at dialysis facilities in the DOPPS. *Nephrol Dial Transplant* 2004; **19:** 2334-2340.

44. Basile C, Casucci F, Lomonte C. Timing of first cannulation of arteriovenous fistula: time matters, but there is also something else. *Nephrol Dial Transplant* 2005; **20:** 1519-1520.

45. Saran R, Pisoni RL, Young EW. Timing of first cannulation of arteriovenous fistula: are we waiting too long? *Nephrol Dial Transplant* 2005; **20:** 688-690.

46. Yoo DW, Yoon M, Jun HJ. Successful Access Rate and Risk Factor of Vascular Access Surgery in Arm for Dialysis. *Vasc Specialist Int* 2014; **30:** 33-37.

47. Robbin ML, Gallichio MH, Deierhoi MH, *et al.* US vascular mapping before hemodialysis access placement. *Radiology* 2000; **217:** 83-88.

48. Allon M, Lockhart ME, Lilly RZ, *et al.* Effect of preoperative sonographic mapping on vascular access outcomes in hemodialysis patients. *Kidney Int* 2001; **60:** 2013-2020.

49. Ilhan G, Esi E, Bozok S, *et al.* The clinical utility of vascular mapping with Doppler ultrasound prior to arteriovenous fistula construction for hemodialysis access. *J Vasc Access* 2013; **14:** 83-88.

50. Silva MB, Jr., Hobson RW, 2nd, Pappas PJ, *et al.* A strategy for increasing use of autogenous hemodialysis access procedures: impact of preoperative noninvasive evaluation. *J Vasc Surg* 1998; **27:** 302-307; discussion 307-308.

51. Okada S, Shenoy S. Arteriovenous access for hemodialysis: preoperative assessment and planning. *J Vasc Access* 2014; **15 Suppl 7:** S1-5.

52. Kamienski RW, Barnes RW. Critique of the Allen test for continuity of the palmar arch assessed by doppler ultrasound. *Surg Gynecol Obstet* 1976; **142:** 861-864.

53. Drew DA, Lok CE. Strategies for planning the optimal dialysis access for an individual patient. *Curr Opin Nephrol Hypertens* 2014; **23:** 314-320.

54. Drew DA, Lok CE, Cohen JT, *et al.* Vascular Access Choice in Incident Hemodialysis Patients: A Decision Analysis. *J Am Soc Nephrol* 2014.

55. Yerdel MA, Kesenci M, Yazicioglu KM, *et al.* Effect of haemodynamic variables on surgically created arteriovenous fistula flow. *Nephrol Dial Transplant* 1997; **12:** 1684-1688.

56. Beathard GA, Arnold P, Jackson J, *et al.* Aggressive treatment of early fistula failure. *Kidney Int* 2003; **64:** 1487-1494.

57. Beathard GA. Hemodialysis arteriovenous fistulas. *wwwesrdnetworkorg* 2003.

58. Romero A, Polo JR, Garcia Morato E, *et al.* Salvage of angioaccess after late thrombosis of radiocephalic fistulas for hemodialysis. *Int Surg* 1986; **71:** 122-124.

59. Beathard GA, Settle SM, Shields MW. Salvage of the nonfunctioning arteriovenous fistula. *Am J Kidney Dis* 1999; **33:** 910-916.

60. Beathard GA. Fistula salvage by endovascular therapy. *Adv Chronic Kidney Dis* 2009; **16:** 339-351.

61. Schon D, Mishler R. Salvage of occluded autologous arteriovenous fistulae. *Am J Kidney Dis* 2000; **36:** 804-810.

62. Praehauser C, Breidthardt T, Moser-Bucher CN, *et al.* The outcome of the primary vascular access and its translation into prevalent access use rates in chronic haemodialysis patients. *Clin Kidney J* 2012; **5:** 339-346.

63. Turmel-Rodrigues L, Pengloan J, Rodrigue H, *et al.* Treatment of failed native arteriovenous fistulae for hemodialysis by interventional radiology. *Kidney Int* 2000; **57:** 1124-1140.

64. Turmel-Rodrigues L, Mouton A, Birmele B, *et al.* Salvage of immature forearm fistulas for haemodialysis by interventional radiology. *Nephrol Dial Transplant* 2001; **16:** 2365-2371.

65. Ahmad I. Salvage of arteriovenous fistula by angioplasty of collateral veins establishing a new channel. *J Vasc Access* 2007; **8:** 123-125.

66. Janicki K, Pietura R, Bojarska-Szmygin A, *et al.* Chronic dialysis fistula thrombosis treatment by means of endovascular recanalization with surgical exclusion of developed collateral circulation. *Ann Univ Mariae Curie Sklodowska Med* 2003; **58:** 219-221.

67. Patel ST, Hughes J, Mills JL, Sr. Failure of arteriovenous fistula maturation: an unintended consequence of exceeding dialysis outcome quality Initiative guidelines for hemodialysis access. *J Vasc Surg* 2003; **38:** 439-445; discussion 445.

68. Rothuizen TC, Wong C, Quax PH, *et al.* Arteriovenous access failure: more than just intimal hyperplasia? *Nephrol Dial Transplant* 2013; **28:** 1085-1092.

69. Lee T, Wang Y, Arend L, *et al.* Comparative analysis of cellular phenotypes within the neointima from vein segments collected prior to vascular access surgery and stenotic arteriovenous dialysis accesses. *Semin Dial* 2014; **27:** 303-309.

70. Roy-Chaudhury P, Wang Y, Krishnamoorthy M, *et al.* Cellular phenotypes in human stenotic lesions from haemodialysis vascular access. *Nephrol Dial Transplant* 2009; **24:** 2786-2791.

71. Sivanesan S, How TV, Bakran A. Sites of stenosis in AV fistulae for haemodialysis access. *Nephrol Dial Transplant* 1999; **14:** 118-120.

72. Ene-Iordache B, Remuzzi A. Disturbed flow in radial-cephalic arteriovenous fistulae for haemodialysis: low and oscillating shear stress locates the sites of stenosis. *Nephrol Dial Transplant* 2012; **27:** 358-368.

73. Chiu JJ, Chien S. Effects of disturbed flow on vascular endothelium: pathophysiological basis and clinical perspectives. *Physiol Rev* 2011; **91:** 327-387.

74. Resnick N, Yahav H, Shay-Salit A, *et al.* Fluid shear stress and the vascular endothelium: for better and for worse. *Prog Biophys Mol Biol* 2003; **81:** 177-199.

75. Chatzizisis YS, Coskun AU, Jonas M, *et al.* Role of endothelial shear stress in the natural history of coronary atherosclerosis and vascular remodeling: molecular, cellular, and vascular behavior. *J Am Coll Cardiol* 2007; **49:** 2379-2393.

76. Malek AM, Alper SL, Izumo S. Hemodynamic shear stress and its role in atherosclerosis. *JAMA* 1999; **282:** 2035-2042.

77. Wentzel JJ, Gijsen FJ, Stergiopulos N, *et al.* Shear stress, vascular remodeling and neointimal formation. *J Biomech* 2003; **36:** 681-688.

78. Remuzzi A, Ene-Iordache B. Novel paradigms for dialysis vascular access: upstream hemodynamics and vascular remodeling in dialysis access stenosis. *Clin J Am Soc Nephrol* 2013; **8:** 2186-2193.

79. Ene-Iordache B, Cattaneo L, Dubini G, *et al.* Effect of anastomosis angle on the localization of disturbed flow in 'side-to-end' fistulae for haemodialysis access. *Nephrol Dial Transplant* 2013; **28:** 997-1005.

80. Albayrak R, Yuksel S, Colbay M, *et al.* Hemodynamic changes in the cephalic vein of patients with hemodialysis arteriovenous fistula. *J Clin Ultrasound* 2007; **35:** 133-137.

81. Schwartz LB, O'Donohoe MK, Purut CM, *et al.* Myointimal thickening in experimental vein grafts is dependent on wall tension. *J Vasc Surg* 1992; **15:** 176-186.

82. Ene-Iordache B, Mosconi L, Antiga L, *et al.* Radial artery remodeling in response to shear stress increase within arteriovenous fistula for hemodialysis access. *Endothelium* 2003; **10:** 95-102.

83. Dammers R, Tordoir JH, Kooman JP, *et al.* The effect of flow changes on the arterial system proximal to an arteriovenous fistula for hemodialysis. *Ultrasound Med Biol* 2005; **31:** 1327-1333.

84. Krishnamoorthy M, Roy-Chaudhury P, Wang Y, *et al.* Measurement of hemodynamic and anatomic parameters in a swine arteriovenous fistula model. *J Vasc Access* 2008; **9:** 28-34.

85. Krishnamoorthy MK, Banerjee RK, Wang Y, *et al.* Hemodynamic wall shear stress profiles influence the magnitude and pattern of stenosis in a pig AV fistula. *Kidney Int* 2008; **74:** 1410-1419.

86. Lu DY, Chen EY, Wong DJ, *et al.* Vein graft adaptation and fistula maturation in the arterial environment. *J Surg Res* 2014; **188:** 162-173.

87. Bakker EN, Matlung HL, Bonta P, *et al.* Blood flow-dependent arterial remodelling is facilitated by inflammation but directed by vascular tone. *Cardiovasc Res* 2008; **78:** 341-348.

88. Corpataux JM, Haesler E, Silacci P, *et al.* Low-pressure environment and remodelling of the forearm vein in Brescia-Cimino haemodialysis access. *Nephrol Dial Transplant* 2002; **17:** 1057-1062.

89. Freidja ML, Toutain B, Caillon A, *et al.* Heme oxygenase 1 is differentially involved in blood flow-dependent arterial remodeling: role of inflammation, oxidative stress, and nitric oxide. *Hypertension* 2011; **58:** 225-231.

90. Lin CC, Yang WC, Lin SJ, *et al.* Length polymorphism in heme oxygenase-1 is associated with arteriovenous fistula patency in hemodialysis patients. *Kidney Int* 2006; **69:** 165-172.

91. Juncos JP, Tracz MJ, Croatt AJ, *et al.* Genetic deficiency of heme oxygenase-1 impairs functionality and form of an arteriovenous fistula in the mouse. *Kidney Int* 2008; **74:** 47-51.

92. Castier Y, Brandes RP, Leseche G, *et al.* p47phox-dependent NADPH oxidase regulates flow-induced vascular remodeling. *Circ Res* 2005; **97:** 533-540.

93. Galis ZS, Khatri JJ. Matrix metalloproteinases in vascular remodeling and atherogenesis: the good, the bad, and the ugly. *Circ Res* 2002; **90:** 251-262.

94. Tronc F, Mallat Z, Lehoux S, *et al.* Role of matrix metalloproteinases in blood flow-induced arterial enlargement: interaction with NO. *Arterioscler Thromb Vasc Biol* 2000; **20:** E120-126.

95. Lehoux S. Redox signalling in vascular responses to shear and stretch. *Cardiovasc Res* 2006; **71:** 269-279.

96. Lehoux S, Castier Y, Tedgui A. Molecular mechanisms of the vascular responses to haemodynamic forces. *J Intern Med* 2006; **259:** 381-392.

97. Haga JH, Li YS, Chien S. Molecular basis of the effects of mechanical stretch on vascular smooth muscle cells. *J Biomech* 2007; **40:** 947-960.

98. Thacher T, da Silva RF, Stergiopulos N. Differential effects of reduced cyclic stretch and perturbed shear stress within the arterial wall and on smooth muscle function. *Am J Hypertens* 2009; **22:** 1250-1257.

99. Raaz U, Toh R, Maegdefessel L, *et al.* Hemodynamic regulation of reactive oxygen species: implications for vascular diseases. *Antioxid Redox Signal* 2014; **20:** 914-928.

100. Roy-Chaudhury P, Spergel LM, Besarab A, *et al.* Biology of arteriovenous fistula failure. *J Nephrol* 2007; **20:** 150-163.

101. Kwei S, Stavrakis G, Takahas M, *et al.* Early adaptive responses of the vascular wall during venous arterialization in mice. *Am J Pathol* 2004; **164:** 81-89.

102. Ando J, Yamamoto K. Vascular mechanobiology: endothelial cell responses to fluid shear stress. *Circ J* 2009; **73:** 1983-1992.

103. Li YS, Haga JH, Chien S. Molecular basis of the effects of shear stress on vascular endothelial cells. *J Biomech* 2005; **38:** 1949-1971.

104. Davies PF. Flow-mediated endothelial mechanotransduction. *Physiol Rev* 1995; **75:** 519-560.

105. Deng Q, Huo Y, Luo J. Endothelial mechanosensors: the gatekeepers of vascular homeostasis and adaptation under mechanical stress. *Sci China Life Sci* 2014; **57:** 755-762.

106. Chien S. Mechanotransduction and endothelial cell homeostasis: the wisdom of the cell. *Am J Physiol Heart Circ Physiol* 2007; **292:** H1209-1224.

107. van Hinsbergh VW. Endothelium--role in regulation of coagulation and inflammation. *Semin Immunopathol* 2012; **34:** 93-106.

108. Giddens DP, Zarins CK, Glagov S. The role of fluid mechanics in the localization and detection of atherosclerosis. *J Biomech Eng* 1993; **115:** 588-594.

109. Manning E, Skartsis N, Orta AM, *et al.* A new arteriovenous fistula model to study the development of neointimal hyperplasia. *J Vasc Res* 2012; **49:** 123-131.

110. Zhou J, Li YS, Chien S. Shear stress-initiated signaling and its regulation of endothelial function. *Arterioscler Thromb Vasc Biol* 2014; **34:** 2191-2198.

111. Fisslthaler B, Dimmeler S, Hermann C, *et al.* Phosphorylation and activation of the endothelial nitric oxide synthase by fluid shear stress. *Acta Physiol Scand* 2000; **168:** 81-88.

112. Montezano AC, Touyz RM. Reactive oxygen species and endothelial function--role of nitric oxide synthase uncoupling and Nox family nicotinamide adenine dinucleotide phosphate oxidases. *Basic Clin Pharmacol Toxicol* 2012; **110:** 87-94.

113. Bedri S, Cizek SM, Rastarhuyeva I, *et al.* Regulation of protein kinase CK1alphaLS by dephosphorylation in response to hydrogen peroxide. *Arch Biochem Biophys* 2007; **466:** 242-249.

114. Panchenko MP, Siddiquee Z, Dombkowski DM, *et al.* Protein kinase CK1alphaLS promotes vascular cell proliferation and intimal hyperplasia. *Am J Pathol* 2010; **177:** 1562-1572.

115. Sella O, Gerlitz G, Le SY, *et al.* Differentiation-induced internal translation of c-sis mRNA: analysis of the cis elements and their differentiation-linked binding to the hnRNP C protein. *Mol Cell Biol* 1999; **19:** 5429-5440.

116. Mittal M, Siddiqui MR, Tran K, *et al.* Reactive oxygen species in inflammation and tissue injury. *Antioxid Redox Signal* 2014; **20:** 1126-1167.

117. Staiculescu MC, Foote C, Meininger GA, *et al.* The role of reactive oxygen species in microvascular remodeling. *Int J Mol Sci* 2014; **15:** 23792-23835.

118. Savoia C, Schiffrin EL. Inflammation in hypertension. *Curr Opin Nephrol Hypertens* 2006; **15:** 152-158.

119. Qi YX, Jiang J, Jiang XH, *et al.* PDGF-BB and TGF-{beta}1 on cross-talk between endothelial and smooth muscle cells in vascular remodeling induced by low shear stress. *Proc Natl Acad Sci U S A* 2011; **108:** 1908-1913.

120. van Nieuw Amerongen GP, van Delft S, Vermeer MA, *et al.* Activation of RhoA by thrombin in endothelial hyperpermeability: role of Rho kinase and protein tyrosine kinases. *Circ Res* 2000; **87:** 335-340.

121. Nelson RK, Frohman MA. Physiological and Pathophysiological roles for Phospholipase D. *J Lipid Res* 2015.

122. Usatyuk PV, Kotha SR, Parinandi NL, *et al.* Phospholipase D signaling mediates reactive oxygen species-induced lung endothelial barrier dysfunction. *Pulm Circ* 2013; **3:** 108-115.

123. Tsapenko MV, d'Uscio LV, Grande JP, *et al.* Increased production of superoxide anion contributes to dysfunction of the arteriovenous fistula. *Am J Physiol Renal Physiol* 2012; **303:** F1601-1607.

124. Davies PF, Civelek M, Fang Y, *et al.* The atherosusceptible endothelium: endothelial phenotypes in complex haemodynamic shear stress regions in vivo. *Cardiovasc Res* 2013; **99:** 315-327.

125. Dekker RJ, Boon RA, Rondaij MG, *et al.* KLF2 provokes a gene expression pattern that establishes functional quiescent differentiation of the endothelium. *Blood* 2006; **107:** 4354-4363.

126. SenBanerjee S, Lin Z, Atkins GB, *et al.* KLF2 Is a novel transcriptional regulator of endothelial proinflammatory activation. *J Exp Med* 2004; **199:** 1305-1315.

127. Komaravolu RK, Adam C, Moonen JR, *et al.* Erk5 inhibits endothelial migration via KLF2-dependent down-regulation of PAK1. *Cardiovasc Res* 2015; **105:** 86-95.

128. Tsihlis ND, Oustwani CS, Vavra AK, *et al.* Nitric oxide inhibits vascular smooth muscle cell proliferation and neointimal hyperplasia by increasing the ubiquitination and degradation of UbcH10. *Cell Biochem Biophys* 2011; **60:** 89-97.

129. Gladwin MT, Kim-Shapiro DB. Vascular biology: Nitric oxide caught in traffic. *Nature* 2012; **491:** 344-345.

130. Mehta D, Malik AB. Signaling mechanisms regulating endothelial permeability. *Physiol Rev* 2006; **86:** 279-367.

131. Touyz RM. Mitochondrial redox control of matrix metalloproteinase signaling in resistance arteries. *Arterioscler Thromb Vasc Biol* 2006; **26:** 685-688.

132. Boon RA, Leyen TA, Fontijn RD, *et al.* KLF2-induced actin shear fibers control both alignment to flow and JNK signaling in vascular endothelium. *Blood* 2010; **115:** 2533-2542.

133. Loirand G, Sauzeau V, Pacaud P. Small G proteins in the cardiovascular system: physiological and pathological aspects. *Physiol Rev* 2013; **93:** 1659-1720.

134. Tzima E. Role of small GTPases in endothelial cytoskeletal dynamics and the shear stress response. *Circ Res* 2006; **98:** 176-185.

135. Loufrani L, Henrion D. Role of the cytoskeleton in flow (shear stress)-induced dilation and remodeling in resistance arteries. *Med Biol Eng Comput* 2008; **46:** 451-460.

136. Malek AM, Izumo S. Mechanism of endothelial cell shape change and cytoskeletal remodeling in response to fluid shear stress. *J Cell Sci* 1996; **109 (Pt 4):** 713-726.

137. Osborn EA, Rabodzey A, Dewey CF, Jr., *et al.* Endothelial actin cytoskeleton remodeling during mechanostimulation with fluid shear stress. *Am J Physiol Cell Physiol* 2006; **290:** C444-452.

138. Shao Y, Mann JM, Chen W, *et al.* Global architecture of the F-actin cytoskeleton regulates cell shape-dependent endothelial mechanotransduction. *Integr Biol (Camb)* 2014; **6:** 300-311.

139. Birukov KG. Small GTPases in mechanosensitive regulation of endothelial barrier. *Microvasc Res* 2009; **77:** 46-52.

140. Dekker RJ, van Thienen JV, Rohlena J, *et al.* Endothelial KLF2 links local arterial shear stress levels to the expression of vascular tone-regulating genes. *Am J Pathol* 2005; **167:** 609-618.

141. Das H, Kumar A, Lin Z, *et al.* Kruppel-like factor 2 (KLF2) regulates proinflammatory activation of monocytes. *Proc Natl Acad Sci U S A* 2006; **103:** 6653-6658.

142. Juncos JP, Grande JP, Kang L, *et al.* MCP-1 contributes to arteriovenous fistula failure. *J Am Soc Nephrol* 2011; **22:** 43-48.

143. Warboys CM, Amini N, de Luca A, *et al.* The role of blood flow in determining the sites of atherosclerotic plaques. *F1000 Med Rep* 2011; **3:** 5.

144. Boon RA, Fledderus JO, Volger OL, *et al.* KLF2 suppresses TGF-beta signaling in endothelium through induction of Smad7 and inhibition of AP-1. *Arterioscler Thromb Vasc Biol* 2007; **27:** 532-539.

145. Fledderus JO, van Thienen JV, Boon RA, *et al.* Prolonged shear stress and KLF2 suppress constitutive proinflammatory transcription through inhibition of ATF2. *Blood* 2007; **109:** 4249-4257.

146. Fledderus JO, Boon RA, Volger OL, *et al.* KLF2 primes the antioxidant transcription factor Nrf2 for activation in endothelial cells. *Arterioscler Thromb Vasc Biol* 2008; **28:** 1339-1346.

147. van Thienen JV, Fledderus JO, Dekker RJ, *et al.* Shear stress sustains atheroprotective endothelial KLF2 expression more potently than statins through mRNA stabilization. *Cardiovasc Res* 2006; **72:** 231-240.

148. Fitts MK, Pike DB, Anderson K, *et al.* Hemodynamic Shear Stress and Endothelial Dysfunction in Hemodialysis Access. *Open Urol Nephrol J* 2014; **7:** 33-44.

149. Simmons GH, Padilla J, Laughlin MH. Heterogeneity of endothelial cell phenotype within and amongst conduit vessels of the swine vasculature. *Exp Physiol* 2012; **97:** 1074-1082.

150. Shin D, Garcia-Cardena G, Hayashi S, *et al.* Expression of ephrinB2 identifies a stable genetic difference between arterial and venous vascular smooth muscle as well as endothelial cells, and marks subsets of microvessels at sites of adult neovascularization. *Dev Biol* 2001; **230:** 139-150.

151. Kullander K, Klein R. Mechanisms and functions of Eph and ephrin signalling. *Nat Rev Mol Cell Biol* 2002; **3:** 475-486.

152. Masumura T, Yamamoto K, Shimizu N, *et al.* Shear stress increases expression of the arterial endothelial marker ephrinB2 in murine ES cells via the VEGF-Notch signaling pathways. *Arterioscler Thromb Vasc Biol* 2009; **29:** 2125-2131.

153. Jadlowiec CC, Feigel A, Yang C, *et al.* Reduced adult endothelial cell EphB4 function promotes venous remodeling. *Am J Physiol Cell Physiol* 2013; **304:** C627-635.

154. Buschmann I, Pries A, Styp-Rekowska B, *et al.* Pulsatile shear and Gja5 modulate arterial identity and remodeling events during flow-driven arteriogenesis. *Development* 2010; **137:** 2187-2196.

155. Rajabi-Jagahrgh E, Krishnamoorthy MK, Wang Y, *et al.* Influence of temporal variation in wall shear stress on intima-media thickening in arteriovenous fistulae. *Semin Dial* 2013; **26:** 511-519.

156. Patel SD, Waltham M, Wadoodi A, *et al.* The role of endothelial cells and their progenitors in intimal hyperplasia. *Ther Adv Cardiovasc Dis* 2010; **4:** 129-141.

157. Allon M, Litovsky S, Young CJ, *et al.* Medial fibrosis, vascular calcification, intimal hyperplasia, and arteriovenous fistula maturation. *Am J Kidney Dis* 2011; **58:** 437-443.

158. Coen M, Gabbiani G, Bochaton-Piallat ML. Myofibroblast-mediated adventitial remodeling: an underestimated player in arterial pathology. *Arterioscler Thromb Vasc Biol* 2011; **31:** 2391-2396.

159. Baker AB, Ettenson DS, Jonas M, *et al.* Endothelial cells provide feedback control for vascular remodeling through a mechanosensitive autocrine TGF-beta signaling pathway. *Circ Res* 2008; **103:** 289-297.

160. Stracke S, Konner K, Kostlin I, *et al.* Increased expression of TGF-beta1 and IGF-I in inflammatory stenotic lesions of hemodialysis fistulas. *Kidney Int* 2002; **61:** 1011-1019.

161. Weiss MF, Scivittaro V, Anderson JM. Oxidative stress and increased expression of growth factors in lesions of failed hemodialysis access. *Am J Kidney Dis* 2001; **37:** 970-980.

162. Hall MR, Yamamoto K, Protack CD, *et al.* Temporal regulation of venous extracellular matrix components during arteriovenous fistula maturation. *J Vasc Access* 2015; **16:** 93-106.

163. George SJ, Zaltsman AB, Newby AC. Surgical preparative injury and neointima formation increase MMP-9 expression and MMP-2 activation in human saphenous vein. *Cardiovasc Res* 1997; **33:** 447-459.

164. Lee ES, Shen Q, Pitts RL, *et al.* Serum metalloproteinases MMP-2, MMP-9, and metalloproteinase tissue inhibitors in patients are associated with arteriovenous fistula maturation. *J Vasc Surg* 2011; **54:** 454-459; discussion 459-460.

165. Lin CC, Yang WC, Chung MY, *et al.* Functional polymorphisms in matrix metalloproteinases-1, -3, -9 are associated with arteriovenous fistula patency in hemodialysis patients. *Clin J Am Soc Nephrol* 2010; **5:** 1805-1814.

166. Goumans MJ, Liu Z, ten Dijke P. TGF-beta signaling in vascular biology and dysfunction. *Cell Res* 2009; **19:** 116-127.

167. Wang X, Li X, Ye L, *et al.* Smad7 inhibits TGF-beta1-induced MCP-1 upregulation through a MAPK/p38 pathway in rat peritoneal mesothelial cells. *Int Urol Nephrol* 2013; **45:** 899-907.

168. Roy-Chaudhury P, Khan R, Campos B, *et al.* Pathogenetic role for early focal macrophage infiltration in a pig model of arteriovenous fistula (AVF) stenosis. *J Vasc Access* 2014; **15:** 25-28.

169. Chang CJ, Ko YS, Ko PJ, *et al.* Thrombosed arteriovenous fistula for hemodialysis access is characterized by a marked inflammatory activity. *Kidney Int* 2005; **68:** 1312-1319.

170. Yang J, Zhang L, Yu C, *et al.* Monocyte and macrophage differentiation: circulation inflammatory monocyte as biomarker for inflammatory diseases. *Biomark Res* 2014; **2:** 1.

171. Shibuya M. Vascular Endothelial Growth Factor (VEGF) and Its Receptor (VEGFR) Signaling in Angiogenesis: A Crucial Target for Anti- and Pro-Angiogenic Therapies. *Genes Cancer* 2011; **2:** 1097-1105.

172. Yang B, Janardhanan R, Vohra P, *et al.* Adventitial transduction of lentivirus-shRNA-VEGF-A in arteriovenous fistula reduces venous stenosis formation. *Kidney Int* 2014; **85:** 289-306.

173. Asif A, Gadalean FN, Merrill D, *et al.* Inflow stenosis in arteriovenous fistulas and grafts: a multicenter, prospective study. *Kidney Int* 2005; **67:** 1986-1992.

174. Maya ID, Allon M. Vascular access: core curriculum 2008. *Am J Kidney Dis* 2008; **51:** 702-708.

175. Crook MF, Newby AC, Southgate KM. Expression of intercellular adhesion molecules in human saphenous veins: effects of inflammatory cytokines and neointima formation in culture. *Atherosclerosis* 2000; **150:** 33-41.

176. Tsao PS, Lewis NP, Alpert S, *et al.* Exposure to shear stress alters endothelial adhesiveness. Role of nitric oxide. *Circulation* 1995; **92:** 3513-3519.

177. Hinz B, Phan SH, Thannickal VJ, *et al.* Recent developments in myofibroblast biology: paradigms for connective tissue remodeling. *Am J Pathol* 2012; **180:** 1340-1355.

178. Forte A, Della Corte A, De Feo M, *et al.* Role of myofibroblasts in vascular remodelling: focus on restenosis and aneurysm. *Cardiovasc Res* 2010; **88:** 395-405.

179. Tomasek JJ, Gabbiani G, Hinz B, *et al.* Myofibroblasts and mechano-regulation of connective tissue remodelling. *Nat Rev Mol Cell Biol* 2002; **3:** 349-363.

180. Desmouliere A, Redard M, Darby I, *et al.* Apoptosis mediates the decrease in cellularity during the transition between granulation tissue and scar. *Am J Pathol* 1995; **146:** 56-66.

181. Rieder F, Kessler SP, West GA, *et al.* Inflammation-induced endothelial-to-mesenchymal transition: a novel mechanism of intestinal fibrosis. *Am J Pathol* 2011; **179:** 2660-2673.

182. Hinz B, Phan SH, Thannickal VJ, *et al.* The myofibroblast: one function, multiple origins. *Am J Pathol* 2007; **170:** 1807-1816.

183. Hinz B. The myofibroblast: paradigm for a mechanically active cell. *J Biomech* 2010; **43:** 146-155.

184. Majesky MW, Dong XR, Hoglund V, *et al.* The adventitia: a dynamic interface containing resident progenitor cells. *Arterioscler Thromb Vasc Biol* 2011; **31:** 1530-1539.

185. Majesky MW, Dong XR, Hoglund V, *et al.* The adventitia: a progenitor cell niche for the vessel wall. *Cells Tissues Organs* 2012; **195:** 73-81.

186. Hinz B. Formation and function of the myofibroblast during tissue repair. *J Invest Dermatol* 2007; **127:** 526-537.

187. Follonier L, Schaub S, Meister JJ, *et al.* Myofibroblast communication is controlled by intercellular mechanical coupling. *J Cell Sci* 2008; **121:** 3305-3316.

188. Duque JC, Vazquez-Padron RI. Myofibroblasts: the ideal target to prevent arteriovenous fistula failure? *Kidney Int* 2014; **85:** 234-236.

189. Nakerakanti S, Trojanowska M. The Role of TGF-beta Receptors in Fibrosis. *Open Rheumatol J* 2012; **6:** 156-162.

190. Speight P, Nakano H, Kelley TJ, *et al.* Differential topical susceptibility to TGFbeta in intact and injured regions of the epithelium: key role in myofibroblast transition. *Mol Biol Cell* 2013; **24:** 3326-3336.

191. Klingberg F, Hinz B, White ES. The myofibroblast matrix: implications for tissue repair and fibrosis. *J Pathol* 2013; **229:** 298-309.

192. Simone S, Loverre A, Cariello M, *et al.* Arteriovenous fistula stenosis in hemodialysis patients is characterized by an increased adventitial fibrosis. *J Nephrol* 2014; **27:** 555-562.

193. Garanich JS, Mathura RA, Shi ZD, *et al.* Effects of fluid shear stress on adventitial fibroblast migration: implications for flow-mediated mechanisms of arterialization and intimal hyperplasia. *Am J Physiol Heart Circ Physiol* 2007; **292:** H3128-3135.

194. Havelka GE, Kibbe MR. The vascular adventitia: its role in the arterial injury response. *Vasc Endovascular Surg* 2011; **45:** 381-390.

195. Bayes-Genis A, Campbell JH, Carlson PJ, *et al.* Macrophages, myofibroblasts and neointimal hyperplasia after coronary artery injury and repair. *Atherosclerosis* 2002; **163:** 89-98.

196. Wipff PJ, Rifkin DB, Meister JJ, *et al.* Myofibroblast contraction activates latent TGF-beta1 from the extracellular matrix. *J Cell Biol* 2007; **179:** 1311-1323.

197. Ohno M, Cooke JP, Dzau VJ, *et al.* Fluid shear stress induces endothelial transforming growth factor beta-1 transcription and production. Modulation by potassium channel blockade. *J Clin Invest* 1995; **95:** 1363-1369.

198. Kokubo T, Ishikawa N, Uchida H, *et al.* CKD accelerates development of neointimal hyperplasia in arteriovenous fistulas. *J Am Soc Nephrol* 2009; **20:** 1236-1245.

199. Liang A, Wang Y, Han G, *et al.* Chronic kidney disease accelerates endothelial barrier dysfunction in a mouse model of an arteriovenous fistula. *Am J Physiol Renal Physiol* 2013; **304:** F1413-1420.

200. Lee T, Somarathna M, Hura A, *et al.* Natural history of venous morphologic changes in dialysis access stenosis. *J Vasc Access* 2014; **15:** 298-305.

201. Lee T, Chauhan V, Krishnamoorthy M, *et al.* Severe venous neointimal hyperplasia prior to dialysis access surgery. *Nephrol Dial Transplant* 2011; **26:** 2264-2270.

202. Wasse H, Huang R, Naqvi N, *et al.* Inflammation, oxidation and venous neointimal hyperplasia precede vascular injury from AVF creation in CKD patients. *J Vasc Access* 2012; **13:** 168-174.

203. Langer S, Kokozidou M, Heiss C, *et al.* Chronic kidney disease aggravates arteriovenous fistula damage in rats. *Kidney Int* 2010; **78:** 1312-1321.

204. Iso T, Hamamori Y, Kedes L. Notch signaling in vascular development. *Arterioscler Thromb Vasc Biol* 2003; **23:** 543-553.

205. Liu ZJ, Tan Y, Beecham GW, *et al.* Notch activation induces endothelial cell senescence and pro-inflammatory response: implication of Notch signaling in atherosclerosis. *Atherosclerosis* 2012; **225:** 296-303.

206. Morrow D, Guha S, Sweeney C, *et al.* Notch and vascular smooth muscle cell phenotype. *Circ Res* 2008; **103:** 1370-1382.

207. Scheppke L, Murphy EA, Zarpellon A, *et al.* Notch promotes vascular maturation by inducing integrin-mediated smooth muscle cell adhesion to the endothelial basement membrane. *Blood* 2012; **119:** 2149-2158.

208. Quillard T, Charreau B. Impact of notch signaling on inflammatory responses in cardiovascular disorders. *Int J Mol Sci* 2013; **14:** 6863-6888.

209. Wang Y, Liang A, Luo J, *et al.* Blocking Notch in endothelial cells prevents arteriovenous fistula failure despite CKD. *J Am Soc Nephrol* 2014; **25:** 773-783.

210. Caliceti C, Nigro P, Rizzo P, *et al.* ROS, Notch, and Wnt signaling pathways: crosstalk between three major regulators of cardiovascular biology. *Biomed Res Int* 2014; **2014:** 318714.

211. Zavadil J, Cermak L, Soto-Nieves N, *et al.* Integration of TGF-beta/Smad and Jagged1/Notch signalling in epithelial-to-mesenchymal transition. *EMBO J* 2004; **23:** 1155-1165.

212. Venkatesh D, Fredette N, Rostama B, *et al.* RhoA mediated signaling in Notch-induced senescence like growth arrest and endothelial barrier dysfunction. *Arterioscler Thromb Vasc Biol* 2011; **31:** 876–882.

213. Noseda M, McLean G, Niessen K, *et al.* Notch activation results in phenotypic and functional changes consistent with endothelial-to-mesenchymal transformation. *Circ Res* 2004; **94:** 910-917.

214. Quillard T, Devalliere J, Chatelais M, *et al.* Notch2 signaling sensitizes endothelial cells to apoptosis by negatively regulating the key protective molecule survivin. *PLoS One* 2009; **4:** e8244.

215. Iso T, Kedes L, Hamamori Y. HES and HERP families: multiple effectors of the Notch signaling pathway. *J Cell Physiol* 2003; **194:** 237-255.

216. Blokzijl A, Dahlqvist C, Reissmann E, *et al.* Cross-talk between the Notch and TGF-beta signaling pathways mediated by interaction of the Notch intracellular domain with Smad3. *J Cell Biol* 2003; **163:** 723-728.

217. Cachofeiro V, Goicochea M, de Vinuesa SG, *et al.* Oxidative stress and inflammation, a link between chronic kidney disease and cardiovascular disease. *Kidney Int Suppl* 2008: S4-9.

218. Cottone S, Lorito MC, Riccobene R, *et al.* Oxidative stress, inflammation and cardiovascular disease in chronic renal failure. *J Nephrol* 2008; **21:** 175-179.

219. Barak H, Surendran K, Boyle SC. The role of Notch signaling in kidney development and disease. *Adv Exp Med Biol* 2012; **727:** 99-113.

220. Kluppel M, Wrana JL. Turning it up a Notch: cross-talk between TGF beta and Notch signaling. *Bioessays* 2005; **27:** 115-118.

221. Dong Y, Jesse AM, Kohn A, *et al.* RBPjkappa-dependent Notch signaling regulates mesenchymal progenitor cell proliferation and differentiation during skeletal development. *Development* 2010; **137:** 1461-1471.

222. van Meeteren LA, ten Dijke P. Regulation of endothelial cell plasticity by TGF-beta. *Cell Tissue Res* 2012; **347:** 177-186.

223. Massague J. TGFbeta signalling in context. *Nat Rev Mol Cell Biol* 2012; **13:** 616-630.

224. Huang F, Chen YG. Regulation of TGF-beta receptor activity. *Cell Biosci* 2012; **2:** 9.

225. Bruce DL, Sapkota GP. Phosphatases in SMAD regulation. *FEBS Lett* 2012; **586:** 1897-1905.

226. Zi Z, Chapnick DA, Liu X. Dynamics of TGF-beta/Smad signaling. *FEBS Lett* 2012; **586:** 1921-1928.

227. Akhurst RJ, Hata A. Targeting the TGFbeta signalling pathway in disease. *Nat Rev Drug Discov* 2012; **11:** 790-811.

228. Pardali E, Ten Dijke P. TGFbeta signaling and cardiovascular diseases. *Int J Biol Sci* 2012; **8:** 195-213.

229. Zhou J, Lee PL, Lee CI, *et al.* BMP receptor-integrin interaction mediates responses of vascular endothelial Smad1/5 and proliferation to disturbed flow. *J Thromb Haemost* 2013; **11:** 741-755.

230. Cai J, Pardali E, Sanchez-Duffhues G, *et al.* BMP signaling in vascular diseases. *FEBS Lett* 2012; **586:** 1993-2002.

231. Lebrin F, Deckers M, Bertolino P, *et al.* TGF-beta receptor function in the endothelium. *Cardiovasc Res* 2005; **65:** 599-608.

232. Egorova AD, Van der Heiden K, Van de Pas S, *et al.* Tgfbeta/Alk5 signaling is required for shear stress induced klf2 expression in embryonic endothelial cells. *Dev Dyn* 2011; **240:** 1670-1680.

233. Nachtigal P, Zemankova Vecerova L, Rathouska J, *et al.* The role of endoglin in atherosclerosis. *Atherosclerosis* 2012; **224:** 4-11.

234. ten Dijke P, Goumans MJ, Pardali E. Endoglin in angiogenesis and vascular diseases. *Angiogenesis* 2008; **11:** 79-89.

235. Jang YS, Choi IH. Contrasting roles of different endoglin forms in atherosclerosis. *Immune Netw* 2014; **14:** 237-240.

236. Blanco FJ, Grande MT, Langa C, *et al.* S-endoglin expression is induced in senescent endothelial cells and contributes to vascular pathology. *Circ Res* 2008; **103:** 1383-1392.

237. Hawinkels LJ, Kuiper P, Wiercinska E, *et al.* Matrix metalloproteinase-14 (MT1-MMP)-mediated endoglin shedding inhibits tumor angiogenesis. *Cancer Res* 2010; **70:** 4141-4150.

238. Park S, Dimaio TA, Liu W, *et al.* Endoglin regulates the activation and quiescence of endothelium by participating in canonical and non-canonical TGF-beta signaling pathways. *J Cell Sci* 2013; **126:** 1392-1405.

239. Park S, Sorenson CM, Sheibani N. PECAM-1 isoforms, eNOS and endoglin axis in regulation of angiogenesis. *Clin Sci (Lond)* 2015; **129:** 217-234.

240. Alev C, McIntyre BA, Ota K, *et al.* Dynamic expression of Endoglin, a TGF-beta co-receptor, during pre-circulation vascular development in chick. *Int J Dev Biol* 2010; **54:** 737-742.

241. Santibanez JF, Letamendia A, Perez-Barriocanal F, *et al.* Endoglin increases eNOS expression by modulating Smad2 protein levels and Smad2-dependent TGF-beta signaling. *J Cell Physiol* 2007; **210:** 456-468.

242. Shi X, DiRenzo D, Guo LW, *et al.* TGF-beta/Smad3 stimulates stem cell/developmental gene expression and vascular smooth muscle cell de-differentiation. *PLoS One* 2014; **9:** e93995.

243. Shi X, Guo LW, Seedial SM, *et al.* TGF-beta/Smad3 inhibit vascular smooth muscle cell apoptosis through an autocrine signaling mechanism involving VEGF-A. *Cell Death Dis* 2014; **5:** e1317.

244. Heine GH, Ulrich C, Sester U, *et al.* Transforming growth factor beta1 genotype polymorphisms determine AV fistula patency in hemodialysis patients. *Kidney Int* 2003; **64:** 1101-1107.

245. Lee CH, Yu CY, Chang SH, *et al.* Promoting endothelial recovery and reducing neointimal hyperplasia using sequential-like release of acetylsalicylic acid and paclitaxel-loaded biodegradable stents. *Int J Nanomedicine* 2014; **9:** 4117-4133.

246. Lopez-Hernandez FJ, Lopez-Novoa JM. Role of TGF-beta in chronic kidney disease: an integration of tubular, glomerular and vascular effects. *Cell Tissue Res* 2012; **347:** 141-154.

247. Walshe TE, dela Paz NG, D'Amore PA. The role of shear-induced transforming growth factor-beta signaling in the endothelium. *Arterioscler Thromb Vasc Biol* 2013; **33:** 2608-2617.

248. Ten Dijke P, Egorova AD, Goumans MJ, *et al.* TGF-beta signaling in endothelial-to-mesenchymal transition: the role of shear stress and primary cilia. *Sci Signal* 2012; **5:** pt2.

249. Pfitzner J. Poiseuille and his law. *Anaesthesia* 1976; **31:** 273-275.

250. Westerhof N, Stergiopulos N, Noble MIM. Snapshots of Hemodynamics: An aid for clinical research and graduate education. *Springer* 2005; http://www.springeronline.com.

251. Caro CG, Dumoulin CL, Graham JM, *et al.* Secondary flow in the human common carotid artery imaged by MR angiography. *J Biomech Eng* 1992; **114:** 147-149.

252. Womersley JR. Method for the calculation of velocity, rate of flow and viscous drag in arteries when the pressure gradient is known. *J Physiol* 1955; **127:** 553-563.

253. Womersley JR. Oscillatory flow in arteries: the constrained elastic tube as a model of arterial flow and pulse transmission. *Phys Med Biol* 1957; **2:** 178-187.

254. Caro CG, Pedley TJ, Schroter RC, *et al.* The Mechanics of the Circulation. *Oxford University Press* 1978.

255. Cezeaux JL, van Grondelle A. Accuracy of the inverse Womersley method for the calculation of hemodynamic variables. *Ann Biomed Eng* 1997; **25:** 536-546.

256. Schwarz JC, Duivenvoorden R, Nederveen AJ, *et al.* Endothelial shear stress estimation in the human carotid artery based on Womersley versus Poiseuille flow. *Int J Cardiovasc Imaging* 2015; **31:** 585-593.

257. Formaggia L, Quarteroni A, Veneziani A. Cardiovascular Mathematics. *Springer* 2009.

258. Moatamedi M, Souli M, Al-Bahkali E. Fluid Structure Modelling of Blood Flow in Vessels. *Mol Cell Biomech* 2014; **11:** 221-234.

259. Ku DN, Giddens DP, Zarins CK, *et al.* Pulsatile flow and atherosclerosis in the human carotid bifurcation. Positive correlation between plaque location and low oscillating shear stress. *Arteriosclerosis* 1985; **5:** 293-302.

260. Dai G, Kaazempur-Mofrad MR, Natarajan S, *et al.* Distinct endothelial phenotypes evoked by arterial waveforms derived from atherosclerosis-susceptible and -resistant regions of human vasculature. *Proc Natl Acad Sci U S A* 2004; **101:** 14871-14876.

261. Pan S. Molecular mechanisms responsible for the atheroprotective effects of laminar shear stress. *Antioxid Redox Signal* 2009; **11:** 1669-1682.

262. Garin G, Berk BC. Flow-mediated signaling modulates endothelial cell phenotype. *Endothelium* 2006; **13:** 375-384.

263. Noguchi N, Jo H. Redox going with vascular shear stress. *Antioxid Redox Signal* 2011; **15:** 1367-1368.

264. Ballermann BJ, Dardik A, Eng E, *et al.* Shear stress and the endothelium. *Kidney Int Suppl* 1998; **67:** S100-108.

265. Dora KA. Intercellular Ca2+ signalling: the artery wall. *Semin Cell Dev Biol* 2001; **12:** 27-35.

266. Yao X, Garland CJ. Recent developments in vascular endothelial cell transient receptor potential channels. *Circ Res* 2005; **97:** 853-863.

267. Ando J, Ohtsuka A, Korenaga R, *et al.* Wall shear stress rather than shear rate regulates cytoplasmic Ca++ responses to flow in vascular endothelial cells. *Biochem Biophys Res Commun* 1993; **190:** 716-723.

268. Andrews AM, Jaron D, Buerk DG, *et al.* Shear stress-induced NO production is dependent on ATP autocrine signaling and capacitative calcium entry. *Cell Mol Bioeng* 2014; **7:** 510-520.

269. Chachisvilis M, Zhang YL, Frangos JA. G protein-coupled receptors sense fluid shear stress in endothelial cells. *Proc Natl Acad Sci U S A* 2006; **103:** 15463-15468.

270. Hsieh HJ, Liu CA, Huang B, *et al.* Shear-induced endothelial mechanotransduction: the interplay between reactive oxygen species (ROS) and nitric oxide (NO) and the pathophysiological implications. *J Biomed Sci* 2014; **21:** 3.

271. Hwang J, Ing MH, Salazar A, *et al.* Pulsatile versus oscillatory shear stress regulates NADPH oxidase subunit expression: implication for native LDL oxidation. *Circ Res* 2003; **93:** 1225-1232.

272. Hahn C, Schwartz MA. Mechanotransduction in vascular physiology and atherogenesis. *Nat Rev Mol Cell Biol* 2009; **10:** 53-62.

273. Yoshizumi M, Abe J, Tsuchiya K, *et al.* Stress and vascular responses: atheroprotective effect of laminar fluid shear stress in endothelial cells: possible role of mitogen-activated protein kinases. *J Pharmacol Sci* 2003; **91:** 172-176.

274. Chien S. Effects of disturbed flow on endothelial cells. *Ann Biomed Eng* 2008; **36:** 554-562.

275. Tarbell JM, Simon SI, Curry FR. Mechanosensing at the vascular interface. *Annu Rev Biomed Eng* 2014; **16:** 505-532.

276. Zeng Y, Tarbell JM. The adaptive remodeling of endothelial glycocalyx in response to fluid shear stress. *PLoS One* 2014; **9:** e86249.

277. Luo Y, Xu X, Lele T, *et al.* A multi-modular tensegrity model of an actin stress fiber. *J Biomech* 2008; **41:** 2379-2387.

278. Wang S, Wolynes PG. Tensegrity and motor-driven effective interactions in a model cytoskeleton. *J Chem Phys* 2012; **136:** 145102.

279. Thi MM, Tarbell JM, Weinbaum S, *et al.* The role of the glycocalyx in reorganization of the actin cytoskeleton under fluid shear stress: a "bumper-car" model. *Proc Natl Acad Sci U S A* 2004; **101:** 16483-16488.

280. Pries AR, Secomb TW, Jacobs H, *et al.* Microvascular blood flow resistance: role of endothelial surface layer. *Am J Physiol* 1997; **273:** H2272-2279.

281. Pries AR, Secomb TW, Gaehtgens P. The endothelial surface layer. *Pflugers Arch* 2000; **440:** 653-666.

282. Reitsma S, Slaaf DW, Vink H, *et al.* The endothelial glycocalyx: composition, functions, and visualization. *Pflugers Arch* 2007; **454:** 345-359.

283. Woodcock TE, Woodcock TM. Revised Starling equation and the glycocalyx model of transvascular fluid exchange: an improved paradigm for prescribing intravenous fluid therapy. *Br J Anaesth* 2012; **108:** 384-394.

284. Van Teeffelen JW, Brands J, Stroes ES, *et al.* Endothelial glycocalyx: sweet shield of blood vessels. *Trends Cardiovasc Med* 2007; **17:** 101-105.

285. Padberg JS, Wiesinger A, di Marco GS, *et al.* Damage of the endothelial glycocalyx in chronic kidney disease. *Atherosclerosis* 2014; **234:** 335-343.

286. Vlahu CA, Lemkes BA, Struijk DG, *et al.* Damage of the endothelial glycocalyx in dialysis patients. *J Am Soc Nephrol* 2012; **23:** 1900-1908.

287. Bai K, Wang W. Spatio-temporal development of the endothelial glycocalyx layer and its mechanical property in vitro. *J R Soc Interface* 2012; **9:** 2290-2298.

288. Tarbell JM. Shear stress and the endothelial transport barrier. *Cardiovasc Res* 2010; **87:** 320-330.

289. Bartlett AH, Hayashida K, Park PW. Molecular and cellular mechanisms of syndecans in tissue injury and inflammation. *Mol Cells* 2007; **24:** 153-166.

290. Okina E, Manon-Jensen T, Whiteford JR, *et al.* Syndecan proteoglycan contributions to cytoskeletal organization and contractility. *Scand J Med Sci Sports* 2009; **19:** 479-489.

291. Yoneda A, Couchman JR. Regulation of cytoskeletal organization by syndecan transmembrane proteoglycans. *Matrix Biol* 2003; **22:** 25-33.

292. Fransson LA, Belting M, Cheng F, *et al.* Novel aspects of glypican glycobiology. *Cell Mol Life Sci* 2004; **61:** 1016-1024.

293. Ebong EE, Macaluso FP, Spray DC, *et al.* Imaging the endothelial glycocalyx in vitro by rapid freezing/freeze substitution transmission electron microscopy. *Arterioscler Thromb Vasc Biol* 2011; **31:** 1908-1915.

294. Pahakis MY, Kosky JR, Dull RO, *et al.* The role of endothelial glycocalyx components in mechanotransduction of fluid shear stress. *Biochem Biophys Res Commun* 2007; **355:** 228-233.

295. Ebong EE, Lopez-Quintero SV, Rizzo V, *et al.* Shear-induced endothelial NOS activation and remodeling via heparan sulfate, glypican-1, and syndecan-1. *Integr Biol (Camb)* 2014; **6:** 338-347.

296. Zeng Y, Ebong EE, Fu BM, *et al.* The structural stability of the endothelial glycocalyx after enzymatic removal of glycosaminoglycans. *PLoS One* 2012; **7:** e43168.

297. Florian JA, Kosky JR, Ainslie K, *et al.* Heparan sulfate proteoglycan is a mechanosensor on endothelial cells. *Circ Res* 2003; **93:** e136-142.

298. Alexopoulou AN, Multhaupt HA, Couchman JR. Syndecans in wound healing, inflammation and vascular biology. *Int J Biochem Cell Biol* 2007; **39:** 505-528.

299. Stricker J, Falzone T, Gardel ML. Mechanics of the F-actin cytoskeleton. *J Biomech* 2010; **43:** 9-14.

300. Langille BL, Graham JJ, Kim D, *et al.* Dynamics of shear-induced redistribution of F-actin in endothelial cells in vivo. *Arterioscler Thromb* 1991; **11:** 1814-1820.

301. Li YS, Shyy JY, Li S, *et al.* The Ras-JNK pathway is involved in shear-induced gene expression. *Mol Cell Biol* 1996; **16:** 5947-5954.

302. Tseng H, Peterson TE, Berk BC. Fluid shear stress stimulates mitogen-activated protein kinase in endothelial cells. *Circ Res* 1995; **77:** 869-878.

303. Ridley AJ, Paterson HF, Johnston CL, *et al.* The small GTP-binding protein rac regulates growth factor-induced membrane ruffling. *Cell* 1992; **70:** 401-410.

304. Masuda M, Fujiwara K. Morphological responses of single endothelial cells exposed to physiological levels of fluid shear stress. *Front Med Biol Eng* 1993; **5:** 79-87.

305. Kraynov VS, Chamberlain C, Bokoch GM, *et al.* Localized Rac activation dynamics visualized in living cells. *Science* 2000; **290:** 333-337.

306. Masuda M, Fujiwara K. The biased lamellipodium development and microtubule organizing center position in vascular endothelial cells migrating under the influence of fluid flow. *Biol Cell* 1993; **77:** 237-245.

307. Sulciner DJ, Irani K, Yu ZX, *et al.* rac1 regulates a cytokine-stimulated, redox-dependent pathway necessary for NF-kappaB activation. *Mol Cell Biol* 1996; **16:** 7115-7121.

308. Ridley AJ, Hall A. The small GTP-binding protein rho regulates the assembly of focal adhesions and actin stress fibers in response to growth factors. *Cell* 1992; **70:** 389-399.

309. Wojciak-Stothard B, Potempa S, Eichholtz T, *et al.* Rho and Rac but not Cdc42 regulate endothelial cell permeability. *J Cell Sci* 2001; **114:** 1343-1355.

310. Li S, Chen BP, Azuma N, *et al.* Distinct roles for the small GTPases Cdc42 and Rho in endothelial responses to shear stress. *J Clin Invest* 1999; **103:** 1141-1150.

311. Zebda N, Tian Y, Tian X, *et al.* Interaction of p190RhoGAP with C-terminal domain of p120-catenin modulates endothelial cytoskeleton and permeability. *J Biol Chem* 2013; **288:** 18290-18299.

312. Wildenberg GA, Dohn MR, Carnahan RH, *et al.* p120-catenin and p190RhoGAP regulate cell-cell adhesion by coordinating antagonism between Rac and Rho. *Cell* 2006; **127:** 1027-1039.

313. Tomar A, Lim ST, Lim Y, *et al.* A FAK-p120RasGAP-p190RhoGAP complex regulates polarity in migrating cells. *J Cell Sci* 2009; **122:** 1852-1862.

314. Pamonsinlapatham P, Hadj-Slimane R, Lepelletier Y, *et al.* p120-Ras GTPase activating protein (RasGAP): a multi-interacting protein in downstream signaling. *Biochimie* 2009; **91:** 320-328.

315. Bradley WD, Hernandez SE, Settleman J, *et al.* Integrin signaling through Arg activates p190RhoGAP by promoting its binding to p120RasGAP and recruitment to the membrane. *Mol Biol Cell* 2006; **17:** 4827-4836.

316. Bernards A, Settleman J. GAP control: regulating the regulators of small GTPases. *Trends Cell Biol* 2004; **14:** 377-385.

317. Nobes CD, Hall A. Rho, rac and cdc42 GTPases: regulators of actin structures, cell adhesion and motility. *Biochem Soc Trans* 1995; **23:** 456-459.

318. Nobes CD, Hall A. Rho, rac, and cdc42 GTPases regulate the assembly of multimolecular focal complexes associated with actin stress fibers, lamellipodia, and filopodia. *Cell* 1995; **81:** 53-62.

319. Lee JS, Chang MI, Tseng Y, *et al.* Cdc42 mediates nucleus movement and MTOC polarization in Swiss 3T3 fibroblasts under mechanical shear stress. *Mol Biol Cell* 2005; **16:** 871-880.

320. Spiering D, Hodgson L. Dynamics of the Rho-family small GTPases in actin regulation and motility. *Cell Adh Migr* 2011; **5:** 170-180.

321. Kim DW, Gotlieb AI, Langille BL. In vivo modulation of endothelial F-actin microfilaments by experimental alterations in shear stress. *Arteriosclerosis* 1989; **9:** 439-445.

322. Gulino-Debrac D. Mechanotransduction at the basis of endothelial barrier function. *Tissue Barriers* 2013; **1:** e24180.

323. Ladoux B, Nelson WJ, Yan J, *et al.* The mechanotransduction machinery at work at adherens junctions. *Integr Biol (Camb)* 2015.

324. Conway DE, Schwartz MA. Mechanotransduction of shear stress occurs through changes in VE-cadherin and PECAM-1 tension: Implications for cell migration. *Cell Adh Migr* 2014: 1-5.

325. Giannotta M, Trani M, Dejana E. VE-cadherin and endothelial adherens junctions: active guardians of vascular integrity. *Dev Cell* 2013; **26:** 441-454.

326. Collins C, Guilluy C, Welch C, *et al.* Localized tensional forces on PECAM-1 elicit a global mechanotransduction response via the integrin-RhoA pathway. *Curr Biol* 2012; **22:** 2087-2094.

327. Shay-Salit A, Shushy M, Wolfovitz E, *et al.* VEGF receptor 2 and the adherens junction as a mechanical transducer in vascular endothelial cells. *Proc Natl Acad Sci U S A* 2002; **99:** 9462-9467.

328. Dejana E. Endothelial cell-cell junctions: happy together. *Nat Rev Mol Cell Biol* 2004; **5:** 261-270.

329. Hartsock A, Nelson WJ. Adherens and tight junctions: structure, function and connections to the actin cytoskeleton. *Biochim Biophys Acta* 2008; **1778:** 660-669.

330. Millan J, Cain RJ, Reglero-Real N, *et al.* Adherens junctions connect stress fibres between adjacent endothelial cells. *BMC Biol* 2010; **8:** 11.

331. Kowalczyk AP, Nanes BA. Adherens junction turnover: regulating adhesion through cadherin endocytosis, degradation, and recycling. *Subcell Biochem* 2012; **60:** 197-222.

332. Bazzoni G, Dejana E. Endothelial cell-to-cell junctions: molecular organization and role in vascular homeostasis. *Physiol Rev* 2004; **84:** 869-901.

333. Balda MS, Matter K. Tight junctions in health and disease. *Semin Cell Dev Biol* 2014; **36:** 147-148.

334. Schulzke JD, Fromm M. Tight junctions: molecular structure meets function. *Ann N Y Acad Sci* 2009; **1165:** 1-6.

335. Steed E, Balda MS, Matter K. Dynamics and functions of tight junctions. *Trends Cell Biol* 2010; **20:** 142-149.

336. Tsukita S, Katsuno T, Yamazaki Y, *et al.* Roles of ZO-1 and ZO-2 in establishment of the belt-like adherens and tight junctions with paracellular permselective barrier function. *Ann N Y Acad Sci* 2009; **1165:** 44-52.

337. Nagasawa K, Chiba H, Fujita H, *et al.* Possible involvement of gap junctions in the barrier function of tight junctions of brain and lung endothelial cells. *J Cell Physiol* 2006; **208:** 123-132.

338. DePaola N, Davies PF, Pritchard WF, Jr., *et al.* Spatial and temporal regulation of gap junction connexin43 in vascular endothelial cells exposed to controlled disturbed flows in vitro. *Proc Natl Acad Sci U S A* 1999; **96:** 3154-3159.

339. Ebong EE, Depaola N. Specificity in the participation of connexin proteins in flow-induced endothelial gap junction communication. *Pflugers Arch* 2013; **465:** 1293-1302.

340. Saffitz JE, Kleber AG. Effects of mechanical forces and mediators of hypertrophy on remodeling of gap junctions in the heart. *Circ Res* 2004; **94:** 585-591.

341. Salameh A, Dhein S. Effects of mechanical forces and stretch on intercellular gap junction coupling. *Biochim Biophys Acta* 2013; **1828:** 147-156.

342. Zebda N, Dubrovskyi O, Birukov KG. Focal adhesion kinase regulation of mechanotransduction and its impact on endothelial cell functions. *Microvasc Res* 2012; **83:** 71-81.

343. Morgan MR, Humphries MJ, Bass MD. Synergistic control of cell adhesion by integrins and syndecans. *Nat Rev Mol Cell Biol* 2007; **8:** 957-969.

344. Wilcox-Adelman SA, Denhez F, Goetinck PF. Syndecan-4 modulates focal adhesion kinase phosphorylation. *J Biol Chem* 2002; **277:** 32970-32977.

345. Woods A, Couchman JR. Syndecan-4 and focal adhesion function. *Curr Opin Cell Biol* 2001; **13:** 578-583.

346. Qin R, Schmid H, Munzberg C, *et al.* Phosphorylation and turnover of paxillin in focal contacts is controlled by force and defines the dynamic state of the adhesion site. *Cytoskeleton (Hoboken)* 2015; **72:** 101-112.

347. Lu Q, Rounds S. Focal adhesion kinase and endothelial cell apoptosis. *Microvasc Res* 2012; **83:** 56-63.

348. Mehta D. Focal adhesion kinase regulation of endothelial barrier function, apoptosis, and neovascularization. *Microvasc Res* 2012; **83:** 1-2.

349. Mitra SK, Hanson DA, Schlaepfer DD. Focal adhesion kinase: in command and control of cell motility. *Nat Rev Mol Cell Biol* 2005; **6:** 56-68.

350. Dwyer SF, Gao L, Gelman IH. Identification of novel focal adhesion kinase substrates: role for FAK in NFkappaB signaling. *Int J Biol Sci* 2015; **11:** 404-410.

351. Wang X, Chen Q, Xing D. Focal adhesion kinase activates NF-kappaB via the ERK1/2 and p38MAPK Pathways in amyloid-beta25-35-induced apoptosis in PC12 cells. *J Alzheimers Dis* 2012; **32:** 77-94.

352. Shyy JY, Chien S. Role of integrins in endothelial mechanosensing of shear stress. *Circ Res* 2002; **91:** 769-775.

353. Hyytiainen M, Penttinen C, Keski-Oja J. Latent TGF-beta binding proteins: extracellular matrix association and roles in TGF-beta activation. *Crit Rev Clin Lab Sci* 2004; **41:** 233-264.

354. Robertson IB, Horiguchi M, Zilberberg L, *et al.* Latent TGF-beta-binding proteins. *Matrix Biol* 2015.

355. Hinz B. The extracellular matrix and transforming growth factor-beta1: Tale of a strained relationship. *Matrix Biol* 2015.

356. Anderson CT, Castillo AB, Brugmann SA, *et al.* Primary cilia: cellular sensors for the skeleton. *Anat Rec (Hoboken)* 2008; **291:** 1074-1078.

357. Egorova AD, van der Heiden K, Poelmann RE, *et al.* Primary cilia as biomechanical sensors in regulating endothelial function. *Differentiation* 2012; **83:** S56-61.

358. Hoey DA, Downs ME, Jacobs CR. The mechanics of the primary cilium: an intricate structure with complex function. *J Biomech* 2012; **45:** 17-26.

359. Patel A. The primary cilium calcium channels and their role in flow sensing. *Pflugers Arch* 2015; **467:** 157-165.

360. Egorova AD, Khedoe PP, Goumans MJ, *et al.* Lack of primary cilia primes shear-induced endothelial-to-mesenchymal transition. *Circ Res* 2011; **108:** 1093-1101.

361. Zemel A. Active mechanical coupling between the nucleus, cytoskeleton and the extracellular matrix, and the implications for perinuclear actomyosin organization. *Soft Matter* 2015; **11:** 2353-2363.

362. Osorio DS, Gomes ER. Connecting the nucleus to the cytoskeleton for nuclear positioning and cell migration. *Adv Exp Med Biol* 2014; **773:** 505-520.

363. Yamamoto K, Protack CD, Kuwahara G, *et al.* Disturbed shear stress reduces Klf2 expression in arterial-venous fistulae in vivo. *Physiol Rep* 2015; **3**.

364. Kuo YC, Chang TH, Hsu WT, *et al.* Oscillatory shear stress mediates directional re-organization of actin cytoskeleton and alters differentiation propensity of mesenchymal stem cells. *Stem Cells* 2014.

365. Noris M, Morigi M, Donadelli R, *et al.* Nitric oxide synthesis by cultured endothelial cells is modulated by flow conditions. *Circ Res* 1995; **76:** 536-543.

366. Koo A, Dewey CF, Jr., Garcia-Cardena G. Hemodynamic shear stress characteristic of atherosclerosis-resistant regions promotes glycocalyx formation in cultured endothelial cells. *Am J Physiol Cell Physiol* 2013; **304:** C137-146.

367. Wentzel JJ, Chatzizisis YS, Gijsen FJ, *et al.* Endothelial shear stress in the evolution of coronary atherosclerotic plaque and vascular remodelling: current understanding and remaining questions. *Cardiovasc Res* 2012; **96:** 234-243.

368. Blackman BR, Barbee KA, Thibault LE. In vitro cell shearing device to investigate the dynamic response of cells in a controlled hydrodynamic environment. *Ann Biomed Eng* 2000; **28:** 363-372.

369. Mooney ME, R.H. The conicylindrical viscometer. *Physica* 1934; **5:** 350-354.

370. Dewey CF, Jr., Bussolari SR, Gimbrone MA, Jr., *et al.* The dynamic response of vascular endothelial cells to fluid shear stress. *J Biomech Eng* 1981; **103:** 177-185.

371. Sdougos HP, Bussolari SR, Dewey CF. Secondary flow and turbolence in a cone and plate device. *J Fluid Mech* 1984; **138:** 379-404.

372. Cox DB. Radial Flow in the Cone-Plate Viscometer. *Nature* 1962; **193:** 670.

373. Pelech ISAH. Flexible Disk Rotating on a Gas Film Next to a Wall. *J Appl Mech* 1964; **31:** 577-584.

374. Fewell MEH, J.D. The secondary flow of Newtonian fluids in cone-and-plate viscometers. *Trans Soc Rheol* 1977; **21:** 535-565.

375. Bussolari SR, Dewey CF, Jr., Gimbrone MA, Jr. Apparatus for subjecting living cells to fluid shear stress. *Rev Sci Instrum* 1982; **53:** 1851-1854.

376. Buschmann MH, Dieterich P, Adams NA, *et al.* Analysis of flow in a cone-and-plate apparatus with respect to spatial and temporal effects on endothelial cells. *Biotechnol Bioeng* 2005; **89:** 493-502.

377. Spruell C, Baker AB. Analysis of a high-throughput cone-and-plate apparatus for the application of defined spatiotemporal flow to cultured cells. *Biotechnol Bioeng* 2013; **110:** 1782-1793.

378. Blackman BR, Garcia-Cardena G, Gimbrone MA, Jr. A new in vitro model to evaluate differential responses of endothelial cells to simulated arterial shear stress waveforms. *J Biomech Eng* 2002; **124:** 397-407.

379. Malek AM, Ahlquist R, Gibbons GH, *et al.* A cone-plate apparatus for the in vitro biochemical and molecular analysis of the effect of shear stress on adherent cells. *Meth in Cell Sci* 1995; **17.**

380. Sucosky P, Padala M, Elhammali A, *et al.* Design of an ex vivo culture system to investigate the effects of shear stress on cardiovascular tissue. *J Biomech Eng* 2008; **130:** 035001.

381. Dardik A, Chen L, Frattini J, *et al.* Differential effects of orbital and laminar shear stress on endothelial cells. *J Vasc Surg* 2005; **41:** 869-880.

382. Sutera SP, Nowak MD, Joist JH, *et al.* A programmable, computer-controlled cone-plate viscometer for the application of pulsatile shear stress to platelet suspensions. *Biorheology* 1988; **25:** 449-459.

383. team OpenFOAM. *The OpenFOAM Foundation* 2014; http://www.openfoam.org.

384. Jaffe EA, Nachman RL, Becker CG, *et al.* Culture of human endothelial cells derived from umbilical veins. Identification by morphologic and immunologic criteria. *J Clin Invest* 1973; **52:** 2745-2756.

385. Rouleau L, Rossi J, Leask RL. Concentration and time effects of dextran exposure on endothelial cell viability, attachment, and inflammatory marker expression in vitro. *Ann Biomed Eng* 2010; **38:** 1451-1462.

386. Rezakhaniha R, Agianniotis A, Schrauwen JT, *et al.* Experimental investigation of collagen waviness and orientation in the arterial adventitia using confocal laser scanning microscopy. *Biomech Model Mechanobiol* 2012; **11:** 461-473.

387. Marin V, Kaplanski G, Gres S, *et al.* Endothelial cell culture: protocol to obtain and cultivate human umbilical endothelial cells. *J Immunol Methods* 2001; **254:** 183-190.

388. Smeets EF, von Asmuth EJ, van der Linden CJ, *et al.* A comparison of substrates for human umbilical vein endothelial cell culture. *Biotech Histochem* 1992; **67:** 241-250.

389. Relou IA, Damen CA, van der Schaft DW, *et al.* Effect of culture conditions on endothelial cell growth and responsiveness. *Tissue Cell* 1998; **30:** 525-530.

390. Imberti B, Seliktar D, Nerem RM, *et al.* The response of endothelial cells to fluid shear stress using a co-culture model of the arterial wall. *Endothelium* 2002; **9:** 11-23.

391. Morigi M, Zoja C, Figliuzzi M, *et al.* Fluid shear stress modulates surface expression of adhesion molecules by endothelial cells. *Blood* 1995; **85:** 1696-1703.

392. Remuzzi A, Dewey CF, Jr., Davies PF, *et al.* Orientation of endothelial cells in shear fields in vitro. *Biorheology* 1984; **21:** 617-630.

393. Bustin SA. Absolute quantification of mRNA using real-time reverse transcription polymerase chain reaction assays. *J Mol Endocrinol* 2000; **25:** 169-193.

394. Benigni A, Corna D, Zoja C, *et al.* Disruption of the Ang II type 1 receptor promotes longevity in mice. *J Clin Invest* 2009; **119:** 524-530.

395. Dekker RJ, van Soest S, Fontijn RD, *et al.* Prolonged fluid shear stress induces a distinct set of endothelial cell genes, most specifically lung Kruppel-like factor (KLF2). *Blood* 2002; **100:** 1689-1698.

396. Novodvorsky P, Chico TJ. The role of the transcription factor KLF2 in vascular development and disease. *Prog Mol Biol Transl Sci* 2014; **124:** 155-188.

397. Lee JS, Yu Q, Shin JT, *et al.* Klf2 is an essential regulator of vascular hemodynamic forces in vivo. *Dev Cell* 2006; **11:** 845-857.

398. Wojciak-Stothard B, Ridley AJ. Shear stress-induced endothelial cell polarization is mediated by Rho and Rac but not Cdc42 or PI 3-kinases. *J Cell Biol* 2003; **161:** 429-439.

399. Scott SA, Selvy PE, Buck JR, *et al.* Design of isoform-selective phospholipase D inhibitors that modulate cancer cell invasiveness. *Nat Chem Biol* 2009; **5:** 108-117.

400. Frohman MA. The phospholipase D superfamily as therapeutic targets. *Trends Pharmacol Sci* 2015; **36:** 137-144.

401. Selvy PE, Lavieri RR, Lindsley CW, *et al.* Phospholipase D: enzymology, functionality, and chemical modulation. *Chem Rev* 2011; **111:** 6064-6119.

402. Disse J, Vitale N, Bader MF, *et al.* Phospholipase D1 is specifically required for regulated secretion of von Willebrand factor from endothelial cells. *Blood* 2009; **113:** 973-980.

403. Qin F, Impeduglia T, Schaffer P, *et al.* Overexpression of von Willebrand factor is an independent risk factor for pathogenesis of intimal hyperplasia: preliminary studies. *J Vasc Surg* 2003; **37:** 433-439.

404. Hsiai TK, Cho SK, Wong PK, *et al.* Monocyte recruitment to endothelial cells in response to oscillatory shear stress. *FASEB J* 2003; **17:** 1648-1657.

405. Nishiya N, Kiosses WB, Han J, *et al.* An alpha4 integrin-paxillin-Arf-GAP complex restricts Rac activation to the leading edge of migrating cells. *Nat Cell Biol* 2005; **7:** 343-352.

406. Goldfinger LE, Tzima E, Stockton R, *et al.* Localized alpha4 integrin phosphorylation directs shear stress-induced endothelial cell alignment. *Circ Res* 2008; **103:** 177-185.

407. Trusolino L, Bertotti A, Comoglio PM. MET signalling: principles and functions in development, organ regeneration and cancer. *Nat Rev Mol Cell Biol* 2010; **11:** 834-848.

408. Stein B, Kung Sutherland MS. IL-6 as a drug discovery target. *Drug Discovery* 1998; **3:** 202-2013.

409. Shoji M, Furuyama F, Yokota Y, *et al.* IL-6 mobilizes bone marrow-derived cells to the vascular wall, resulting in neointima formation via inflammatory effects. *J Atheroscler Thromb* 2014; **21:** 304-312.

410. Gerszten RE, Garcia-Zepeda EA, Lim YC, *et al.* MCP-1 and IL-8 trigger firm adhesion of monocytes to vascular endothelium under flow conditions. *Nature* 1999; **398:** 718-723.

411. Rectenwald JE, Moldawer LL, Huber TS, *et al.* Direct evidence for cytokine involvement in neointimal hyperplasia. *Circulation* 2000; **102:** 1697-1702.

412. Weber A, Wasiliew P, Kracht M. Interleukin-1 (IL-1) pathway. *Sci Signal* 2010; **3:** cm1.

413. Leon LR, Kozak W, Kluger MJ. Role of IL-10 in inflammation. Studies using cytokine knockout mice. *Ann N Y Acad Sci* 1998; **856:** 69-75.

414. Tilg H, Ulmer H, Kaser A, *et al.* Role of IL-10 for induction of anemia during inflammation. *J Immunol* 2002; **169:** 2204-2209.

415. Urschel K, Cicha I, Daniel WG, *et al.* Shear stress patterns affect the secreted chemokine profile in endothelial cells. *Clin Hemorheol Microcirc* 2012; **50:** 143-152.

416. Marrone D, Pertosa G, Simone S, *et al.* Local activation of interleukin 6 signaling is associated with arteriovenous fistula stenosis in hemodialysis patients. *Am J Kidney Dis* 2007; **49:** 664-673.

417. Allen KE, Varty K, Jones L, *et al.* Human venous endothelium can promote intimal hyperplasia in a paracrine manner. *J Vasc Surg* 1994; **19:** 577-584.

418. Moonen JA, Lee ES, Schmidt M, *et al.* Endothelial-to-mesenchymal transition contributes to fibro-proliferative vascular disease and is modulated by fluid shear stress. *Cardiovasc Res* 2015.

419. Lilly B. We have contact: endothelial cell-smooth muscle cell interactions. *Physiology (Bethesda)* 2014; **29:** 234-241.

420. Schepers A, Eefting D, Bonta PI, *et al.* Anti-MCP-1 gene therapy inhibits vascular smooth muscle cells proliferation and attenuates vein graft thickening both in vitro and in vivo. *Arterioscler Thromb Vasc Biol* 2006; **26:** 2063-2069.

421. Chan CY, Chen YS, Ma MC, *et al.* Remodeling of experimental arteriovenous fistula with increased matrix metalloproteinase expression in rats. *J Vasc Surg* 2007; **45:** 804-811.

422. Chan JS, Campos B, Wang Y, *et al.* Proliferation Patterns in a Pig Model of AV Fistula Stenosis: Can we Translate Biology into Novel Therapies? *Semin Dial* 2014; **27:** 626-632.

423. Asakawa H, Kobayashi T. The effect of coculture with human smooth muscle cells on the proliferation, the IL-1 beta secretion, the PDGF production and tube formation of human aortic endothelial cells. *Cell Biochem Funct* 1999; **17:** 123-130.

424. Chiu JJ, Chen LJ, Lee PL, *et al.* Shear stress inhibits adhesion molecule expression in vascular endothelial cells induced by coculture with smooth muscle cells. *Blood* 2003; **101:** 2667-2674.

425. Shav D, Gotlieb R, Zaretsky U, *et al.* Wall shear stress effects on endothelial-endothelial and endothelial-smooth muscle cell interactions in tissue engineered models of the vascular wall. *PLoS One* 2014; **9:** e88304.

426. Jiang Z, Yu P, Tao M, *et al.* Interplay of CCR2 signaling and local shear force determines vein graft neointimal hyperplasia in vivo. *FEBS Lett* 2009; **583:** 3536-3540.

427. Knippschild U, Kruger M, Richter J, *et al.* The CK1 Family: Contribution to Cellular Stress Response and Its Role in Carcinogenesis. *Front Oncol* 2014; **4:** 96.

428. Gross SD, Loijens JC, Anderson RA. The casein kinase Ialpha isoform is both physically positioned and functionally competent to regulate multiple events of mRNA metabolism. *J Cell Sci* 1999; **112 (Pt 16):** 2647-2656.

429. Fu Z, Chakraborti T, Morse S, *et al.* Four casein kinase I isoforms are differentially partitioned between nucleus and cytoplasm. *Exp Cell Res* 2001; **269:** 275-286.

430. Venerando A, Marin O, Cozza G, *et al.* Isoform specific phosphorylation of p53 by protein kinase CK1. *Cell Mol Life Sci* 2010; **67:** 1105-1118.

431. Ishibashi M, Hiasa K, Zhao Q, *et al.* Critical role of monocyte chemoattractant protein-1 receptor CCR2 on monocytes in hypertension-induced vascular inflammation and remodeling. *Circ Res* 2004; **94:** 1203-1210.

432. Salcedo R, Ponce ML, Young HA, *et al.* Human endothelial cells express CCR2 and respond to MCP-1: direct role of MCP-1 in angiogenesis and tumor progression. *Blood* 2000; **96:** 34-40.

433. Weber KS, Nelson PJ, Grone HJ, *et al.* Expression of CCR2 by endothelial cells : implications for MCP-1 mediated wound injury repair and In vivo inflammatory activation of endothelium. *Arterioscler Thromb Vasc Biol* 1999; **19:** 2085-2093.

434. Valen-Sendstad K, Piccinelli M, Steinman DA. High-resolution computational fluid dynamics detects flow instabilities in the carotid siphon: implications for aneurysm initiation and rupture? *J Biomech* 2014; **47:** 3210-3216.

435. Ene-Iordache B, Semperboni C, Dubini G *et al.* 2015 Disturbed flow in a patient-specific arteriovenous fistula for hemodialysis: Multidirectional and reciprocating near-wall flow pattern. *J Biomech* 2015; **48:** 2195-2200.

436. Rossi J, Rouleau L, Tardif JC, *et al.* Effect of simvastatin on Kruppel-like factor2, endothelial nitric oxide synthase and thrombomodulin expression in endothelial cells under shear stress. *Life Sci* 2010; **87:** 92-99.

437. Dick M, MacDonald K, Tardif JC, *et al.* The effect of simvastatin treatment on endothelial cell response to shear stress and tumor necrosis factor alpha stimulation. *Biomed Eng Online* 2015; **14:** 58.

438. Rossi J, Rouleau L, Emmott A, *et al.* Laminar shear stress prevents simvastatin-induced adhesion molecule expression in cytokine activated endothelial cells. *Eur J Pharmacol* 2010; **649:** 268-276.

439. Florescu MC, Birch N. Statin therapy and hemodialysis vascular access--were we bringing a knife to a gunfight and were hoping to win? *Semin Dial* 2012; **25:** 700-702.

440. Ali F, Zakkar M, Karu K, *et al.* Induction of the cytoprotective enzyme heme oxygenase-1 by statins is enhanced in vascular endothelium exposed to laminar shear stress and impaired by disturbed flow. *J Biol Chem* 2009; **284:** 18882-18892.

441. Rossi J, Jonak P, Rouleau L, *et al.* Differential response of endothelial cells to simvastatin when conditioned with steady, non-reversing pulsatile or oscillating shear stress. *Ann Biomed Eng* 2011; **39:** 402-413.

442. Bharat A, Jaenicke M, Shenoy S. A novel technique of vascular anastomosis to prevent juxta-anastomotic stenosis following arteriovenous fistula creation. *J Vasc Surg* 2012; **55:** 274-280.

443. Mohamied Y, Rowland EM, Bailey EL, *et al.* Change of Direction in the Biomechanics of Atherosclerosis. *Ann Biomed Eng* 2015; **43**: 16-25.

444. Wang C, Lu H, Schwartz MA. A novel in vitro flow system for changing flow direction on endothelial cells. *J Biomech* 2012; **45**: 1212-1218.

445. Wang C, Baker BM, Chen CS, et al. Abraham DJ. Endothelial cell sensing of flow direction. *Arterioscler Thromb Vasc Biol.* 2013; **33**: 2130-2136.

446. Feaver RE, Gelfand BD, Blackman BR. Human haemodynamic frequency harmonics regulate the inflammatory phenotype of vascular endothelial cells. *Nat Commun* 2013; **4**: 1525.

447. Katsube K, Sakamoto K, Tamamura Y, *et al.* Role of CCN, a vertebrate specific gene family, in development. *Dev Growth Differ* 2009; **51:** 55-67.

448. Holbourn KP, Acharya KR, Perbal B. The CCN family of proteins: structure-function relationships. *Trends Biochem Sci* 2008; **33:** 461-473.

449. Leask A, Abraham DJ. All in the CCN family: essential matricellular signaling modulators emerge from the bunker. *J Cell Sci* 2006; **119:** 4803-4810.

450. Bleau AM, Planque N, Perbal B. CCN proteins and cancer: two to tango. *Front Biosci* 2005; **10:** 998-1009.

451. Kawaki H, Kubota S, Suzuki A, *et al.* Cooperative regulation of chondrocyte differentiation by CCN2 and CCN3 shown by a comprehensive analysis of the CCN family proteins in cartilage. *J Bone Miner Res* 2008; **23:** 1751-1764.

452. Riser BL, Najmabadi F, Perbal B, *et al.* CCN3 (NOV) is a negative regulator of CCN2 (CTGF) and a novel endogenous inhibitor of the fibrotic pathway in an in vitro model of renal disease. *Am J Pathol* 2009; **174:** 1725-1734.

453. Abd El Kader T, Kubota S, Janune D, *et al.* Anti-fibrotic effect of CCN3 accompanied by altered gene expression profile of the CCN family. *J Cell Commun Signal* 2013; **7:** 11-18.

454. Leask A. It's a knockout: CCN3 suppresses neointimal thickening. *J Cell Commun Signal* 2010; **4:** 109-110.

455. Lin Z, Natesan V, Shi H, *et al.* A novel role of CCN3 in regulating endothelial inflammation. *J Cell Commun Signal* 2010; **4:** 141-153.

456. Neth P, Nazari-Jahantigh M, Schober A, *et al.* MicroRNAs in flow-dependent vascular remodelling. *Cardiovasc Res* 2013; **99:** 294-303.

457. Andreou I, Sun X, Stone PH, *et al.* miRNAs in atherosclerotic plaque initiation, progression, and rupture. *Trends Mol Med* 2015; **21:** 307-318.

458. Ni CW, Qiu H, Jo H. MicroRNA-663 upregulated by oscillatory shear stress plays a role in inflammatory response of endothelial cells. *Am J Physiol Heart Circ Physiol* 2011; **300:** H1762-1769.

459. Wu W, Xiao H, Laguna-Fernandez A, *et al.* Flow-Dependent Regulation of Kruppel-Like Factor 2 Is Mediated by MicroRNA-92a. *Circulation* 2011; **124:** 633-641.

460. Peiffer V, Sherwin SJ, Weinberg PD. Computation in the rabbit aorta of a new metric-the transverse wall shear stress- to quantify the multidirectional character of disturbed blood flow. *J Biomech* 2013; **46:** 2651–2658.

461. Usatyuk PV, Kotha RS, Parinand NL, *et al.* Phospholipase D signaling mediates reactive oxygen species-induced lung endothelial barrier dysfunction. *Pulm Circ* 2013; **3**:108-315.

462. Lum H, Roebuck KA. Oxidant stress and endothelial cell dysfunction. *Am J Physio Cell Physiol* 2001; **280**: C719-41.

463. Chistiakov DA, Sobenin IA, Orekhov AN, et al. Human miR-221/222 in physiological and atherosclerotic vascular remodeling. *Biomed Res Int* 2015; 1-18.

464. Anand S, Majeti BK, Acevedo LM, *et al.* MicroRNA-132-mediated loss of p120RasGAP activates the endothelium to facilitate pathological angiogenesis. *Nat Med.* 2010; **16**: 909-14.

465. Marin T, Gongol B, Chen Z, *et al.* Mechanosensitive microRNAs-role in endothelial responses to shear stress and redox state. *Free Radic Biol Med* 2013; **64**: 61-8.

466. Qi L, Zhang Y. The microRNA 132 regulates fluid shear stress-induced differentiation in periodontal ligament cells through mTOR signaling pathway. *Cell Physiol Biochem.* 2014; **33**:433-45.

Appendix A

To evaluate the influence of the mesh used to discretize the fluid volume in the CFD simulation of the Cone-and-Plate device, we performed a mesh sensitivity test using three different meshes. A coarse (69K elements), medium (138K elements) and fine mesh (270K elements) were constructed and used in flow simulations as describe in Chapter 3. Here we reported the results of the test.

A1) Mesh sensitivity test

As shown in figure A1, in the plate region of interest, no major differences using the three meshes were found in calculating the effective WSS delivered at plate level for PUL_A waveform. However, the used meshes return different WSS value at the outer border of the plate (r=6.75 cm, figure A2), and in particular coarser meshes return higher values of WSS. Similar results were obtained in REC_A simulation (figures A3 and A4). Furthermore no appreciable differences were found in terms of WSS peak magnitude and mean value, as shown in the table of the figures A2 and A4.

According to these results, since no differences emerged respect to 270K mesh, the 138K mesh has been used to simulate the WSS waveforms of the present studies, as described in Chapter 3.

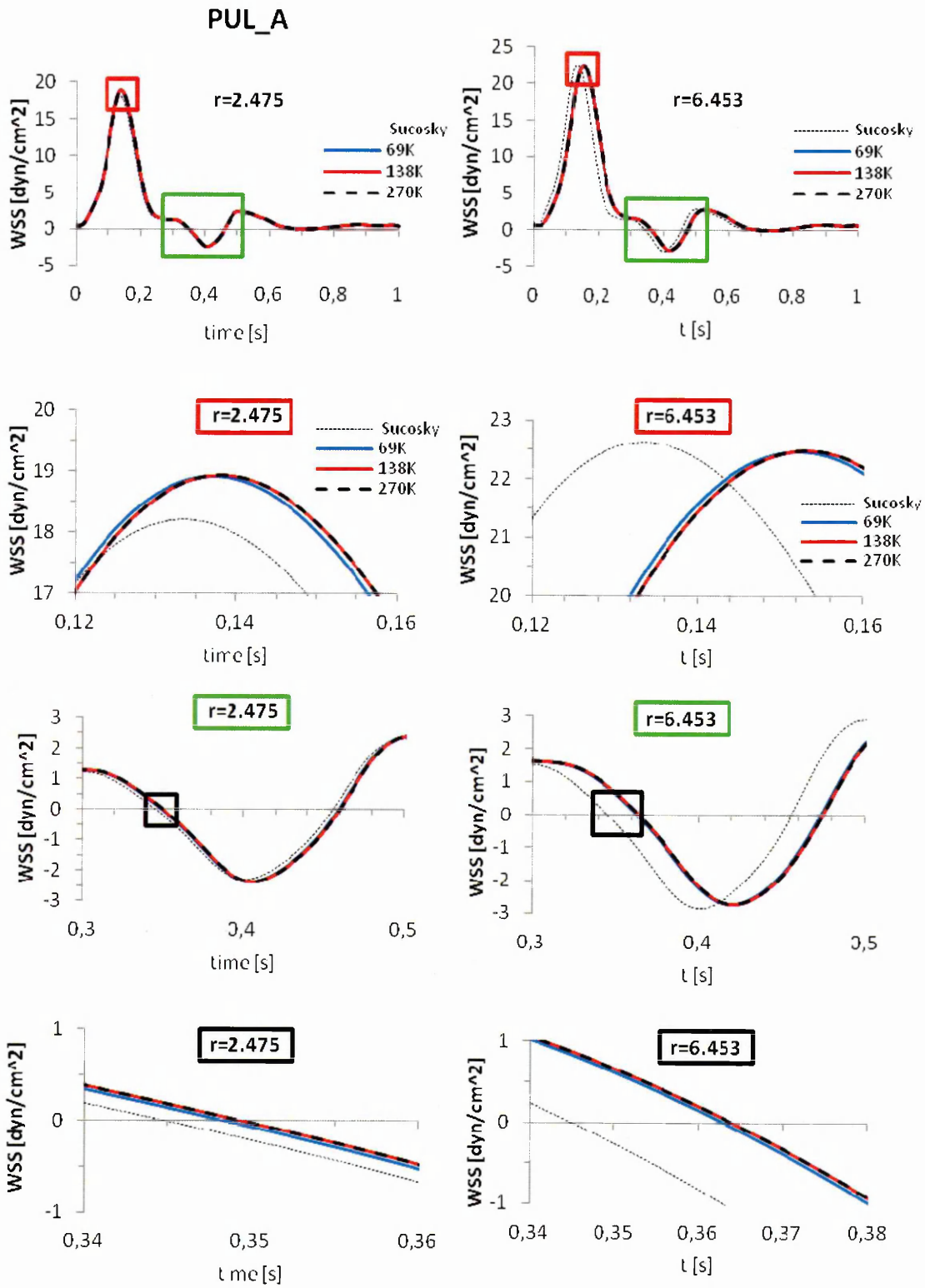

Fig.A1: The graphs represent the result obtained by simulating PUL_A WSS profile with the three different meshes, at different radial positions (r = 2.475 cm and r = 6.453 cm), compared to results obtained using Sucosky formula [3] at the same radius.

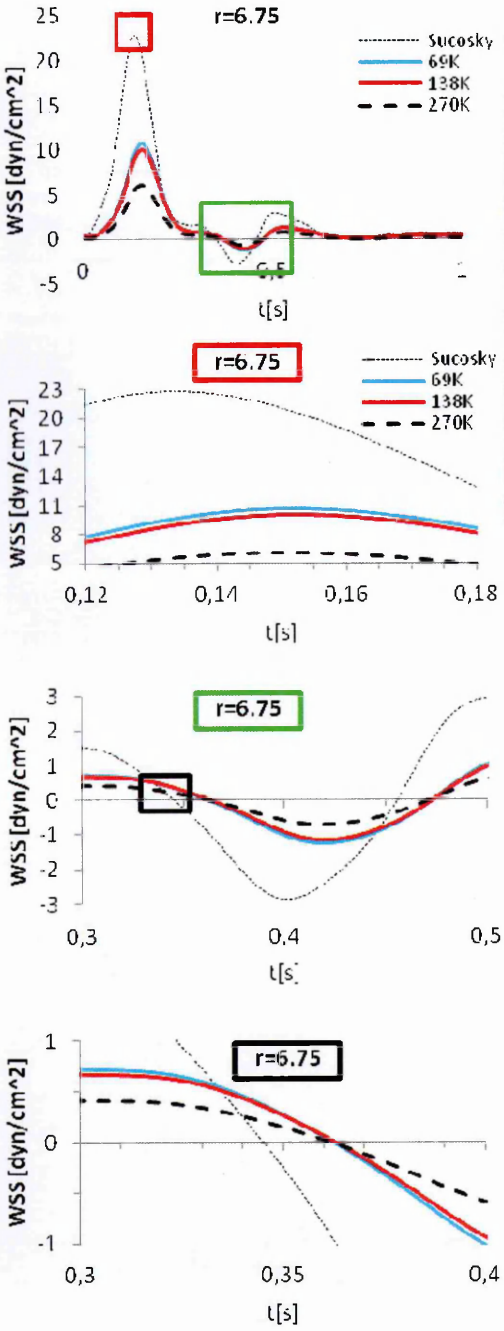

PUL_V

r=2,475 cm	69K	138K	270K	Sucosky
WSS peak	18,919	18,925	18,925	18,214
WSS mean	2,391	2,392	2,392	2,292
OSI	0,058	0,058	0,058	0,059
r=6,453 cm	69	138	270	Sucosky
WSS peak	22,476	22,483	22,483	22,629
WSS mean	2,981	2,982	2,982	2,848
OSI	0,055	0,055	0,055	0,059
r=6,75 cm	69	138	270	Sucosky
WSS peak	10,680	10,010	6,122	22,780
WSS mean	1,380	1,289	0,785	2,867
OSI	0,055	0,055	0,055	0,059

Fig.A2: The graphs represent the result obtained by simulating PUL_A WSS profile with the three different meshes, at the outer border of the fluid domain (r = 6.75 cm), compared to results obtained using Sucosky formula [3] at the same radius. The table shows the WSS peak and mean values obtained in the different conditions.

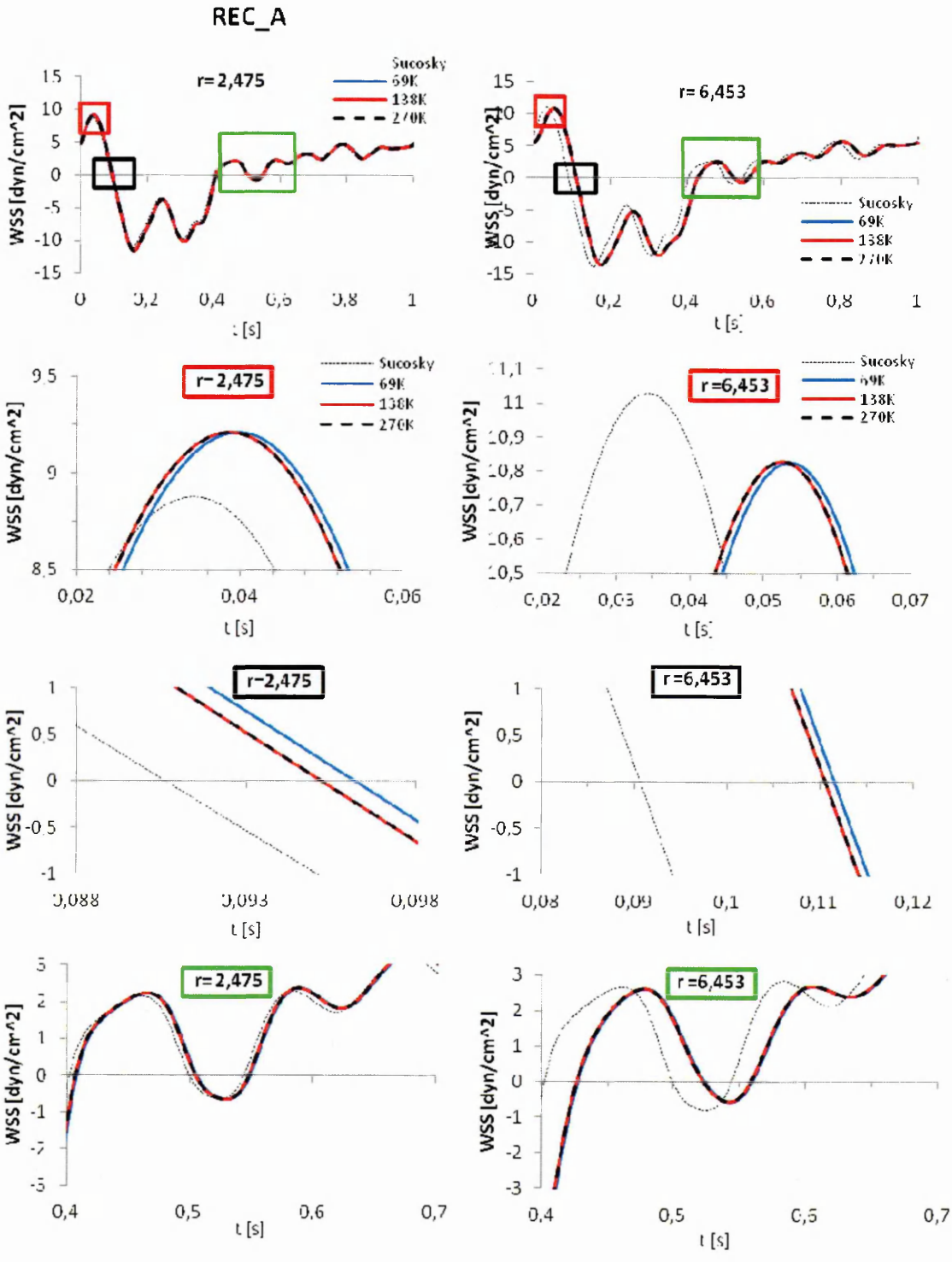

Fig.A3: The graphs represent the result obtained by simulating REC_A WSS profile with the three different meshes, at different radial positions (r = 2.475 cm and r = 6.453 cm), compared to results obtained using Sucosky formula [3] at the same radius.

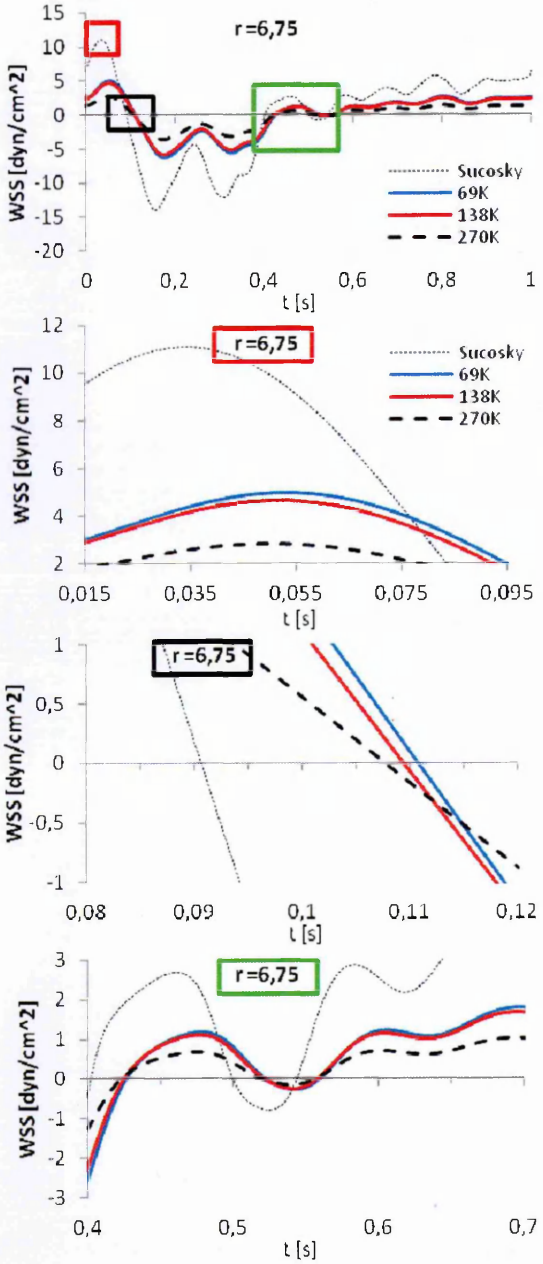

REC_A

r=2,475 cm	69K	138K	270K	Sucosky
WSS peak	9,209	9,212	9,212	8,877
WSS mean	0,054	0,054	0,054	0,053
OSI	0,494	0,494	0,494	0,494
r=6,453 cm	**69**	**138**	**270**	**Sucosky**
WSS peak	10,825	10,829	10,829	11,029
WSS mean	0,068	0,068	0,068	0,065
OSI	0,494	0,494	0,494	0,494
r=6,75 cm	**69**	**138**	**270**	**Sucosky**
WSS peak	4,982	4,657	2,853	11,103
WSS mean	0,021	0,019	0,013	0,066
OSI	0,495	0,495	0,495	0,494

Fig.A4: The graphs represent the result obtained by simulating REC_A WSS profile with the three different meshes, at the outer border of the fluid domain (r = 6.75 cm), compared to results obtained using Sucosky formula [3] at the same radius. The table shows the WSS peak and mean values obtained in the different conditions.

Appendix B

To evaluate the cytoskeleton reorganization and the cell shape of HUVECs exposed to different flows, two open-source software have been used. The orientation of F-actin stress fibers was evaluated using an ImageJ plug-in, OrientationJ, developed by the EPFL (Lousanne, CH). Furthermore, Cell Profiler, developed by the Broad Institute (Cambridge, USA) has been used to measure cells elongation and alignment. Herein are reported the detailed methods used to obtain the results presented in the Chapter 4.

B1) OrientationJ

The software acquires the immunofluorescence image of HUVECs monolayer stained for F-actin (red) and nuclei (blue). The image is split into its RGB colour components. The red channel image is then transformed into a 32bit image in order to be processed by the software. In the images below (figure B1.A and B1.B) are reported the software settings and an example of the results.

B2) Cell Profiler

The software acquires the immunofluorescence images of HUVECs monolayer stained for tight junction protein ZO-1 (green) and nuclei (blue). The image is then processed according to a "*pipeline*" defined by the user within the software interface. A cascade of modules that perform different activities composes each pipeline. Two pipelines were defined (figures B2.A and B2.B), one for elongated cells and one for the cobblestone shape cells. Basically the software acquires the image and processes it in order to ameliorate the signal. After image processing, a dedicate module performs the automatic recognition of nuclei according the user specification. From the recognized

nuclei, the software recognizes the surrounding cell body according the method defined by the user. The main difference between the two pipelines is the method used to identify cell body. Elongated cells were recognized by "*Watershed-gradient*" filter while cobblestone cells were recognized by "*Propagation*" filter. However, both the pipelines have a module to manually correct the eventual errors made the automatic recognition modules.

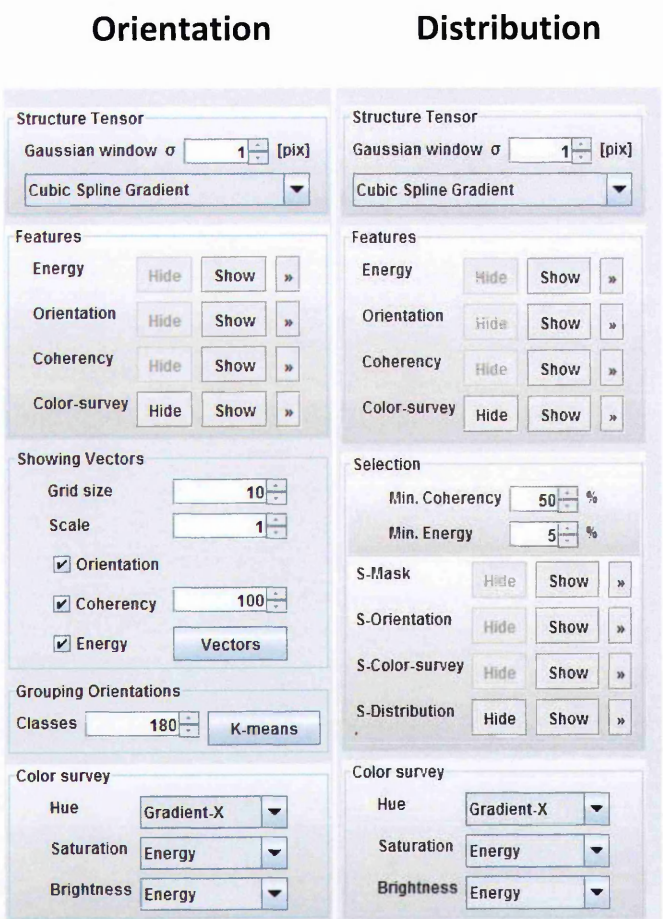

Fig.B1.A: OrientationJ settings used to analyze immunofluorescence images.

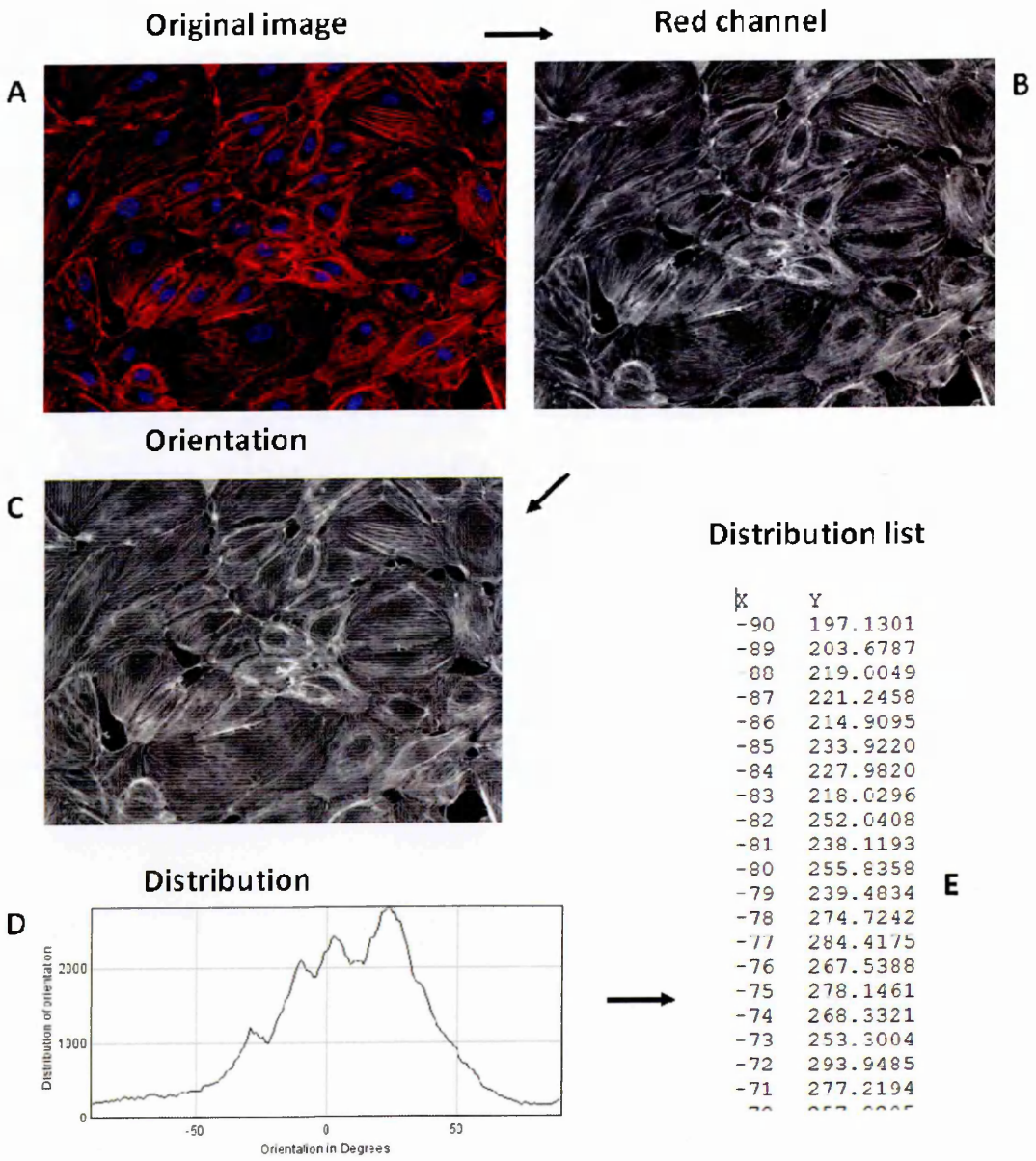

Fig.B1.B: Flowchart of the procedure used to analyze immunofluorescence images.

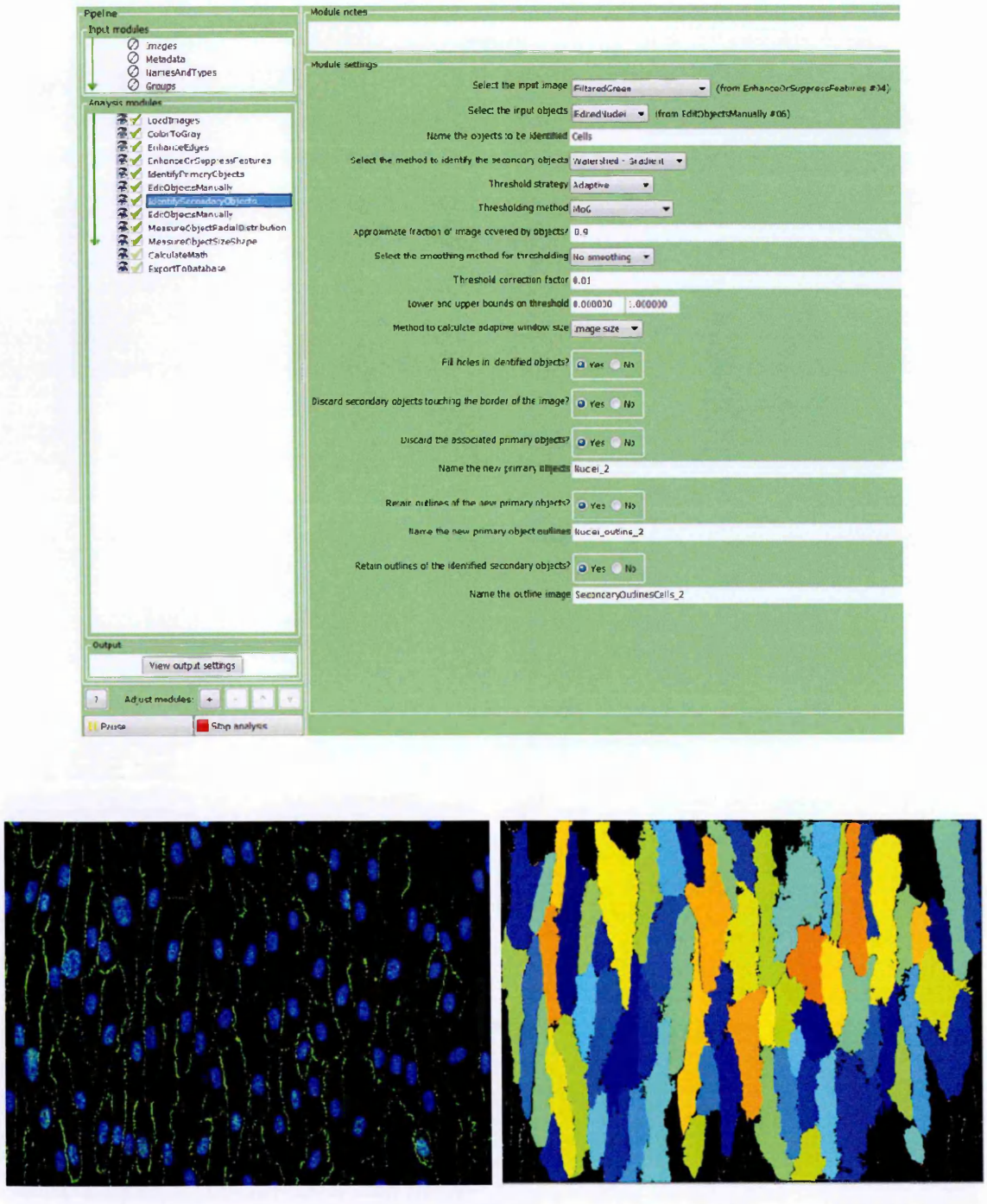

Fig.B2.A: Pipeline used to identified elongated cells and an example of result.

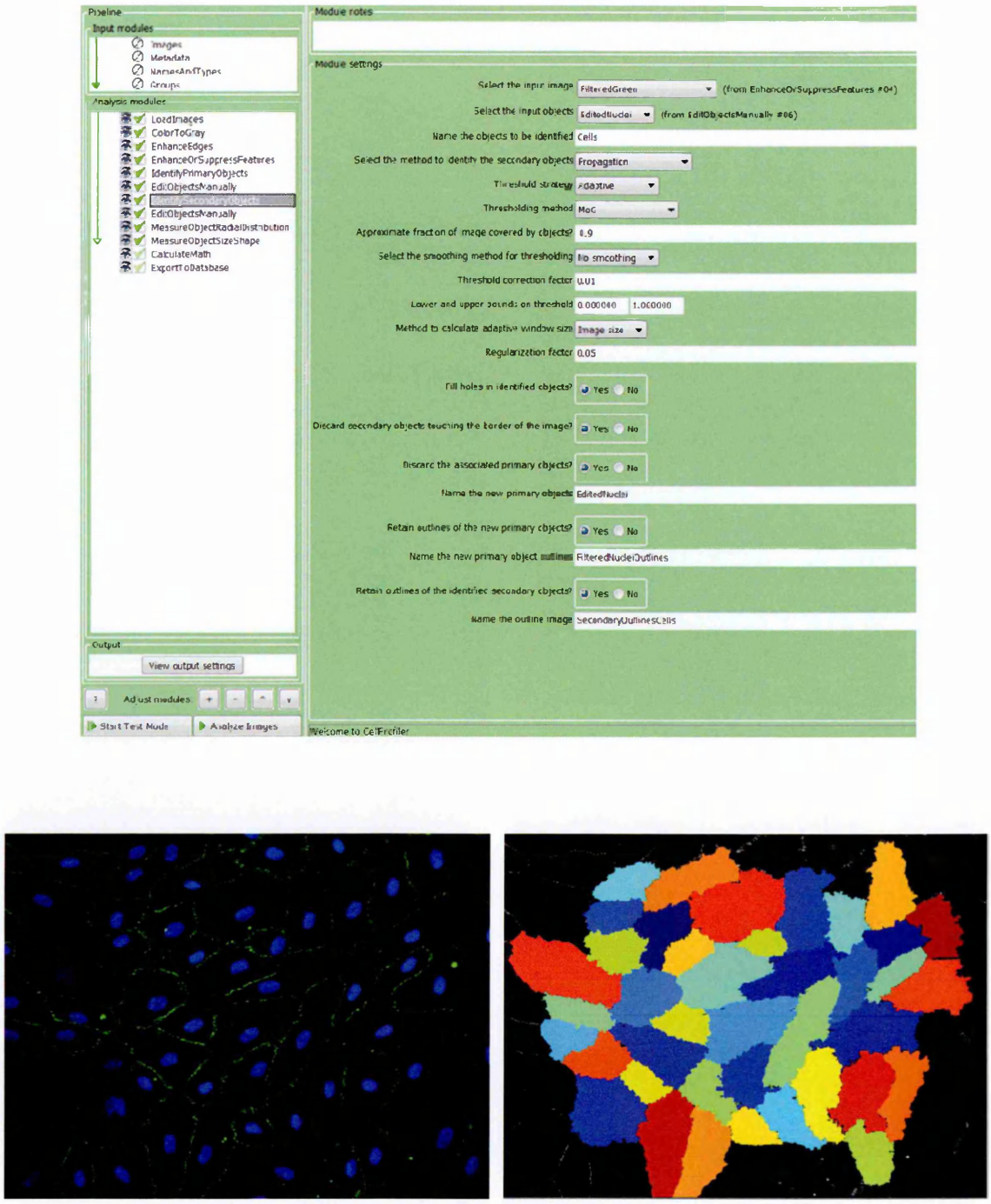

Fig.B2.B: Pipeline used to identified cobblestone cells and an example of result

Acknowledgments

Contributes to the thesis by other researchers

The work presented in this thesis has been carried on at the laboratory of Tissue Engineering for Regenerative Medicine of the "Mario Negri" Institute (IRFMN). Part of the presented data have been obtained with the collaboration of other researchers as follows:

Irene Cattaneo (BSc, Laboratory of Tissue Engineering for Regenerative Medicine, IRFMN) has collaborated to the flows exposure experiments, ELISA analysis and Smooth Muscle Cell proliferation experiments.

Bogdan Ene-Iordache (MEng, PhD, Head of Laboratory of Biomedical Technologies, IRFMN) provided the Wall Shear Stress waveforms investigated in the present work and has collaborated to Cone-and-Plate device flow simulations.

Lorena Longaretti (MBiolSc, Laboratory of Gene Therapy and Cellular Reprogramming, IRFMN) has collaborated to gene assay and RT-PCR analysis.

Rubina Novelli (MBiolSc, Laboratory of Advanced Microscopy, IRFMN) has collaborated to SEM imaging.

Andrea Resovi (MBiolSc, Laboratory of Tumor Angiogenesis, IRFMN) has collaborated to Milliplex analysis.

Furthermore a great contribute to the project was given by:

Marina Figliuzzi (MBiolSC, Head Laboratory of Tissue Engineering for Regenerative Medicine, IRFMN) for the contribution to the results analysis.

Andrew James Narracott (MPhys, PhD, Lecturer at the Department of Cardiovascular Science, University of Sheffield) for the contribution to the preparation of this script.

Andrea Remuzzi (EngD, Head of Biomedical Engineering Department, IRFMN) for the contribution to experimental design and to the results analysis.

Publications emanating from this work

"The Molecular Mechanisms of Arteriovenous Fistula Failure" (Review, Kidney international, in press).

"Design of a Cone-and-Plate device for controlled realistic wall shear stress stimulation on endothelial cell monolayers" (**M. Franzoni** et al, Original research article, Cytotechnology, accepted).

"Endothelial cell activation by hemodynamic shear stress derived from arteriovenous fistula for hemodialysis" (**M. Franzoni** et al, Am J Physiol Heart Circ Physiol. 2015 Oct 23. doi: 10.1152/ajpheart.00098.2015.).

Congress presentations performed by PhD candidate, Marco Franzoni

Poster presentations

"In-vitro Exposure of Endothelial Cells to Shear Stress Derived from Hemodialysis Vascular Access". M. Franzoni et al. *Gruppo Nazionale di Bioingegneria*, Pavia, Italy, 2014.

"A Compact Apparatus for Stimulation of Endothelial Cells with Realistic Flow Patterns". M. Franzoni et al. *World Congress of Biomechanics*, Boston, USA, 2014.

Oral presentation

"In-vitro Wall Shear Stress Waveforms Derived from Arteriovenous Fistula Elicit Endothelial Cell activation and Neointimal Hyperplasia Related Molecule Production" M. Franzoni et al. *European Congress of Biomechanics*, Prague, CZ, 2015.

Acknowledgments

I would like to express my appreciation and gratitude to the International Non-profit Foundation "Aiuti per la Ricerca sulle Malattie Rare" (Fondazione Internazionale Onlus "Aiuti per la Ricerca sulle Malattie Rare") and in particular to the "Giuseppe Maestri" foundation for the donation in the memory of Mirina Penna of the scholarship that founded my PhD program and in general for their great contribution to the research activities performed at the "Mario Negri" Institute.

I am deeply grateful to Dr. Andrea Remuzzi, Director of Studies, for giving me opportunity to attend PhD course and for his support and patience over these years.

My gratitude goes also to Dr. Andrew James Narracott, external supervisor, for the tutoring I received and for the time he dedicated to supervise my work.

I am mainly in debt to Dr. Irene Cattaneo, for her invaluable contribution in all the experimental phases and for the expertise that she kindly transfer to me.

Special thanks to all the contributors of this study and to the personnel of the "Mario Negri" Institute that has harbored me during these four years.

Finally to my family and my friends, who support and encourage me daily.